ALMA MATER STUDIORUM
UNIVERSITÀ DI BOLOGNA

DOTTORATO DI RICERCA IN

Ingegneria Biomedica Elettrica e dei Sistemi IBES

Ciclo XXXVI

Settore Concorsuale: 9/E1 Elettrotecnica

Settore Scientifico Disciplinare: ING-IND/31

Development of flux pump-based supply systems for superconducting coils

Presentata da: *Giacomo Russo*

Coordinatore Dottorato

Prof. Michele Monaci

Supervisore

Prof. Antonio Morandi

Co-supervisore

Prof. Pier Luigi Ribani

Abstract

Conventional power supplies for superconducting magnets rely on dissipative power electronic converters and current leads, which are a thermal path connecting room temperature to cryogenic superconductors, as well as an additional source of joule dissipation, thereby imposing a significant heat load on the cooling system.

Flux pumps offer a contactless, low-voltage, and high-current alternative to power electronics exciters and current leads solutions. However, as flux pumps physical mechanism is complex and counterintuitive, their engineering process and development of viable and executive designs have proved to present major challenges.

This Ph.D. project focused on numerical modeling, investigation, and engineering analysis of flux pumps. The research aimed to address gaps in scientific research surrounding the technology and its potential disruptive impact on enabling contactless and efficient energization of superconducting magnets. First, a numerical model was developed and validated against experimental results to unveil the intricacies related to voltage rectification in traveling field flux pumps. The model embeds artificial intelligence methods to address the relationship between critical current and n-value of HTS tapes concerning temperature and magnetic field. A new complete equivalent circuit was derived and exploited for fast system-oriented analysis of flux pumps. The numerical model was further exploited to develop an application-oriented optimal design procedure for traveling field flux pumps, which was tested to design and characterize a HTS dynamo and a linear flux pump for real applications. The study found that the performance of the flux pumps is highly dependent on the rated current and its total resistance and discussed the influence of these two load parameters on the viability of flux pumps.

Overall, this Ph.D. project aimed to overcome the empirical approach with which flux pumps have been designed and analyzed for decades and applied a systematic engineering method to facilitate its implementation in real applications.

Acknowledgements

Contents

"Nothing is too wonderful to be true,
if it be consistent with the laws of nature"

Michael Faraday

1. Chapter 1: Introduction to flux pumps and state of the art

1.1. Context and motivation

Superconducting magnet technology is nowadays rapidly progressing with the advent of modern commercial High Temperature Superconductor (HTS) materials. It is a matter of fact that HTS magnets will play a key role in sustainable transportation, energy, research, and industry in the future. Current injection and maintenance in HTS magnets are obtained with metal current leads connected to room temperature power supply, combined with rotary joints when the magnet is employed in rotating machines for power generation or propulsion. These components severely limit the potential of superconducting magnets by negatively impacting the efficiency, cost, and reliability of the systems. When a high current is to be reached, like in the case of fusion reactor magnets, the power supply itself is extremely complex and costly, and causes significant harmonic disturbance on the power grid too. All these limitations that prevent a complete penetration of high-performance HTS magnets systems make the case for innovative supply concepts.

Flux pumping is a promising technology, potentially able to produce breakthrough innovation in the supply of HTS magnets, which offers a contactless, low-voltage, and high-current alternative to power electronics exciters and current leads solutions. A flux pump is essentially a superconducting contactless power transfer device, connecting a DC superconducting load to its AC power supply. Figure 1 shows a schematic comparison of the conventional solution based on current leads for energizing a superconducting (SC) magnet (a), against the alternative based on a flux pump (b). First, it must be pointed out that blocks labelled as "Power supply and converters" refer to different technologies and devices from Figure 1.a and Figure 1.b. The typical power supplies of conventional solution are based on power electronic

converters which are designed to carry the same high current of the magnet, resulting in large dissipations (and great reactive power absorption too). The converters shown in Figure 1.b are specifically designed to supply the exciter of the flux pump. They do not carry the same current of the magnet and are not required to manage excessive power, resulting in significantly lower dissipation compared to conventional solutions. In Figure 1.a, the power supplies are not the only bulky components; the current leads may also demand extensive space, often necessitating complex and convoluted pathways. A heat load of approximately 40-50 W/kA is also associated to each current lead penetrating the cryostat wall. The 'Flux pump' block, delineated by the green dashed line in Figure 1.b, serves as a general schematic representation of the device and does not specifically depict any particular topology. In cases involving transformer rectifiers, for instance, the components of the flux pump within the cryostat should be illustrated with a minimum of two switches. In reference to Figure 1.b, a crucial general characteristic illustrated is the thermal and electrical separation between the exciter and the superconducting component responsible for generating the output voltage (as denoted by the symbols + and − in the diagram). This separation allows to save all the current leads heat load that has been described earlier for the traditional solution.
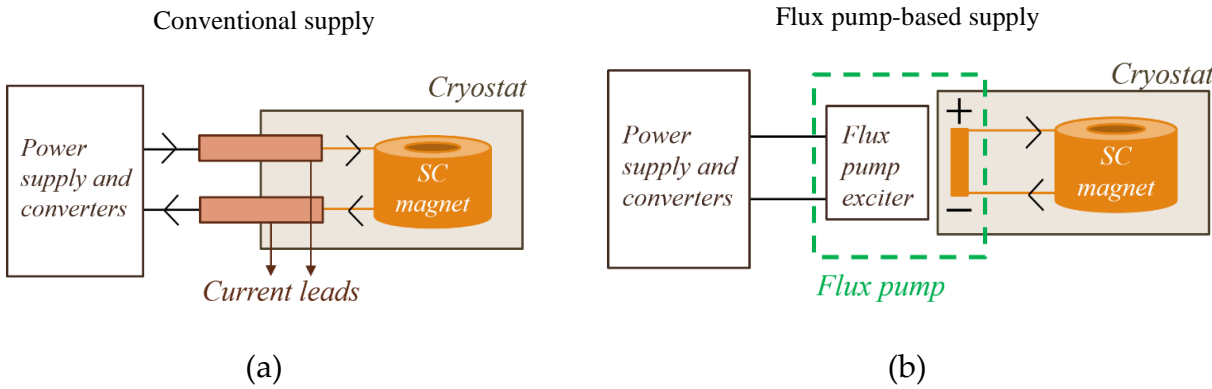
Figure 1 (a) Schematic of a traditional power supply chain of superconducting magnets vs a (b) Schematic of a flux pump-based power supply chain of superconducting magnets

Recent studies have also quantitatively addressed the potential advantages of flux pumps in comparison to conventional solutions for the supply of superconducting magnets in practical applications. For the case of wind power generators exciters, Sung et al. calculated a heat load of 10.2 W using a flux pump against 31.8 W employing current leads when supplying a 12 MW wind generator [1] [2]. Rice et al. estimated a potential reduction of 90 % and 98 % of cryogenic load for charging and maintaining 60 kA into the toroidal field coils of fusion magnets, proving massive space saving as well [3]. Flux pumps could also bring benefits to the biomedical industry, in fact, Wang et al. designed and constructed a compact 1.5 T HTS MRI system dedicated for human joint diagnosis [4] [5], whilst Coombs et al. are currently constructing a portable MRI for human head scanning employing a flux pump [6]. The potential of flux pumps was recently acknowledged for HTS-enhanced Applied-Field Magnetoplasmadynamic (AF-MPD) thrusters as well, where as much as 80 %–90 % of the total cooling power requirement is related to the heat load of the current leads [7].

Despite flux pumps have received increased attention in recent years, the underneath concept is not new. To my knowledge, the first suggestion to use induction for eliminating the heat conduction due to current leads dates back to 1933, when a so-called flux concentrator was developed by Mendelssohn [8]. Several methods to store magnetic energy that are equivalent to the combination of an AC transformer and a rectifier were proposed the following years, like in 1938, when Felici first used the term "aasuperconducting switches" [9]. In 1940, Felici also recalled the concept of the dynamo on a theoretical level [10]. In the following decades, massive efforts were spent to reproduce, validate, and upscale the flux pump technology, and excellent reviews were produced to record them [11] [12] [13] [14]. Despite numerous studies and experimental demonstrations, there hasn't been a significant breakthrough establishing flux pumps as the leading technology for energizing superconducting magnets during the 20th century. This lack of progress can be attributed partly to the absence of necessity for flux pumps when dealing with low-temperature superconducting (LTS) magnets handling moderate currents. In fact, the possibility to

achieve zero resistance in LTS joints allows for a persistent current operation for this class of magnets, enabling solutions involving detachable current leads used during charging and removed afterward, along with a parallel superconducting switch. This switch remains open during magnet charging and closes just before removing the current leads, allowing it to carry the magnet's current nearly indefinitely. However, in the case of HTS magnets or those requiring frequent field adjustments, the scenario changes. The persistent current mode cannot be sustained due to the HTS intra-magnet joints, which would cause the current to decay if a parallel superconducting switch was used. Furthermore, the prospect of ultra-high current LTS magnets, reaching tens of thousands of amperes, currently under consideration for emerging technologies like fusion reactors, could significantly benefit from contactless power supplies by eliminating the requirement for energy-intensive high current power electronic converters. The advent of high current superconduting applications and the maturity of the HTS technology have made a new case for flux pumps, reviving new interest around them.

1.2. The flux pump general behavior

No one argues that when a loop experiences a periodically varying linked magnetic flux, the electromagnetic force that is induced according to the well-known Faraday-Lenz law is also periodic and has no DC component, meaning its average over one period of the magnetic flux is zero. This law governs the mechanism of all electrical machines, from motors to generators and transformers. The reason for stating such obvious sentences is stressing the state of confusion that a flux pump provokes the first time it is encountered. Constructively speaking, a flux pump is equivalent to any electrical machine, hence it comprises an exciter, which creates a periodic magnetic flux of whichever waveform, and an induced part. The only constructive feature that characterizes flux pumps is the superconducting nature of one or more of its components. If the output voltage is measured at the terminals of the flux pump during its operation, it can be calculated that its average over one period of the magnetic flux is not zero, thus apparently violating the Faraday-Lenz law. Of course, no violation to any physics law is ever in place, but this counterintuitive phenomenon has been largely debated over the last few decades, generating theories and speculations. Resuming the stages of the debate is not the purpose of the present Ph.D. project, therefore, in this section, I offer a general description of the behavior, with detailed explanations for each topology's physical mechanism to be presented later.

The fact that the average of the output voltage over a period of the excitation field is not zero is a clear manifestation that, operationally speaking, a flux pump functions as a rectifier-type converter. Indeed, the flux pump general behavior is widely described using an electrical circuit which is very similar to the one of the rectifiers, as it is also shown in Figure 2.a for the case of a half wave type. In the equivalent electrical circuit of Figure 2.a, which refers to a current loop composed by the flux pump and a superconducting magnet as the load, the components have the following meanings:

- *emf* is the electromotive force occurring due to a varying magnetic flux ϕ which is linked to the loop.

- V_{out} is the output voltage at the terminals of the flux pump, namely the voltage that a load experiences when it is connected to the flux pump.

- $L_{flux\ pump}$ is the coefficient of auto inductance associated to the sub loop inside the box labelled as "Flux pump" in Figure 2.a.

- S_1 and S_2 are two ideal switches whose operation change the topology of the circuit. Such components correspond to real switches for the transformer rectifier flux pump type, whereas they are not present for other topologies where their effect is imitated in other physical ways that are described in the next sections.

- L_{load} represents the coefficient of auto inductance of the superconducting magnet which is energized by the flux pump, and I is the current flowing through it at one instant.

- T represents the period (in seconds) of the *emf*.

The general behavior of the flux pump is illustrated starting from Figure 2.b: a positive *emf* is present because of a time-varying flux ($-d\phi/dt$) in the loop while S_1 is closed and S_2 is open. For analytical simplicity, a linear variation of the flux is considered, resulting in a constant *emf*. During this phase, that lasts half a period, I increases and the magnet gets energized.

The first change in topology of the circuit is shown in Figure 2.c, where S_2 is closed. S_1 is still closed too at this point because, in the meantime, the flux ϕ that had been added in the loop in the previous phase starts to be removed, resulting in an *emf* sign inversion. S_1 and S_2 must stay both closed for some time because of $L_{flux\ pump}$ that prevents the current I_1 (in red in Figure 2.c) to change instantly. After I_1 reaches zero and I_2 (in blue in Figure 2.c) equalizes I, S_1 opens and phase (d) begins. Nothing happens during the phase of Figure 2.d, and no decay of I occurs because all resistive dissipations are neglected. One operation period is concluded when phase (d) ends, and the cycle repeats until final energization. It is specified that when phase (b) starts for a second time it is anticipated by another subphase, during which both S_1 and S_2

are closed, dedicated to the complete redistribution of current from I_2 to I_1. This subphase is not shown in Figure 2 for the sake of simplicity.
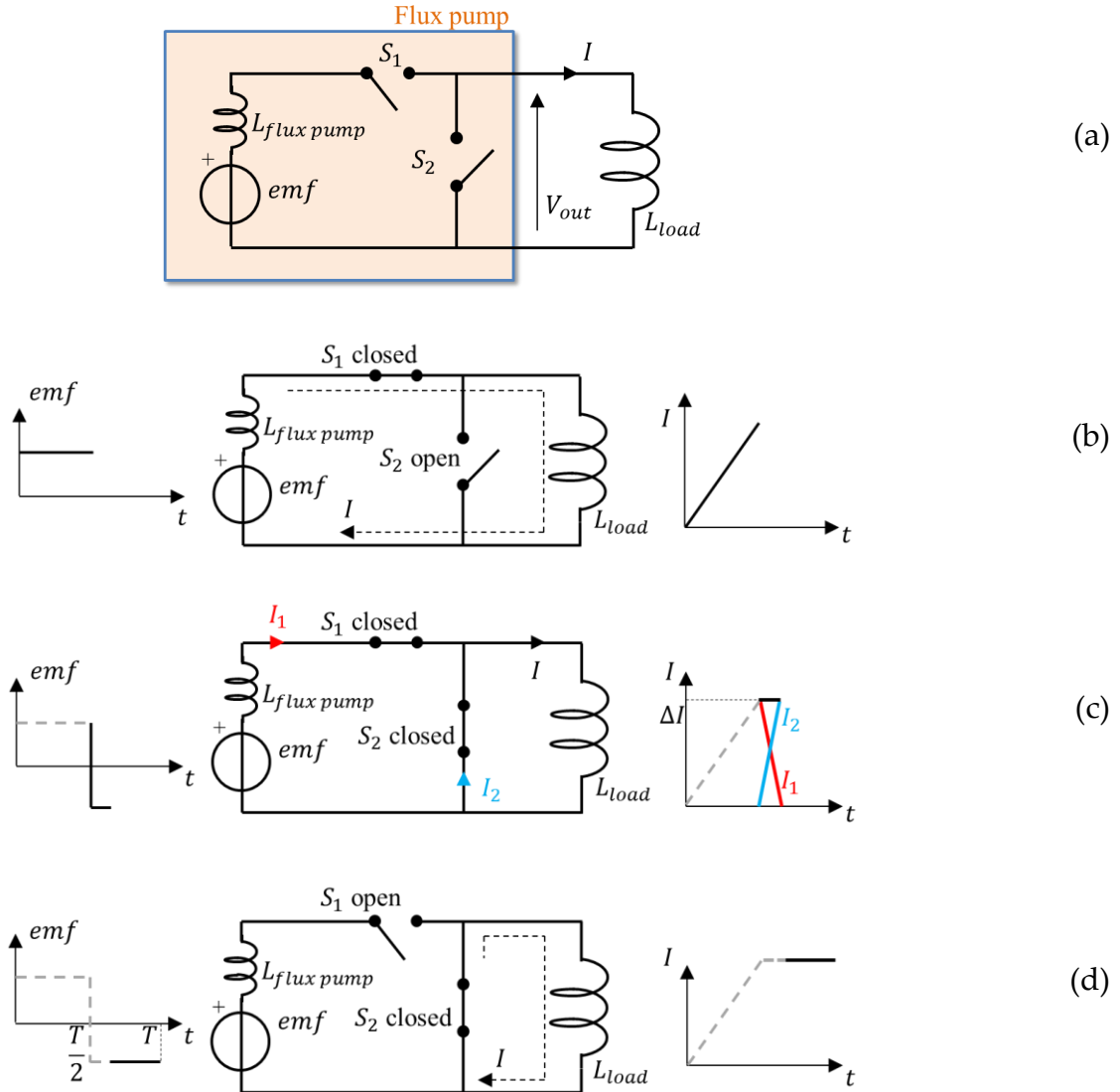
Figure 2 (a) Electrical scheme for describing the general behavior of flux pumps in terms of voltage rectification. Stages (b)-(d) describe the periodical operation that results in the energization of a inductive load coil that is coupled with the flux pump.

Current I does not continue to increase indefinitely but reaches saturation after some time. To explain the reason for this, the operation of the circuit of Figure 2 is described quantitively hereafter. During phases (b) lasting $\Delta t = 1/2f$ (where f is the frequency equal to $1/T$, in the assumption that phases (b) and (c) both take half period T) I increases of a quantity ΔI according to Eq. (1).

$$\frac{emf \times \frac{1}{2f}}{L_{coil} + L_{flux\ pump}} = \Delta I \qquad (1)$$

Therefore, period after period, phases (c) will have to redistribute more current from I_1 to I_2. It will arrive at a point that this redistribution will take the entire duration of phase (c), according to Eq. (2).

$$\frac{emf \times \frac{1}{2f}}{L_{flux\ pump}} = I_{max} \qquad (2)$$

Where I_{max} is the final value of current I reached at the end of the previous phase (b). It is evident from Eq. (2) that optimizing the current capacity of the rectifier flux pump corresponds to minimizing the inner inductance of the source and maximizing the applied electro motive force. The previous considerations apply when for S_1 and S_2 are soft switches that open at the current zero crossing.

Subsequent phase (d) will be also completely dedicated to the opposite current redistribution, according to Eq. (2). It follows that I_{max} corresponds to the saturation current, which is the maximum value attainable by the flux pump. In descending order of importance, some considerations can be derived from here:

- Assuming the load is purely inductive, I_{max} does not depend on the load, but only on its internal characteristics ($L_{flux\ pump}$), the external magnetic field forming the linked flux, and the dynamic of the operation (f).
- Eq. (1) and (2) are valid in the ideal assumption of no joule dissipation in the circuit. Introducing resistances in circuit to account for real losses would imply a current decay during phases (c), (d), and the one after (d) during which redistribution of current from I_2 to I_1 must take place. Both a ripple and a reduction of the maximum current would be observed; hence I_{max} can be redefined as the ideal maximum attainable current of the flux pump.
- For non-simplified analysis with varying V, its integral over time should be used in Eq. (1) and (2).

- If $L_{flux\ pump}$ was zero, I_{max} would be infinite.

- Eq. (2) applies for a flux pump in which only the first half cycle is exploited to make current I increase (as it will be explained in section 1.3).

Given that components S_1 and S_2 of the flux pump and the energized magnet are all superconducting, it is reasonable to neglect any resistance associated with the load and the switches when they are closed. Nevertheless, a critical aspect has been overlooked in both this analysis and in the majority of prior studies on flux pumps. The circuits depicted in Figure 2 assume that when the switches are open, no current flows. This assumption entails associating an infinite resistance with the switches, leading to the complete absence of any loss during the open state. However, in real flux pumps switching is achieved through the interruption or suppression of superconductivity, mainly thermally (by increasing the superconductor temperature above the critical value) or magnetically (by applying an external magnetic field to inhibit the critical current of the superconductor). This switching effect is not at all ideal in the off phase, since infinite resistance is never reached for a quenched superconductor component. The consequence of this on the dynamic performance and the operation limits of the flux pump is explored in more detail in the next section.

Since S_1 and S_2 are subject to a certain voltage during their open state while their resistance is not infinite, non-negligible losses would arise according to Eq. (3).

$$P_{open\ state}^{switch} = \frac{V^2}{R_{open\ state}^{switch}} \qquad (3)$$

Where V is the voltage at the terminals of the switch and $R_{open\ state}^{switch}$ its resistance during off state. The largest $R_{open\ state}^{switch}$ would be preferable, but its value is limited by the normal state resistance of the superconductor. Moreover, V can be as high as the *emf* during phase (d), but since the *emf* is a key factor to increase I_{max}, it follows that a tradeoff is inevitable between maximum current capacity and manageable dissipation of the flux pump.

In the next sections, the different topologies of flux pumps are presented and described based on their physical mechanism and distinctive construction details.

1.3. The operating mechanism of the transformer rectifier flux pump

The most straightforward constructive solution to reproduce the flux pumping rectification effect described in section 1.2 is the transformer rectifier. In this apparatus, a step-down transformer composed of two mutually coupled coils is employed. At least one of these coils, typically the secondary, is superconducting. This transformer is connected to a downstream rectifier that can be either half wave or full wave type. Schematics of the half wave and full wave transformer rectifiers are shown in Figure 3 and Figure 4, respectively. In these figures, current I_1 and voltage V_1 are the inputs of the transformer (the power supply delivering them is not shown), M represents the mutually coupled inductances forming the transformer with a very high turns ratio, S_1, S_2, S_3, and S_4 are ideal switches, and L_{load} is the inductance of the superconducting coil which is energized by the flux pump. No resistance is included in the circuit at this stage, similarly to the general analysis related to Figure 2. The working mechanism of the half wave type is also described similarly to the general behavior description of section 1.2. In Figure 3.b the current injection in the coil takes place by setting S_1 closed and S_2 open while a positive voltage V_1 is transformed into V_2. When V_1 and V_2 change sign, S_1 and S_2 switch state to let the current I in the load flow without decaying, as shown in Figure 3.c. Different from the analysis of section 1.2, the sub phases dedicated to the current redistribution between the switches is not shown for simplicity. However, the same considerations outlined in section 1.2 for these sub-phases still apply as a consequence of the self-inductance coefficient of the loop formed by M, S_1 and S_2.
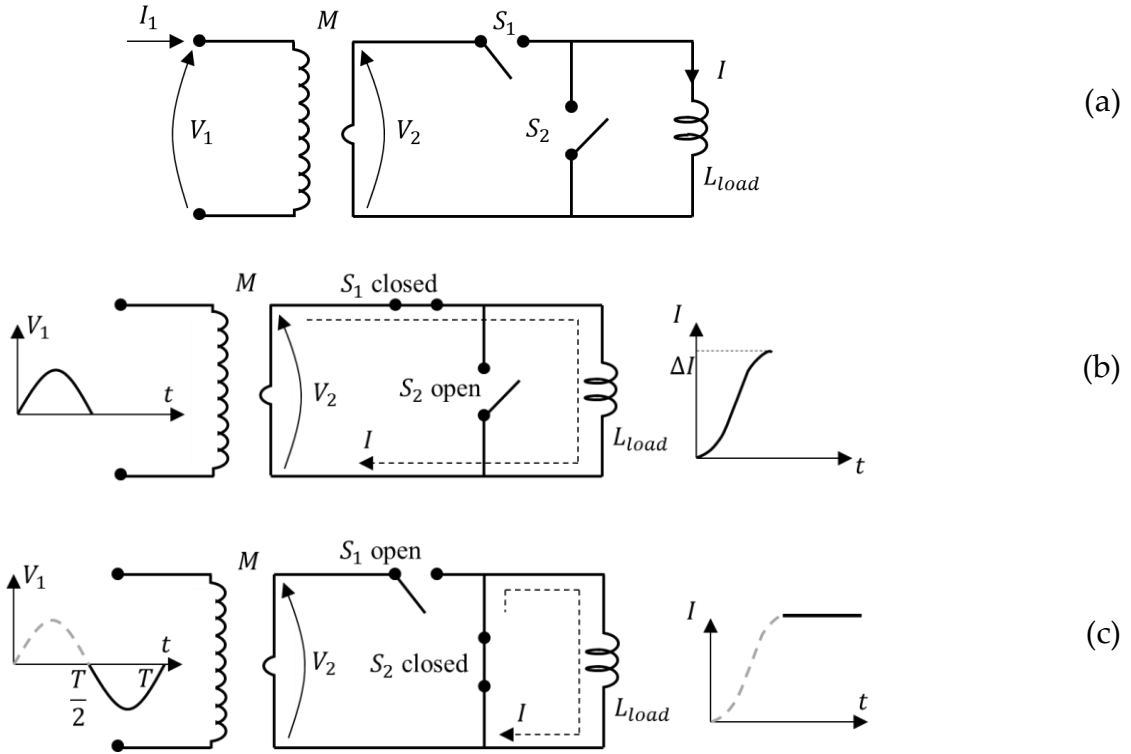
Figure 3 (a) Electrical scheme for describing the periodical operating mechanism of a half wave transformer rectifier flux pumps. Stages (b) and (c) describe the state of components during the current injection and maintenance, respectively.

In Figure 4, the mechanism of the full wave transformer rectifier is schematically presented. In this apparatus, both the two half periods are exploited to inject current into the magnet by means of four switches. Switches pair S_1-S_4 shares the same state all the time, as well as the pair S_2-S_3. In Figure 4.b it is shown that while V_2 is positive S_1 and S_4 are closed whereas S_2 and S_3 are open. During this phase I increases, as well as does I_2 in compliance to its reference in the scheme. Ignoring the current redistribution between switches like it was done for the half wave type, Figure 4.c shows that during the negative half wave of V_2 the current injection in the magnet continues. During this phase, however, the current I_2 changes sign.
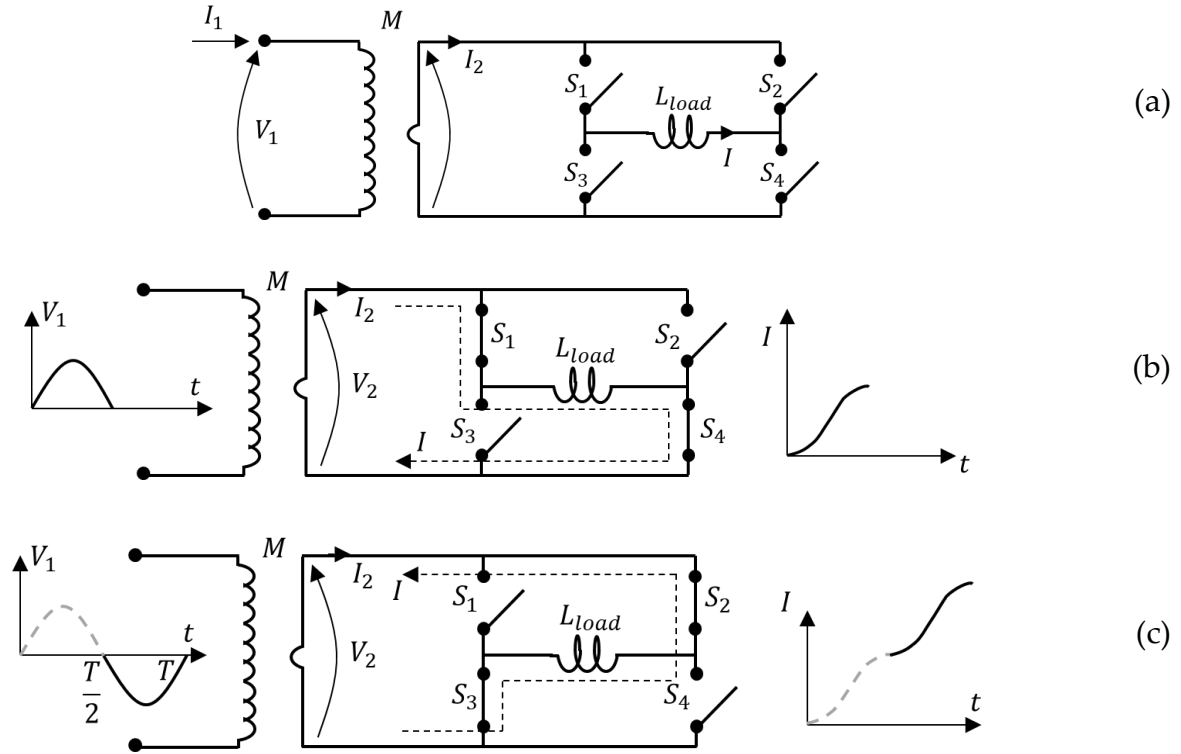
Figure 4 (a) Electrical scheme for describing the periodical operating mechanism of a full wave transformer rectifier flux pumps. Stages (b) and (c) describe the state of components during two half period of operation characterized by different circuit topologies. Current injection can occur during both half periods.

A couple additional considerations should be made on the current redistributions between switches occurring from one half phase to the other. In contrast to the half-wave type, in the full-wave flux pump the current I_2 does not exhibit an excursion ranging from the current of the coil to zero, but rather its double, since it has to experience a complete inversion. This marks a substantial different from the half wave which also implies modifications in the analysis. For instance, Eq. (2) needs to adapt to the different excursion in current. Assuming $L_{flux\,pump}$ is the inductance associated to the secondary of the transformer, Eq. (4) governs the current excursion between two phases (b) and (c) where $I_b(end)$ is the value of the current I at the end of the phase (b).

$$\frac{\int_{\frac{T}{2}}^{T} V_2(t)dt}{L_{flux\ pump}} = 2 \times I_b(end) \qquad (4)$$

The fact that I_2 exhibits a larger excursion between half periods entails that the maximum attainable value for the current I of the full wave (that will depend on the inductance of the load, the period duration, and the V_2 waveform) will be smaller than the half wave counterpart. On the contrast, the average current slope over a cycle is larger for the full wave rather than the half wave because it exploits the full period for the current injection. The full wave flux pump suffers an additional drawback with respect to its half wave counterpart: at any instant, for the presented configuration, two switches are in the open state instead of only one and experience the same voltage of the coil at its terminals causing dissipation according to Eq. (3) (S_2-S_3 dissipate during phase (b), and S_1-S_4 dissipate during phase (c)). Consequently, the need of employing superconducting switches with maximized resistance during open state is of critical importance for the full wave transformer rectifier flux pump. A superconducting switch is a device that operates in the superconductive state when the switch is intended to be closed, transitioning to a normal state (or, at least, a flux flow regime to exhibit a macroscopic significant resistance) when the switch is meant to be open. A superconductor enters its superconducting state when it meets specific operating conditions: the current density, external magnetic field, and temperature all need to remain below their corresponding critical values. Graphing these critical values in three-dimensional plots results in what is known as a 'critical surface.' The critical surfaces for the most commonly used superconductors (NbTi, Nb$_3$Sn, and REBCO, where RE stands for Rare-Earth) are displayed in Figure 5 [15].
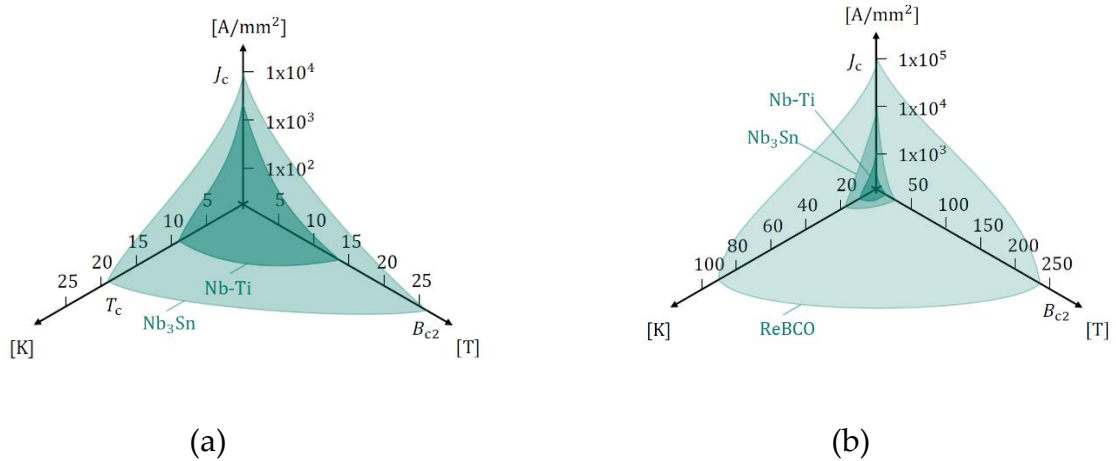
Figure 5 Critical surfaces of (a) LTS superconductors (NbTi, Nb₃Sn) and (b) HTS superconductors (REBCO).

As a result of the material properties of superconductors, three types of transformer rectifiers emerge, distinguished by their switching characteristics:

- Magnetically activated switches based [16] [17] [18] [19] [20] [21] [22] [23] [24]
- Thermally activated switches based [25] [26] [27] [28] [29] [30]
- Overcurrent switches based (also called automatic flux pumps, or self-switching flux pumps) [31] [32] [33] [34] [35] [36] [37]

The underlying concept for each of the aforementioned topologies is to shift the operating conditions beyond the critical surface. This is achieved by increasing either the external magnetic field, temperature, or current density, ideally surpassing the respective critical value.

In the following sections, a state of the art of the three outline types of transformer rectifiers is carried out.

1.3.1. Magnetically activated transformer rectifier flux pumps

One recent experiment on a half wave rectifier flux pump which employes magnetic switches can be found in [23]. The image of the experimental apparatus is shown in Figure 6.a, and its equivalent electrical circuit is reported in Figure 6.b. It can be seen in Figure 6.b that, different from the analysis of the previous section, resistive

components accounting for the joints' losses are present in the equivalent electrical circuit. The primary and secondary windings of the transformer are thermally separated, as the former operates at ambient temperature, whereas the latter (which is superconducting) is cooled down to the same cryogenic temperature of the switches and the load. This entails the complete absence of current leads. Moreover, what the authors of reference [23] control in their apparatus is the primary current i_1 and the magnetic field to the switches. What is worth reporting is that the flux pump manages to load the coil up to its critical current of 115 A in a few hundreds of seconds, with a calculated efficiency (related to the rectifier component only) for charging the 90% of the load current equal to 34%. Although this value may appear low, it's actually quite satisfactory when viewed in context. Comparatively, it's essential to assess it against the performance of the corresponding current leads solution. In typical engineering cases, a heat load of 50 W/kA is assumed for each of the current leads [38]. For the depicted scenario with a coil current of 115 A, this amounts to 11.5 W. According to the authors of [23], the maximum heat load from the switches is reported as 140 mW, hence significantly lower than that of the current leads-based counterpart. Given that the analysis neglects transformer losses in the flux pump case and omits power supply dissipation in the analysis involving current leads, the comparison made can be considered fair. However, one crucial aspect which plays in favor of the flux pump solution should be highlighted: the reported 34% efficiency and 140 mW switch loss are related to the charging phase up to 90% of the load current, but once the energization is complete, it is now clear that the flux pump would be working in quasi-persistent current mode exhibiting no dissipation, expect for the joint resistance only, while the coil remains charged with 115 A. On the contrary, in the current lead scenario the estimated 11.5 W heat load would be always present during the regime of current maintenance in the load coil.
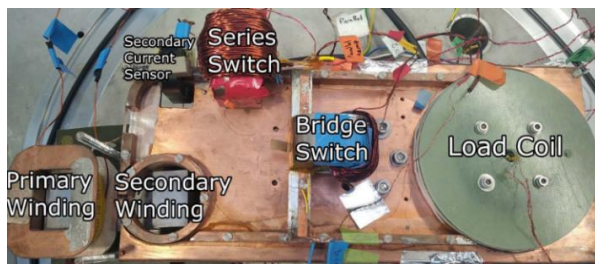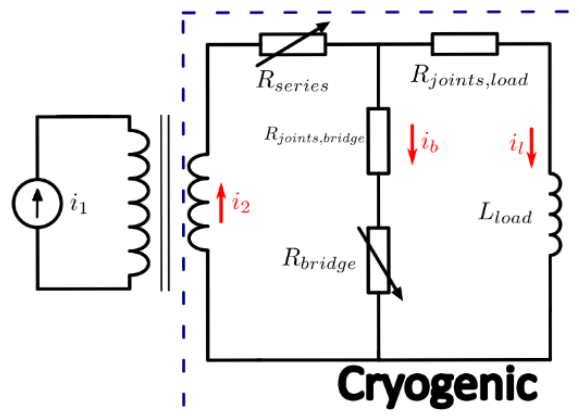
(a)   (b)

Figure 6 (a) Picture of the experimental flux pump of [23] with its components, including the electromagnet coils for the magnetic series and bridge switches, and (b) Equivalent circuit diagram of the flux pump of [23]. © [2023] IEEE

One variant of the full wave rectifier that uses two switches (instead of four like Figure 4) is reported in reference [21]. The picture of the corresponding apparatus and its electrical equivalent circuit are shown in Figure 7.a and Figure 7.b, respectively. In this modified design, the number of superconducting switches required is limited to two due to the center-tapped transformer secondary. By implementing a feedback control on the flux pump, the current I_L is increased up to 275 A and subsequently halted to maintain a safety margin from the critical current of the load coil, which is 315 A. In the discussion of this work, the authors stress the crucial aspect of the voltage applied to the switches in the open state that is a cause of losses, similarly to what was discussed in the previous section of this thesis. For this flux pump the losses issue is particularly critical, as it is mentioned that the dissipation, if not properly limited through the control, could destroy the switches.
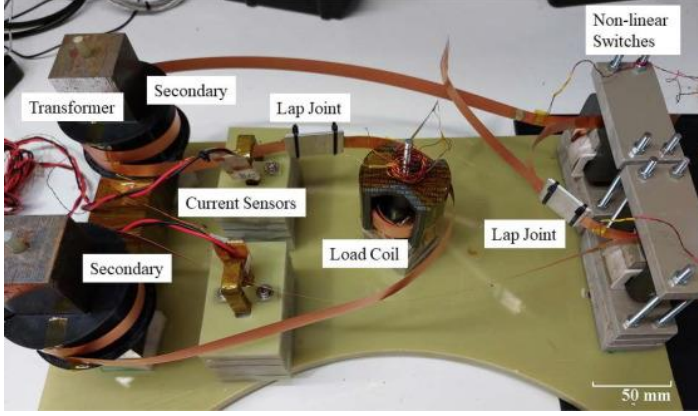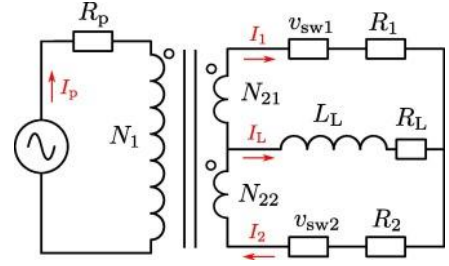
Figure 7 (a) Picture of the experimental flux pump of [21] with its components and (b) Equivalent circuit diagram of the flux pump of [21]. Published in Superconductivity journal, International License (CC-BY-NC-ND 4.0 DEED).

One solution for magnetically activate switches, that is particularly physically intriguing, is exploiting the so-called dynamic resistance phenomenon which emerges when a superconductor slab carries a DC transport current and is subject to an external AC magnetic field. Oomen et al [39] calculated that, under the aforementioned operating conditions, a superconductor exhibits the dynamic resistance R_{dyn} as written in Eq. (5) [39].

$$R_{dyn} = \frac{4afL}{I_{c0}}\left(B_a - B_{a,th}\right) \quad\quad (5)$$

Where a is the half of the width of the slab, L denotes its length, I_{c0} is the critical current of the slab at zero field applied, B_a is the amplitude (half of the peak-to-peak excursion) of the AC external field applied perpendicular to both the length and the width of the slab, f is the frequency of the AC external field, and $B_{a,th}$ is the so called threshold field amplitude [40], also known as the B_a threshold field under which R_{dyn} is zero. Eq. (5) applies when a constant critical current density is considered for the slab, but variations of the formula that account for the field-dependent critical current

density and the non-linear contribution of the external magnetic field are reported in references [39] and [41] respectively.

One clear example of the exploitation of the dynamic resistance to reproduce a flux pumping is present in reference [17], and the schematic of its experimental apparatus is shown in Figure 8.
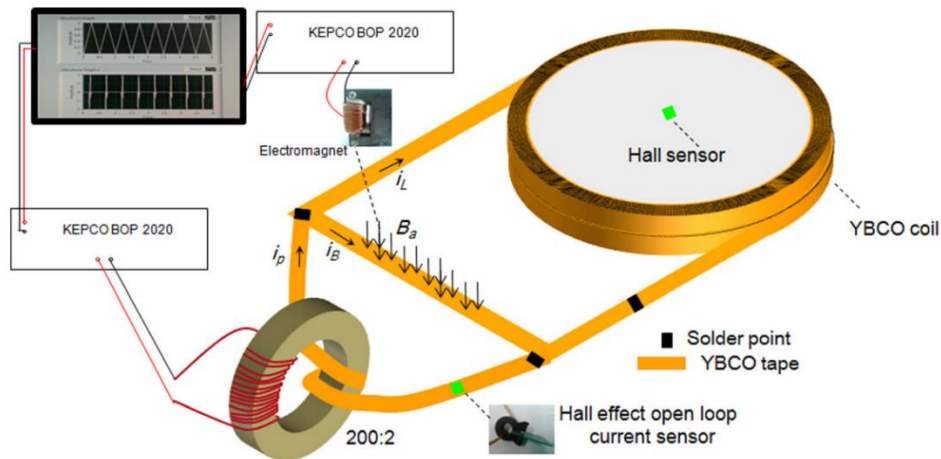
Figure 8 Schematic of the half wave transformer rectifier of [17] based on the dynamic resistance bridge. Reprinted from [Geng, J.; Coombs, T. Mechanism of a high-Tc superconducting flux pump: Using alternating magnetic field to trigger flux flow. Appl. Phys. Lett. 2015, 107, 142601], with the permission of AIP Publishing.

The flux pump tested in [17] is a variant of the half wave rectifier, in which only the transversal switch is present. When the alternating current i_p reaches one polarity the external field B_a is applied and that triggers the dynamic resistance in the transversal portion of the tape, that the authors call "bridge". This produces an analogue effect to opening the switch S_2 in Figure 3, and that makes the current of the coil i_2 increase. The described operation is depicted in Figure 9. The flux pump tested in [17] eventually reaches 57.5 A of current in the coil, but the authors do not provide any information on the dissipation taking place during the experiment.
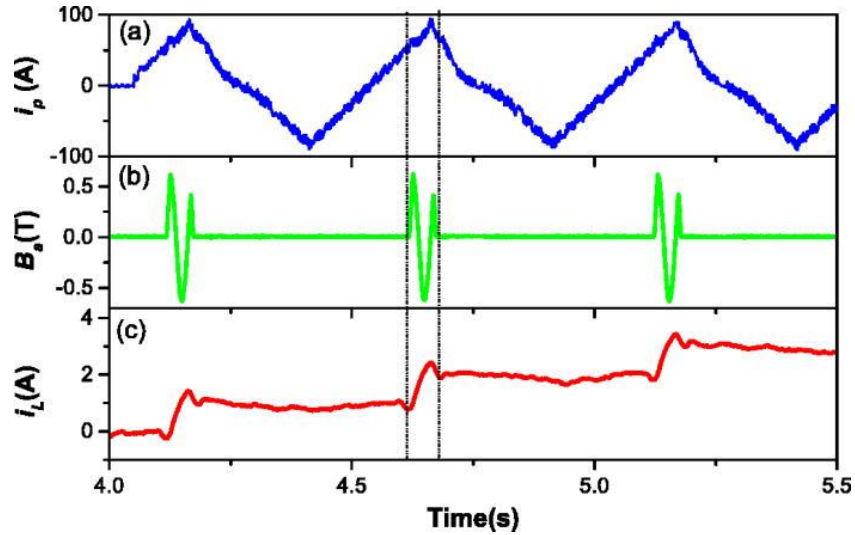
Figure 9 Plot of the trends of (a) the transformer primary current, (b) the magnetic field applied to the bridge, and (c) the load current of the flux pump of [17] during operation. Reprinted from [Geng, J.; Coombs, T. Mechanism of a high-Tc superconducting flux pump: Using alternating magnetic field to trigger flux flow. Appl. Phys. Lett. 2015, 107, 142601], with the permission of AIP Publishing.

Previous studies have focused on magnetically activated switches transformer rectifiers that exploit the phenomenon of the dynamic resistance [42]. However, this is not a good engineering solution to implement for developing transformer rectifiers that aim at high performance and high efficiency to comply with real applications requirements. In fact, it was explained in the previous sections that a transformer rectifier flux pump, in order to be efficient, needs to employ switches that are in the superconducting state when they are meant to be closed and carry current, and should exhibit the largest possible resistance in the open state in order not to carry any current and experience the least possible losses. The dynamic resistance doesn't prevent the flow of transport current in the superconductor, nor does it minimize losses in the open state; instead, it operates in the opposite manner regarding both aspects. The presence of a DC transport current is a prerequisite for the occurrence of dynamic resistance. Additionally, dynamic resistance doesn't correlate with physical resistivity but rather represents the actual losses occurring within the superconductor as an effect of the external varying magnetic field and the transport current. This is well explained in [39], where the power loss Q in the slab is calculated at first as an integral of electric

field multiplied by current density over a period of the external AC magnetic field. Then, a fictitious resistance, that is the dynamic resistance, is derived by saying that $Q = R_{dyn}I^2$, where I is the transport current flowing in the slab. The paradoxical conclusion arising when aiming to create a superconducting switch exploiting the dynamic resistance is that achieving the highest resistance entails inducing significant losses in the superconductor. This scenario poses detrimental effects on the system's overall efficiency and escalates the risk of triggering quench of the switch, that is the uncontrolled transition to the normal state. It should also be considered that previous studies on the dynamic resistance only consider the electromagnetic effect and assume constant temperature, while it is clear at this point that in such a context dissipative phenomena are significant.

Effective and viable solutions for making superconducting switches should aim at increasing the real local resistivity and limiting transport current as much as possible. Applying a substantial DC magnetic field to a superconductor, as opposed to an AC field, would impede its critical current and elevate its resistivity, hindering its ability to function in an open state without incurring unnecessary and unwanted losses. The largest possible resistance of a superconducting switch is its normal state resistance. This is impossible to achieve magnetically for HTS superconductors since their critical field is very large, up to hundreds of tesla (see Figure 5.b). On the other hand, magnetic switches have the advantage of being able to reach high switching frequency, which is the reason why they have attracted great interest recently. One excellent study that explains the superiority of DC field switches for flux pumps can be found in reference [22]. In this paper, a half wave transformer rectifier employing switches that are magnetically activated by means of electromagnets producing a field up to 1.2 T in the 1 mm air gap where the HTS tape (SuNAM HCN04200) is located. In the study the flux pump charges a 2.4mH coil up to 55 A in about 25 seconds. In the second part of the paper, the authors carry out an analytical analysis that arrives at two formulas that give the theoretical maximum efficiencies (valid for the current

maintenance regime exclusively) for the half wave (Eq. (6)) and full wave (Eq. (7)) transformer rectifier types in the case DC field switches are used.

$$\eta_{half} = \frac{I_L}{I_L + 2I_C(B_{app})} \tag{6}$$

$$\eta_{full} = \frac{I_L}{I_L + I_C(B_{app})} \tag{7}$$

Where I_L is the final load current, and $I_c(B_{app})$ is the critical current of the switch tape when the DC magnetic field B_{app} is applied [22]. These theoretical formulas make use of the following simplifying assumptions: ignoring the joints and residual AC loss resistances, and assuming the Kim-Anderson model [43] [44] for the superconducting behavior of the switches. The calculated maximum efficiencies for both the half wave and full wave types, at 77 K, are calculated in [22] for the SuNAM SAN series YBCO and the InnoST Bi-2223 wire superconductors. The results are reported here in Figure 10.
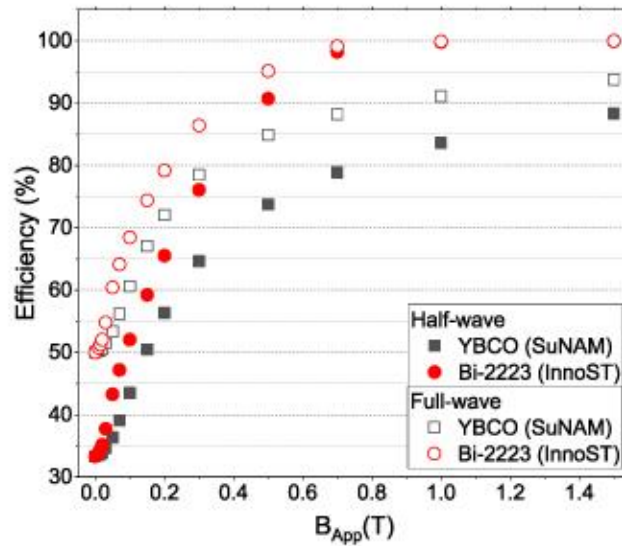
Figure 10 Calculated maximum efficiencies for half and full wave transformer rectifier flux pumps that employ switches based on thee SuNAM SAN series 2G YBCO wire and the InnoST 1G Bi-2223 wire, at 77 K, under an applied DC field of amplitude B_{App} [22]. © IOP Publishing. Reproduced with permission. All rights reserved.

The authors of [22] also utilize identical calculations to assess the maximum efficiency of AC field switches (which exploit the dynamic resistance). Their findings indicate that a full-wave rectifier of this type would be restricted to a maximum efficiency of 50% (if the SuNAM YBCO tape is used), in contrast to the 92% achieved by its DC field switch counterpart. This study, which to my knowledge is the first to investigate a transformer rectifier that makes use of DC field HTS switches, demonstrates the advantages of maximum weakening of the critical current of the tape when it must operate as an open switch. The next section introduces the thermal switches-based transformer rectifiers, demonstrating that interrupting superconductivity, rather than solely weakening it, leads to the best flux pump performance.

For reference, other magnetic switches were studied and developed in [45] [46] [47] [48] [49].

1.3.2. Thermally activated transformer rectifier flux pumps

Since low temperature superconductors (LTS) have been known for longer and they facilitate the exploitation of the operating temperature for making superconducting switches, thermally activated transformer rectifier flux pumps are the most studied and tested of all topologies. Moreover, since overcoming the critical temperature of superconductors (LTS and HTS) is much easier and more convenient than applying a magnetic field greater than their critical value, thermal transformer rectifiers are generally superior to magnetic ones. The first study that came to this conclusion dates back to 1989 [50].

As further evidence supporting these claims, the exceptional performance of this type of transformer rectifiers is exemplified by the achievement of the world's largest current, that being 25 kA, using a flux pump, as demonstrated by Mulder *et al* in 1991 [29]. The flux pump of [29] makes use of LTS superconductors (NbTi) and consists of a half wave transformer rectifier. The frequency of the input current Ip is 0.5 Hz to cope with the thermal dynamic capabilities of the switches, whose recovery times are

150-300 ms. The flux pump was initially designed to have a current capability of 100 kA, but the value of 25 kA is a consequence of the limitation posed by the superconducting coil that is charged as load in the experiment. During individual tests on the transformers and switches, unexpected quenches occurred at 50 to 70 kA of the former, contingent on the ramp rate, for which the authors were unable to find an explanation. However, up to 25 kA and 30 W of output power, it was assessed by experiments that the rectifier system was safe against quenches. The schematic of the flux pump of reference [29] and its equivalent electrical circuit are shown in Figure 11.

(a)   (b)
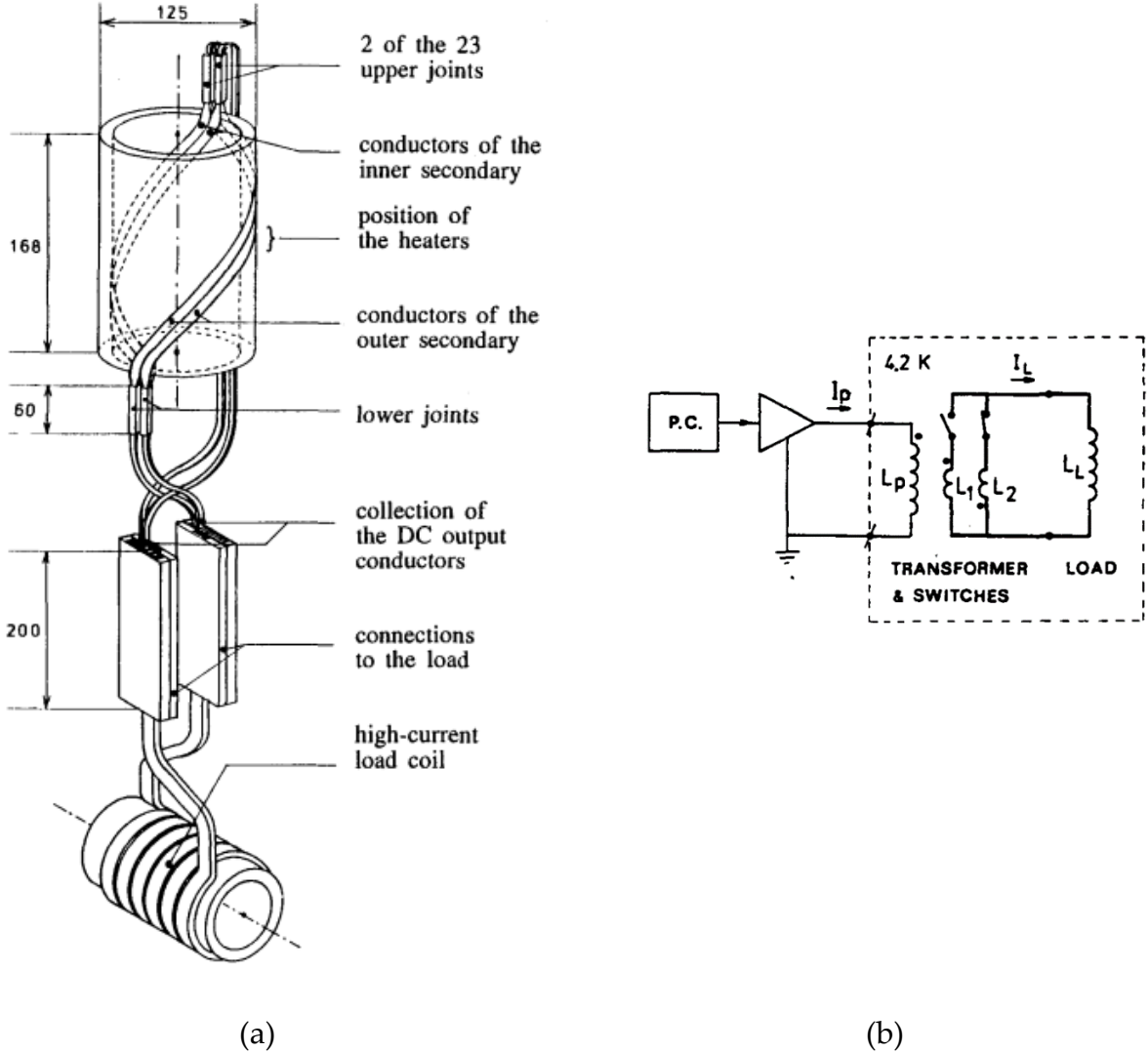
Figure 11 (a) Schematic of the thermally activatedrectifier flux pump of [29] with its components and (b) Equivalent circuit diagram of the flux pump of [29]. © [1991] IEEE

Authors do not provide calculations of the energetic and performance and efficiency of the flux pump of [29]. However, this aspect was investigated in another study two years later [30], when a similar apparatus exceeded a remarkable 96% efficiency during current injection in the coil load, and 98% in maintaining it. The equivalent circuit of this half wave machine is shown in Figure 12.a, whereas Figure 12.b graphically describes the phases of its control mechanism by reporting the trends of the following quantities: the primary current of the transformer, the resistance of the switches 1 and 2, and the coil load current. The rectifier operated successfully at frequencies up to 100 Hz, showing the great dynamic response of the switches. The output voltage reached 0.6 V, and the maximum pumped current (which was limited by a quench of the load magnet) and output power were 320 A and 100 W respectively. The fantastic efficiency of this transformer rectifier was achieved as a result of the very large resistance of the switches during open state (0.96 Ω and 1.4 Ω for the first and second switch respectively). This experiment serves as proof that as early as 1993, it was evident that completely interrupting superconductivity is a significantly superior option compared to merely weakening it when aiming to create efficient flux pumps. To conclude about this apparatus, the authors forecasted that improvements in the components of the rectifier could bring the pumping efficiency to 98% and the output voltage to 1 V.
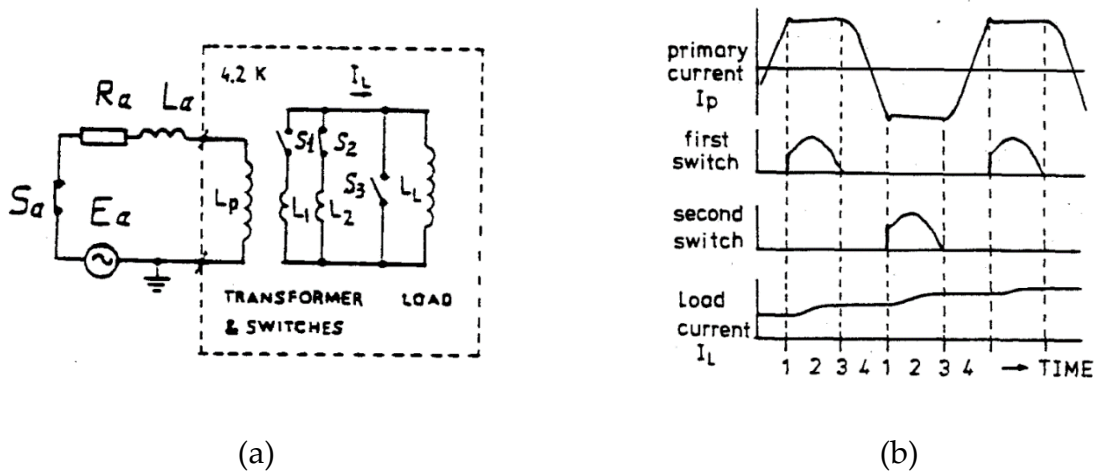
Figure 12   a) Equivalent circuit diagram of the flux pump of [30] and b) trend over time of the transformer primary current, resistance of switches, and load current. © [1993] IEEE

Flux pumps of references [29] and [30] included the entire transformer in the cryostat, hence requiring current lead to bring the primary current from the ambient temperature power supply to the cryogenic transformer. However, it is reminded that the involved transformers are characterized by large turns ratio, which results in low primary current and hence a low heat load due to the current leads. These presented flux pumps are also LTS, which means that they are forced to operate at around 4 K, preventing their usage for some applications where high temperature is preferred. Recent works are exploring the possibility of producing thermally activated HTS superconducting switches with sufficient performance to produce efficient flux pumps at around 77 K. A recent milestone is this direction was published in [51]. In this paper, the authors report the results of the tests on two novel thermal switches made with a 4 mm single HTS SuperPower tape. To increase the normal state resistance, the copper coating was completely removed, and the thickness of the silver layer reduced, resulting in a remarkable resistance per unit length of 4.2 Ωm^{-1} at 100 K. The critical current of the switches is over 500 A, and their turn-off and turn-on response times are 1 s and 1.1 s respectively, showing potential for flux pumps applications. Pictures of the HTS switches and their thermal dynamic performance are depicted in Figure 13.a and Figure 13.b respectively.
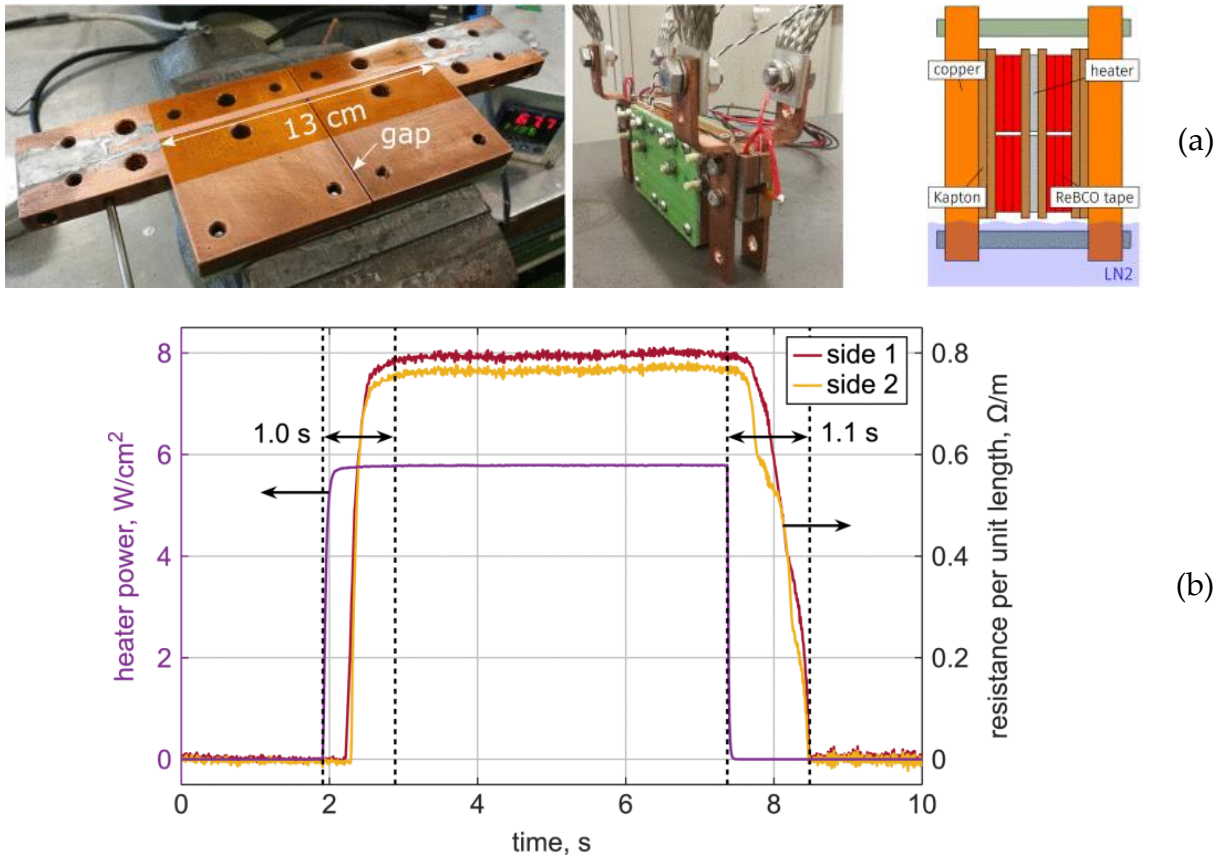
Figure 13 (a) Picture and lateral schematic view and the HTS thermal switch of [51] and (b) Thermal dynamic responce of the HTS thermal switch of [51]. © [2019] IEEE

In the summary of reference [51], the authors established a mid-term goal to manufacture and test a full wave transformer rectifier employing HTS switches at temperatures around 50 K. A sketch of the future HTS switches bridge is shown in Figure 14, whereas for making the secondary winding of the transformer and the load coil it is planned to use CORC cables [52]. The estimated operating current of the prototype is 10 kA, achievable using 15 HTS tapes per switch, each of which being 12 mm wide.
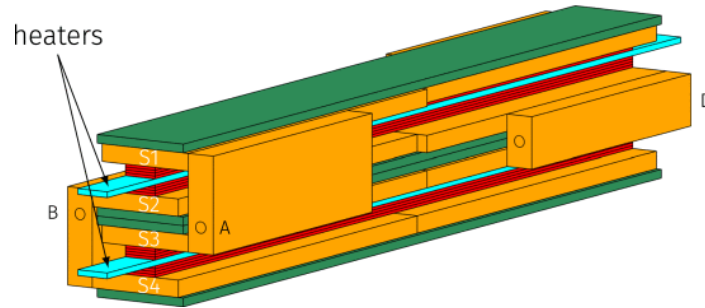
Figure 14 3D schematic of a switch bridge for a transformer rectifier flux pump [51]. © [2019] IEEE

1.3.3. Overcurrent switches-based transformer rectifier flux pumps

Constructively, the overcurrent switch (or self-switching) transformer rectifier flux pump mirrors the machine presented in [17] and depicted in Figure 8, but with one major distinction: it lacks any electromagnet associated with the bridge, ensuring it remains unaffected by any externally applied magnetic field. In order to obtain rectification, the transformer primary current is controlled to rise and fall quickly over a short portion of the period and change slowly over the rest of the cycle. By changing the current in the described way, the bridge is driven resistive in the portion of the period when the current slope is very high, and this is the time frame during which the current of the coil load increases. For clarity, hereafter the term "bridge" is used to indicate the transversal switch of transformer rectifier, as this is common nomenclature of most literature references. Throughout the remaining period, the bridge operates in a fully superconducting state, resulting in the load current either remaining constant or gradually diminishing if the joints' resistance is notable. Consequently, this particular type of transformer rectifier inherently functions as a half wave system. Because the bridge must sustain at least its own self-field critical current to generate substantial voltage across the coil terminals, the challenges related to losses, previously highlighted and extensively discussed for the other flux pump topologies, potentially become more pronounced in this configuration. Nonetheless,

the overcurrent transformer rectifier offers unparalleled benefits in terms of compactness and reduced weight when compared to its counterparts. This is a consequence of the absence of any additional component, such as heaters or electromagnets, to drive the bridge resistive. Such feature is well highlighted in the recent study presented in [36]. The overcurrent flux pump of [36] is displayed in Figure 15.a, while Figure 15.b presents an example of the current waveform induced at the transformer's secondary (i_2) per unit critical current of the bridge ($I_{c,bridge}$). This waveform periodically triggers the transition of the bridge to a resistive state, thereby augmenting the load current (i_l). It's crucial to note that both the primary and secondary windings of the transformer, which has a turns ratio of 45, consist of copper. Considering that feasible transformer rectifiers are anticipated to utilize a superconducting secondary winding (if not the primary as well), the experimental findings concerning the losses in this study pertain exclusively to the superconducting bridge. In terms of the system's temperature, the cryogenic environment encompasses the secondary winding of the transformer, the superconducting bridge, and the load coil.
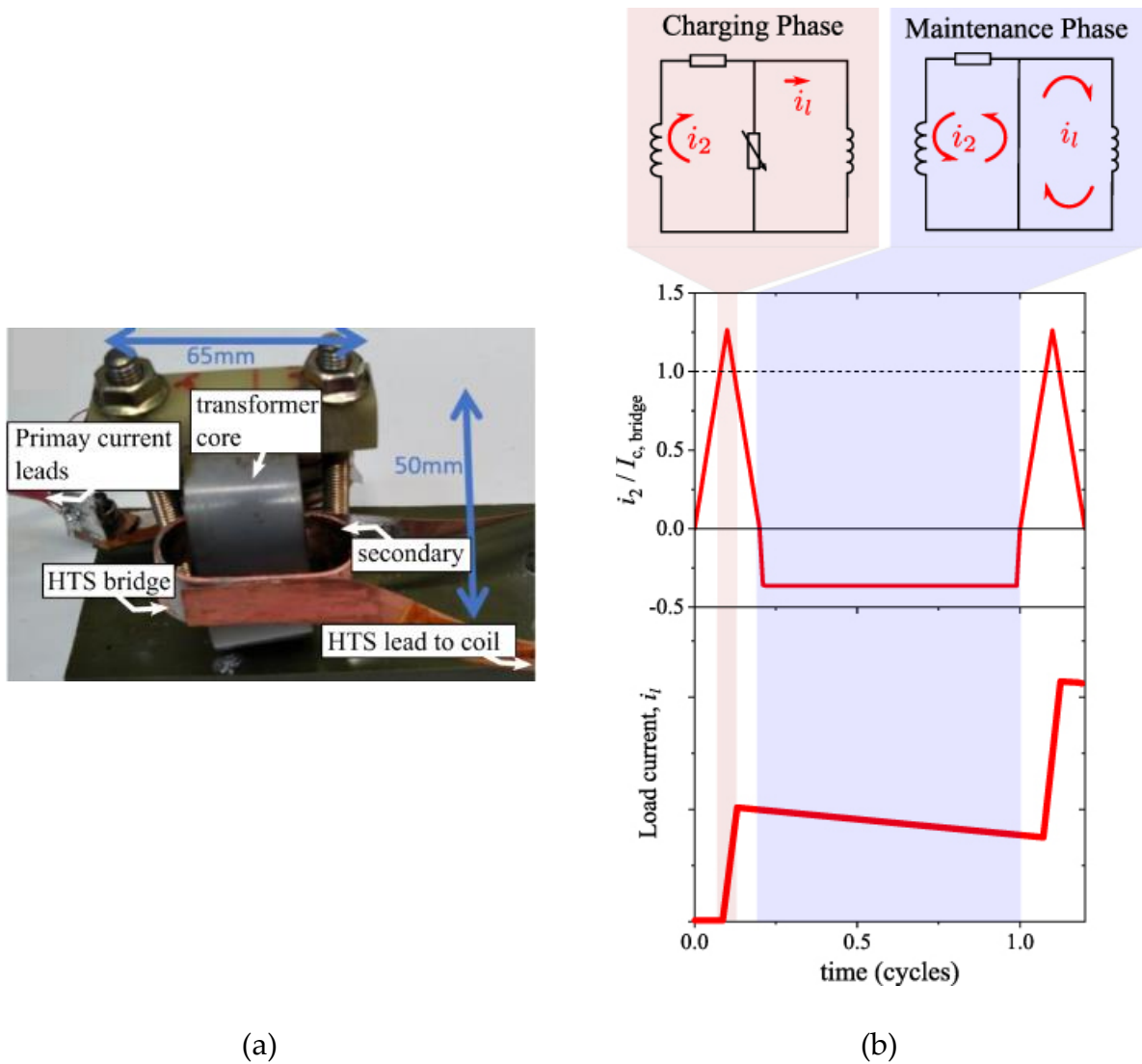
Figure 15 (a) Schematic of the rectifier flux pump of [36] with its components and (b) Equivalent circuit diagram of the flux pump of [36] during charging and current maintenance mode reporting the trends over time of the transformer secondary current and the load current. Published in Superconductor Science and Technology journal, International License (CC BY 4.0 DEED).

As a load for the overcurrent flux pump, a 2.5 µH coil was produced in the study by dry-winding eight turns of HTS tape. The current profile of the coil during ramp up and a few seconds of its maintenance are depicted in Figure 16.a, where the experimental data is overlapped with the numerical results obtained with a circuit model developed in Matlab by the authors of [36]. The frequency of the current waveform of the primary of the transformer, which follows a qualitatively similar trend of the one in Figure 15.b, is 10 Hz. Figure 16.b also reports the experimental

voltage measured and calculated by the circuit model at the terminals of the load coil. The load voltage exhibits peaks of up to 65 mV in the initial cycle of the ramp-up, while during the current maintenance it settles to a waveform oscillating between triangular profiles with 20 mV peaks and approximately zero Volts,.

(a)   (b)
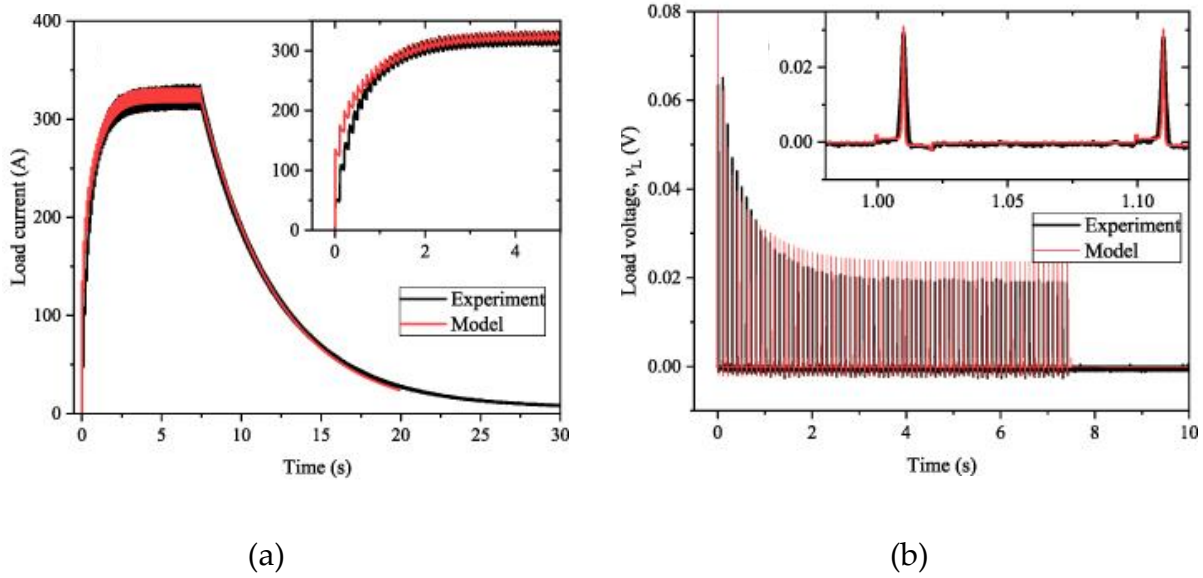
Figure 16 (a) Load coil charging transient and free decay using the flux pump of [36] and (b) trend over time of the output voltage of the flux pump of [36]. Model vs experiments. Published in Superconductor Science and Technology journal, International License (CC BY 4.0 DEED).

The capability of the ultra-compact machine of [36] to inject 320 A into a superconducting load coil is definitely remarkable. However, the pivotal concern associated with this overcurrent transformer rectifier arguably isn't solely its current capacity (an inherent advantage of flux pumps) but rather the dissipation it incurs to achieve it. While numerous studies commend the substantial current capacities of diverse flux pump designs, the technology's practical application demands the validation and resolution of various factors, with losses emerging as a paramount consideration. Subsequently, the flux pump discussed in [36] serves as a case study to emphasize this concept. Consider the dissipation occurring in the bridge during the experiments, here shown in Figure 17 (along with the analogue quantity and other dissipation contributions computed by means of the circuit model in [36]).

31
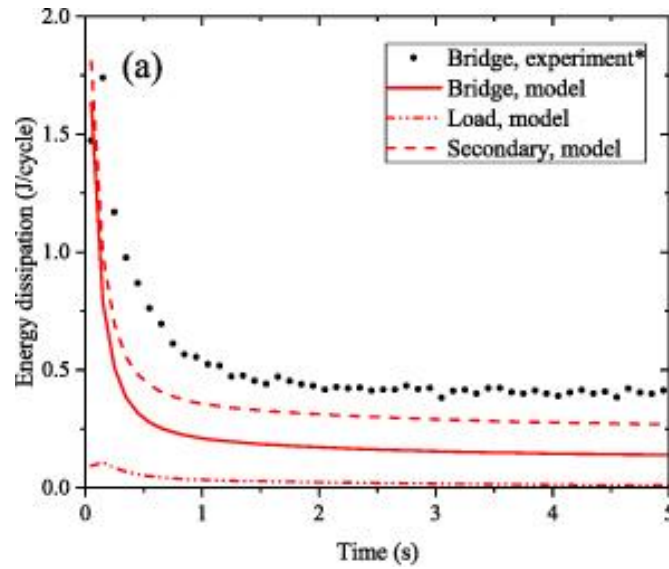
Figure 17 Model and experiments losses contribution of the load supplied by the flux pump of [36]. Only the bridge losses are obtained experimentally. Published in Superconductor Science and Technology journal, International License (CC BY 4.0 DEED).

Experimental results of Figure 17 confirm that, as far as losses are concerned, flux pumps show very distinguished behaviors based on whether the ramp up or the current maintenance regime is considered. Therefore, these two operating conditions are analyzed separately. First, the current maintenance regime is addressed. By making the assumption that the majority of the heat load occurs in the superconducting bridge, it can be seen from Figure 17 that, during current maintenance mode, the dissipation at cryogenic temperature settles to about 0.5 J each cycle, which corresponds to an average power loss of 5 W (it is reminded that the frequency of operation is 10 Hz). For reference, the heat load that would be caused by the usage of two current leads to feed 320 A into the coil load would be continuously around 32 W (assuming a typical 50 W every 1000 A of current). If the scope is merely the maintenance of the load current, the conveniency of the self-switching flux pump over a supply system based on current leads is evident. Regarding the ramp up regime, as soon as the coil load charging transient begins, Figure 17 shows that the energy dissipation of the bridge in the first cycle peaks at about 1.75 J, resulting in an average power loss of 17.5 W. This is much higher than what is dissipated during current

32

maintenance, but still significantly lower than the current leads heat load to maintain 320 A (32 W). However, because the dissipation in the bridge varies during the ramp up, and so does the current leads heat load for the corresponding scenario, it's the total energy dissipated during the transient that should be used as comparison metric for this part of the operation. An exponential fit of the bridge power dissipation (deduced from experimental data) of Figure 17 yields Eq. (8).

$$P_{bridge}(t) = 19.9e^{-\frac{t}{0.29}} + 4.3 \tag{8}$$

Integration of Eq. (8) from 0 to 2.5 seconds (the current charging duration estimated from Figure 16.a) yields the energy dissipated by the bridge of the flux pump during the ramp up, equal to 16.6 J. To make a fair comparison, for the current leads scenario a linear ramp up lasting 2.5 seconds is considered. It is easy to calculate that the energy dissipated in current leads heat load during the transient in this scenario is 40 J. Therefore, according to the data reported in [36], this flux pump is energetically convenient in comparison to a corresponding current leads solution even during the charging regime, when it is most dissipating. However, data leading to this conclusion should be approached with caution for several reasons: first, the experimental dissipation in Figure 17 is an estimation, since the current in the bridge was not measured but relied on the approximation that the current across the secondary is N times that of the primary. Because the transformer is not ideal, this approximation is imperfect. Second, several loss contributions are not accounted, like the joints in the superconducting circuit and the transformer (which, if superconducting, would give rise to non-negligible ac losses). It cannot be ruled out that if the total amount of losses of the transformer rectifier was considered, the outcome of the ramp dissipation comparison between the two scenarios would change significantly. Another important point must be underlined: the flux pump test described in [36] charges the load coil in only a few seconds because of its limited inductance, which was only 2.5 μH. As a result, the energy dissipation during the ramp-up was insignificant. However, larger-

scale superconducting magnets typically exhibit high inductances, sometimes reaching several Henrys. The ramp-up transients for such magnets using flux pumps can extend over several days, operating at maximum dissipation for extended periods. This situation poses a challenge not only for the cooling system's capacity but also risks compromising the integrity of the flux pump components. As this thesis progresses, it will become evident that significant open circuit losses and low output voltages (leading to extended magnet charging times) are typical characteristics of flux pumps.

Despite the many assumptions that are used in [36] to deal with the losses of the flux pump, to the very best of my knowledge this is currently the reference that investigate the dissipation of this type of apparatus more in detail. Future studies that will comprehensively focus on the power loss of transformer rectifiers, hence including all the contributions, from the transformer to the switches, will be of paramount importance toward the engineering progress on flux pumps.

1.3.4. Non-conventional transformer rectifier flux pumps

To my knowledge, the literature lacks a unique definition of what a flux pump is. Generally speaking, for a device to be classified as a flux pump, it should possess the following features:

- Galvanic isolation from the supplied circuit (contactless functionality)
- Rectification capability, producing a DC output voltage
- Being fully or partially superconducting
- Support for persistent current mode in the load to flow in a fully superconducting loop

Despite the last point might seem unnecessary, that feature represents one of the major benefits offered by flux pumps when compared to conventional supply systems, concurring to making a case for their development and application. Nevertheless, a few studies can be found in literature describing cryogenic power supplies of superconducting magnets that integrate power electronics switches (typically MOSFETS) in the rectifier, which are presented as flux pumps. Examples such

apparatuses can be found in [26] [53]. These machines implement the same operating principles, devices, and strategy controls of conventional power supplies, with the distinction of integrating the transformer (both windings or only the secondary) and the rectifier at cryogenic temperatures. This feature allows to avoid high current leads on one hand, which provides an advantage, but entails that all the power electronic losses occur at low temperature on the other, which is a drawback because extracting heat at cryogenic temperature requires a much larger energy spent at ambient temperature by the cooling systems. Flux pumps that respect the definition given at the beginning of this section provide lossless persistent current mode during maintenance regime, whereas power electronic based flux pumps do not. In fact. current will always be forced to flow into a resistive switch and considering that the typical voltage drop of power electronic switches is in the order of 1 V, this entails the presence of up to several tens of Kilowatts of losses at cryogenic temperatures for flux pumps of this kind serving high field fusion magnets. Loss reduction can be obtained by employing several MOSFETs in parallel, as it was done in [53].

1.4. Dynamo flux pumps

Different from the transformer rectifier topology, the dynamo flux pump does not comprise any physical transformer or switch to provide voltage rectification. While the former's operating mechanism is relatively straightforward and equivalent to that of any conventional electrical rectifier converter, the dynamo type belongs to the category of flux pumps that need a travelling magnetic field investing a superconducting tape. Their physical mechanism has been largely debated, remaining obscure for a long time. At its core, a dynamo transforms mechanical energy into electrical power, generating a DC biased output voltage at its terminals even at open circuit conditions. Alternatively, if a transport current within certain limits flows through the tape of the dynamo, this DC voltage component is in the same direction as the current, hence the dynamo works in generator mode. This process involves a rotating shaft that holds a flux source, often permanent magnets, directing their field

across stationary or differently rotating superconducting tapes. Before HTS superconductors where discovered [54], several LTS dynamos were investigated [55] [56] [57] [58] [59] [60] [61] [62] [63] [64] and represented the foundations for patents [65] [66] [67] [68] [69] [70] [71] [72] [73] [74]. These machines relied on the interruption of superconductivity in a spot of the tape which is subject to the field of the permanent magnet. A general scheme of the apparatus, that can be found in [12], is shown here in Figure 18.
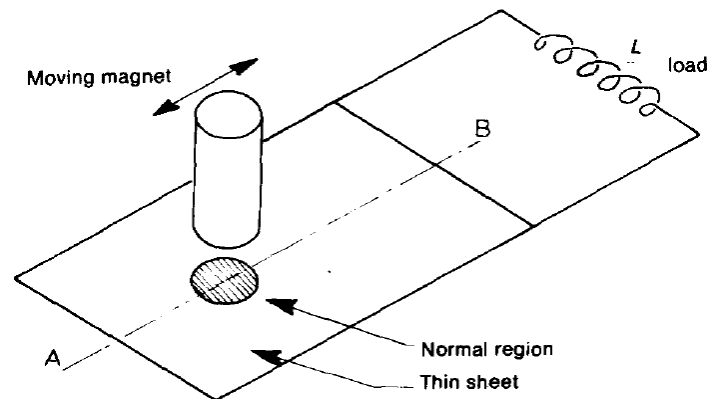
Figure 18 Simple superconducting DC dynamo [12]. Reprinted from Fully superconducting rectifiers and fluxpumps Part 1: Realized methods for pumping flux, Vol 21 /edition number 4, Van de Klundert, L. J. M., & ten Kate, H. H., Cryogenics, Pages No. 195-206, Copyright (1981), with permission from Elsevier

Early stage research was so promising that a 50 kA dynamo was suggested in 1978 [75], even though it seems its creation was never achieved. Recent studies have favored investigating HTS dynamos instead [76] [77] [78] [79] [80] [81] [82] [83] [84] [85] [86] [87] [88] [89]. In HTS dynamos superconductivity is only weakened by the external magnetic field, as it is practically impossible to interrupt it using a permanent magnet. Regardless the type, the operating mechanism is at least counterintuitive. Despite being equivalent to any electrical machine, the rise of a DC component of the output voltage at the terminals of the superconducting tape is an apparent violation of the Faraday-Lenz's law [90]. Certainly, this is not the case, as it will get clear shortly, but such a phenomenon has generated much surprise and speculation in the scientific

community, including suggestions of theories the evoke vortices mechanisms [91] [92]. Today, it is acknowledged that the origin of this singular behavior is caused by the non-linearity of the local resistivity of superconductors which causes the rectification [93] [94]. For the sake of completeness, a detailed description of the voltage rectification phenomenon is provided in the next section. This analysis also applies for the linear travelling wave flux pump type, which is described later.

1.4.1. The travelling field flux pumps physical mechanism

As anticipated, the analysis carried out in this section applies for the HTS dynamo and the linear flux pump types.

The occurrence of flux pumping, characterized by an average DC output voltage at the terminals of a HTS tape, necessitates the following operating conditions:

- Perpendicular Magnetic Field Waveform: The HTS tape must be exposed to a periodic magnetic field waveform that is perpendicular to its surface (or that at least the perpendicular component is dominant). The magnetic field can also include components in other directions, but they will not impact the phenomenon.

- Traveling Magnetic Field: The magnetic field waveform must move along the width of the HTS tape with a defined velocity, denoted by v_B.

- The wavelength of the magnetic field waveform should be shorter than the width of the HTS tape. This ensures that the tape experiences varying magnetic field intensities across its width.

- Uniformity along the Length: The magnetic field waveform should remain relatively uniform (or at least not undergo significant variations) along the length of the HTS tape.

- Asymmetry with Respect to Time Axis: Plotting one period of the magnetic field waveform, this curve must be asymmetrical with respect to the time axis.

The need for these conditions will become clearer as the analysis proceeds, in particular the last point that will be elucidated in section 2.1.3 with the help of numerical results. For now, consider the simple scenario depicted in Figure 19: two narrow HTS bands (narrow enough to assume uniform magnetic field over their width) subject to a magnetic field waveform compliant with the same requirements of the list above. At the end of this paragraph, the analysis will be extended from the two narrow bands to a continuous tape. With regard to the considered case, the magnetic field lines have only the component in the y direction, and the waveform is travelling in the x direction with velocity v_x^B. The two HTS bands are parallel to each other and to the z axis, share the same coordinate y, and are distant enough over the direction x to instantly experience different values of magnetic field.
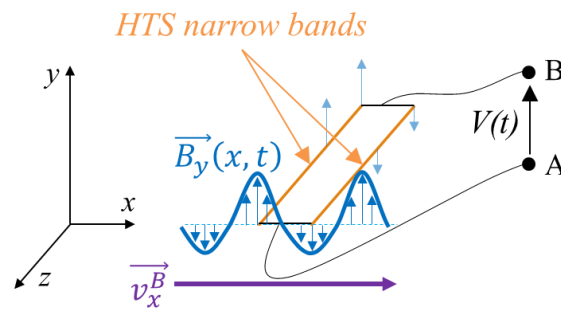
Figure 19 Schematic of the operating conditions for two parallel HTS bands to exhibit flux pumping

Assuming that the terminals of the two HTS bands are short circuited at each corresponding end, they are denoted as electrical nodes "A" and "B". At this stage, the scope of the analysis is to arrive at a formula for *V(t)* to later find that its average over one period of the magnetic waveform is not zero. $\overrightarrow{B_y}$ can be expressed as the rotor of a generic vector potential $\vec{A}$ with arbitrary divergence. $div(\vec{A}) = 0$ is chosen imposing $\vec{A}$ only exists in the z direction. Because of the employed assumptions and ignoring the field contribution of the time varying currents induced in the bands, expressing Faraday's law at any point in space gives Eq. (9).

$$E = -\frac{\partial A_z}{\partial t} - \nabla \phi \qquad (9)$$

Where the $\partial A_z/\partial t$ term is due to the varying external magnetic field, and ϕ is the electric scalar potential. Integrating (9) along the centroid axis in the z direction of the two HTS bands yields Eq. (10) and (11).

$$R_1(x_1,t)I_1 = emf_1(x_1,t) + V(t) \qquad (10)$$

$$R_2(x_2,t)I_2 = emf_2(x_2,t) + V(t) \qquad (11)$$

Where x_1 and x_2 are the x coordinates of the first and second HTS band respectively, while I_1 and I_2 are the currents flowing through them. $V(t)$, which arises from $\nabla \phi$, is not a function of the position because of the hypothesis that the two HTS bands are short circuited at each corresponding end (equipotentiality). Since the bands are superconductive, the power law [95] [96], written in Eq., is used to express R_1 and R_2.

$$R(x,t) = L_{bands}\frac{E_0}{I_C(x,t)}\left|\frac{I(x,t)}{I_C(x,t)}\right|^{n(x,t)-1} \qquad (12)$$

Where L_{bands} is the length of The HTS bands, E_0 is a conventional parameter used as a criterion for the definition of the conventional critical current I_c (a value of 1 µVcm^{-1} is assumed), and the dimensionless n exponent, also known as n-value, is chosen to make Eq. (12) fit the experimental E-J line for a given superconductor. It is noted that I_c is a function of the position (x) and time (t) because of the fact that $\overrightarrow{B_y}$ is both varying in time and not uniform in space and I_c is a function of the external magnetic field (see Figure 5). The same also applies for the n exponent [97]. It is also noted that a simple multiplication can be used to represent the result of the integral along the bands length because of the hypothesis that $\overrightarrow{B_y}$ is invariant of the position

along z (similarly, the *emf* and *V(t)* are related to $\partial A_z / \partial t$ and $\nabla \phi$, respectively). Eq. (10) and (11) combined form the equivalent circuit of Figure 20.
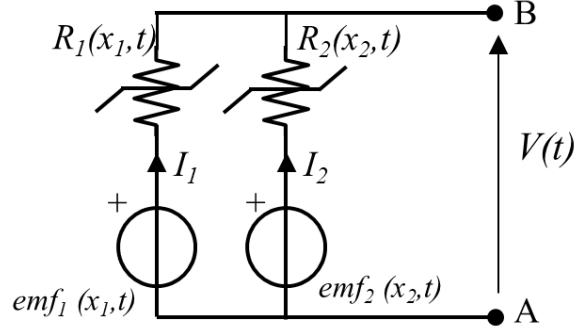
Figure 20 Simplified equivalent circuit of the two HTS bands of Figure 19

Before proceeding with the analysis, it is worth commenting on the elements of the equivalent circuit of Figure 20:

- At a specific instant, *emf₁* and *emf₂* differ due to the distinct magnetic field values encountered by the two HTS bands at time *t*. However, over the entire period of the external magnetic field, they exhibit the same overall trend, just shifted in time.

- Given the operating conditions, the parallel of the two HTS bands is an open circuit, which corresponds to writing $I_1 = -I_2$ at any time. Because of this, it can be deduced from Eq. (12) that R_1 and R_2 exhibit distinct values at a specific instant because they depend on different critical currents and the n-values, which are dependent on the external magnetic field. Similarly to the *emfs*, R_1 and R_2 also exhibit the same time-shifted trend.

An expression for $V(t)$ can be found using Millman's theorem [98] on the circuit of Figure 20.

$$V(t) = \frac{\dfrac{emf_1(x_1,t)}{R_1(x_1,t)} + \dfrac{emf_2(x_2,t)}{R_2(x_2,t)}}{\dfrac{1}{R_1(x_1,t)} + \dfrac{1}{R_2(x_2,t)}}$$

(13)

Simple manipulation of Eq. (13) yields Eq. (14):

$$V(t) = \frac{R_2(x_2,t) \times emf_1(x_1,t)}{R_1(x_1,t) + R_2(x_2,t)} + \frac{R_1(x_1,t) \times emf_2(x_2,t)}{R_1(x_1,t) + R_2(x_2,t)} \qquad (14)$$

Using T to denote the period of variation of the external magnetic field, the average of $V(t)$, here called V_{ave}, can be computed over a cycle as in Eq. (15).

$$V_{ave} = \frac{1}{T}\int_0^T \frac{R_2(x_2,t) \times emf_1(x_1,t)}{R_1(x_1,t) + R_2(x_2,t)} dt + \frac{1}{T}\int_0^T \frac{R_1(x_1,t) \times emf_2(x_2,t)}{R_1(x_1,t) + R_2(x_2,t)} dt \qquad (15)$$

Since the magnetic field that generates the *emfs* is periodic, if the resistances were constant in time V_{ave} would be obviously equal to zero.

$$V_{ave} = \frac{1}{T} \times \frac{R_2}{R_1 + R_2} \times \int_0^T emf_1(x_1,t)dt + \frac{1}{T} \times \frac{R_1}{R_1 + R_2} \times \int_0^T emf_2(x_2,t)dt = 0 \qquad (16)$$

Eq. (16) is no surprise, as it describes what happens in every conventional system of type of Figure 19 without superconductors involved. Differently, Eq. (15) could yield a non-zero average output voltage as a consequence of the time dependent non-linear resistances inside the integral. It is highlighted that the presence of both the two HTS bands is necessary for producing the voltage rectification. In fact, if only the HTS band number one was present, the equivalent circuit of Figure 20 would only include its corresponding branch. Consequently, and since no transport current is considered, V_{ave} would change according to Eq. (17).

$$V_{ave}^{single\ HTS\ band} = \frac{1}{T}\int_0^T emf_1(x_1,t)dt = 0 \qquad (17)$$

The general explanation of voltage rectification attributed to the superconductor's resistance variation was previously presented in a similar manner [93] [94]. However, this explanation only generically addresses the rectification to the

41

non-linearity of the resistance. To enrich the analysis, a possible and realistic operating mechanism of the circuit of Figure 20, that reproduces the general mechanism described in section 1.2, is presented hereafter. After connecting a superconducting load (represented by the inductance L_{load}) at the terminals A-B, let the external magnetic field waveform applied on the HTS bands be such that the equivalent circuit of Figure 20 exhibits the distinct phases depicted in Figure 21.
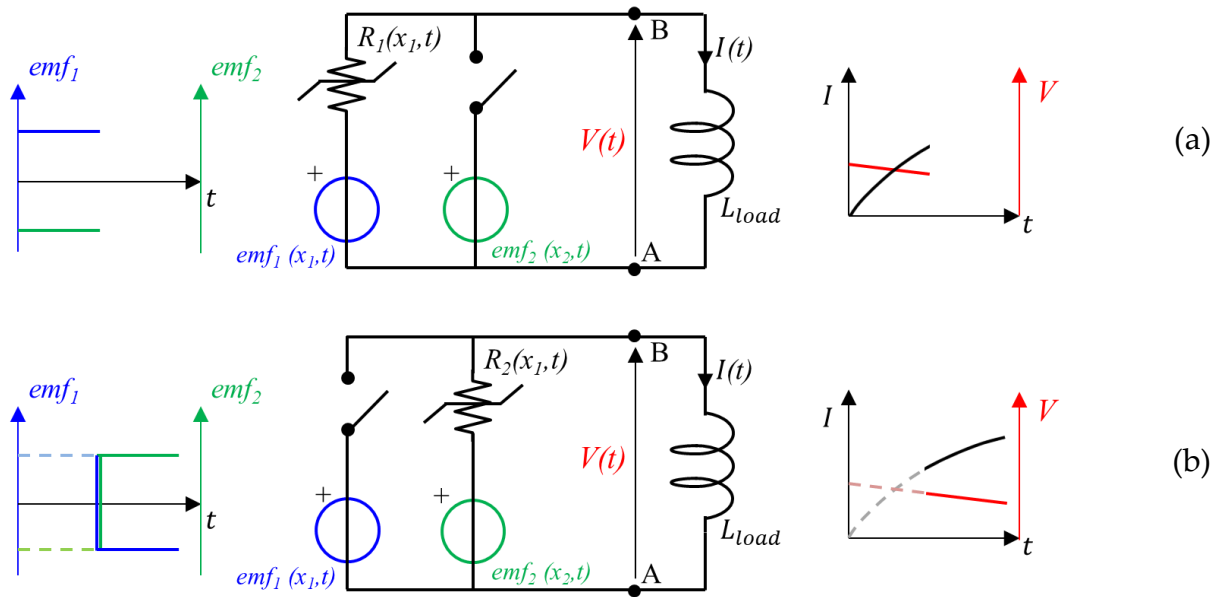
Figure 21 Ideal flux pumping operation of two HTS bands experiences a travelling magnetic field waveform: (a) band number one experiences a positive emf and limited suppression of superconductivity while band number two experiences a negative emf and strong suppression of superconductivity (ideally represented by being open circuited), current of the load coil (L_{load}) increases as a result of a positive voltage V(t), and (b) the two HTS bands have swapped operating conditions, V(t) remains positive, hence the energization of the load coil continues.

In the first phase (a), the magnetic field waveform produces opposite *emfs* in the HTS bands (positive *emf₁* and negative *emf₂*) and at the same time strongly inhibits the critical current of the band number two while does not significantly impact the critical current of band number one (which is the one exhibiting positive *emf*). The impact of the field on the critical current of the bands results in $R_2 \gg R_1$, which can be approximated in the equivalent circuit by making R_2 being represented with an open

circuit. At the first instant of the energization, the current in the load coil is still zero, therefore the same conditions from which Eq. (14) emerges apply and it can be approximated to incorporate the specific resistances value.

$$\lim_{\substack{R_2 \\ \overline{R_1} \to \infty}} V(0) = emf_1(x_1, 0) \tag{18}$$

However, as soon as the current in the load coil increases and starts to be non-zero, $V(t)$ diverges from $emf_1(x_1, t)$ and can be found through simple circuit analysis of Figure 21.a

$$phase\ (a)\ for\ t > 0, \quad \lim_{\substack{R_2 \\ \overline{R_1} \to \infty}} V(t) = emf_1(x_1, t) - R_1(x_1, t) \times I(t) \tag{19}$$

Eq. (19) implies that during phase (a), as the current in the load coil $I(t)$ increases (following a first order transient trend), the output voltage delivered by the flux pump decreases because of the voltage drop occurring on R_1. At some point during the cycle, in the considered scenario the parameters of the equivalent circuit change as a result of the travelling magnetic field wave. This corresponds to the beginning of phase (b), depicted in Figure 21.b. During phase (b), the resistances and the *emfs* of the vertical branches have swapped values: now *emf₂* is positive and *emf₁* is negative, while $R_1 \gg R_2$. Similarly to phase (a), R_1 is considered large enough to be represent by an open switch. Despite the significant changes in the topology and quantities of the internal equivalent circuit of the flux pump, the output voltage $V(t)$ is still positive and is caused by the circuit branch corresponding to the HTS band number two.

$$during\ phase\ (b), \quad \lim_{\substack{R_1 \\ \overline{R_2} \to \infty}} V(t) = emf_2(x_2, t) - R_2(x_2, t) \times I(t) \tag{20}$$

It can be seen in Eq. (20) that as $I(t)$ keeps increasing, $V(t)$ continues its decreasing trend. The coil load energization will stop when the *emf* is equal to the voltage drop on the resistance of the corresponding branch. Therefore, an expression for the maximum current $I(t)$ could be derived from Eq. (20) or (19) by simply setting

$V(t) = 0$. This appears contradictory compared to the earlier comments on Eq. (2). In fact, according to Eq. (2) the flux pump maximum current depends not only on the internal *emf*, but also on an internal inductance parameter ($L_{flux\ pump}$) that was included in the circuit of Figure 2 to account for the magnetic energy linked to the current flowing in the branch containing switch S_1. This resulted in transient sub-phases where the current redistributed between the branches of S_1 and S_2. It is also reminded that in the circuit of Figure 2, in which ideal switches were assume, any dissipation was neglected, hence no resistance was included in the scheme. On the other hand, no inductance is present in the circuit of Figure 20 because the field contribution due to the currents in the bands was neglected, leaving the resistances to be the only cause of current saturation of the flux pump. The same approximation is reasonable also if an entire tape is considered instead of two bands (as it is for practical systems and is generalized later in this section). It should be evident by now that the equivalent circuit of Figure 2 can be used to describe the voltage rectification typical of flux pumps but is only suitable for predicting the operating mechanism of transformer rectifiers. For this topology of flux pumps, the influence of the $L_{flux\ pump}$ parameter typically outweighs the effect of resistive contributions on current saturation, while the latter play a more significant role in determining the maximum current for HTS dynamos and linear flux pumps. Both circuits and analysis presented in Figure 2 and Figure 20 employ simplifications. In practical applications, the combined effect of inductive and resistive voltage drops determines the actual maximum current of a flux pump. Accounting for both factors is crucial for accurate calculations. However, this chapter focuses on a qualitative understanding of flux pumps, and both circuits effectively convey the most critical factors influencing current saturation across different flux pump topologies.

Moreover, there are other numerous idealizations employed in the analysis of Figure 21 that make Eq. (19) or (20) not useful on a practical level. These idealizations can be summarized as follows:

- The waveforms of *emf₁* and *emf₂* are shifted in time of half a period, meaning only one is positive at a time.

- Resistances R_1 and R_2 always assume their maximum value when the corresponding *emf* in series is negative, whereas they assume their minimum value when the corresponding *emf* in series is positive.
- For large R_1 or R_2, its corresponding equivalent circuit parameter is an open switch.

In practical scenarios, the *emfs* may exhibit different phase shifts relative to each other, leading to instances where they both simultaneously possess positive or negative values, and the functions of R_1 and R_2 may not be perfectly aligned to their trends as in Figure 21. Moreover, assuming an open circuit switch to account for a large resistance is a strong approximation which may significantly differ from practical circumstances. In fact, all the challenges that are encountered when attempting to increase the resistivity of a superconductor by magnetically inhibiting its critical current are already discussed and stressed in sections 1.3 and 1.3.1. Accounting for all the non-idealises described above would definitely impact the output of the flux pump, yielding worsening effect such as the undesired redistribution of currents between branches 1 and 2 of the circuit (causing incremental dissipation), the temporary inversion of the slope of current $I(t)$ (current ripple), and the reduction of the core effect of the flux pump, that is the cycle average of $V(t)$. However, the simplified analysis illustrated in Figure 21 effectively highlights the crucial factor that determines whether flux pumping, and consequently voltage rectification, can occur: the critical current of the superconductor must be substantially inhibited in the HTS band that, according to a specific convention, exhibits a negative *emf*. This condition ensures that the term in Eq. (14) that is positive at a particular time t is generally dominant in terms of absolute value, leading to a non-zero average of $V(t)$ over a period. Mathematically, it can be observed that achieving a dominant positive term in Eq. (14) is also achievable, in principle, by manipulating the *emf*; however, for practical systems, it is more straightforward and efficient to rely on the resistance rather than the *emf*. This is an indirect consequence of the superconductor's Power Law material property, as demonstrated in the subsequent chapters of this thesis where

simulations of real apparatuses are carried out and presented. Additionally, understanding the crucial role of the synchronization between the *emfs* variations and resistance changes reveals how the dynamo and linear flux pumps operate as rectifiers, in fact, this was already witnessed in the circuit of Figure 2, where the switches' states are determined by the voltage generator's value.

The extension of the previous analysis from two HTS bands to one continuous tape can be carried out now. Consider an analogue case of Figure 19 where the two HTS bands are replaced by one HTS tape whose surface lies in the xz plane. This is depicted in Figure 22.
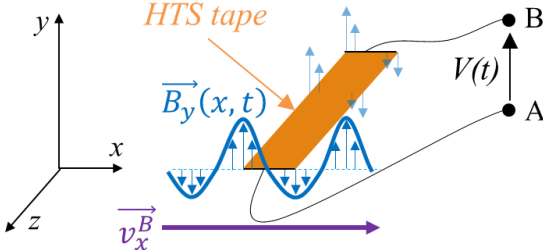
Figure 22 Schematic of the operating conditions for a HTS tape to exhibit flux pumping

Partitioning the HTS tape into n narrow bands, each with its centroid aligned parallel to the z-axis and each sufficiently narrow to consider the magnetic field as uniform across its width, and applying the same numerical analysis previously employed for the two HTS bands, leads to the equivalent circuit represented in Figure 23, which effectively captures the system's behavior.
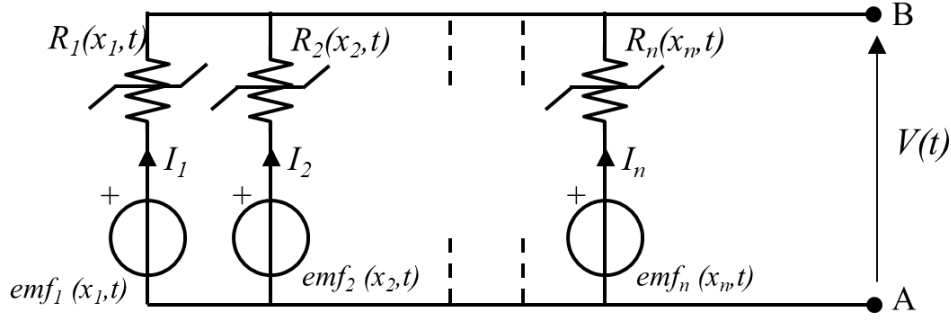
Figure 23 Simplified equivalent circuit of the HTS tape of Figure 22.

Where branches for bands between 3 and $n-1$ are not shown for simplicity. Using Millman's theorem on the circuit of Figure 23 to find $V(t)$ yields Eq. (21).

$$V(t) = \frac{\sum_{i=1}^{n} \frac{emf_i(x_i, t)}{R_i(x_i, t)}}{\sum_{i=1}^{n} \frac{1}{R_i(x_i, t)}} \qquad (\,21\,)$$

Similarly to Eq. (15), the non-linear relationship between the resistances and the applied magnetic field makes them time-varying, thereby leading to a nonzero average of $V(t)$ on one period of the field if the positive terms of the numerator summation significantly outweigh the negative ones in terms of absolute value. The exploitation of Eq. (21) to arrive at a general comprehensive formula that gives the accurate value of the average output voltage of a flux pump is arguably not feasible analytically. In fact, the appropriate discretization of the HTS tape relies on the instantaneous emf at the considered points, which in turn may exhibit different trends and shapes depending on the type of flux source generating it, whether it's permanent magnets of specific dimensions for HTS dynamos or electromagnets for linear type flux pumps. Moreover, the actual values of the resistances follow the highly nonlinear Power Law relation of Eq. (12), boosting complexity and ruling out any possibility of algebraic solution of Eq. (21). To my personal knowledge up to date, accurate and reliable evaluation of the quantities of any system such as the one depicted in Figure 22 is only feasible by means of numerical modeling approaches. In the following chapter, a

thorough numerical model is developed that replicates the mathematical approach outlined in this section without resorting to simplifying approximations that could impede its accuracy, such as neglecting the field contribution of the currents induced in the superconductor. This model will show how the non-idealities, like the losses from current redistributing between branches where resistances are not fully increased, affect the flux pump. It will also underline that the voltage rectification in the flux pump happens because of a combination of the magnetic field waveform's effect on the variable *emf* and resistivity across the width of the HTS tape, where the latter must be generally larger in the HTS tape regions exhibiting negative *emf*.

This is how HTS dynamos operate, as well as any travelling wave flux pump.

1.4.2. HTS dynamos state of the art

The concept of the HTS dynamo to supply an HTS magnet was demonstrated by Hoffmann et al in [76]. The experimental setup of the study involves a HTS dynamo unit with a motor, where cylindrical magnets are mounted on discs that rotate over strips of HTS tape, as shown later. The magnets' motion is perpendicular to the length of the tape, and the entire setup is immersed in liquid nitrogen during operation. The flux pump is connected to the leads of a superconducting coil by soldered joints, forming a mostly superconducting closed circuit. The coil used in the experiments is a double pancake coil, constructed using 40 m of HTS tape with specific dimensions, 55 A of critical current, and 2.7 mH inductance. A cryogenic hall sensor is mounted centered with the coil-axis to detect the field and correlate it to the current circulating through calibration using a power supply. The HTS conductor employed in the flux pump is supplied by Superpower. The flux pump unit is driven by a 4 W DC motor with a motor-controller unit, and the rotation speed is limited to 4 Hz. The experimental setup and a schematic of the dynamo are depicted in Figure 24. Figure 24.a reports a picture of the real apparatus, while Figure 24.b shows a 2D schematic of the dynamo.
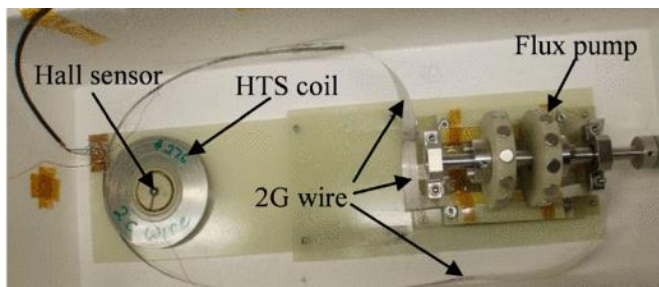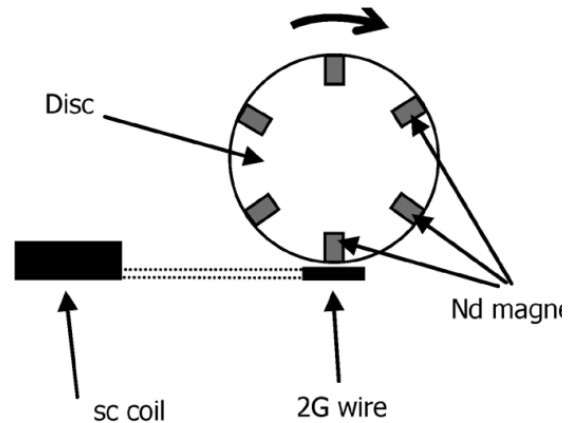
(a)   (b)

Figure 24 (a) The flux pump and the superconducting circuit are contained within a styrofoam box, and during operation, the entire assembly is submerged in liquid nitrogen, and (b), Diagram illustrating the flux pumping method: The disk housing the permanent magnets rotates above the HTS tape [76]. © [2011 IEEE

In one experiment of this study the shaft and disks rotate at a frequency of 4 Hz for 800 s in one direction and then in the reverse direction. The magnetic field of the coil and the generated current are measured during the experiment. The coil is energized to a current of 48 A within 175 s and held there for 600 s. When the rotation direction is reversed, the current is pumped down to zero within 52 s and then started to energize the coil in the opposite direction to 48 A. Both current and generated field over time are shown in Figure 25. The results demonstrate that the flux pump operates in a bipolar manner depending on the direction of disc-rotation. The current limit of 48 A is reached when the voltage generated by the flux pump equals the voltage drop caused by the resistive joints (which in the study is found to equal to 40 nΩ) and the intrinsic resistance of the HTS tape of the dynamo.
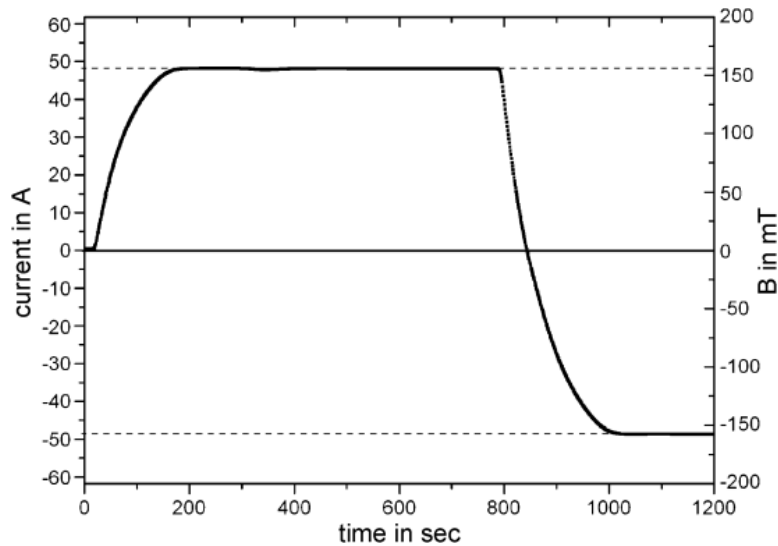
Figure 25 Current, displayed on the left scale, and magnetic field, shown on the right scale, are illustrated within the coil. The field reverses its orientation whenever the disc's rotation changes direction. In both directions, the coil is energized to 48 A [76]. © [2011 IEEE

The authors of this study report to have experienced a high sensitivity of the generated output voltage of the dynamo to the distance between magnet and the HTS tape, which hereafter is referred to as airgap. It is worth highlighting this aspect here, as later in this thesis the impact of this factor will be stressed, particularly when numerical models are utilized to simulate similar apparatuses. In addition, it is evident that the output and performance of a flux pump are affected by numerous factors that alter the traveling magnetic field waveform in the HTS tape. A multitude of factors, including the magnetization, dimensions, and number of permanent magnets, the radius of the disk in which they are embedded and its distance from the HTS tape, converge to determine the magnetic field experienced by the HTS tape, which itself can exhibit varying properties. Therefore, recent studies have focused on the impact of the design parameters on the performance, including: the frequency of rotation [99], the ratio between the permanent magnet and HTS tape widths [100], the airgap [101], the number of permanent magnets [102] and their geometry [103].

One often overlooked yet crucial aspect concerning flux pumps, especially in HTS dynamo systems, is the issue of losses. The incomplete suppression of critical

current when applying the magnetic field of permanent magnets to the tape leads to a modest increase in resistivity. As depicted in Figure 22, the eddy currents in the tape are voltage-driven. Consequently, as per Eq. (3), significant dissipation occurs within the superconductor if the critical current is only moderately inhibited. Even the pioneering study of [76] does not dig into this aspect quantitatively, although the authors do indicate in the discussion that the dominant loss contributor in the superconducting loop comprising the flux pump, the HTS coil, and the joints, is the flux pump itself.

One of the first studies to cover quantitively the losses aspect is reported in [87], where losses of the flux pump were calculated by measuring the input power to the dynamo and subtracting the output power delivered to the HTS circuit. The losses due to non-superconducting components, such as magnetic drag and iron losses, were also measured and subtracted from the results. The power delivered to the HTS circuit from the dynamo was calculated as the operating current multiplied by the output voltage, as measured with voltage taps on each of the HTS flyleads. The input power was obtained multiplying the torque measured at the rotor driveshaft and its angular frequency. The experimental set up of this study is the multi-stator squirrel cage superconducting dynamo depicted in Figure 26, which comprises four Nd-Fe-B permanent magnets and eight HTS stators, all being within the cryogenic environment at 77 K. The authors refer to the HTS tapes of this dynamo as HTS stators.
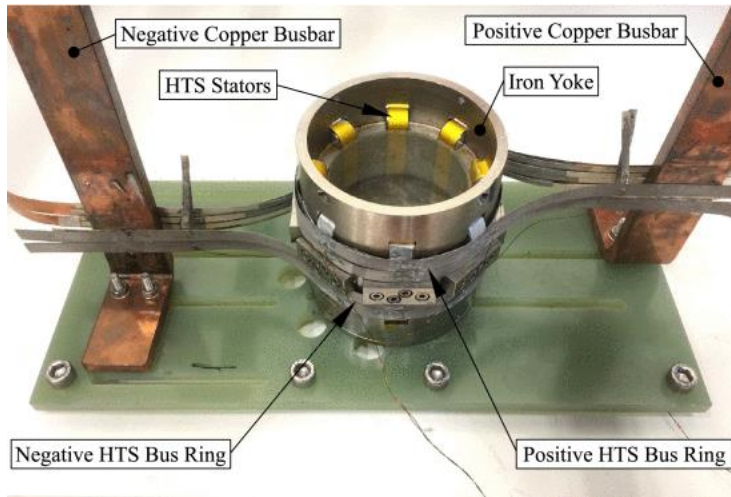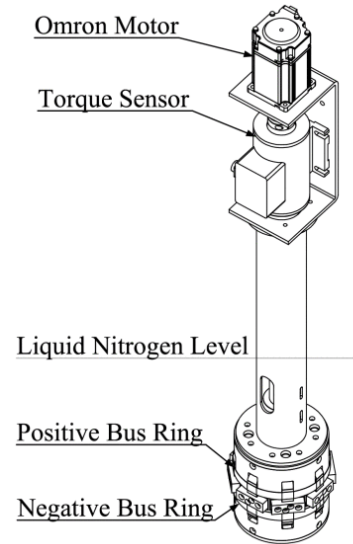
(a)   (b)

Figure 26 (a) Squirrel Cage Dynamo stator components, and (b), schematic of the rotor [87]. © [2020] IEEE

The electric characteristics of the experimental setup, measured for different angular velocities of the rotor, are shown in Figure 27. These results certificate two typical flux pumps characteristics: large current capabilities (up to about 1700 A in this case) but very modest DC output voltage (3.87 mV peak was obtained in [87] at open circuit conditions and 600 rpm of the rotor). This data is also compliant with the analysis of section 1.4.1 in which a maximum current that would set the output voltage to zero was theoretically predicted. A thorough discussion of the quasi-linear trend of the flux pump electrical characteristics can be found in section 2.1.3.
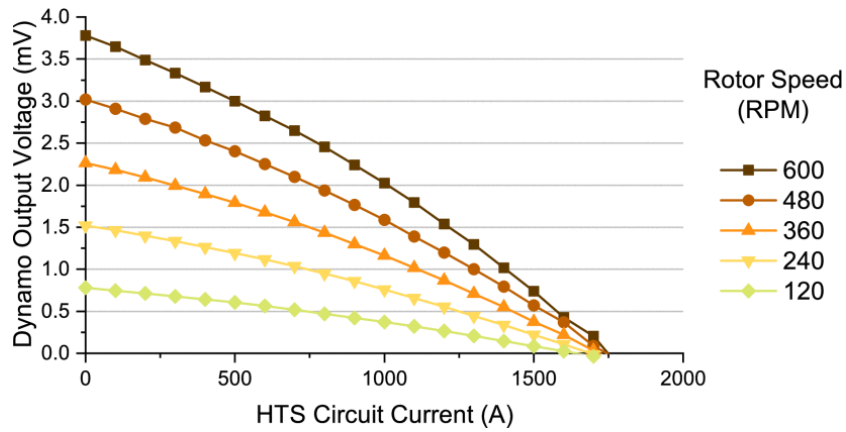
Figure 27 The electric characteristics of the HTS dynamo, measured for different angular velocities of the rotor (in rpm) [87]. © [2020] IEEE

Despite the large current capability, which itself is a remarkable result, the major novelty in [87] is the energetic performances. Figure 28.a shows the output power of the dynamo versus its total transport current at different rotor speed velocities, while Figure 28.b the efficiency of the flux pump in the same scenarios. It must be noted that the efficiency is defined in [87] as the ratio between the electrical output and mechanical input power of the dynamo.

(a)   (b)
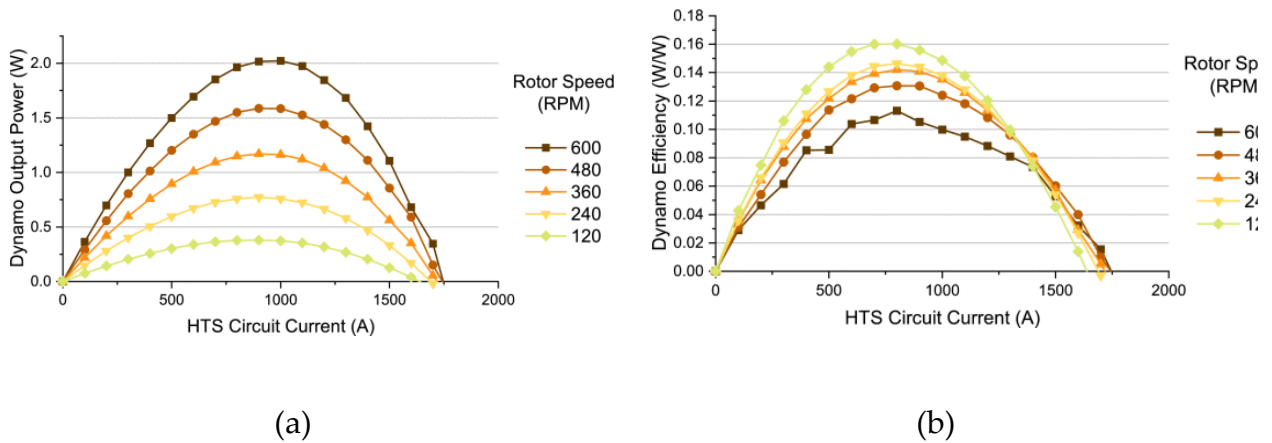
Figure 28 (a) Squirrel Cage Dynamo output power, and (b), Squirrel Cage Dynamo efficiency [87]. © [2020] IEEE

The most important observations that can be derived from the experimental results of Figure 28 are listed below:

- Given a specific rotor speed, the maximum values of the output power and efficiency of the dynamo occur around half of the current capability (with the output power maximum tending to higher current and the efficiency maximum to lower current).

- Due to the enhanced output voltages observed at higher rotor speeds (as depicted in Figure 27), larger rotor speeds lead to higher output powers. However, it is the lower rotor speeds that deliver higher efficiencies, suggesting that the speed of the magnetic field interacting with the HTS stators is somewhat proportional to the dynamo's internal losses (and undoubtedly has a more substantial impact than the increase in output voltage).

- Figure 28.b indicates that the dynamo efficiency is generally modest, as the maximum measured value is around 16 %.

The last point of the list above is a common characteristic of all flux pumps, as it will become evident later in this thesis. It is also consistent with previous theories about how eddy currents in the dynamo's HTS tape cause losses. These losses occur in areas of the superconductor where some resistivity is present, due to the partial suppression of the critical current caused by the magnetic field.

In the next session, another type of flux pumps whose voltage mechanism is triggered by a travelling magnetic field waveform is presented: the linear flux pump.

1.5. Linear type flux pumps

In section 1.4.1 , the properties a travelling magnetic field wave needs to have to initiate flux pumping in a superconducting slab were listed, explained, and discussed. The type of travelling wave flux pump is determined by the physical source of the magnetic field wave: a HTS dynamo produces the field using rotating permanent magnets, whereas if the field wave travels along a straight trajectory and is generated through a set of coils in which certain currents flow, the flux pump falls within the "linear" category. The schematic of a linear flux pump is depicted in Figure 29.

(a)   (b)
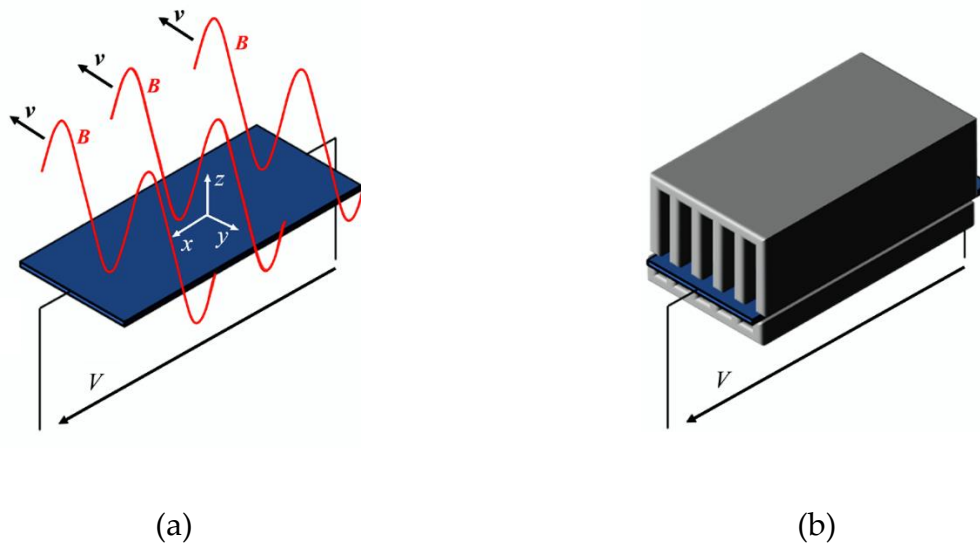
Figure 29 Schematic of a linear flux pump. (a) HTS tape and travelling magnetic field B. (b) layout of a possible ferromagnetic core to embed the set of coils used for producing the traveling magnetic field on the HTS tape. In principle the ferromagnetic core is not necessary, different from the set of excitation coils, but is commonly used to enhance the field applied on the HTS tape

Even if in principle the coils that generate the magnetic field could be also superconducting, so far only copper coils have been used for this purpose [104] [105] [106] [107] [108] [109] [110] [111] [112] [113] [114]. A copper coils configuration that has been tested and demonstrated for a flux pump is well presented in [106]. The flux pumping method of [106] utilizes a linear electromagnetic pump composed of eight copper coils, iron cores, and an iron frame. The superconducting tapes that are

employed for flux pumping and four 80 mm×12 mm superconducting tapes (Superpower SF12100). Using the solder method, these superconducting tapes are positioned to short the two ends of the superconducting coils that are exploited as loads for the flux pump (three coils are used in total: one pancake coil, one rectangular coil and another rectangular coil but with an iron core). The apparatus of this study is depicted in Figure 30.
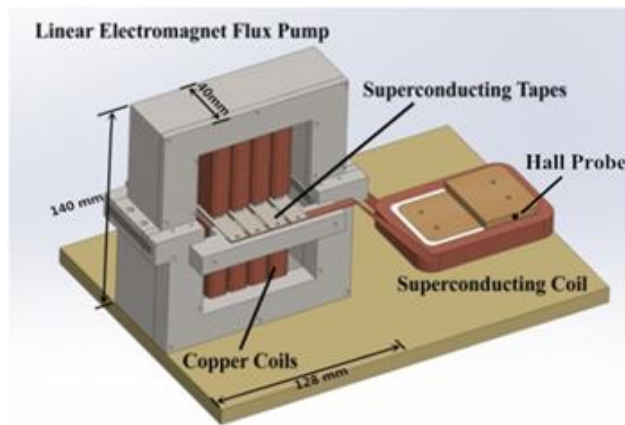
Figure 30 3D structure of the flux pump of [106] connected to a superconducting coil. The superconducting tapes are sandwiched between the air gap of the magnetic poles, and a superconducting coil is secured to the supporting plate. © IOP Publishing. Reproduced with permission. All rights reserved.

Current-source driver circuits are used to control the current through the copper coils of the electromagnets. During the experiment, the currents applied to the copper coils were either unipolar sinusoidal waves, trapezoidal waves, and triangular waves. One example of triangular current profiles that were fed into the copper coils are depicted in Figure 31.
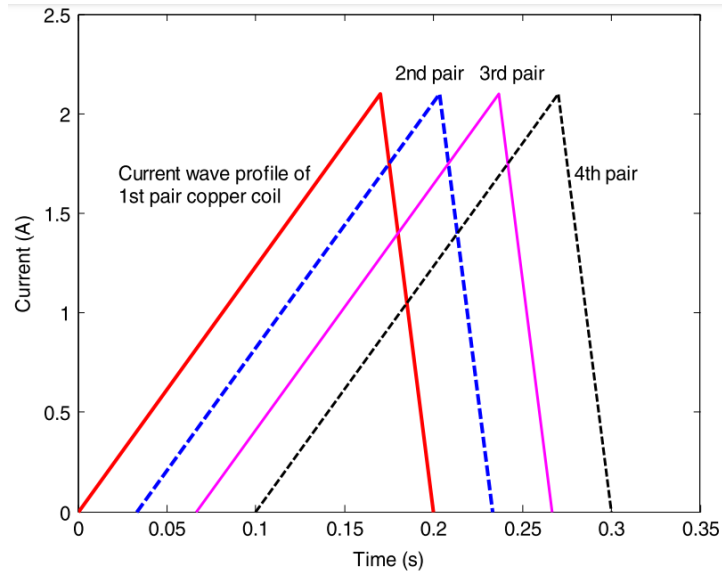
Figure 31 Triangular wave profiles that were employed in the copper coils of [106], utilizing 5 Hz frequency, 2.1 A amplitude, and a 60-degree phase shift between adjacent poles. © IOP Publishing.

During the experiment, a calibrated cryogenic Hall sensor was used to measure the trapped field in the superconducting coil during the flux pumping process, from which its current was derived. The impact of the copper coils current profiles and frequency on the load coil energization are shown in Figure 32.a and Figure 32.b respectively.
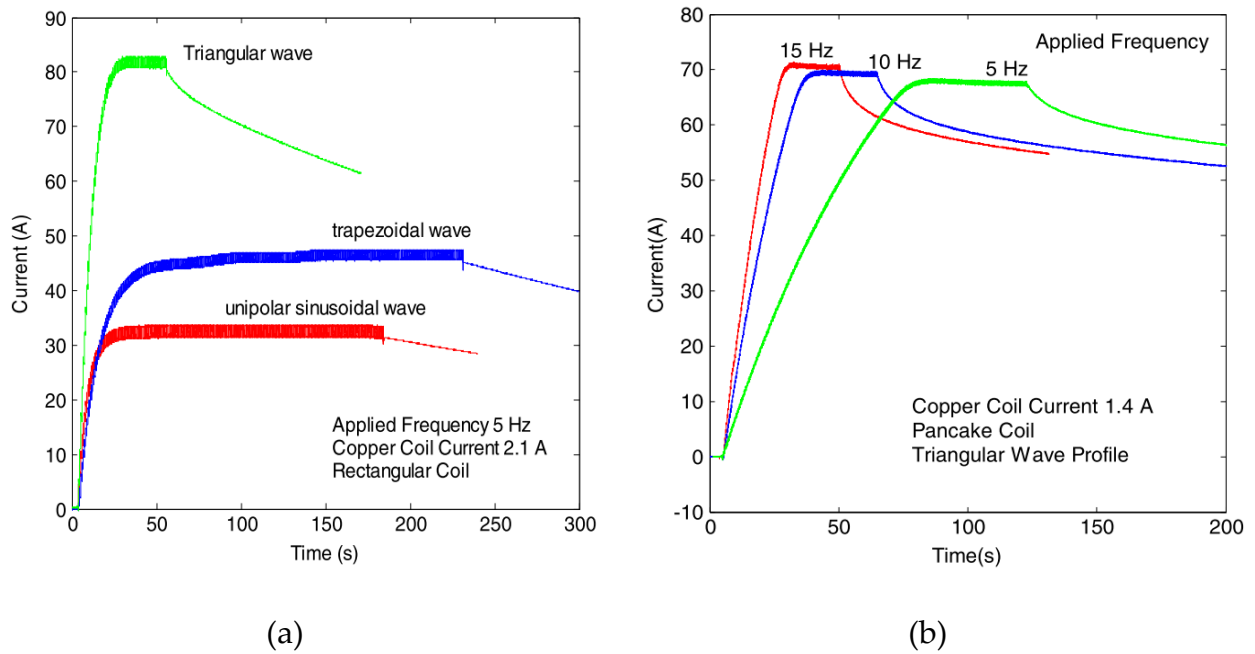
Figure 32 (a) Impacts of a unipolar sinusoidal wave, trapezoidal wave, and triangular wave with a frequency of 5 Hz, and a peak of 2.1 A as copper coil current on the magnetization of the rectangular coil [106], and (b), impact of the copper coils currents frequency on the pancake coil magnetization [106].

Figure 32.a clearly shows that the triangular wave is the most effective current profile to be fed into the copper coils of the linear flux pump of [106] to maximize the current injected in the load coil. In Figure 32.b , the impact of the copper coil's current frequency appears less significant on the maximum load current compared to the wave profile. However, the charging transient notably varies with this parameter, potentially due to an increase in the DC output voltage of the flux pump. It's important to consider that the critical current for rectangular coils is 94 Amps and for pancake coils, 77 Amps. This suggests that the triangular wave profile can effectively energize the coils close to their maximum current capabilities. However, when sinusoidal or trapezoidal waves are applied to copper coils, current saturation occurs far below the critical current of the superconducting load coils. This could be due to reduced *emfs* and/or increased local resistances within the flux pump's tapes, which limit the maximum pumped current, as indicated by the analysis of the circuit in Figure 20,

section 1.4.1. Unfortunately, the authors haven't provided details on the flux pump's dissipation, nor on the induced voltages, so this theory remains unconfirmed.

Another approach to create a linear flux pump is to design the copper coils to generate a traveling sinusoidal magnetic field accompanied by a DC component. This is a relatively simple electrical engineering task, akin to building a linear electrical machine (three-phase AC copper windings) with an additional coil for the DC field component. A flux pump of this type recently achieved a pumped current of 1600 Amps in [115]. The kilo-amp linear type flux pump described in the study is designed to generate a DC biased AC traveling magnetic wave in its air gaps. The travelling wave is generated by AC windings located in slots and four DC windings, whose current is controlled by an inverter. The rest of the magnetic circuit is an iron core that includes the two air gaps, each able to enclose six 12 mm-wide HTS tapes. The travelling wave in the air gaps has five active poles. The flux pump also comprises a total of 12 HTS tapes, each connected in a single loop and in parallel with each other, immersed in a liquid nitrogen bath at 77 K during operation. The pumped current in the 12 HTS tapes is measured by two open-loop Hall current sensors, with each sensor measuring six HTS tapes. A picture of the flux pump of [115] is depicted in Figure 33.
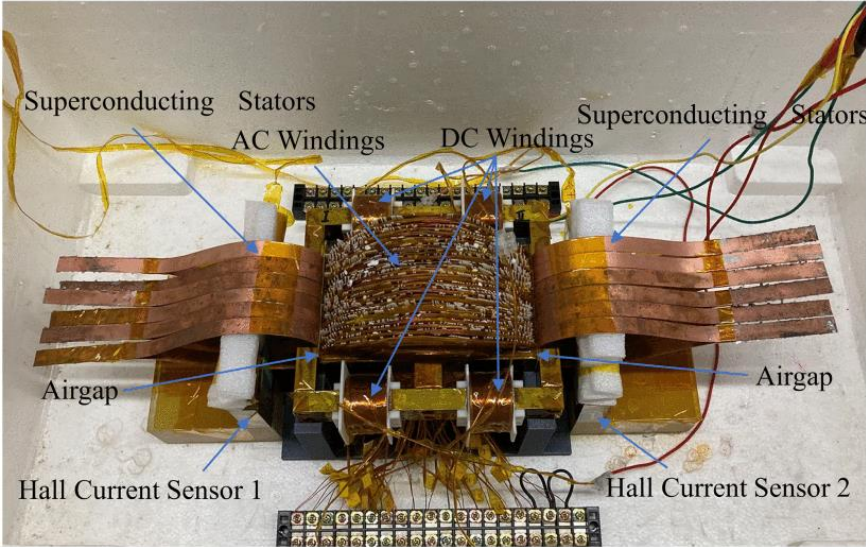
Figure 33 The kilo-amp linear type flux pump of [115]. © [2022] IEEE

The authors of [115] report that magnetic travelling waves reaching maximum values of 0.2 T, 0.3 T, 0.4 T, and 0.5 T were attempted, even if they do not provide measurements of the actual field profiles in the airgaps. The pumped currents that arise in the HTS tapes as a result of the aforementioned applied magnetic field waves are shown in Figure 34. The maximum measured pumped current of 1619 A, obtained with a magnetic travelling wave with a peak of 0.5 T, is a remarkable result. It is evident from Figure 34 that the current charging transient lasts for a few seconds before reaching saturation. Since no HTS coil is used in this study, but rather 12 HTS tapes serve as the load, it is reasonable to assume that the inductance of the superconducting loop is extremely small. This, coupled with the transient's duration of a few seconds, suggests a very limited output voltage. Unfortunately, and similarly to the study of [106], no other output or performance of the flux pump was measured during the experiments, therefore the theory of low output voltage remains unconfirmed.
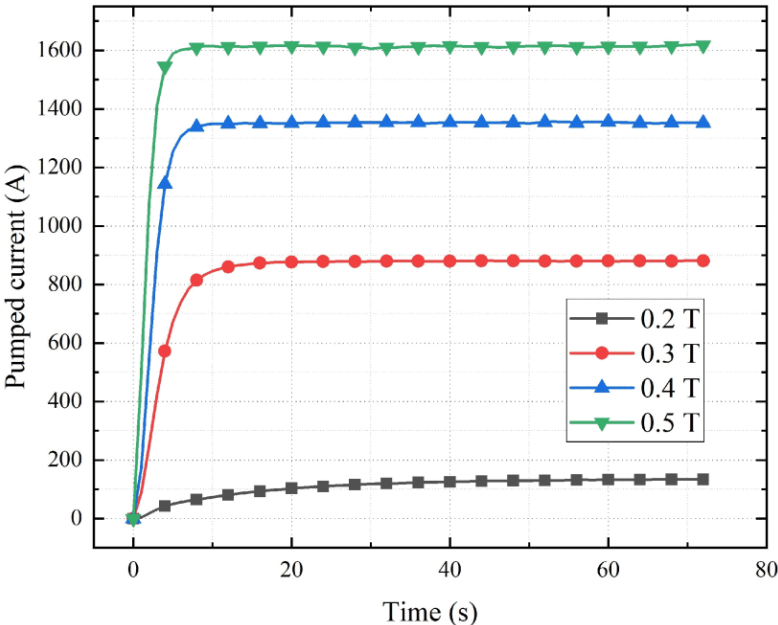
Figure 34 The total amount of current pumped by the 12 HTS tapes was measured under different air gap magnetic field intensities. The maximum pumped current of 1619 A was recorded. [115]. © [2022] IEEE

More generally on linear flux pumps, it is evident by now that its performances are determined by the characteristics of the travelling magnetic field wave applied on the HTS tapes. Limited studies have investigated the influence of the traveling wave properties on flux pump outputs, but their results are not broadly applicable [112] [113]. Later in this thesis, the influence of the magnetic travelling wave is accounted by means of numerical models and optimization algorithms that find the optimal profile based on the desired performance a linear flux pump. Moreover, the lack of experimental data regarding the losses of the linear type of flux pump is, to my view, one of the largest research gap around this technology. It was already stressed several times in this thesis, and will be stressed again, that a certain amount of dissipation is inherent in flux pumps, and this aspect is of paramount importance to investigate their viability in real applications. Therefore, this topic was also numerically addressed during this Ph.D. project, and some results are shown in one of the subsequent chapters where a linear flux pump is designed.

To conclude this introductory chapter, references are provided as the most relevant and recent flux pump reviews, enabling readers to deepen their understanding of these devices and gain a comprehensive overview of the latest advancements in flux pump technology. [12] [13] [116] [117] [118] [119] [120] [121].

2.Chapter 2: Development of a validated numerical model of flux pumps

Much of sections 2.1, 2.1.1, 2.1.2, 2.1.3, 2.1.4, 2.1.5, and 2.1.6 of this chapter has been published in:

Much of sections 2.2, 2.2.1, 2.2.2, 2.2.3, 2.2.4, 2.2.5, 2.2.6, and 2.2.6 of this chapter has been published in:

And much of sections 2.3, 2.4, and 2.5 of this chapter has been published in:

Exploring flux pumps behavior through accurate numerical models represents a fast and efficient method to provide optimal design criteria and to explore their losses and possible limits during practical operation. In recent years, flux pumps mechanism and charging capacity have been investigated both through numerical simulation [122] [123] [124] [125] [126] [127] [128] [129] [130] [131]. Since the flux pump's main purpose is the energization of HTS magnets, the ability to predict the charging dynamic and the steady state coil's current, as well as the current ripple, is the mandatory step for the design of flux pump device of interest in practical applications. Of utmost importance is also the identification and the quantitative assessment of loss phenomena during operation and the identification of possible current and voltage limits that the flux pump could not overcome. The operational limits in which the device can operate as a generator, delivering electric power to the load and absorbing

input power, are also crucial aspects that a useful and serviceable numerical model must be able to calculate.

This chapter reports the research work during this Ph.D. project dedicated to developing a numerical model for travelling field flux pumps (HTS dynamo and linear type) that is validated against experimental results and can capture all the aforementioned features of these devices.

2.1. A volume integral equation method for modelling travelling field flux pumps

In the sub sections of **2.1**, a volume integral equation (VIE) method for modelling flux pumps is developed and described. The finite element method (FEM) is used to calculate the energetic performance and the outputs for a HTS dynamo flux pump, as well as to derive a new complete equivalent circuit that has the same outputs of the real system and properly takes all dissipation mechanisms into account.

2.1.1. The simulated apparatus for the model development and its operating conditions

The model is first developed for the dynamo flux pump reported in [132] [133]. The device consists of a 12 mm width HTS wire exposed to the field produced by a permanent magnet rotating anticlockwise past the wire with angular velocity ω. An external two-terminal component (or load) can be connected to the terminals of the HTS wire, and the overall behavior of the system is affected by the type of component. A 3D view of the flux pump connected to the external component is shown in Figure 35.a, where the current I and the voltage V denote the total delivered current and the voltage appearing at the terminal of the flux pump respectively. The generator convention, whereby the reference direction of the voltage is oriented toward the outgoing terminal of the current, is assumed for the flux pump. With this assumption a positive VI product denotes a power supplied by the flux pump and absorbed by the external component, and vice versa. Both the current I and the voltage V can, in general, change with time. Two different operating conditions will be considered for the flux pump in the following:

1. Current driven operation – the flux pump is connected to an external ideal current source that imposes the delivered current I. The open circuit operation of the flux pump can be seen as a limit case of this operating condition in which I = 0.

2. RL load – the flux pump is connected to an HTS coil. Electrically, this is equivalent to an external RL load where with resistance R_{ext} and inductance L_{ext} accounting for the joints and the superconducting winding respectively. This operating condition can be used to model the charging of a HTS coil up to any current below the critical value. The short circuit operation of the flux pump can be seen as the limit case in which $R_{ext} = 0$ and $L_{ext} = 0$, though this operating condition has no practical interest. In this work we consider a superconducting coil with 0.24 mH inductance and 0.88 $\mu\Omega$ resistance due to joints, as in [133]. Besides the joints, no further resistive effects are considered for the HTS coil.

We report that different operating conditions, possibly including voltage sources, could be modelled depending on the final application of the flux pump, but these are out of the scope of this study and will not be considered. A 2D schematic section view of the flux pump is shown in Figure 35.b. All the relevant parameters of the considered flux pump are summarized in Table 1. A critical current of 283 A is assumed for the HTS wire. No dependence of the critical current on the magnetic field is assumed at this stage.

Table 1 HTS dynamo parameters [133]

Width of the permanent magnet (PM), a^{PM}	6 mm
Height of the PM, b^{PM}	12 mm
Depth of the PM, l^{PM}	12.7 mm
Remanence of the PM, B_r	1.25 T
Width of the HTS tape, a^{tape}	12 mm
Thickness of the HTS layer, b^{HTS}	1 μm
Critical current (77K, self field), I_c	283 A
n value	20
External radius of the rotor, R^{rotor}	35 mm
Airgap between the PM and the HTS tape, δ	3.7 mm
Frequency of rotation of the PM, f	25 Hz (1500 rpm)
Angular velocity of the PM, ω	157.08 rad/s

(a)   (b)
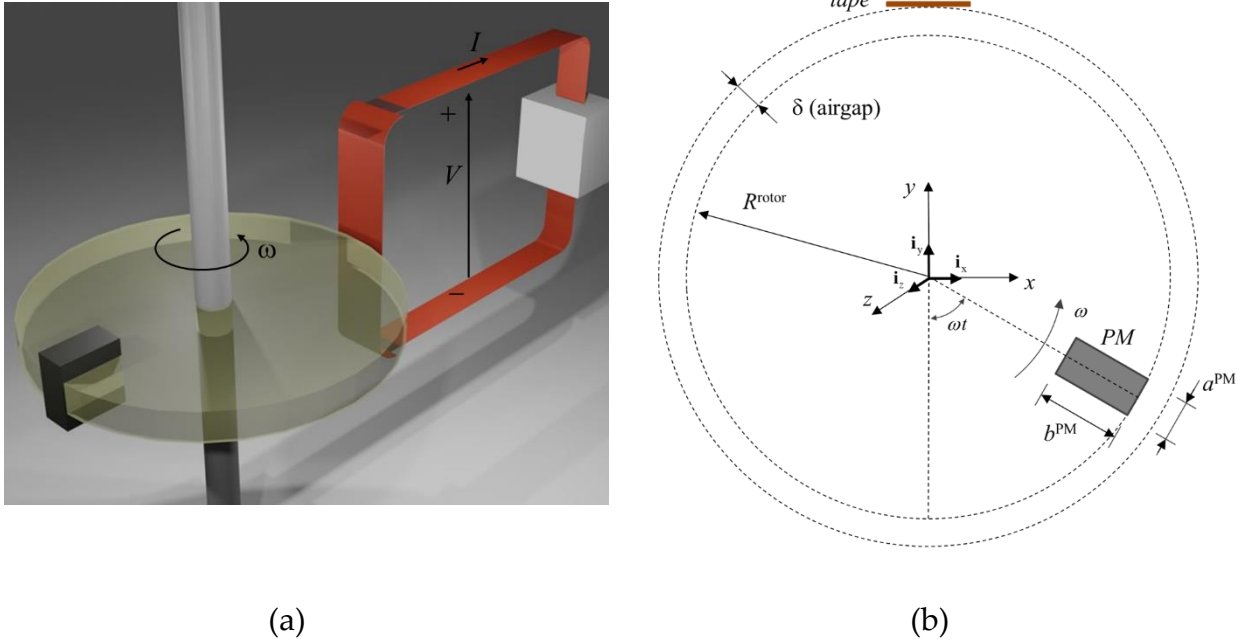
Figure 35 (a) 3D view of the flux pump connected to the external component. (b) schematic 2D section view of the flux pump.

2.1.2. The mathematical model and the energy balance of the flux pump

The numerical model used in this study is an extension of the VIE-based equivalent circuit previously used and briefly explained in [134]. The latter has been adjusted in order to be suitable to simulate the operating conditions described in the previous section. The mathematical formulation of the model is fully described in this section. In the considered system the total electromotive force is given by the sum of a transformer-like contribution due to the time-varying field produced by the current induced in the superconductor and a second contribution due to the movement of the PM. As a consequence, the Faraday's law at any point in the superconductor gives [135]:

$$E = -\frac{\partial A^J}{\partial t} - v \times B^{PM} - \nabla\phi \qquad\qquad (22)$$

where A^J is the vector potential of the currents of the superconductor, B^{PM} is the field of the permanent magnet (PM), v is the velocity of B^{PM} at the considered point and ϕ is the electric scalar potential. It is specified that term $-v \times B^{PM}$ in equation (22) can be replaced by $-\frac{\partial A^{PM}}{\partial t}$, where A^{PM} is the vector potential of the field of the permanent magnet. Assuming the power law as the constitutive equation relating the electric field E to the current density J of the superconductor, hence Eq.(22) is rewritten as follows.

$$\rho(J)J = -\frac{\partial A^J}{\partial t} - v \times B^{PM} - \nabla\varphi$$

$$\text{with } \rho(J) = \frac{E_0}{J_c}\left(\frac{J}{J_c}\right)^{n-1}$$

(23)

For now, J_c is taken constant. Based on Eq. (23), a 2D model can also be obtained under simplifying assumptions and is discussed in detail in the following. The constraints imposed by the external component coupled with the flux pump play the role of boundary conditions and are naturally included in the circuit model developed.

The cartesian reference frame (x, y, z) shown in Figure 35.b, with the z-axis parallel to the long dimension of the HTS wire, is introduced. For obtaining the 2D model we use the infinite long approximation, that is, we assume that all along the wire length the induced current only flows in the z-direction, that the field produced by the PM only lies in the cross section of the wire (the xy plane) and that neither the field nor the current depend on the z coordinate. This corresponds in practice to neglecting the effects of the terminal sections (at the ends of the PM, or where the HTS tape is connected to the external component in case of PM longer than the tape) where both the current and/or the field of the PM can follow a more complex path. It is worth to note that since the induced current J only flows in the z-direction also the magnetic vector potential A^J associated with it only has z component. The permanent magnet along with the flux lines of the produced magnetic field can be considered as a unique rigid body rotating with angular velocity ω around the center O of the flux pump. Thus, the velocity v of the field at a generic point of the cross section is given by:

$$v = \omega i_z \times r \tag{24}$$

Where i_z denotes the unit vector of the reference frame in the z direction. By expressing the Faraday's law for the infinite long case depicted earlier and by using Eq.(24) we obtain.

$$\rho(J)J = -\frac{\partial A^J}{\partial t} - \omega r \cdot B^{PM} - \nabla\varphi \tag{25}$$

It can be seen from Eq.(25) that only the radial component of the magnetic field produced by the PM contributes to generating the motional electromotive force exciting the system. The numerical solution of Eq.(25) is obtained by using the weighted residual approach. The superconductor cross section is subdivided into a finite number of rectangles. An element-wise uniform distribution of current is assumed, and it is required that Eq.(25) be satisfied in the weak form over each element of the discretization. In essence, by means of this procedure, the whole conducting domain is subdivided in a number N of thin wires with rectangular sections, and the following solving system is obtained.

$$\bar{\bar{M}}\frac{d\bar{I}_w}{dt} = -\bar{\bar{R}}\bar{I}_w + \bar{u} - \bar{1}\nabla\varphi \tag{26}$$

where $\bar{I}_w$ is the set of currents of the thin wires, $\bar{1}$ is a column vector of as many ones as the number of thin wires of the subdivision, $\bar{\bar{M}}$ is the matrix of self/mutual induction coefficients, $\bar{\bar{R}}$ is the diagonal matrix of resistances, $\bar{u}$ is the vector of motional electromotive forces acting on the thin wires with unit length and are defined by

$$m_{hk} = \frac{\mu_0}{4\pi} \int_{S_h} \int_{S_k} \ln \frac{1}{|r - r'|^2} \, dS' \, dS$$

$$r_{hh} = \rho \left(\frac{I_h}{S_h} \right) \frac{1}{S_h}, r_{hh} = 0 \quad \text{if} \quad h \neq k \tag{27}$$

$$u_h = -\omega \frac{1}{S_h} \int_{S_h} r \cdot B^{\text{PM}} \, dS$$

By multiplying Eq. (26) for the active length of the flux pump, that is the depth l^{PM} of the permanent magnet, the following equation is finally obtained.

$$l^{PM} \overline{\overline{M}} \frac{d\bar{I}_w}{dt} = - l^{PM} \overline{\overline{R}} \bar{I}_w + l^{PM} \bar{u} - \bar{1} V \tag{28}$$

Where V is the voltage across the flux pump ($l^{PM} \nabla \varphi$), and the total current I circulating in the flux pump, and in the external component connected to it, is given by the sum of currents of the wires ($\bar{1}^t \bar{I}_w$). V ad I are depicted in Figure 35.a.

Eq. (28) corresponds to the finite element based equivalent circuit of Figure 36.a and Figure 36.b, referring to the flux pump operating in current driven mode (i.e., connected to a current source) or supplying a RL load respectively. This equivalent circuit of the flux pump contains, per each branch, a voltage source u representing the electromotive force impressed by the moving magnet, a non-linear resistor r, accounting for the resistive voltage drop inside the superconductor, and a coupled inductor representing the electromotive force induced by the time-varying field produced by the current of the superconductor. All the branches are connected to the external component (current source or RL load, in the cases considered here) carrying the total current I and subject to the voltage V of the flux pump. In order to solve the problem, the constitutive equation of the external component needs to be specified. If the flux pump is connected to an ideal current source, combining the total current is an assigned quantity and Eq. (28) form an algebraic-differential system that can be solved yielding, at any instant, the current distribution within the flux pump (vector $\bar{I}_w$) and the voltage V across it. Once the voltage V is calculated at any instant, the average value in one period $T = 2\pi/\omega$ of rotation can be defined as:

$$V_{average} = \frac{1}{T} \int_{t}^{t+T} V(t') dt' \qquad (29)$$

On the other hand, if the flux pump is connected to an RL load, then the voltage *V* across it is subject to

$$V = R_{ext} I + L_{ext} \frac{d}{dt} I \qquad (30)$$

Hence, by substituting (30) in (28) and by using the condition of $I = \bar{1}^t \bar{I}_w$, the following differential equation is obtained which allows to calculate the current distribution (vector $\bar{I}_w$) at any instant.

$$\left(l^{PM} \bar{\bar{M}} + L_{ext} \bar{1}^t \bar{1} \right) \frac{d}{dt} \bar{I}_w = -\left(l^{PM} \bar{\bar{R}} + R_{ext} \bar{1}^t \bar{1} \right) \bar{I}_w + l^{PM} \bar{u} \qquad (31)$$

The voltage *V* of the flux pump can be obtained afterward by using equation (30), or one of the equations of the system (28). The average voltage across the flux pump can finally be obtained by using (29). It is stressed that, when operating with a current, either impressed by a current source or supplied to a coil, the flux pump is able to transfer power to the external component only if a non-zero and positive average voltage is generated across it.

(a)   (b)
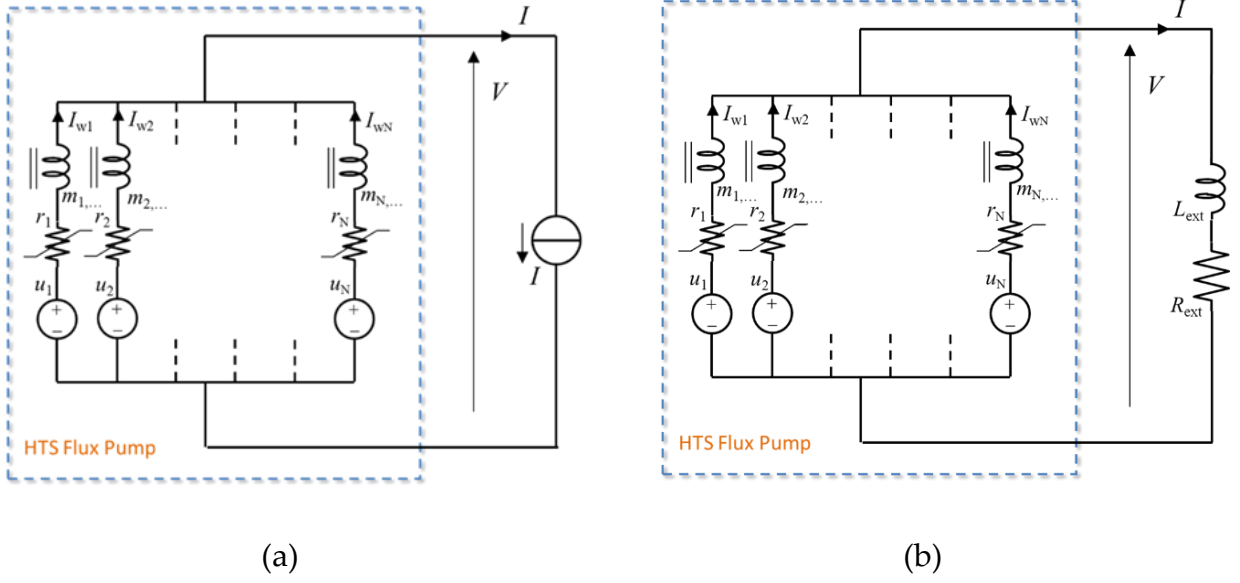
Figure 36 Finite element based equivalent circuit of the flux pump (a) connected to a current source (b) connected to an RL load.

For stating the energy balance, the Faraday's law is rewritten in the following vector form:

$$\rho J i_z = -\frac{\partial A^J i_z}{\partial t} - (\omega i_z \times r) \times B^{\mathrm{PM}} - \nabla \varphi i_z \qquad (32)$$

After scalar multiplication by the vector current density $J i_z$ and integration over the volume occupied by the active length of the flux pump of Eq. (32), the final energy balance of Eq. (33) is obtained.

$$-T_{mecc}\omega = VI + P_J + \frac{d}{dt}W_{\mathrm{mag}} \qquad (33)$$

where P_J is the total joule loss occurring in the superconductor (attributed to $\bar{\bar{R}}$ in the discretized form), W_{mag} is the stored magnetic energy (attributed to $\bar{\bar{M}}$ in the discretized form) and T_{mecc} is the resistant mechanical torque produced onto the rotor, via the Lorentz force, by the current of the superconductor and is given by

71

$$T_{mecc} = 1^{\text{PM}} \int_S (Ji_z \times B^{\text{PM}}) \times r dS \qquad (34)$$

Eq. (33) states that, at any instant, the mechanical power $-T_{mecc}\omega$ supplied to the rotor is transferred, up to the dissipation P_{joule} and the change of magnetic energy of the superconductor, to the external component connected to the flux pump whose absorbed power is given by the product VI. Since during cyclic operation no net change of the magnetic energy occurs, the net mechanical energy $E_{\text{mechanical}}$ supplied to the rotor in one cycle, is in part transferred through the terminals to the external component and in part dissipated into the superconductor due to Joule heating. Accordingly, by denoting with E and E_{joule} the transferred electrical energy and the dissipated energy respectively, the efficiency of the flux pump can be defined as η in Eq. (35).

$$\eta = \frac{E}{E_{\text{mechanical}}} = \frac{E}{E + E_{\text{joule}}} = \frac{\int_t^{t+T} VI dt'}{-\int_t^{t+T} \omega T dt'} \qquad (35)$$

2.1.3. Computation of the electrical characteristic of a flux pump

All results shown were obtained by including in the model the superconductor layer only and neglecting the other constituents of the composite HTS tape, namely the substrate and the shunt layer. The inclusion of these further layers in the model implies a higher number of variables and a longer calculation time and does not change significantly the conclusion arrived at in this section. Furthermore, the results shown were obtained by meshing the HTS layer with 60 elements, obtained by using 60 subdivisions along the tape width and 1 subdivision along the layer's thickness. The use of only one subdivision along the thickness is equivalent to assuming the thin sheet approximation for the superconductor's current. More subdivisions can be used for modeling the distribution of the current along the layer's thickness into account. It was verified, however, that no substantial difference emerges in the numerical results by using more subdivisions both along the width and the thickness of the tape.

The average motional electromotive force produced by the PM onto the elements (thin wires) of the discretization during one rotation cycle is shown in Figure 37. This is the voltage impressed by the voltage sources of the FEM-based equivalent circuit of Figure 36, corresponding to terms u_h in Eq. (27). They apply both for the current driven operation (Figure 36.a) and for the RL load (Figure 36.b). The curves shown in Figure 37 refer to elements of the subdivision lying at various positions along the tape's length. All electromotive forces have, individually, zero average value during one period. Nevertheless, it is their presence that, combined with the non-linearity of the superconductor, produce an average DC voltage at the terminal of the flux pump, as previously explained in section 1.4.1. Again, the voltage rectification is due to the non-linearity of the superconductor that manifests itself in the local resistance, and it cannot be reached by the terms u_h alone. Moreover, because the velocity of the field at one specific point is constant, if all electromotive forces have, individually, zero average value during one period, so does the corresponding magnetic field. This impeccably refutes previous speculations that claimed that a DC biased magnetic field was necessary for creating flux pumping [108]. In fact, as this might be a sufficient condition for linear travelling waves, it is not a necessary requirement for every flux pump to work, as the synchronous electromotive force and local resistance variations in HTS tapes that produce voltage rectification according to the mechanism discussed in section 1.4.1 can be produced with a magnetic field that has zero average value during one period. This is actually the case of HTS dynamos, where the magnetic field waveform produced by the PM is highly non-symmetrical with respect to the x axis (it is proportional to the one of Figure 37) and because of this it produces the conditions for flux pumping by forcing different values of electromotive force and local resistance along the width of the HTS tape.

The highest electromotive force is obtained at the middle of the tape, which reaches up to 15.1 mV (absolute value), since this is the element closest to the PM (reaching the lower distance corresponding to the airgap δ of 3.7 mm -– see Figure 35.b). Electromotive forces referring to symmetric positions during the rotation (e.g.,

begin and end of the tape, or ¼ and ¾ of the tape's width) have the same (mirrored) waveform but are displaced by the time needed by the PM to span the angle between them. In the case of tape bent along the circumference so to form an air gap constant in all positions the emf of all elements would have the same waveform, displaced in time.
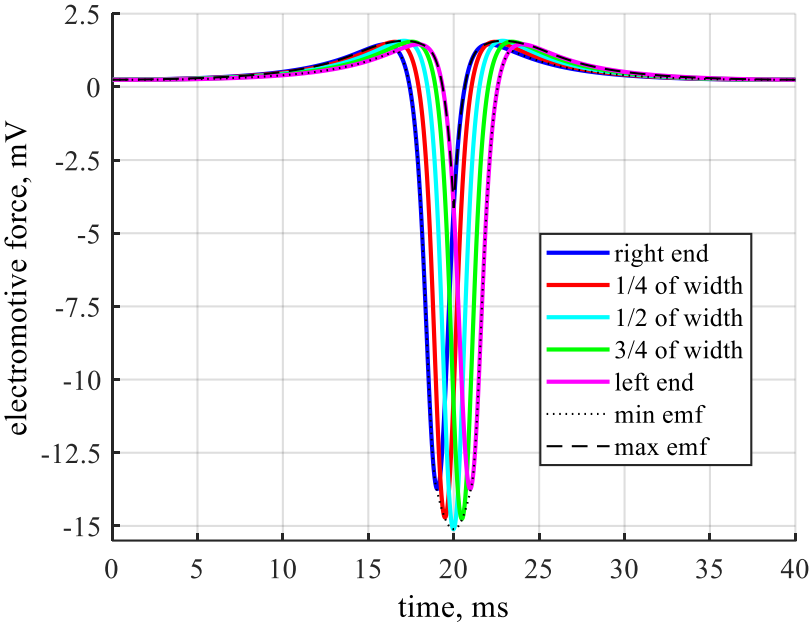
Figure 37 Electromotive force induced by the PM during one rotation cycle at various position along the tape's width (see Figure 35.b). The curves shown refer to the right end of the tape, ¼ of the width from the right, ½ of the width, at ¾ of the width from the right and to the left end of the tape. The minimum and the maximum emf occurring in the tape at any instant are also shown by means of dotted and dashed lines respectively.

The results of the current driven operation model version are described hereafter.

The open circuit operation of the flux pump can be seen as the limit case in which $I = 0$. Results shown refer to the case where first the transport current is applied and after the rotation is started, and more in particular:

- The impressed current is linearly increased from zero to its final DC value I during a time interval corresponding to two revolutions. No rotation of the PM occurs during the ramp-up of the current.

- A resting interval, lasting one revolution, is applied after reaching the final value *I*. No rotation of the PM occurs during this interval.

- The PM starts to rotate after the resting interval while the impressed current is kept constant to the final value *I*. Cyclic operation of the flux pump is reached.

The terminal voltage *V* of the flux pump during one cycle is displayed in Figure 38 for various values of the current *I* impressed by the external source in the range from −20 A to +50A. The open circuit voltage of the flux pump, corresponding to *I* = 0, is included in the figure. The maximum and minimum electromotive force acting all over the tape width during the cycle, taken from Figure 37, are also replicated in Figure 38. It can be seen that, for all impressed currents in the considered range, the terminal voltage is always comprised between the minimum and the maximum emf produced by the PM motion onto the tape. Moreover, despite the fact that all electromotive forces produced by the PM on the tape have zero average value (see Figure 37), the terminals' voltages of Figure 38 have non-zero average value in one cycle. This average can be positive or negative depending on the impressed DC current. To show this, the time integral of the terminal voltage during one cycle is shown in Figure 39, for the different impressed currents. The corresponding average voltage $V_{average}$ of the flux pump in one cycle, obtained by means of Eq. (29), is shown in Figure 40 as a function of the impressed DC current *I*. It is clear from these figures that, besides the fluctuating time behavior of Figure 38, the terminals' voltage of the flux pump is characterized by a non-zero DC average when it operates with an impressed DC current in the considered range. This DC voltage component is the result of the distributed electromotive force produced by the PM on the tape combined with the non-linear resistivity of the superconductor (the inductive terms have, in fact, a negligible effect on the formation of the terminal voltage). It is important to point out that screening currents reaching overcritical values are continuously induced in the tape for producing the rectification effect at the terminals. These currents circulate also in no load condition (open circuit operation with *I* = 0) and have a major impact on the energy balance of the flux pump.

It must be pointed out that, even though the instantaneous terminal voltage reaches well beyond 10 mV (absolute value), the average (DC component) voltage only reaches a few tens of μV, as discussed in detail later. It is important to note, from Figure 40, that the average (DC) voltage of the flux pump decreases linearly with the impressed DC current and reaches 0 V at $I = I_0 = 34.2$ A. Beyond this value, a negative DC voltage appears at the terminal of the flux pump. Hence, as far as the DC impressed current is in the range $[0 -\!- I_0]$, due to the fact that positive current and average voltage are observed at the terminals, and since the generator convention is assumed for the reference direction of I and V (see Figure 35.a), a positive average power $P_{average}$ = $V_{average} \times I$ is delivered in one period by the flux pump, that operates in generator mode. However, if the DC impressed current is increased beyond I_0, the average voltage at the terminals reverses and the average delivered power becomes negative, meaning that the power is absorbed by the flux pump. Hence, value I_0 fixes the limit beyond which the flux pump exits the generator mode and enters the dissipative mode. Similarly, if the impressed DC current is negative, the average terminal voltage remains positive and a negative average delivered power is obtained, meaning that the flux pump is operating in the dissipative mode. It is pointed that, despite the fact that a null average voltage occurs at the terminals corresponding to it, current I_0 and should not be interpreted as the short circuit current of the flux pump, but the limit of its generation ability instead.
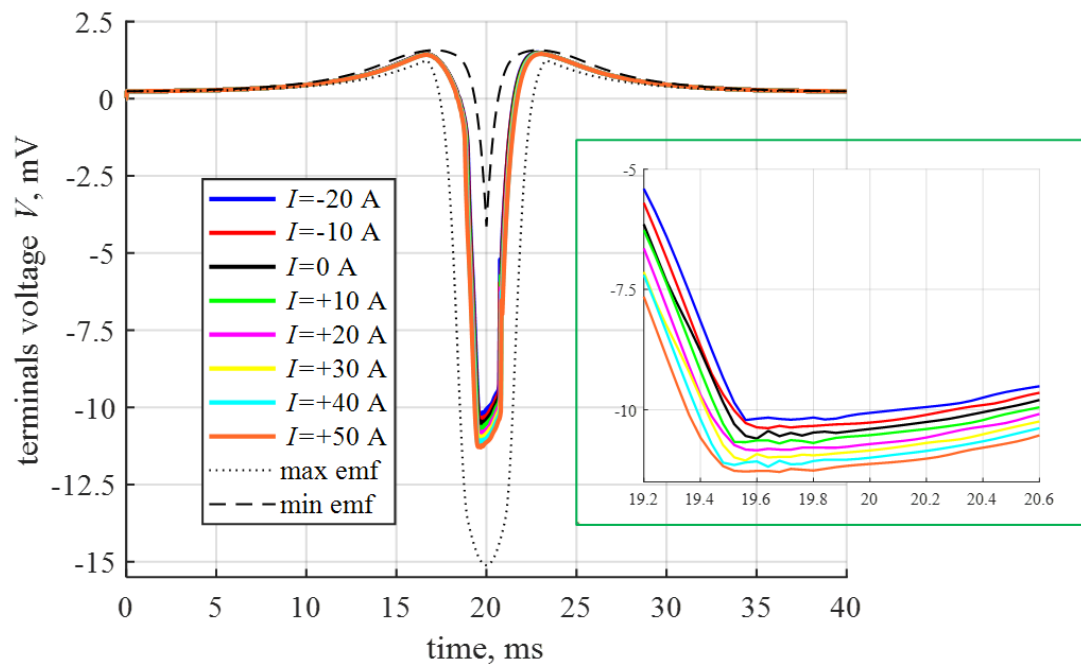
Figure 38 Terminal voltage V of the flux pump versus time in one cycle for various values of impressed DC current I. The black curve, corresponding to I=0, is the instantaneous open circuit voltage of the flux pump. The insert of the figure shows the detail of the waveform in a more restricted time interval. The monotone decrease of the terminal voltage with increasing current, visible in the insert, is observed at all instants of the cycle.
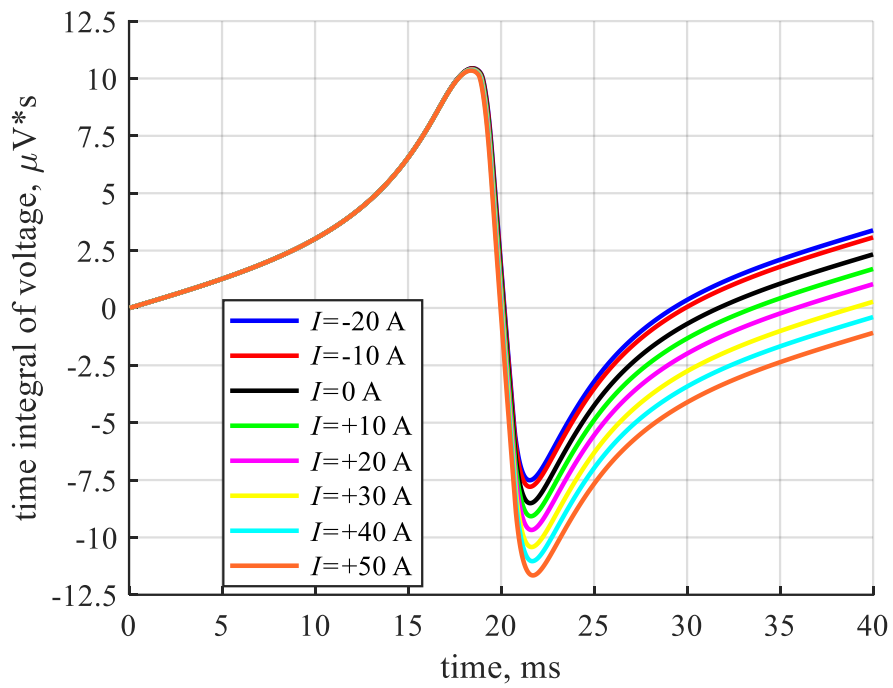
Figure 39 Time integral of the terminal voltage V of the flux pump during one cycle for various values of impressed DC current I.
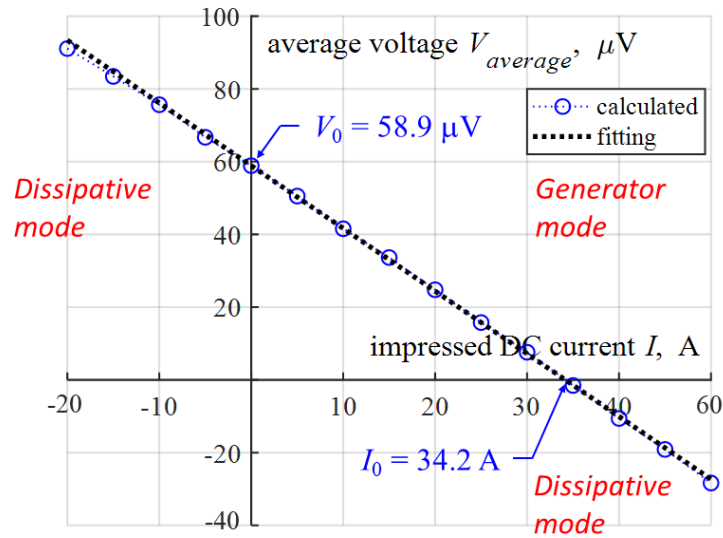
Figure 40 Average voltage Vaverage of the flux pump in one cycle for various values of impressed DC current I. The dotted line represents the linear V-I trend intersecting the I and V axis at points (I0, 0) and (0, V0) respectively.

The open circuit voltage, corresponding to the operation of the flux pump with no impressed DC current ($I = 0$), is denoted with V_0 in Figure 40 and is 58.9 μV. The flux pump can only operate in the generator mode if the operating point lies in the first quadrant of the I-$V_{average}$ plane, with both positive current and voltage. This only occurs if the impressed current is in the range [0 - I_0] and the corresponding average voltage is in the range [V_0 - 0]. Beyond these limits, either the voltage or the current becomes negative. The operating point falls respectively in the second or the fourth quadrant of the I-$V_{average}$ plane, and a dissipative behavior occurs. To better emphasize how the rotation of the PM affects the energy behavior of the flux pump, in Figure 41 the average terminal voltage is compared with the voltage that would occur across the tape in case of no rotation, over a wide range of DC impressed currents. It is clear from the figure that the effects of the rotation are:

- Shifting the VI curve into the first quadrant allowing power generation. This is effect is clearly visible in Figure 40, which is a magnification of Figure 41 around the origin. In case of no rotation, the VI curve only lies in the second

and fourth quadrant corresponding to the dissipative operation. However, the current and voltage intervals in which generation is allowed are very narrow. In particular, the maximum current I_0 (34.2 A) for which power generation is possible is much lower than the critical current I_c of the tape (283 A – see Table 1). Supplying power to a load requiring a current greater than I_0 is not possible by means of the flux pump. It is stressed that, for fixed air gap and angular velocity, I_0 is an intrinsic parameter of the flux pump and does not depend on the load connects to it.

- Increasing the power to be supplied for impressing a DC current when the flux pump does not operate in the generation mode. In fact, in case of no rotation, appreciable voltage (developed according to the power-law characteristic of the material) and, hence, power dissipation, only occurs for impressed currents well beyond the critical value. On the opposite, loss free current cannot be impressed in the tape if rotation is in progress since substantial voltage is detected even at small current and power must be supplied for keeping the current circulating.
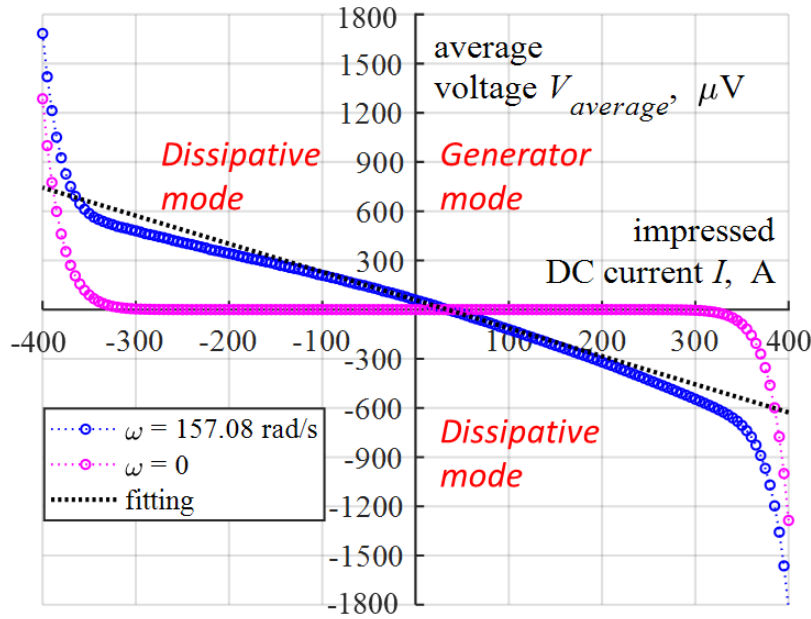
Figure 41 Average voltage Vaverage of the flux pump rotating at 157.08 rad/sec (25 Hz) compared with the voltage developing at the tape's terminal in case of no rotation over a wide range of impressed DC currents. The dotted line represents the linear V-I trend intersecting the axes at points (I0, 0) and (0, V0) as in Figure 40.

2.1.4. Computation of the energy balance of a flux pump

For stating the overall energy balance of the flux pump the energy terms that must be considered are:

- the total joule heating P_{joule} produced, at any instant, within the tape.
- the mechanical power $P_{mechanical}$ that must be supplied to the rotor for maintaining the rotation.
- the change rate $P_{magnetic}$ of the magnetic energy stored in the magnetic field produced by the currents of the tape.

The calculated time behavior of the four power terms of the flux pump during one rotation period is shown in Figure 42 for different values of the DC impressed current. The corresponding energy during 10 cycles, obtained via the integration of the power terms, is shown in Figure 43. A monotone increasing trend can be observed in

Figure 43 for the mechanical energy supplied to the rotor, for the energy dissipated into the tape due to Joule heating, and for the energy supplied by the external component, meaning that net unidirectional energy transfer occurs. Mechanical energy is always positive meaning that no energy can be extracted from the rotor (motor behavior). The net electric energy transferred to the external components can be both positive or negative, depending on if the flux pump operates in the generator or the dissipative mode respectively. In the latter case, the energy is indeed delivered by the external component to the flux pump and is converted, along with the energy supplied to the rotor, into heat into the tape. As expected, a cyclic behavior is observed for the magnetic energy that, hence, does not contribute to the overall energy balance.

In the case of open circuit operation (I = 0 A) no power is exchanged at the terminals. Nevertheless, currents are induced in the tape during the rotation that generate the power loss P_{joule} and, at the same time, a non-zero average voltage at the terminals $V_{average}$ = V_0 = 58.9 μV. This power is more intense when the magnet passes below the tape and reaches a peak of about 2.18 W. The dissipated energy in ten cycles is 54.38 mJ, corresponding to an average power of 135.9 mW. The induced currents create a resistant torque on the rotor, which requires mechanical energy to maintain the rotation. A total mechanical energy of 54.38 mJ is supplied to the rotor in ten cycles and is integrally converted into heat in the tape. When the flux pump operates with a DC impressed current I = 17.1 A (the half of I_0 – see Figure 40) it operates in the generator mode and transfers the maximum possible power to the load (the reason why the power is maximum in this condition is related to the linearity of the V-I curve in the first quadrant). The instantaneous power exchange with the external component can be both positive and negative. Nevertheless, a positive average voltage $V_{average}$ = 30.1 μV is developed across the terminals, caused by the nonlinear E-J relation, which is responsible for the power transfer. The net energy transferred by the flux pump to the external load in ten cycles is 0.21 mJ, corresponding to an average power of 0.53 mW (also obtainable as $V_{average} \times I$). The joule dissipation is 54.49 mJ. The mechanical energy transferred to the rotor in this operating condition is 54.70 mJ and is nearly

completely converted in joule dissipation with only a small part (0.21 mJ) transferred to the load. When the DC impressed current is lower than zero or greater than the limit I_0 of the generator region (34.1 A) then the average voltage and power at the terminal of the flux pump reverse. Energy is transferred from the external component to the flux pump and is converted, along with the mechanical power supplied to the rotor, in dissipation into the tape.
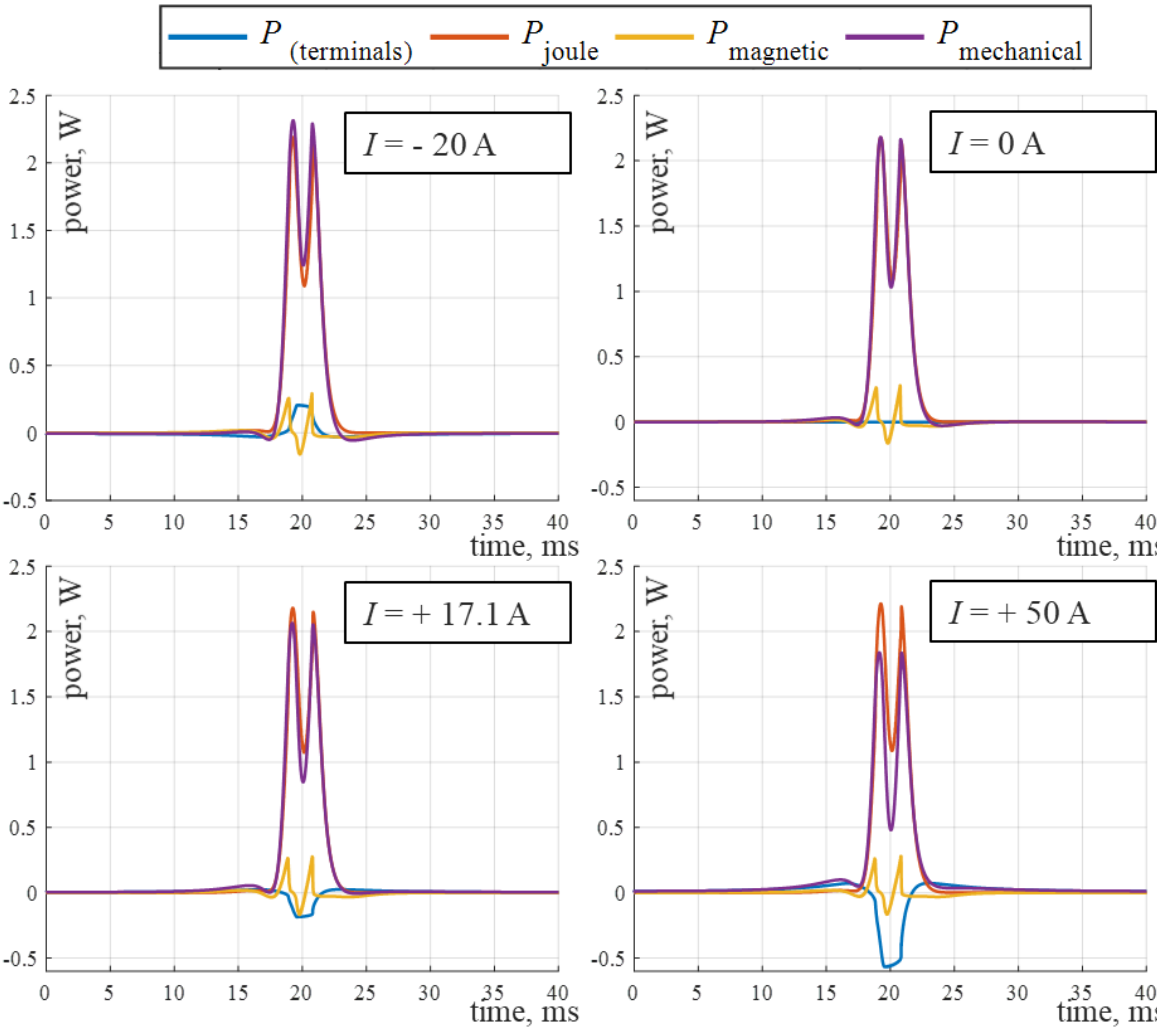
Figure 42 Power terms of the flux pump during one rotation cycle for different values of the DC impressed current.
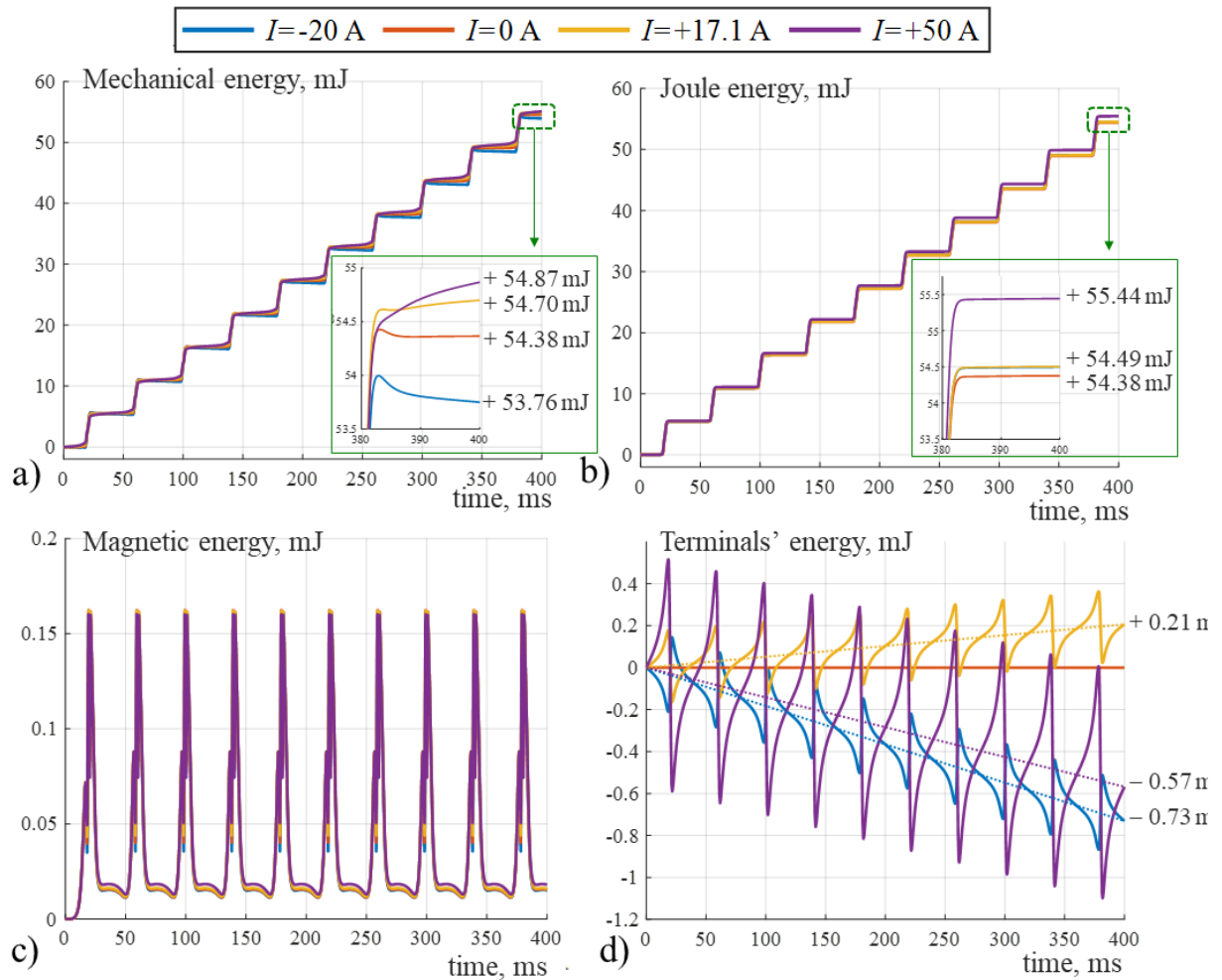
Figure 43 Energy terms of the flux pump during ten rotation cycles for different values of the DC impressed current. The dotted line corresponds to the energy exchanged by the flux pump with external load in case of operation with constant average power.

It is stressed that the joule heating is an inherent phenomenon, due to the overcritical currents induced by the rotation of the magnet in the tape and is little affected by the operating DC current of the flux pump. To show this, the profile of current density and the corresponding profile of power dissipation at the middle of the rotation cycle (t = 20 ms + kT) is shown in Figure 44. It can be seen that, as far as it does not overcome the critical value I_c, the impressed DC current I has a small effect on the current and power distribution within the tape, which are dominated by the rotation and occurs also in case of no transport current. A minimum joule dissipation of 54.38 mJ is obtained in no load conditions, and the dissipation corresponding to

different DC impressed currents, both in the generator mode and the dissipative mode, is only slightly higher. In all cases, the mechanical power supplied to the rotor equals the joule heating plus or minus the power exchanged with the external component, depending on if the flux pump operates in the generator or the dissipative mode respectively.
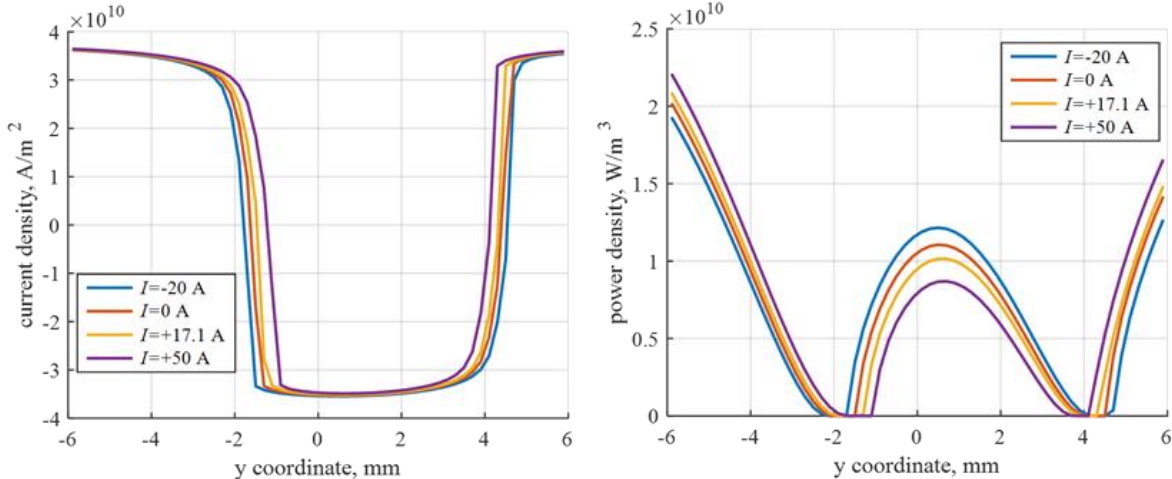
Figure 44 Profiles of current density and power density (E×J) along the tape at t=20 ms (half cycle, magnet aligned with the tape) for different values of the DC impressed current.

Moreover, the power exchanged with the external component is much lower than the joule dissipation. As a result, the efficiency of the flux pump, calculated according to Eq. (35), is very low. In case of maximum power transfer to the external load (0.52 mW at I = 17.1 A) an efficiency of 0.39 % is obtained. To further assess the energy performance of the flux pump, the average joule power, terminals' power and mechanical power in one cycle are shown in Figure 45.a-c for different values of the DC impressed current. The corresponding efficiency is shown in Figure 45.d. It is confirmed that:

- A positive average power is delivered to the external component by the flux pump, which acts as a generator, as far as the operating current is in the range $[0 - I_0]$. Outside of this interval the power is delivered by the external component and absorbed by the flux pump. In no case the mechanical power,

supplied to the rotor, is negative (this is true over any current range, much wider than the one shown in Figure 45.c). Hence, outside the generator mode, the flux pump only acts in the purely dissipative mode and never in the motor mode.

- Only a small part of the mechanical power supplied to the rotor is transferred to the external load in the generator region. This is due to the inherent dissipation associated with the induced current, responsible for the DC voltage, occurring also in no load conditions. As a result, the efficiency is low. A maxim efficiency of 0.39% is reached at 17.1 A (I_0 /2).

It must be reminded that a constant critical current density is being considered at this stage. The quantitative assessment of this crucial impact is carried out later in the thesis to dedicate a specific section to its decisive contribution.
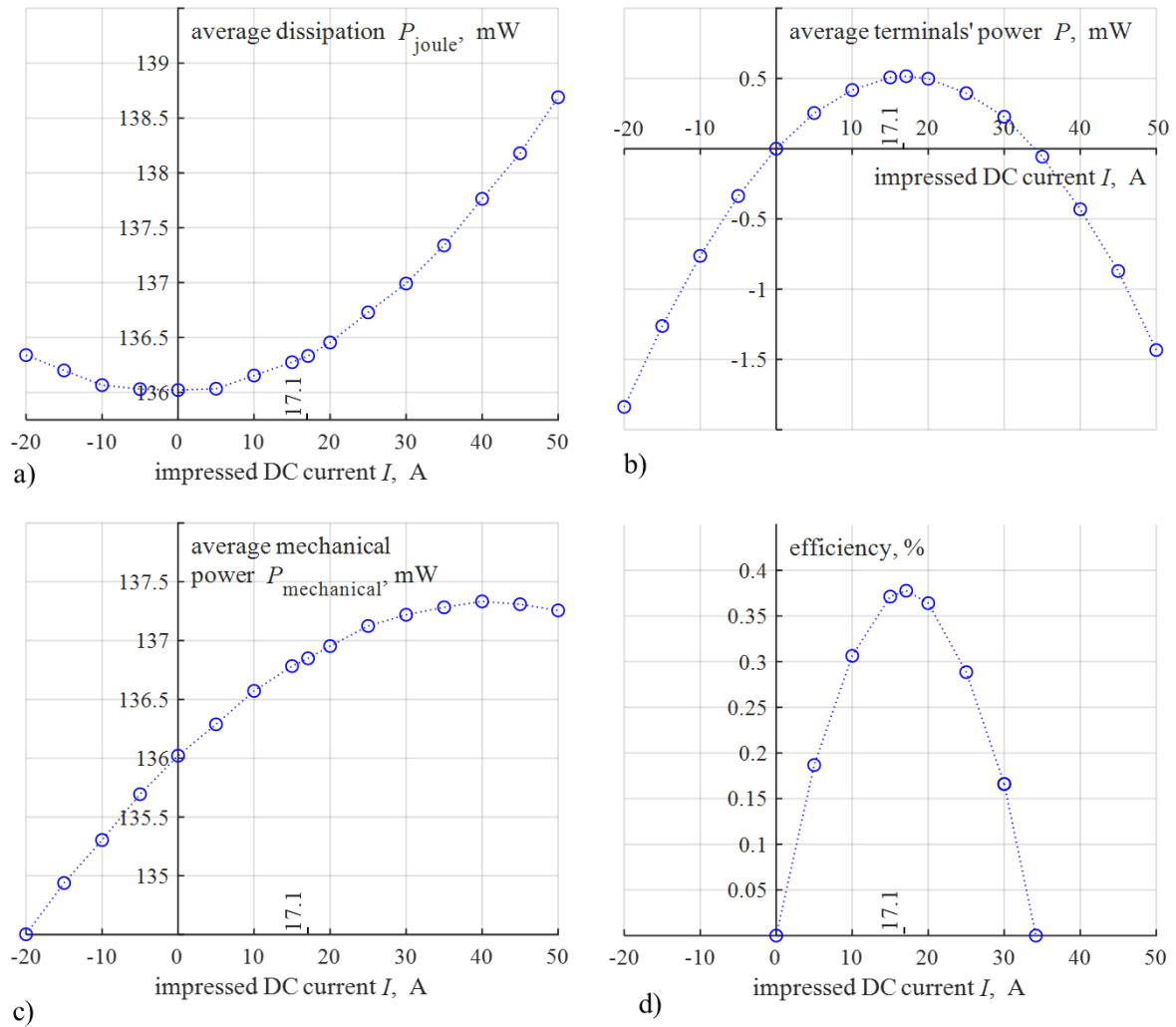
Figure 45 Average power per cycle and efficiency of the flux pump for different values of the DC impressed current.

2.1.5. Complete, empirical, and serviceable equivalent circuit of flux pumps

The electromagnetic behavior of the flux pump is fully reproduced by means of the finite element based equivalent circuit of section 2.1.2. However, the macroscopic behavior at the terminals can be reproduced by means of a simpler circuit obtained from empirical observation. This novel empirical equivalent circuit allows to investigate with good accuracy the interaction of the flux pump with an external component. For deducing this circuit, it is first pointed out that both the instantaneous voltage V and the average voltage $V_{average}$ are, strictly speaking, affected by the total

current I of the flux pump. To discuss the possible effects of this dependence, these two quantities are denoted with $V(t,I)$ and $V_{average}(I)$, respectively, in the following. It is observed in Figure 38 that, at any instant, the higher the impressed current, the higher the deviation of the terminal voltage from the value obtained in no load conditions. Hence, the terminal voltage at any instant can be expressed as:

$$V(t, I) = V(t, 0) - R(t, I)I$$
(36)

where R is a parameter that depends, in general, both on t and I. By taking the time average of both sides of Eq. (36) in one period the following expression of the average voltage across the flux pump terminals is obtained.

$$V_{\text{average}}(I) = V_0 - R_{\text{effective}}(I)I$$
(37)

in which V_0 is the average voltage in open circuit (no load) condition ($V_0 = 58.9$ µV - Figure 40) and $R_{effective}$ is a parameter referred to as effective resistance of the flux pump and defined as:

$$R_{\text{effective}}(I) = \frac{\int_t^{t+T} V(t', 0)dt' - \int_t^{t+T} V(t', I)dt'}{I} = \frac{V_0 - V_{average}(I)}{I}$$
(38)

From Figure 40 and Figure 41 a linear dependence of $V_{average}(I)$ is observed over a wide range of impressed currents. This trend applies for an operating current approximately within the interval from −100 A to +100 A (see Figure 41). Thus, within this linear interval, the following expression can be introduced for the average terminal voltage.

$$V_{average}(I) = V_0 - \frac{V_0}{I_0}I$$
(39)

By substituting (39) in (38), Eq. (40) is obtained.

$$R_{\text{effective}} = \frac{V_0}{I_0}, \quad \text{independent of } I \qquad\qquad (\,40\,)$$

An effective resistance $R_{effective}$ =1.73μΩ is obtained from the values of V_0 and I_0 for the considered flux pump. Consistently with the results of Figure 40 and Figure 41, Eq. (40) states that the effective resistance is not dependent on the DC operating current of the flux pump, and is simply denoted with $R_{effective}$ in the following. It is now assumed that, provided that the current I is in the linear interval from −100 A to +100 A, the constant effective resistance $R_{effective}$ determines the difference between the instantaneous terminal voltage and the no load voltage. In other words, we assume that the time and current dependent resistance $R(t,I)$ in Eq. (36) can be replaced with the constant resistance $R_{effective}$ giving:

$$V(t,I) = V(t,0) - R_{\text{effective}}I \qquad\qquad (\,41\,)$$

Based on Eq. (41) the empirical equivalent circuit of Figure 46 is obtained. It is stressed that replacing $R(t,I)$ with a constant $R_{effective}$ is a merely heuristic assumption, that is validity is checked in the next section by comparing the results with those obtained with the finite element based equivalent circuit. It will be shown that, despite the equivalent circuit being deducted with reference to a DC operating current, it also applies when the current change with time, provided that the linear limit is not exceeded. The equivalent circuit of Figure 45.a, which is widely used in present literature [80] [84] [93] [94] [101] [126] [136], is an effective approximation of the dynamo in terms of output voltage and effect on the connected load. However, no dissipation is prescribed by the empirical equivalent circuit of Figure 45.a in case of open circuit operation, which has to be accounted for a comprehensive analysis of the device. Instead, by now it is evident that dissipation also occurs during no load conditions, and it is little affected by the operating current. In order to take this intrinsic dissipation into account the complete empirical equivalent circuit of Figure 46.b is introduced. As a novel addition, in this circuit a resistor $R_{intrinsic}$ is added in

parallel to the voltage source that is responsible for the intrinsic joule dissipation in no load condition. By denoting P_{joule0} with the average joule dissipation in one cycle occurring in no load conditions the value of $R_{intrinsic}$ is defined by

$$P_{joule0} = \frac{\int_{t}^{t+T} \frac{V^2(t,0)}{R_{\text{intrinsic}}} dt'}{T} \tag{42}$$

which finally gives

$$R_{\text{intrinsic}} = \frac{V_{\text{rms0}}^2}{P_{\text{joule0}}} \tag{43}$$

where V_{rms0} is the rms value of the open circuit voltage $V(t,0)$, that for the considered flux pump is 2.2 mV_{rms}. By considering the average dissipation of 135.9 mW in no load condition an intrinsic resistance $R_{intrinsic}$ = 34.2 μΩ is obtained for the flux pump. It must be noted that the Thevenin equivalent of the complete empirical equivalent circuit coincides with the partial one. Thus, with respect to the behavior at the terminals, the addiction of the resistor $R_{intrinsic}$ does not produce any effect. The same behavior is predicted for an external component connected to both circuits. During DC operation with impressed current I the average power in one cycle at the terminals follows the parabolic dependence given by $P_{terminals} = V_0 \times I - R_{external} \times I^{\wedge 2}$ for both the circuits and is maximum at $I = I_0/2$. The difference only exists in the average power delivered by the voltage source, that for the two circuits is given by

$$P_{\text{source(partial)}} = V_0 I = VI + R_{\text{effective}}I^2 = P_{\text{terminals}} + R_{\text{effective}}I^2$$

$$P_{\text{source(complete)}} = V_0 I + \frac{V_{\text{rms0}}^2}{R_{\text{intrinsic}}} = VI + R_{\text{effective}}I^2 + \frac{V_{\text{rms0}}^2}{R_{\text{intrinsic}}} = \tag{44}$$

$$= P_{\text{terminals}} + \underbrace{R_{\text{effective}}I^2 + P_{\text{joule0}}}_{\text{overall joule dissipation}}$$

In the complete equivalent circuit, the voltage source delivers, besides the power at the terminal, the Joule power occurring in no load condition and an additional joule term corresponding to the dissipation on the effective resistance. A quadratic

90

dependence of the overall joule dissipation on the current is obtained which is consistent with the parabolic trend shown in Figure 45.a, obtained with the FEM based model. The overall power delivered by the voltage source coincides with the mechanical power supplied to the rotor of the flux pump. The efficiency of the flux pump can be calculated as

$$\eta_{(complete)} = \frac{P_{terminals}}{P_{source(complete)}} = \frac{P_{terminals}}{P_{terminals} + R_{effective}I^2 + P_{joule0}} \qquad (45)$$

(a)   (b)
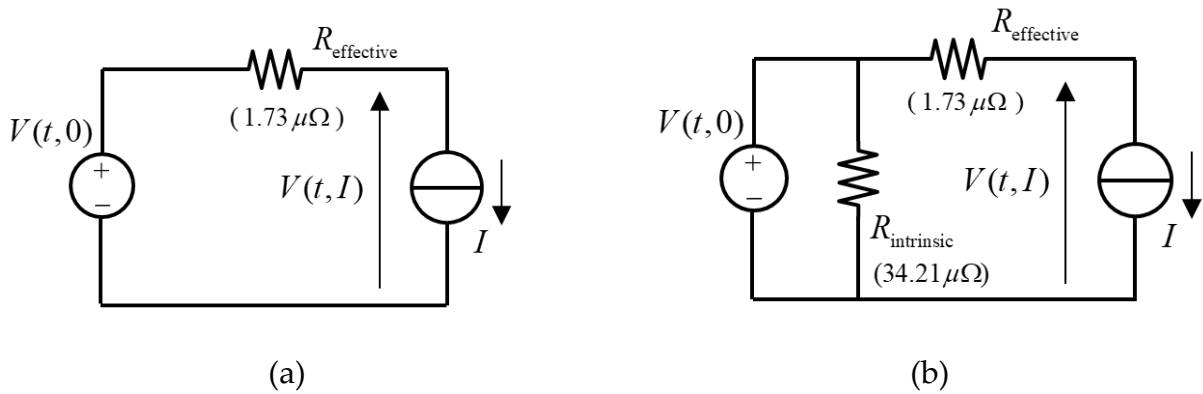
Figure 46 (a) partial empirical equivalent circuit of the flux pump (b) complete empirical equivalent circuit of the flux pump taking internal dissipation into account.

The average joule power, terminals' power and mechanical power in one cycle obtained with the complete equivalent circuit are shown in Figure 47.a-c. for different values of the DC impressed current and compared with FEM based data. The corresponding efficiency is shown in Figure 47.d. The maximum difference between FEM data and complete circuit data is below 1.2 %. A good agreement exists, indicating that the partial equivalent circuit can replace the FEM based one with acceptable accuracy. An increasing mismatch is observed with increasing operating current, indicating that the circuit cannot be employed at high operating currents, outside the identified linear interval from −100 A to +100 A. No correspondence exists instead between the power of the voltage source, or the loss due to the effective resistance, of the partial equivalent circuit with the physical dissipation mechanisms

occurring in the flux pump. No considerations on energy balance and efficiency can be done by means of this circuit.
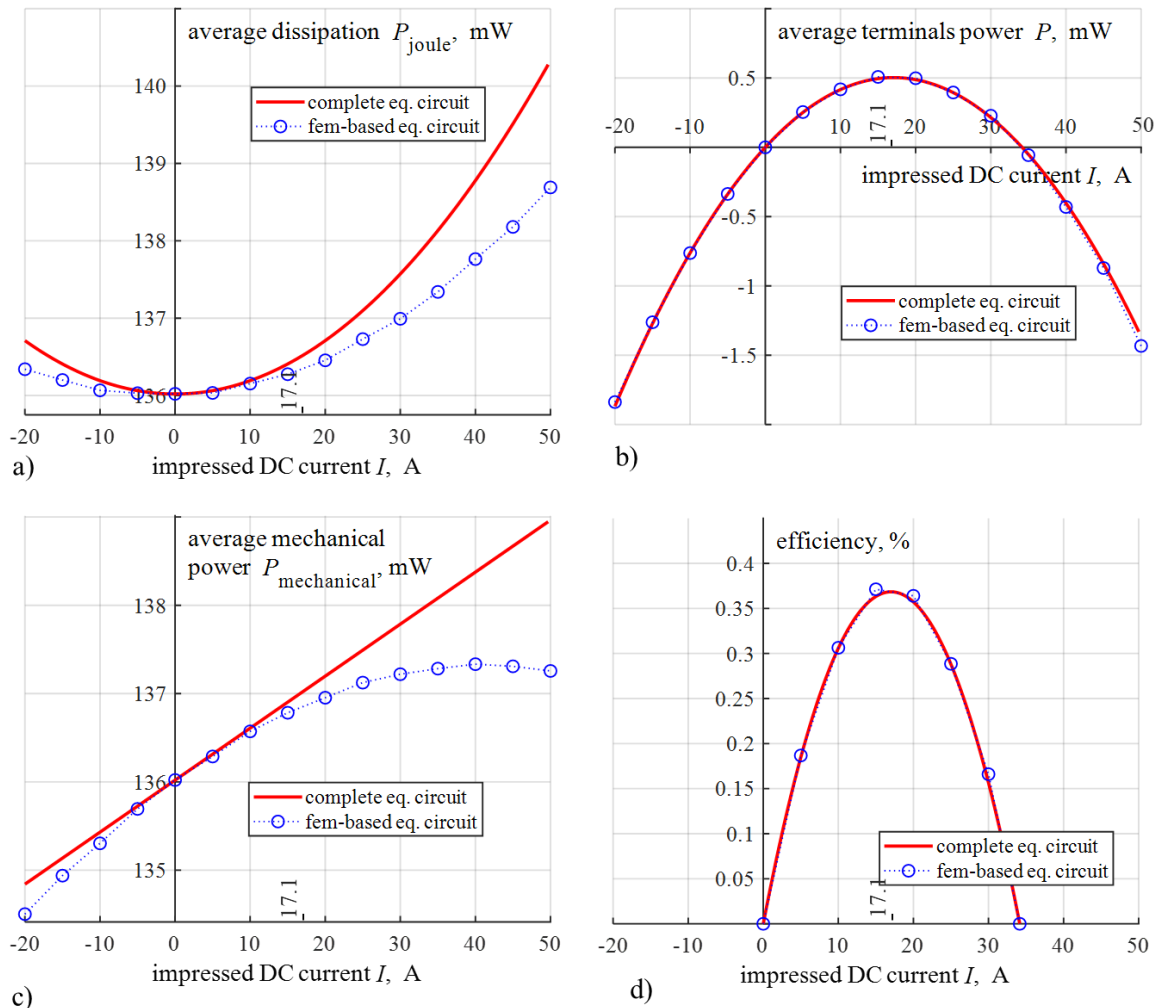
Figure 47 Average power per cycle and efficiency of the flux pump calculated by means of the complete equivalent circuit of Figure 46.b. FEM based data are also replicated here for comparison.

2.1.6. Flux pump connected to an RL load and short circuit operation

The numerical results referring to the flux pump supplying an RL load are discussed in this sub section. This operating condition can be used to model the charging of a HTS coil up to any current below the critical value. The short circuit

operation of the flux pump can be seen as the limit case in which both the resistance and the inductance are set to zero.

As in [133], a coil with an inductance L_{ext} = 0.24 mH and resistance R_{ext} = 0.88 $\mu\Omega$ (due to joints) is considered in the following. The current of the RL load during 500 s is shown in Figure 48.b. Both the results obtained by means of the finite element model of section 2.1.2 and by means of the complete equivalent circuit of section 2.1.5 are shown. The latter are obtained by connecting the RL load to the complete equivalent circuit of the flux pump, as it is schematized in Figure 48.a. It is stressed again that the current of the coil is not at all affected by the intrinsic resistor. In other terms, both including or not including $R_{intrinsic}$ in the circuit of in Figure 48.a, the same current in the coil is obtained. Including $R_{intrinsic}$ is only needed when a consistent energy balance of the flux pump needs to be assessed. This is obtained by using a DC voltage source corresponding to the average value V_0 of the voltage V_0 (t,0) across the flux pump terminals in open circuit conditions. A final current $I_f = V_0/(R_{effective} + R_{ext})$ = 22.62" A" is injected into the coil by the flux pump, following the exponential charging law of the RL circuit with a time constant $\tau = L_{ext}/(R_{effective} + R_{ext})$ = 92.16 s. Here the equivalent circuit is used to capture the full time domain behavior to the coil's current, including the ripple. This is achieved by using a time changing voltage source which implements the full time evolution of the open circuit V_0 (t,0) voltage at any instant of one cycle, and replicating it in all simulating cycles.
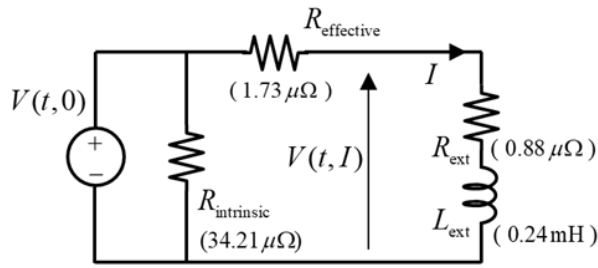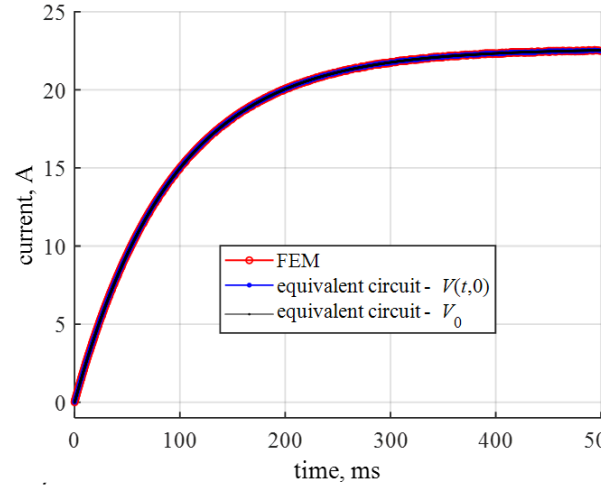
Figure 48 (a) Complete equivalent circuit of the flux pump connected to a RL load (b) Current of the RL load.

Figure 49 shows the detail of the current during 5 cycles after instant $t = 0$ (corresponding to current $I = 0$), and after instant $t = 150$ s (corresponding to current $I = 18.18$ A), is shown. No appreciable difference is observed between the FEM results and the results obtained with the equivalent circuit. This confirms that replacing $R(t,I)$ with a constant $R_{effective}$ in Eq. (40) is indeed a viable approximation and the equivalent circuit, deduced with reference to a DC operating current, can be applied for time domain analysis, provided that the linear limit is not exceeded. It is noted that when V_0 is used in the equivalent circuit, to assess a consistent energy balance of the flux pump $R_{intrinsic}$ must be redefined as:

$$R_{\text{intrinsic}} = \frac{V_0^2}{P_{\text{joule0}}} \tag{46}$$
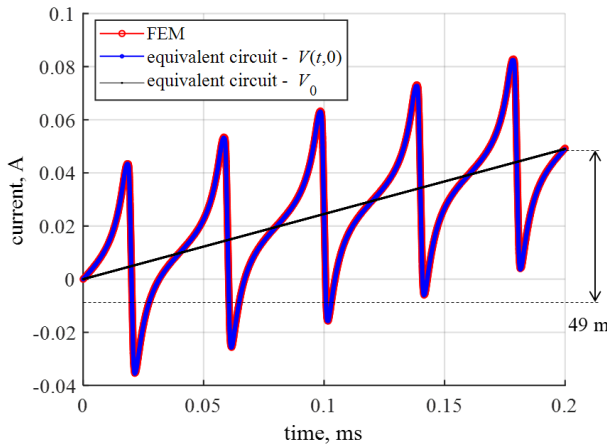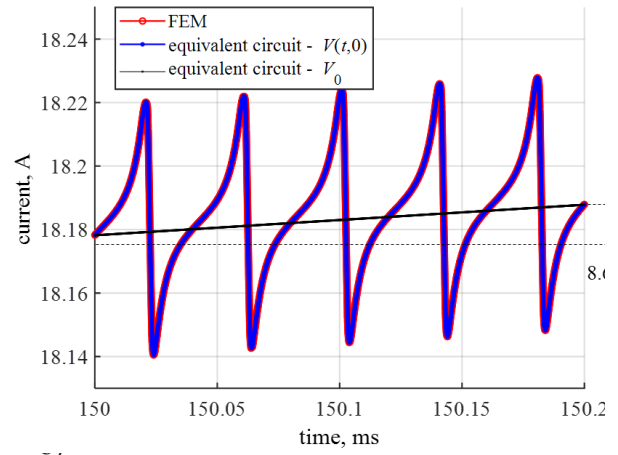
Figure 49 Detail of the current during 5 cycles after instant t=0 (when the current is null (a)), and after instant t=150 s (when the current has reached reaches I = 18.18 A (b)).

It was shown earlier that, beyond I_0, an average negative voltage appears on the flux pump that enters the dissipative mode. I_0 sets the limit of the generation ability of the flux pump and, despite the null voltage, should not be interpreted as the short circuit current of the flux pump, that is the current circulating in the flux pump when a short circuit connection is created at the terminals. The current circulating in this latter condition, calculated by means of the FEM based equivalent circuit by setting $R_{ext} = 0$ and $L_{ext} = 0$. It can be observed in Figure 50.a that it changes periodically from −400 A to +400 A, resulting in a mean current of 225.9 A. In contrast, the current obtained by putting $R_{ext} = 0$ and $L_{ext} = 0$ in the equivalent circuit of Figure 48.a is shown in Figure 50.b. A completely different time behavior, with an average value of 34.2 A, is obtained in this case. This means that the short circuit of the flux pump creates operating conditions that are beyond the limit of applicability of the equivalent circuit. In particular, a peak current beyond 6 kA (absolute value) is reached in this case, which is inconsistent with the critical current of the wire that is 283 A. Using the FEM model, a peak current of 400 A is reached, which is about 41 % above I_c. The highly resistive behavior of the tape developed according to the power law prevents the current to

overcome this value. Hence, the equivalent circuit of the flux pump can only be used if the predicted current does not exceed, at any instant, this limit. This condition is usually satisfied when a current smoothing inductive load is considered.

(a)   (b)
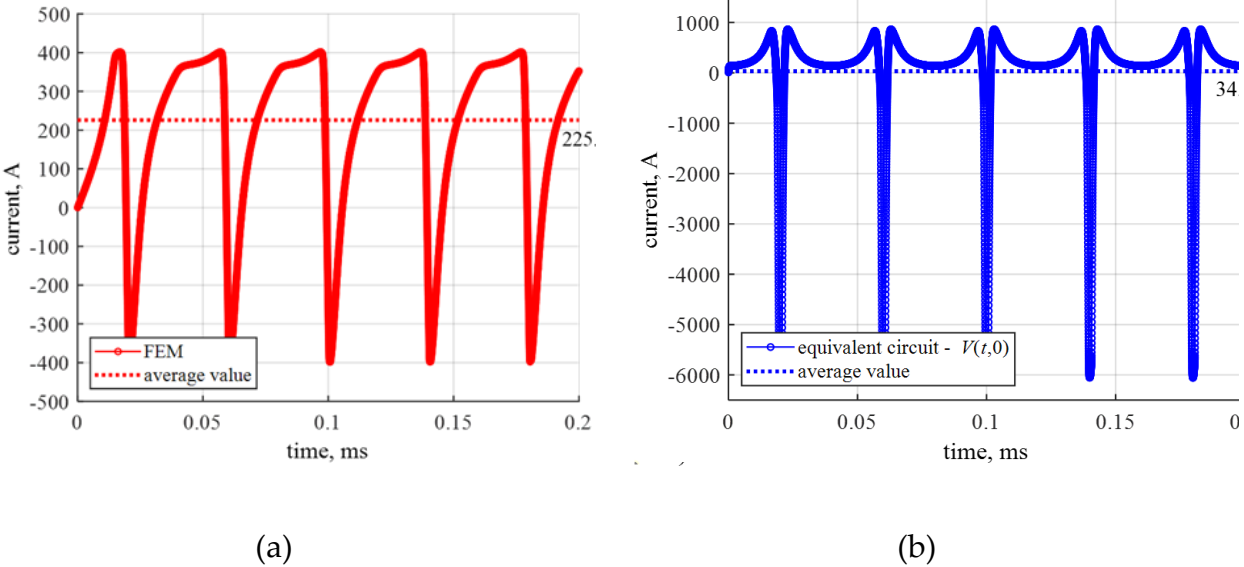
Figure 50 Total transport current flowing in the flux pump tape in case of short circuit operation (a) calculated by means of the fem model (b) calculated by means the equivalent circuit.

In the next sub sections, interpolators base on artificial intelligence (AI) are developed for addressing the relation between the n-value and the critical current of HTS tapes and the operating conditions (temperature and magnetic field). Next, this interpolar is embedded in the numerical FEM model described so far to reach accuracy and validation against experimental results.

2.2. AI models for reconstructing the critical current and n-value surfaces of HTS tapes

The critical current I_c, as well as the index value known as n-value, of practical high temperature superconducting (HTS) tapes, depends on the magnitude of the magnetic field B acting on tape, field orientation θ with respect to the tape surface, and the operating temperature T. As this will become clear in the following, this

relationship has a significant impact on the accuracy of FEM models in simulating flux pumps, therefore it is crucial to know the $I_c(B,\theta,T)$ and $n(B,\theta,T)$ functions. The most common way to include the $I_c(B,\theta,T)$ dependence in numerical models is through analytical formulas [137] [138] [139] [140] [141]. However, analytical approaches rely on fitting parameters to be preliminarily evaluated and consequently suffer lack of enough accuracy in complicated problems. Look-up tables are an alternative, but they are not implementable in all coding environments and rely on the availability of dense experimental data. In the sub sections related to the present one, an alternative method to address the problem of the determination of the $I_c(B,\theta,T)$ and $n(B,\theta,T)$ relations using Artificial intelligence (AI) techniques. This relation will later be included in the FEM model of the flux pump to reach accuracy able to validate its results against experimental data. It should be mentioned that this study was carried out during a collaboration in the framework and with the support of the COST Action CA19108, "High-Temperature SuperConductivity for AcceLerating the Energy Transition" funded by EU commission [142].

Like any other AI task, an adequately large and representative dataset is required to properly train a model. Therefore, the publicly open, accessible database of "High-Temperature Superconductor critical current data" provided by the Robinson Research Institute (Victoria University of Wellington, New Zealand) [143] [144] played a key role in the investigations of this work. In [143], plenty of data relating the critical current and the n-value to temperature, external magnetic field amplitude and angle is provided for different HTS tape specimens. The available data ranges over large intervals of the input features involved. For this study, the SuperOx GdBCO 2G HTS database was used because of the relatively large range of values it provides for both the temperature and the magnetic field magnitude. However, it is worth pointing out that any other tape specimen could have been chosen for applying the same approach to the corresponding data. The complete dataset that we used in this work is composed of 14747 combinations of critical current (I_c), critical current per unit width (I_{cw}), n-value, operating temperature (ranging from 15 to 90 K), external magnetic field

amplitude (ranging from 0 to 7 T) and external magnetic field angle (ranging from 0°
to 240°, where θ = 0° corresponds to the field applied perpendicular to the tape
surface). The dataset was randomly decomposed into two sets, one dedicated to
developing the model (both training and validating the quality of the training process)
and the other for its testing. In this study, 70% of the complete dataset has been
dedicated to training/validation, whereas the remaining 30% was used for testing.
Since an AI method that reaches the best performance for any problem a priori does
not exist, different AI techniques were chosen and their performance was evaluated.

Three AI-based models were developed: Artificial Neural Networks (ANN),
eXtreme Gradient Boosting (XGBoost), and Kernel Ridge regressor (KKR).

As performance metrics to report the error and quality of estimation of the
models, the Root Mean Squared Error (RMSE), and the goodness of fit (R^2) were used
for practical reasons [145].

$$RMSE = \sqrt{\frac{\sum_{i=1}^{n_s}(y_i - x_i)^2}{n_s}} \qquad (47)$$

$$R^2 = \frac{\sum_{i=1}^{n_s}(\bar{x} - x_i)(\bar{y} - y_i)}{\sqrt{\sum_{i=1}^{n_s}(\bar{x} - x_i)^2 \sum_{i=1}^{n_s}(\bar{y} - y_i)^2}} \qquad (48)$$

where, x_i is the actual value, y_i is the predicted value, $\bar{x}$ is the mean of actual (real
experimental) values, $\bar{y}$ is the mean of predicted values, and n_s is the number of data
samples.

In order to avoid overfitting and thus achieving fairly well estimations over the
whole range of features, a visual comparison of the critical surfaces of the models was
included among the evaluating criteria as well. Great effort has also been paid to
hyperparameters tuning and sensitivity analysis to optimize the AI models and
comprehensively investigate their performance dependence on their own controlling
parameters. In fact, the capability of any AI model to extract specific trends from a
dataset is strictly related to certain parameters, named hyperparameters. Established

hyperparameter tuning techniques were applied in this study, such as the so-called grid-search method [146], which generates a user-defined grid of possible combinations of hyperparameters and trains the model for each of them and keeps the best case based on the chosen evaluation criteria. Grid-search was applied to the training set with a K-fold cross-validation procedure: the training set is divided into K splits in which, for each split, a different training of the model is carried out: the chosen split is used as a validation set for evaluating the performance of the training process, for which the remaining K-1 splits are used. This procedure is performed for each combination of the hyperparameters grid.

The main features and characteristics of the three models that were identified are used briefly in the subsections 2.2.1-2.2.3. In subsections 2.2.4 and 2.2.5 the results obtained with the three AI techniques are reported. The numerical and visual results of the AI models in predicting the targets I_{cw} and n-value (the ones for I_c would be analogue and proportioned to the ones of I_{cw}) are shown. It should be noted that, for each of the three target cases, the quantities B, θ, and T always remain the features of the models, but every target requires dedicated training to reproduce the corresponding trend. Among the visual results, the reconstruction of the critical surfaces of the targets, obtained by interpolation between the experimental points of the complete dataset (which are also included in the plots for comparison) are reported. These critical surfaces are reconstructed at 20 and 65 K, as they are considered relevant and strategic operating temperatures in large-scale power applications in applied superconductivity. In subsection 2.2.6 the results of a series of sensitivity analyses on controlling parameters of the three proposed AI models are shown.

2.2.1. A brief description of Artificial Neural Networks (ANN)

ANN [147] are computational systems that can model and predict sophisticated characteristics with a high level of non-linearity. The ANN performance is inspired by how the human brain works. To make the performance of the ANN models clearer,

Figure 51 illustrates the structure of a brain neuron and how ANN resembles brain behavior to model physics and engineering problems. In this system, dendrites serve as inputs that receive the data from other cells and neurons. Dendrites inject the data into the nucleus laid at the cell body and are considered a node of the system. The nucleus activity is modeled as a function applied to inputs to compute the output. Synapses are considered as the weights of the neural system that help the model predict or estimate the characteristic of dendrites. Finally, the axon provides the output of the process and connects the neuron to other neurons. To create ANN models based on a real neural systems, multiple layers are considered. The very first layer is the input layer which receives the input data. After that, data are fed into series of hidden layers, which calculate or estimate the characteristic of the input data. Each hidden layer consists of some neurons, weights vector, bias factor, and activation function. It is mentioned that an activation function is a mathematical function applied to the output of each neuron (or node) in a neural network to determine whether a neuron should be activated (i.e., produce an output) or not. At last, there is an output layer that offers the result of the estimation process.
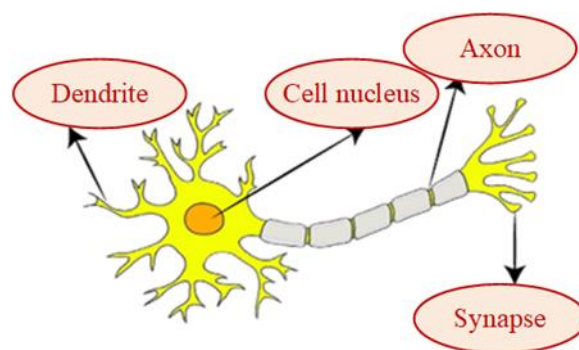
Figure 51 A simplified structural schematic of a neuron.

A simple structure of the model of a neuron in an ANN is shown in Figure 52 [148].
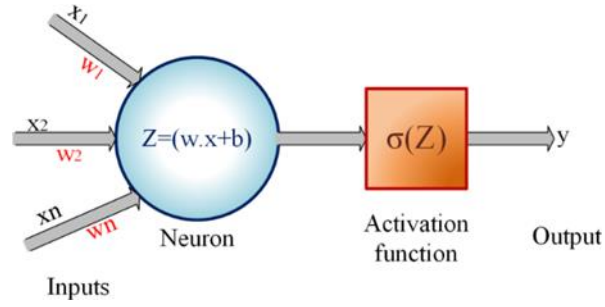
Figure 52 Structure of the model of a neuron used in an ANN.

To estimate the output, a simple neuron uses Eq. (49) [149].

$$\hat{y} = f(\vec{W}^T \vec{x} + b) \qquad\qquad (49)$$

where, $\hat{y}$ is the output, $\vec{x}$ is the input vector, f is the activation function, $\vec{W}$ is the weights vector, and b is the bias factor.

The objective of the training stage is to reduce the error of the predicted values and the real ones, known as the loss function. When the loss function is minimized, the ANN model uses the rest of the data for validation and test phases. It should be mentioned that the loss function minimization during the training phase is usually conducted by an optimization procedure of weights vector and bias factor based on a method known as backpropagation (BP). In backpropagation, initially, the training is conducted by considering weights as some small random numbers; after that, and for the first stage, the so-called loss function is calculated. To minimize and update the values of weights, the gradient descent method is used as an optimizer that can be handled using the Levenberg-Marquardt method [150].

The proposed structure of the ANN model used in this work consists of 4 hidden layers, in which hidden layers 1, 2, and 3 consist of 15 neurons each, while the last one, i.e. hidden layer 4, consists of 5 neurons. The sigmoid activation function is used as an activation function in this study. In the training stage, the Levenberg-Marquardt method is used to train the model based on 70% of the total input data. To minimize the loss function, a maximum of 1000 epochs is considered to reduce the RMSE.

Figure 53 shows the structure of the proposed ANN for the modeling purpose. In this figure, the three inputs are temperature, magnetic field magnitude and orientation angle. The H1 to H4 are hidden layers, and their neurons are shown with orange circles. At last, there is the output layer which could be I$_c$, or I$_c$ per cm width (I$_{cw}$), or n-value.
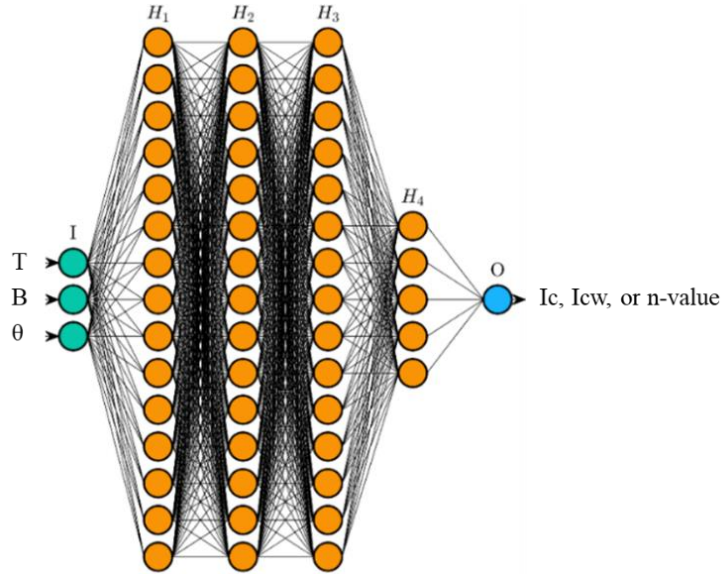
Figure 53 The structure of the proposed ANN model for critical surface predictions.

2.2.2. A brief description of the eXtreme Gradient Boosting (XGBoost)

XGBoost is a decision-tree-based ensemble machine learning algorithm that uses a gradient boosting framework [151]. Briefly, many decision trees are created in an additive manner as the model is trained with the input data. Since it is not possible to evaluate all possible tree structures, the algorithm starts from a single node and iteratively adds branches in the form of split candidates. The formula used for evaluating the instance split candidate nodes I$_L$ (left) and I$_R$ (right) from the starting node I is reported in Eq. (50) [151]:

$$L_{split} = \frac{1}{2}\left(\frac{G_{I_L}^2}{H_{I_L} + \lambda} + \frac{G_{I_R}^2}{H_{I_R} + \lambda} - \frac{G_I^2}{H_I + \lambda} \right) - \gamma \qquad (50)$$

where G is the sum of the residuals (namely the difference between the real value and the effective prediction, which is set to a default value at the first iteration) that refer to the corresponding node, H is the number of residuals that refer to the corresponding node, and λ and γ are regularization parameters [152]. The former regularization parameter is intended to reduce the prediction sensitivity to individual observations, thus avoiding overfitting. In contrast, the latter determines whether a further partition is to be made (the higher γ the more conservative the model will be by pruning branches). It is worth mentioning that in this work, the appropriate parameters were searched and optimized by operating hyperparameters tuning. The slip candidate from node I, which returns the higher value of L_{split}, is chosen, since it is the best one at splitting the residuals into the cluster of similar values. Once a tree structure is determined, its outputs for every leaf j are calculated with Eq. (51).

$$\omega_j = -\frac{G_j}{H_j + \lambda} \qquad (51)$$

Once the complete decision tree is generated during training, it can be exploited for predicting the target based on a given set of features. Details about the algorithm with which the decision trees are created can be found in [152]. In order to further clarify the decisional mechanism of the trained model of this work, one of the trees is shown in Figure 54. It should be mentioned here that this is only a small part of the decision tree created during the training stage and actually, can be considered a small branch of it. Finally, the green blocks in Figure 54 represent the leaves of the tree, namely the possible values that the model can predict.
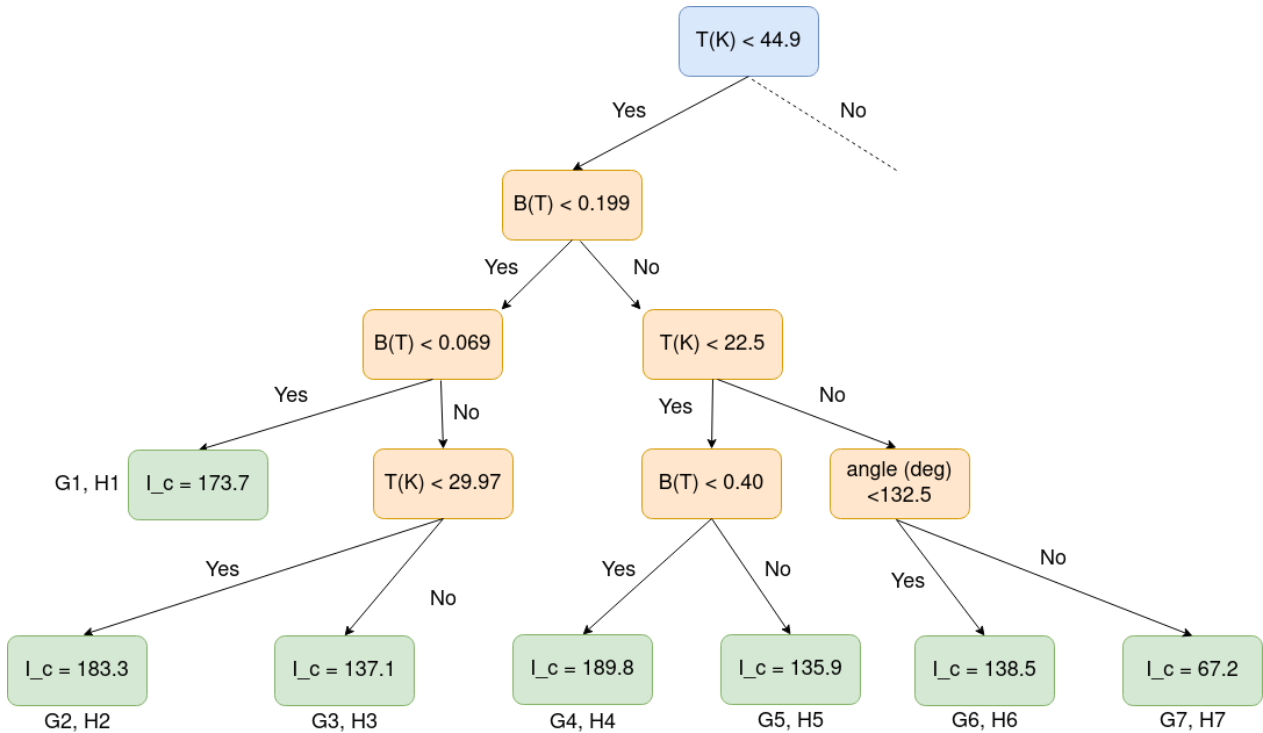
Figure 54 One decision tree of the XGBoost regressor trained model.

2.2.3. A brief description of the Kernel Ridge regressor (KRR)

KRR [153] is a linear transform method that allows working with too complex data to be directly addressed through a linear relationship. It uses the kernel trick [154] to transform the dataset to the image space in which it performs a ridge regression [155]. The particularity of the ridge regression that differentiates it from the simple linear regression is the l2-norm regularization [156], namely the addition of a regularization term which is the sum of the squares of the model parameters. The objective function that the ridge regression minimizes is shown in Eq. (52).

$$Obj_{KRR} = \frac{\sum_{i=1}^{n_s}(y_i - x_i)^2}{n_s} + \sum_{i=1}^{m} \beta_i{}^2 \qquad (\ 52\ )$$

where β_i is the i-th model parameter, m is the total number of parameters, and y_i, x_i, and n_s are the same as explained in Eq. (47)and (48).

The regularization term penalizes the minimization of the sum of the squared residuals of the first term but prevents the model parameter from becoming very large and therefore, limits the model bias. Moreover, the appropriate kernel choice for the problem is fundamental to make the KRR operate properly. In this work, the Rational Quadratic kernel, k_{RQ} [157], was used, which is shown as follows:

$$k_{RQ}(x_i, x_j) = \left(1 + \frac{d(x_i, x_j)^2}{2\alpha l^2} \right)^{-\alpha} \qquad (53)$$

where α is the scale mixture parameter and determines the relative weighting of large-scale and small-scale variations, l is the length scale of the kernel, and $d(\cdot,\cdot)$ is the Euclidean distance [158]. The best combination of α and l parameters was exhaustively looked for over a wide range of possible values using the grid-search technique. More details about the KRR can be found in [159], whereas another representative case study for such a method is reported in [160].

2.2.4. Results of the evaluation of the I_c per unit width using the AI models

Table 2 Performance metrics comparison for the I_c per cm width prediction of the three AI models.

Model	RMSE	R^2
ANN	0.0076	0.99998
XGBoost	14.01	0.99951
KRR	73.77	0.98643

By using ANN, the I_{cw} targets can be estimated with high accuracy at any combination of features, as Table 2 reports that RMSE is only 0.0076, R^2 is extremely close to 1 (i.e. 0.99998), and Figure 55 shows that most of the estimated data are located on the Y = Target line (where Target stands for the experimental value of the target and Y for its corresponding prediction). Figure 55 is the linear regressions between the experimental values of the target belonging exclusively to the testing subset and the

105

predictions of the AI models for the same combinations of B, θ, and T. XGBoost and KRR are less accurate, resulting in RMSE equal to 14.01 and 73.77, and R^2 equal to 0.99951 and 0.98643, respectively.
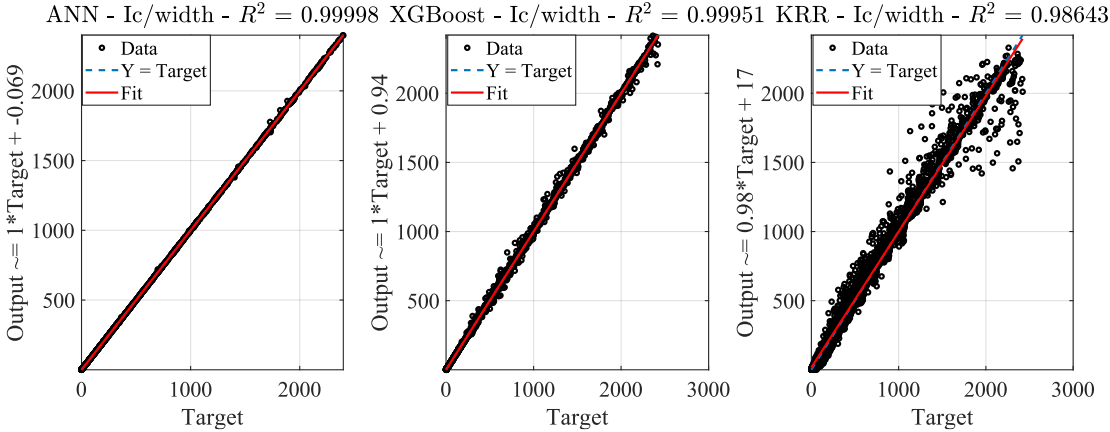
Figure 55 Regression plot for Ic per cm width comparison between experimental values (targets) and predictions made by AI models.

Figure 55 also shows that the KRR performance is negatively impacted by the relatively large error for I_{cw} values over 1000 A/cm, as many predictions do not lay on the Y = T line. Nevertheless, this model can effectively reconstruct the critical surface, as it is shown in Figure 56.
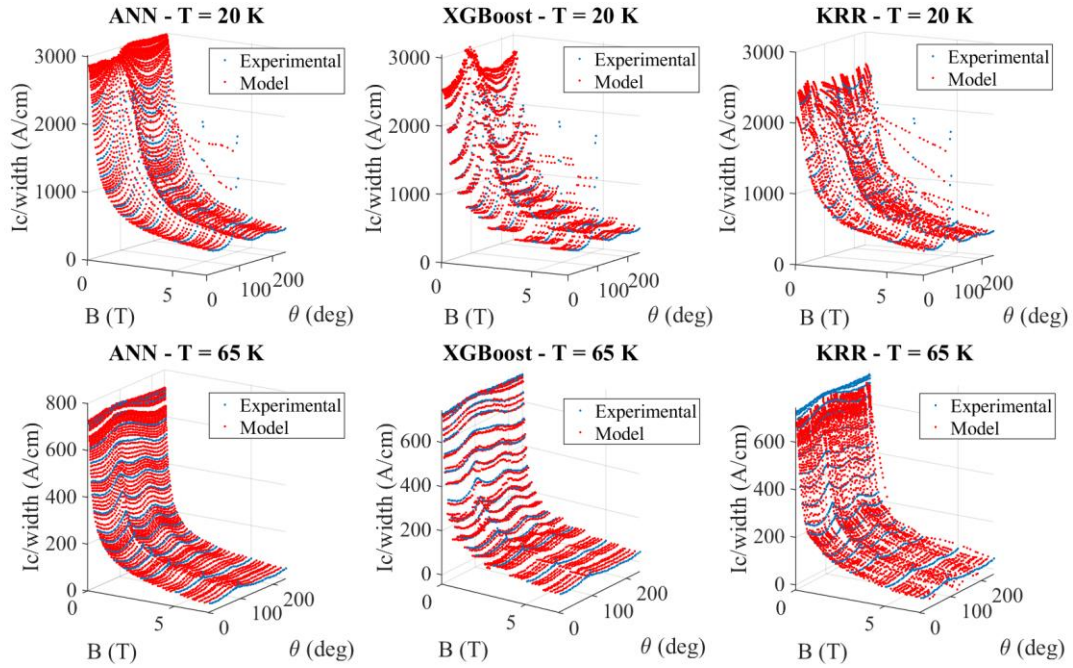
Figure 56 Critical currents per cm width predictions against the experimental data at 20 K and 65 K.

It is worth mentioning again that the red points labelled as "Model" are predicted for different feature combinations than the ones of the experimental dataset, which means they are in positions that the model has never encountered during training. ANN and XGBoost also produce critical surfaces in very good agreement with the experimental data. However, the critical surfaces produced by the XGBoost are not smoothly reconstructed but are composed of a series of bushes of predictions nearby the available experimental data, each separated by a considerable discontinuity from one another. For instance, at T = 20 K, with low field magnitude and angle, the prediction of the I_c per cm width changes by about 500 A/cm over a short range of a few tens of mT. Such a trend should be no surprise since it was explained that the XGBoost decision tree and, in turn, its leaves are derived to reduce a set of residuals between the prediction and the dataset target. It is noted that the nature of the dataset itself might have therefore played a major role in producing such a bias of the model over certain target values. In fact, the experimental dataset used in this study follows a particular pattern according to which the B field is kept constant over a certain

number of tests during which the field angle is iteratively changed from 0° and 240°. After a set of experiments at a constant B field is complete, the B field is changed and kept constant again until all the whole 0°-240° range of field angle values are explored. The fact that the XGBoost is only trained for certain values of B might have biased the model towards the production of the bushes. Figure 57 shows the relative error of the AI models over the whole B-θ grid at 20 K and 65 K are shown to quantify and detect the weak regions for the operation of such models. Figure 57 underlines the limits of this model in predicting the I_c per cm width in the regions of very large relative errors of over 50% at 20 K and over 150% at 65 K. It must be noted that, in the experimental dataset, I_c and I_c per unit width dramatically drop at high magnetic fields. For instance, at 65 K the maximum value of I_{cw} is 743.52 A/cm at B = 0.02 T and θ = 90°, whereas its minimum value is 34.34 A/cm at B = 7 T and θ = 20°. Therefore, the lack of accuracy of the model at high fields and temperatures can be explained by such a substantial drop in the value of the target; in fact, an absolute error of 30 A/cm would result in a relative error of 4% for its maximum value at 65 K and a relative error of 87% for its minimum value at the same temperature.
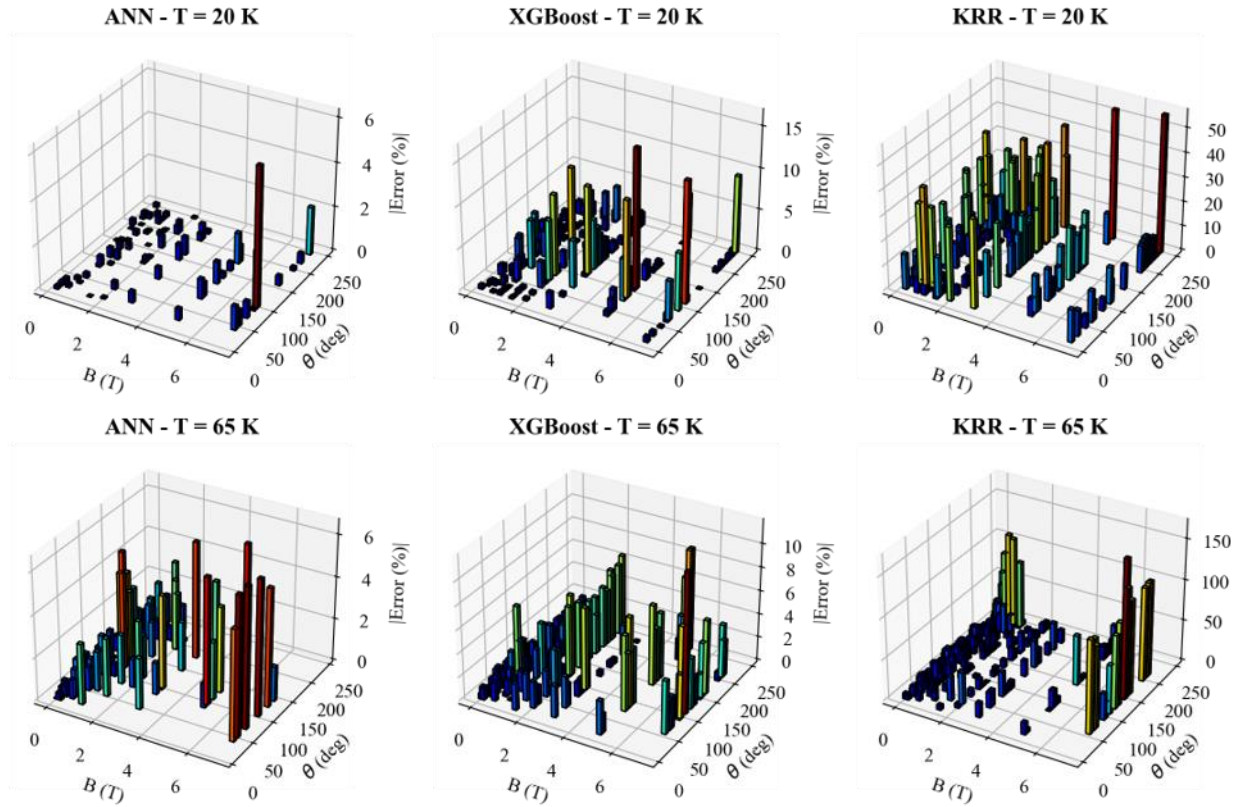
Figure 57 Absolute value of the relative error between Icw experimental and predicted data (only testing data is considered).

2.2.5. Results of the evaluation of the n-value using the AI models

Table 3 Performance metrics comparison for the n-value prediction of the three AI models.

Model	RMSE	R^2
ANN	0.1510	0.98754
XGBoost	0.8707	0.98263
KRR	1.974	0.91100

Table 3 show that, in terms of R^2, the performance of all three AI models in estimating the n-value is worse than the one achieved for the I_{cw}, showing that the trend of this target is more challenging to be intelligently reproduced. In fact, R^2 is calculated equal to 0.98754, 0.98263, and 0.91100 for ANN, XGBoost, and KRR, respectively. Figure 58 shows that ANN predicts large values at 20 K and very low

fields. To explain this, it must be underlined that the experimental data at 20 K temperature is only available above 0.2 T, which means the surface at this temperature is reconstructed even slightly outside of the range of the data that the model was trained with.
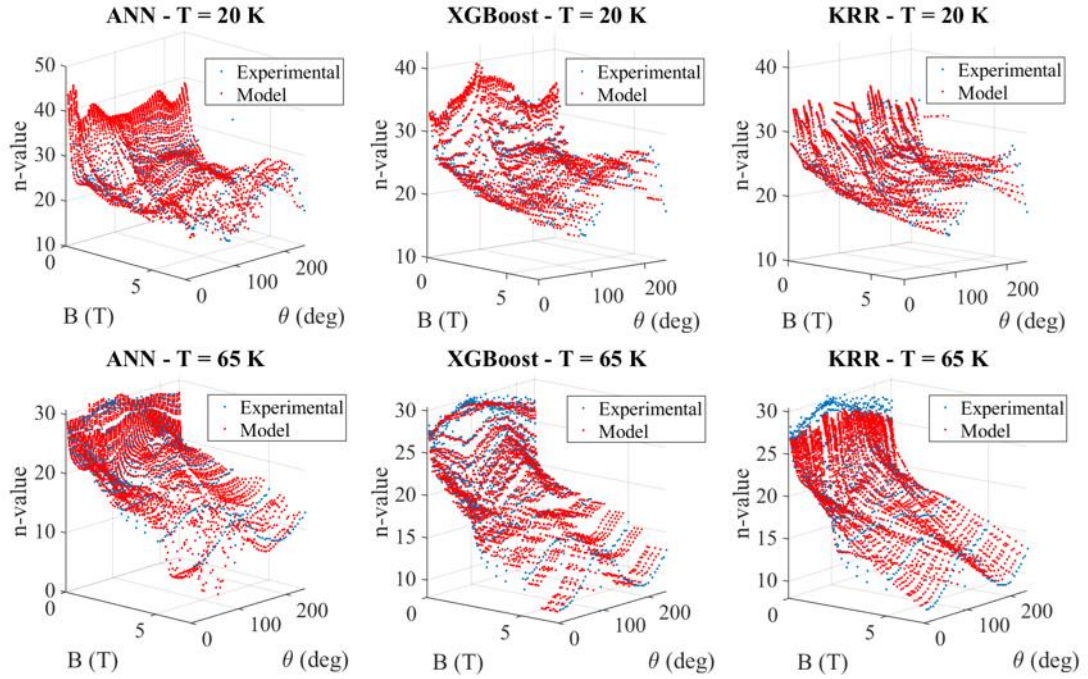
Figure 58 n-value predictions against the experimental data at 20 K and 65 K.

2.2.6. Sensitivity analyses on the hyperparameters of the AI models

A sensitivity analysis is also conducted to evaluate the impact of changes in controlling parameters of ANN, including the number of neurons and number of hidden layers on the final estimation results, for I_c at 20 K temperature. In general, the higher the number of neurons and hidden layers get, the longer the estimation computation time for testing the neural network would be. Accuracy would be increased as well, and RMSE value reduced. Also, it can be conceived that the increase in the number of hidden layers makes the simulations more accurate but slower in comparison to the situation that numbers of hidden layers remain constant and only the number of neurons increases. Table 4 shows the sensitivity analysis results, which

are consistent with all previous statements. The selection of the number of neurons and hidden layers is more related to the requirements of the application. For instance, if the ANN model is applied to characterize a superconducting device in design stage, the highest possible accuracy is needed, and so the most complex ANN model with multiple hidden layers and 15 to 20 neurons in each layer could be selected without any concerns about estimation computation time. On the other hand, if the ANN model is going to be used for real-time condition monitoring purposes or real-time modeling of the HTS device, the ANN with lower numbers of hidden layer(s) and 10-20 neurons in this layer could be selected (depends on the nature of the problem) which would not only give us a high accuracy but also characterize the superconductor behavior in a much faster manner from a computation time point of view. It should also be mentioned that the results for computation time are reported based on running the ANN model on a personal computer equipped with Cor™ i7-3612QM 2.1 GHz CPU and 8.0 GB RAM, DDR 3. Thus, any improvements in computation resources could reduce the simulation time to even less than milliseconds without negatively impacting the accuracy of estimation.

Table 4 Impact of changes in controlling parameters of the ANN model on the results of I_c estimation.

Hidden layers number	Neurons	R^2	RMSE	Training computation Time (s)
1	5	0.98856	0.1434	4.873
	10	0.99287	0.1267	5.436
	15	0.99415	0.1123	7.012
	20	0.99554	0.0965	7.555
2	5	0.99738	0.0752	6.559
	10	0.99973	0.0235	8.504
	15	0.99989	0.0152	17.069
	20	0.99988	0.0156	30.778
3	5	0.99897	0.0464	7.124
	10	0.99989	0.0157	12.837
	15	0.99993	0.0138	31.786
	20	0.99995	0.0115	85.814
4	5	0.9985	0.0532	9.522
	10	0.99982	0.0208	20.122
	15	0.99995	0.0104	64.747
	20	0.99995	0.0113	158.594
5	5	0.99935	0.0358	9.476
	10	0.99991	0.0141	27.186
	15	0.99994	0.0114	89.734
	20	0.99997	0.0092	287.384

Moreover, the stability of estimated results is tested to show that the estimations are reproducible and repeatable. In fact, because of its stochastic nature, reproducibility of results by ANN cannot be simply taken for granted and it is therefore investigated. To do this, the results of I_c estimation at 20 K were studied after 100 runs. Figure 59 shows the distribution of RMSE and R^2 values after 100 repetitions. As seen in these figures, the value of R^2 is stable during 100 times of simulation and changes at a maximum of around 0.005%. On the other hand, for RMSE, it can be

observed that the values of RMSE remain lower than 0.02, which is quite acceptable for such an estimation purpose. In Figure 59 (a) and (b), mean and standard deviation values are also reported. After analyzing Figure 59, stability, reproducibility, and repeatability of the estimations by the ANN model can be well guaranteed. This is solid proof of the fact that the reported estimated values of I_c, I_c per width, and n-value could be achieved by anyone who applies the presented structure of ANN to a reasonable amount of data.

(a)   (b)
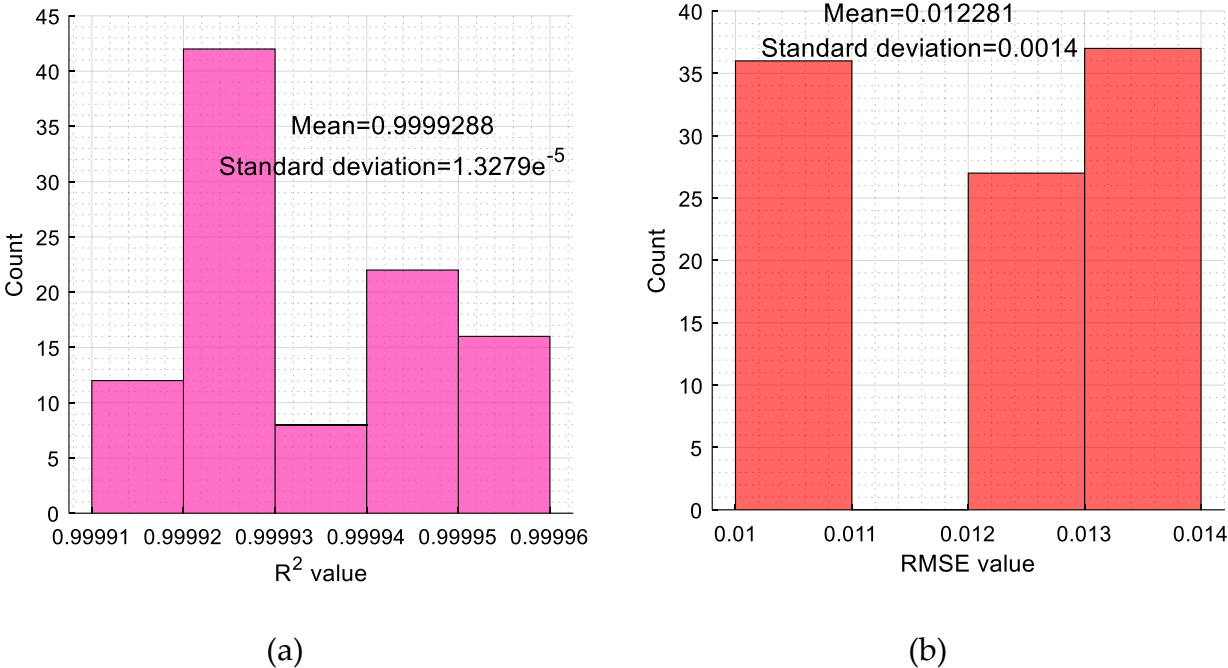
Figure 59 The stability, repeatability, and reproducibility of ANN results after 100 times of repetition of Ic estimation at 20 K temperature for (a) R2 and (b) RMSE.

Table 5 and Table 6 report the sensitivity analyses results for the XGBoost and the KRR, respectively. In both tables, the results corresponding to the tuned hyperparameters are highlighted in bold, i.e. $\lambda = 0.2$ and $\gamma = 0.6$ for the XGBoost model and $\alpha = 0.15$ and $l = 1.2$ for the KRR. Therefore Table 5 shows the impact of the hyperparameters λ and γ on the I_c per cm width prediction over all available data, whereas Table 6 is referred to the impact of the hyperparameters α and l on the Ic per cm width. As it can see in the tables, differently from the ANN, for both of the two

models changing hyperparameter values doesn't affect the computational time of the two algorithms. This is related to the fact that these hyperparameters are not responsible for the structure of the algorithm, but only for the final results of the performance. As for the ANN model, for both XGboost and KRR the R^2 metrics is almost stable with respect to all possible combinations of the hyperparameters, while the best and the worst RMSE are slightly different between the worst and the best combination of hyperparameters for both of the two models.

Table 5 Impact of λ and γ on the I_c per cm width prediction of the XGBoost model.

γ	λ	R^2	RMSE	Computation Time (s)
	0.1	0.999431	15.0568	0.849808
0.5	0.2	0.999497	14.1565	0.820797
	0.3	0.999419	15.2112	0.824097
	0.1	0.999435	14.9958	0.796851
0.6	**0.2**	**0.999507**	**14.01**	**0.792583**
	0.3	0.999417	15.2351	0.799748
	0.1	0.999434	15.0142	0.8126
0.7	0.2	0.999497	14.1492	0.828052
	0.3	0.999434	15.0067	0.812855

Both these two sensitivity analyses are carried out with a computer equipped with Intel(R) Xeon(R) CPU E5-2620 v3 @ 2.40GHz 2.40 GHz (2 CPUs) and 256 GB RAM.

Table 6 Impact of α and l on the I_c per cm width prediction of the KRR model.

α	l	R^2	RMSE	Computation Time (s)
	0.7	0.981097	86.7479	27.2499
0.05	1.2	0.983074	82.0868	27.2099
	1.7	0.982716	82.9488	27.8582
	0.7	0.984281	79.1056	24.7503
0.15	**1.2**	**0.986329**	**73.7715**	**26.3436**
	1.7	0.985203	76.7509	25.7341
	0.7	0.978944	91.556	26.0707
0.6	1.2	0.982994	82.2801	26.6068
	1.7	0.981495	85.8296	26.9218

2.3. Numerical validation of the final FEM model of travelling field flux pumps

Effective design of flux pumps must rely on accurate modelling. The suppression of the critical current I_c of HTS tapes due to the temperature T as well as the magnetic field amplitude B and orientation θ has been identified as a major factor that impact the overall performance of the flux pump [93] [94], both in terms of output DC voltage and efficiency. From here on, θ refers to the relative angle between magnetic field vector and the direction perpendicular to the HTS tape, as in [144]. The $J_c(B,θ,T)$ and $n(B,θ,T)$ relations are therefore included in Eq. (23) of the FEM model described in section 2.1.2 using the AI models presented in sections 2.2 (and its corresponding subsections) after training on the data of [143]. The AI model actually addresses the $I_c(B,θ,T)$ relation, from which $J_c(B,θ,T)$ is derived by dividing it by the area cross section of the corresponding tape. Since B represents the external magnetic field, the aforementioned method neglects the effect of the self-field of the tape, that is implicitly involved in the $I_c(B,θ,T)$ dataset from which the AI model is trained. Despite this approximation is not expected to affect the conclusions of this section, more accurate versions of the model will be developed in the future by directly extracting the proper $J_c(B,θ,T)$ relation [140].

The validation of the numerical model is carried out by simulating the flux pump apparatus of [79] and by comparing the numerical results with the experimental data that is reported in that paper. Considering for the apparatus the same schematic and nomenclature of Figure 35, its specifications are listed in Table 7. The flux pump of the experimental campaign employs a 12 mm wide HTS tape produced by Superpower, whose main characteristics are listed in Table 8. An external electronic current supply is connected to the HTS tape of the flux pump to enforce the transport current I during the experiments, while voltage taps are used for measuring the voltage V of Figure 35.a. This occurs when flux pumping is taking place, that is when the HTS tape is cooled down to reach the superconducting state and the permanent magnet is rotating with angular velocity ω. Different rotation velocities, in the range 178.2 – 1489.8 rpm (corresponding to 2.97 – 24.83 Hz) are considered for the rotor in the experimental campaign. More details of the experimental set-up and its functioning can be found in [79]. The flux pump operation is simulated in current-driven conditions, which means that a constant transport current I is assigned in the FEM model (for example, the case of open circuit corresponds to $I = 0$ A).

Table 7 Main specifications of the reference HTS dynamo flux pump of [79]

Specification	Value
Width of the permanent magnet (PM), a^{PM}	3.2 mm
Height of the PM, b^{PM}	12.7 mm
Depth of the PM, l^{PM}	12.7 mm
Remanence of the PM	1.3 T
Width of the HTS tape, a^{tape}	12 mm
Operating temperature	77 K
External radius of the rotor, R^{rotor}	35 mm
Airgap between the PM and the HTS tape, δ	3.7 mm

Table 8 Main characteristics of the Superpower HTS tape used in the reference HTS dynamo flux pump of [79]

Specification	Value
Width of the HTS tape, a^{tape}	12 mm
Thickness of the HTS layer	1 μm
Thickness of the substrate (Hastelloy)	50 μm
Thickness of the Silver stabilizer layer	2 μm
Thickness of the Cu stabilizer layers (at the top and the bottom of the tape)	25 μm

The calculated DC voltage V of the flux pump (that is, the average voltage at the terminals in one period) is shown in Figure 60.a for different values of the operating current and the frequency of the rotor. The corresponding experimental data are shown in Figure 60.b. All curves show a linear decrease of the DC terminal voltage with the operating current. The current I_{lim} at which the voltage becomes zero fix the limit of operability of the flux pump as a power supply. Beyond that value the terminal voltage is reversed and so the power flow at the device terminal. Hence, electric power is absorbed rather than delivered at the flux pump terminals, and is converted, along with the mechanical power supplied to the rotor, in heat dissipation into the device. It can be noted that the model predicts lower values of both the DC voltage and the limit current for every frequency of rotation. More in particular, the difference between the experimental DC open circuit voltage (at $I = 0$ A) and the numerical value is 32 % on average, whereas the difference between the experimental and the numerical values of the limit current (at which $V = 0$ V) is 22 % on average.

(a)   (b)
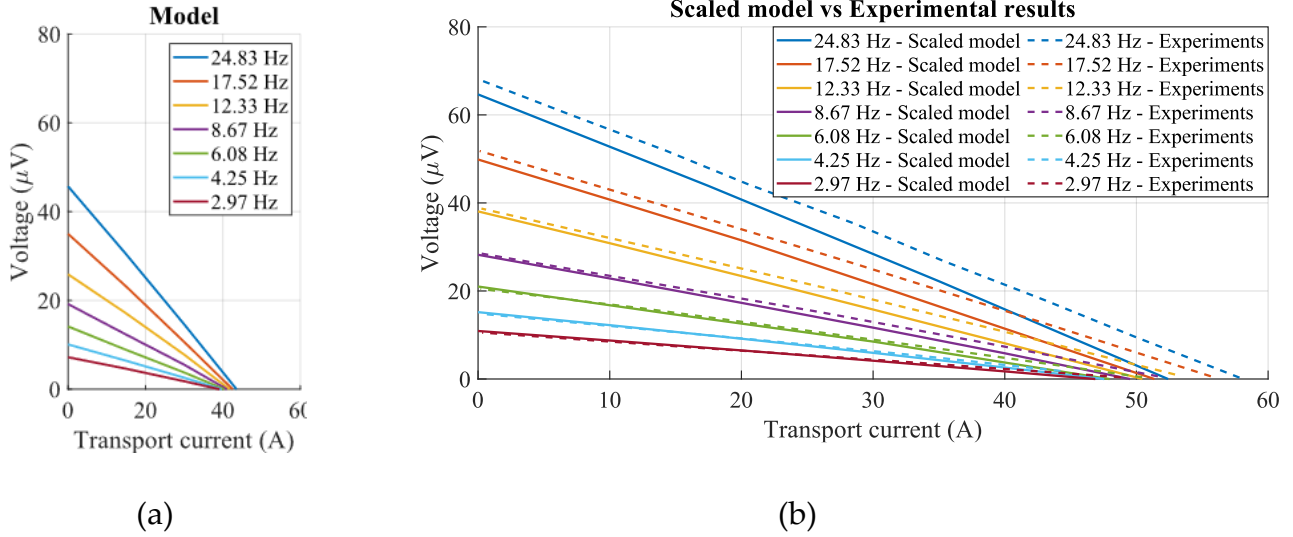
Figure 60 Numerical and experimental curves of the reference dynamo flux pump. The curves show the dependence of the DC terminal voltage on the transport current at different rotating frequencies (a) numerical results obtained with the model using data from Table 7, comprising an air gap of 3.7 mm (b) experimental results from [79].

The mismatch between the numerical and the experimental results Figure 60.a and Figure 60.b respectively is mainly due to the uncertainty on the actual value of the airgap between the magnet and the tape during flux pump operation [161] [162]. In fact, at least 0.5 mm reduction of the airgap with respect to the measured value at room temperature is estimated to occur at 77 K in a similar flux pump apparatus due to thermal contractions [161]. Hence, in order to obtain a proper match between the model and the experimental V-I curves, a comparable reduction of the airgap needs to be considered. In Figure 60.b the calculated V-I curves of the flux pump with a reduced airgap of 3 mm are shown. It can be observed that these curves fit the experimental data much better, with an error dropped to 3 % and 6 % for the DC open circuit voltages and the limit current of the flux pump respectively. The applied reduction of 0.7 mm of the airgap with respect to the room temperature value needed for obtaining a proper fitting of the experimental data is in the range suggested in [161] due to thermal contraction.

2.4. Performance of different commercial HTS tapes for flux pump applications

The integration of the $J_c(B,\theta,T)$ and n-value(B,θ,T) relations in the numerical FEM model makes it suitable for simulating a flux pump employing any tape for which the aforementioned functions are known. Leveraging the data from [143] on various commercial HTS tapes, AI models were trained to enable numerical evaluation and comparison of the performance of flux pumps employing different commercially available HTS tapes. The aim is to point out the main trends of the impact of the critical current density suppression on the flux pump outputs, as well as provide a useful insight toward the future development of optimum-designed flux pumps. All the quantitative performance indicators shown in this section refer for simplicity to the basic flux pump design dealt with in section 2.3, employing one HTS tape and one rotating permanent magnet (PM) with assigned layout ad dimensions, and do not apply if optimized flux pump systems, with different layouts and/or dimensions, are considered. In comparative terms, however, the results of the present section apply to any flux pump device since this will consist of a number of HTS tapes periodically swept by a PM, similar to the case considered here. In particular, the selected tape allowing to reach the best performance in terms of efficiency and DC output voltage for the considered basic flux pump design, will allow to reach the best performance in all flux pump designs of practical interest.

The following commercially available tapes have been simulated and compared.

- THEVA Pro-Line 2G HTS;
- Shanghai Superconductor Low Field High Temperature 2G HTS;
- SuperOx GdBCO 2G HTS;
- SuperOx YBCO 2G HTS;
- SuperPower Advanced Pinning 2G HTS;
- Fujikura FYSC 2G HTS;
- SuNAM HAN04200 2G HTS.

Table 7 are considered for all simulations, with the only exception of the airgap length, which, as discussed in section 2.3, is set to 3 mm in order to reproduce the experimental data of the validation case with good accuracy. A width of 12 mm is assumed for all HTS tapes. The frequency of rotation of the permanent magnet is 24.83 Hz. An operating temperature of 77 K is considered for all simulated cases.

The results for all tapes under the aforementioned operating conditions are reported in Figure 61. In particular, in Figure 61.a the dependence of the DC terminal voltage V on the operating current is shown. A wide spread of the open circuit voltage, ranging from 48 µV for the Fujikura tape to 93 µV for the SuperOx YBCO tape, can be observed from the figure. The limit current at which the flux punt can operate in the generator mode also depends on the tape. A limit current of 90 A is obtained for the THEVA tape, whereas a nearly double valued of 176 A is observed for the SuperOx YBCO one. Despite having the lowest open circuit voltage, the Fujikura tape has the second largest limit current of the generator mode, which stresses the fact that the tape choice also affects the slope of the V-I curve and, hence, the deliverable power and the efficiency. Figure 61.b displays the AC losses of the dynamos at different transport currents. It is stressed that losses at zero transport current, i.e. open circuit condition, is non-zero and the trend of the AC losses against the transport current is quadratic, as previously observed in section 2.1.3. The power that delivered by the dynamos and the corresponding efficiency are shown in Figure 61.c and Figure 61.d respectively. Because of the quasi-linear trend of the V-I curves, the maximum deliverable power and efficiency are closely located at the half of current limit of the generator mode. The maximum overall output power of 4.5 mW is reached by the SuperOx YBCO tape. This is no surprise since it was already observed that this tape has both the largest open circuit voltage and the largest generator mode current limit. Since the losses are in the order of hundreds of mW whereas the output powers are in the order of the mW, low efficiencies in the range of 1 % to 3.5 % are reached. While low efficiencies are common in flux pumps, it's important to note that these results are notably low due to the small-scale laboratory apparatus employed in this study. Therefore, the efficiency range of

1-3.5% observed here holds no immediate practical significance. In the literature, efficiencies of up to 16% have been reported for dynamos [87], indicating a substantial room for improvement.
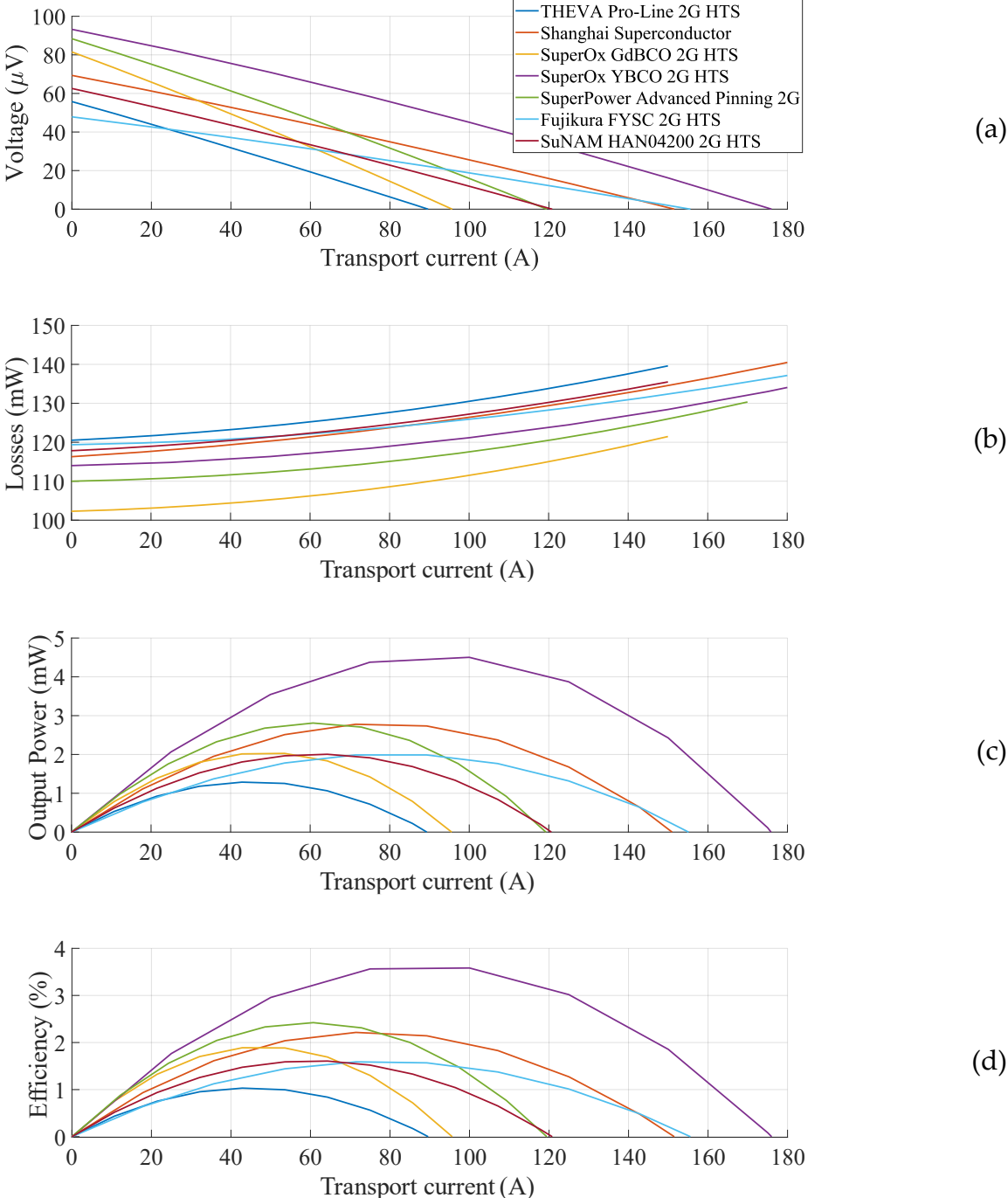

Figure 61 Performance and operating limits of the dynamo flux pumps employing different commercial HTS tapes at 77 K: (a) V-I curve, (b) Loss of the dynamos at different transport currents, (c) Output power of the dynamos versus transport currents, (d) Efficiency of the dynamos versus transport currents

For context, it is useful to show the $I_c(B)$ per unit width at $\theta = 90°$ (field parallel to the tape) and the $I_c(\theta)$ per unit width curve at 0.3 T of all tapes, in Figure 62.a and Figure 62.b respectively. The fact that the Fujikura tape exhibits a large flux pumping current capability but the lowest open circuit output voltage (see Figure 61.a) can be attributed to the fact that it also generally has the largest I_c per unit width and, consequently, may exhibits limited local resistance. This aspect is both counterintuitive and crucial in the context of traveling field flux pumps: if tapes with remarkable current capacities are used for flux pumping, they are not expected to perform well in terms of voltage rectification. This opposes to the current research trend which aims at producing HTS tapes with largest possible I_c per unit width and lowest possible magnetic field sensitivity (field isotropy). In fact, maximum local critical current suppression is favorable for producing local resistivity in the HTS tape and in turn optimal voltage rectification, as explained in the important section 1.4.1. On the other hand, a very poor I_c might translate into a low generation current limit for a flux pump, as this is the case for the SuperOx GdBCO tape. Evidently, a tradeoff is desirable, and for the considered study this is obtained for the SuperOx YBCO which outperforms all other HTS tapes in terms of flux pumping performance. It can also be seen in Figure 62.b that the SuperOx YBCO exhibits one of the largest relative I_c per unit width excursions for different magnetic field orientations. This confirms another important point that anisotropy is also favorable for travelling field flux pumping, because this implies that, at a given time, the flux pump HTS tape will exhibit different resistivities along its width, and this was already explained to be desirable with regard to Figure 20 and Figure 23 in section 1.4.1.
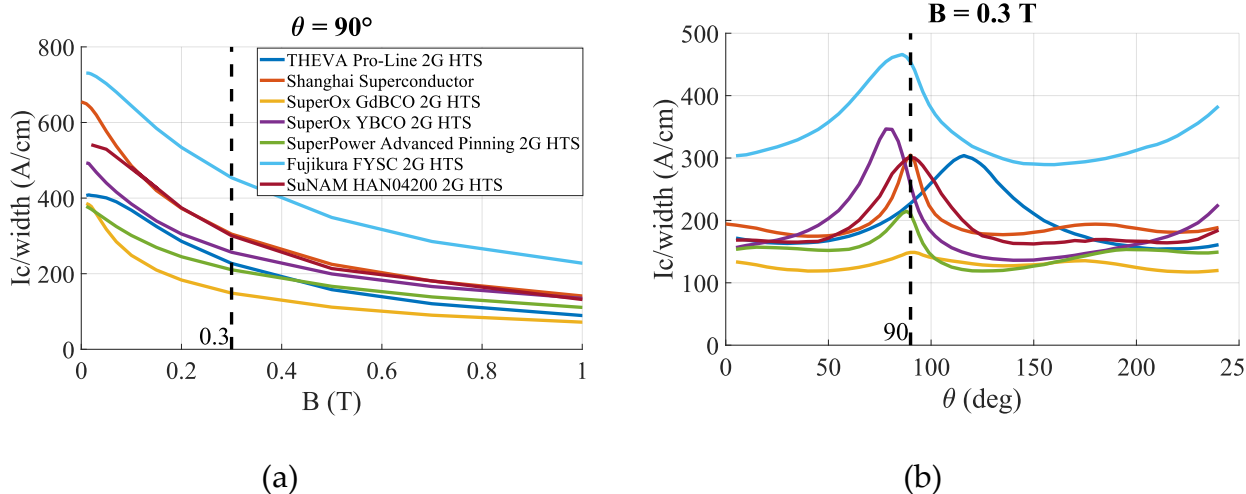
Figure 62 (a) Ic per unit width vs B curve of the commercial HTS tapes at T= 77 K and θ = 90° (field parallel to the tape) (b) Ic per unit width vs θ curve of the commercial HTS tapes at T= 77 K and B = 0.3 T.

2.5. Impact of operating temperature on the performance of travelling field flux pumps

Based on the results of section 2.4, the SuperOx YBCO 2G HTS is chosen for carrying out the investigation of the impact of temperature on the performance of the dynamo flux pump. The following temperatures have been investigated: 55 K, 65 K, 70 K, 77 K, 80 K, and 85 K. Temperatures lower than 55 K have not been investigated due to the fact that the resulting performance of the flux pump in terms of open circuit voltage are too low to be of interest. At each operating temperature, the following performance and operating limits have been numerically evaluated:

- Open circuit voltage;
- Limit current of the generator mode;
- Maximum output power;
- AC loss in open circuit condition;
- Maximum efficiency.

The numerical results are reported in Figure 63. In particular, Figure 63.a and Figure 63.b report the dependence of the open circuit voltage and the limit current of

the generator mode on the temperature. In these plots it can be seen that the largest value of open circuit voltage is obtained between 80 K and 85 K (according to the polynomial interpolation), whereas the maximum value of the limit current is located at approximately 65 K, therefore it is not possible to find a temperature that maximizes both these performances and a trade-off is needed in the final design. It is worth noting that the open circuit voltage drastically drops for temperatures below about 75 K. This is explained by the improvement of the critical current of the tape and its reduced dependence on the external magnetic field which occurs at lower temperatures. At low temperatures the impact of the field produced by the permanent magnet is so minor that flux pumping barely happens, resulting in the V- I characteristic to escaping the first quadrant and lying almost exclusively in the fourth one (low open circuit voltage and generation current limit). On the other hand, the decrease of the open circuit voltage at high temperatures (above 80 K) is explained by the reduction of the non-linearity due to lower n values, whereas the decrease of the limit current is due to suppression of the superconducting properties which appears when the critical temperature is approached.

Figure 63.c and Figure 63.d show how the energetic performance of the dynamo is affected by temperature. In Figure 63.c it can be seen that the maximum output power that the dynamo can deliver to the load, which is reminded to occur approximately at half of the limit current of the generator mode, is maximized when the dynamo operates at roughly 80 K, in Figure 63.d it is observed that the largest value of open circuit AC loss lies between 70 K and 77 K. As a result, the maximum efficiency (over 4 %) is clearly located around 80 K, as Figure 63.e displays. Similar to Figure 61.d, the low efficiency itself is not significant, as it pertains to a non-optimized laboratory-scale apparatus. However, what is crucial is its observed trend versus the transport current. It is plausible to assume that this same trend would scale towards higher efficiencies in the case of large-scale, optimized dynamos [87]. Based on the results of Figure 63, it could be discussed that choosing the operating temperature of a flux pump is no trivial task. Indeed, the generally poor efficiency should be a driver to

make the flux pump to operate at higher temperatures, where both the efficiency and output power are maximized. However, it should not be forgotten that the very large current capability must be reached when the flux pump is needed for the supply of high current systems like for example fusion magnets, and the best operating temperature in this regard is at about 65 K. Nevertheless, decreasing the operating temperature below 70 K is not viable due to the dramatic drop of the open circuit voltage that it involves. Therefore, the best of the operating temperature of the flux pump, allowing maximum operating voltage, output power and efficiency, is somewhat in the range 70-85 K. This choice is also technically convenient and cost-effective, as temperature below 77 K can be obtained with liquid nitrogen cooling at ambient pressure and do not require additional apparatus. Increased current capacity, when need, must be reached by using more tapes in parallel, and this would allow preferring higher temperatures.
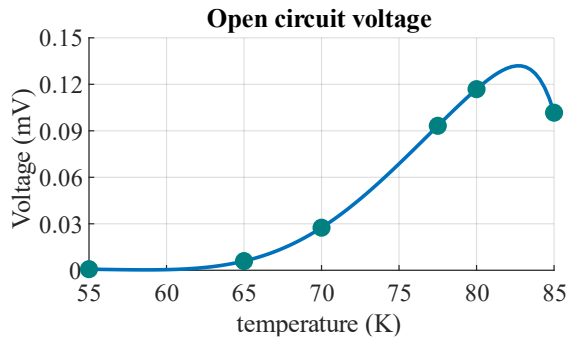
(a)
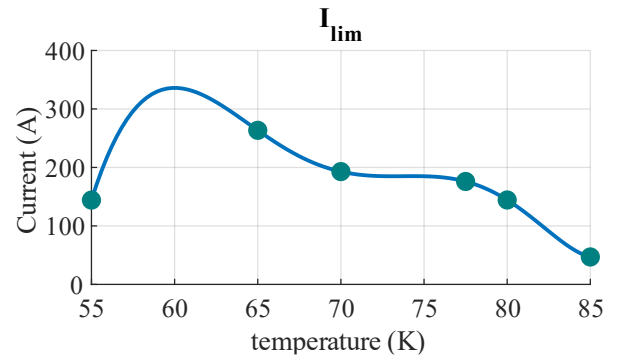
(b)
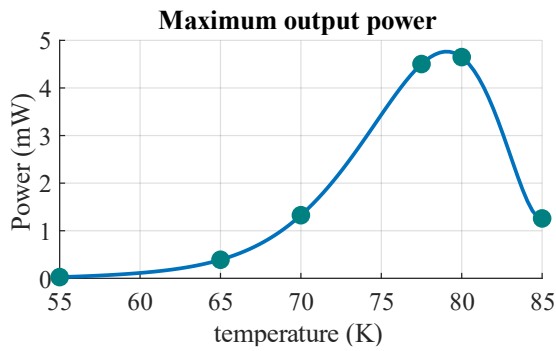
(c)
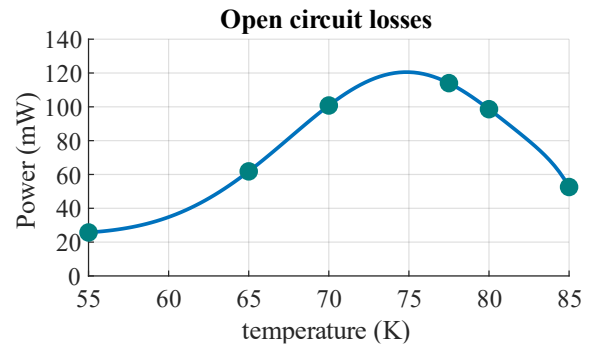
(d)
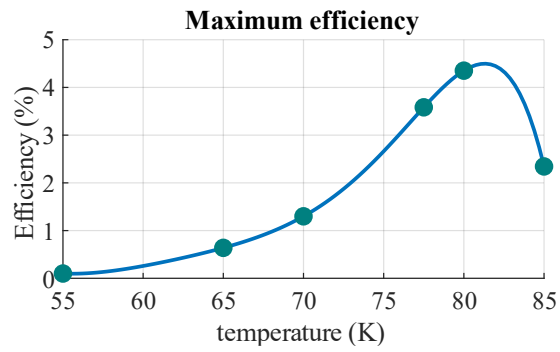
(e)

Figure 63 Impact of temperature on dynamo performance, the case of the SuperOx YBCO 2G HTS tape
(points are the results of the model, lines are their polynomial interpolation).

3. Chapter 3: Application-oriented optimal design of travelling field flux pumps

In the previous chapters of this thesis, the lack of proper designing actions for flux pumps was pointed out. Despite previous studies have empirically investigated the impact of individual design parameters on the outputs of travelling field flux pumps, they are not generalizable nor suitable for proper designing activities. Furthermore, to date, no analytical formulas have been derived to address the design of flux pumps.

This chapter presents the development of an application-oriented engineering procedure that starts from the requirements and constraints imposed by a given HTS magnet to be supplied in terms of nominal current, total resistance and inductance, proceeds with the identification of the degrees of freedom of the flux pump (i.e. its designing parameters that are to be found concerning the applied field, the HTS tapes and the geometrical and operational characteristics of the flux pump), and establishes objective functions that need to be minimized for obtaining flux pump design that is optimal for supplying the selected load.

This chapter also includes the designs of a few travelling field flux pumps that were produced using the aforementioned procedure targeting specific applications: HTS generators (wind turbine) and Toroidal Field (TF) coils of fusion reactors.

Comprehensive analysis on the operation and performance of each design flux pump is carried out and discusses as well.

3.1. The application-oriented optimal design procedure of travelling field flux pumps

The application-oriented optimal design procedure of travelling field flux pumps that was developed during this Ph.D. project is schematically described in the flowchart of Figure 64 where the mentioned physical quantities have the following meanings:

- I_{rated} is the rated current of the HTS magnet load that the flux pump is designed to energize.

- L_{coil} is the self inductance coefficient of the HTS magnet load that the flux pump is designed to energize.

- R_{joints} is the total resistance of the superconducting loop of the HTS magnet, accounting for all its joints.

- V_{oc} is the open circuit output voltage that the flux pump needs to have to meet the load requirements.

- I_{lim} is the generator mode limit current (defined in section 2.1.3) that the flux pump needs to have to meet the load requirements.

- And finally, P and η denote, for a given transport current I, the output power and efficiency of the flux pump, respectively.

The procedure starts from receiving the requirements (step A) and constraints (step A.1) imposed by a given HTS magnet to be supplied in terms of nominal current, total resistance and inductance, based on which the target electrical characteristics (V-I curve and energetic performance) that the flux pump will need to have are determined (step B). The procedure then proceeds with the identification of the degrees of freedom (DoF) of the flux pump (step C), i.e. its designing parameters that

are to be found concerning the applied field, like the HTS tapes and the geometrical and operational characteristics of the flux pump and establishes objective functions that need to be minimized for obtaining flux pump design that is optimal for supplying the selected load.

For the sake of clearness, an example of DoF for the case of HTS dynamos is the specifications list of Table 7 (to which other parameters could be added like the number of permanent magnets, the frequency of rotation, and the HTS tape type and dimensions) or one of its possible subsets.

Step D is carried out employing the FEM model described in chapter 2 to provide a relation between the DoF of the flux pump and the objective function of the optimization problem which uses AI-based optimization algorithms such as the genetic algorithm (GA) [163] and the particle swarm optimization (PSO) [164]. Step D involves implementing the FEM model as a MATLAB function that takes the DoF as inputs and provides multiple outputs, including V_{oc}, I_{lim}, the maximum output power, the maximum efficiency, or any combination of these parameters depending on what is needed to be known. After completing step D, the design compliance with all requirements and load constraints is checked and, if necessary, corrections of specific parameters (step E) or DoF (step F) are applied. An example of carrying out step E is changing the number of HTS tapes in parallel or of identical modules of flux pumps like the one obtained from step D (this situation could be encountered for HTS magnets requiring a very large rated current which is challenging to reach with only one flux pump, like in the case of fusion reactor magnets). Instead, step F might be used if no acceptable design can be found based on the DoF combination established at the previous attempt, hence the flux pump needs to go through drastic changes to meet the load requirements.
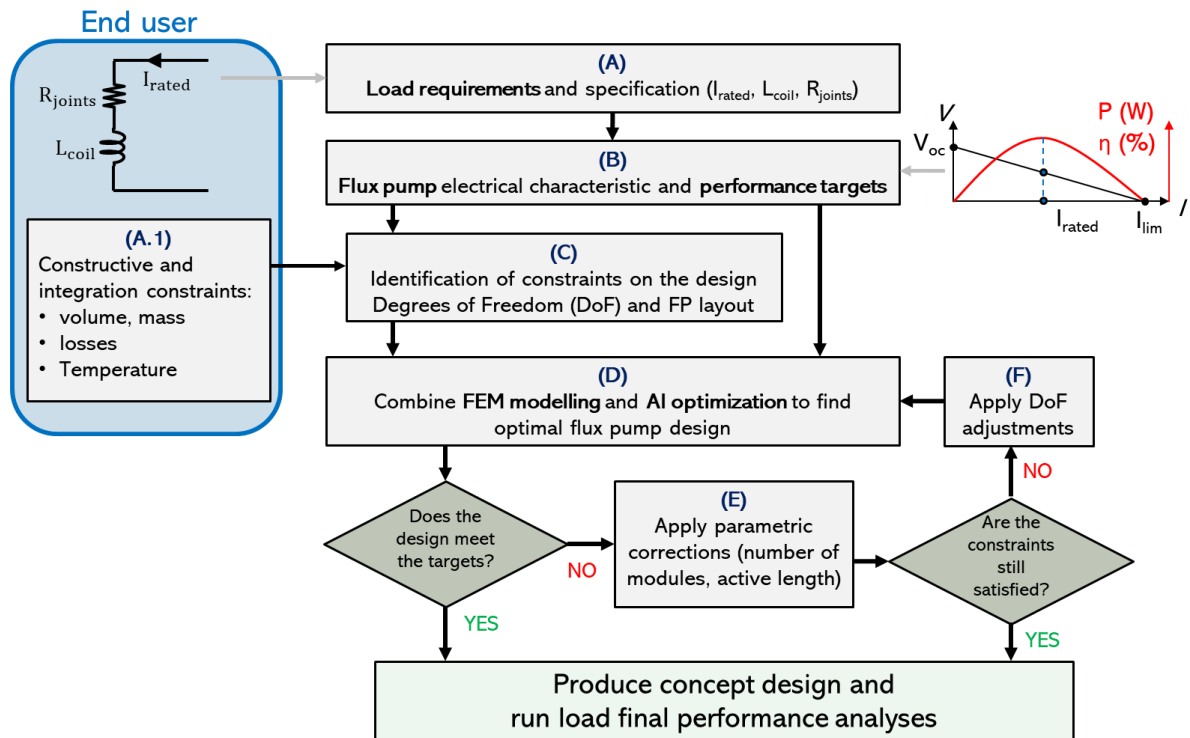
Figure 64 Flowchart of application-oriented optimal design procedure of travelling field flux pumps.

Based on the results of the analysis of sections 2.1.3 and 2.1.4, and on other experimental evidence (see Figure 27 and Figure 28), the target electrical characteristic (*V-I* curve) of the flux pump that is looked for is approximated to be a linear curve lying in the first quadrant, whereas the maximum output power and efficiency operating conditions are assumed to occur at about $I = I_{lim}/2$, yielding the standard condition: $I_{rated} = I_{lim}/2$. In most cases, only one quantity serves as a requirement, while the others act as constraints. For example, the I_{lim} parameter might be a strict requirement for a HTS magnet with a specific rated current, whereas its acceptable charging duration, which depends on the output voltage of the flux pump, could be anything lower that a certain time. In this case, defining V_{oc_MIN} as the open circuit output voltage of the flux pump that would charge the HTS magnet in the maximum acceptable time interval, any V_{oc} compliant with the constraint $V_{oc} \geq V_{oc\_MIN}$ would be acceptable. Since the flux pump output voltage (*V*) is a function of the transport current (*I*), V_{oc_MIN} is not straightforward and requires a more detailed mathematical analysis.

This mathematical analysis was carried out during a master project for which the undersigned has been supervisor [165].

The final block of the flowchart of Figure 64, named "Produce concept design and run load final performance analyses", indicates the final step which, if necessary and/or possible, includes adding constructive details to the design and simulating the energization of the coil of the end user with the designed flux pump. The final result of the optimization is a combination of the DoF, which only determines the active components of the flux pump. The addition of concept details is a mandatory step toward the realization of an operating design, CAD scheme, and eventually executive designs. However, the development of executive designs suitable for manufacturing and experimental validation belongs to the future steps of this Ph.D. project and was not accomplished yet. On the other hand, the numerical simulations of the flux pumps integration with the intended loads have been carried out for the conceptual designs produce during this work, and for this purpose the equivalent circuit of Figure 48.a was used. This approach allowed to calculate important quantities and flux pump performance of the coil energization such as the total dissipation (both during current ramp up and maintenance), and the charging time. In the next sections, a novel flux pump exploitation strategy based on a hysteresis control, that minimizes the operating losses, and is also presented and discussed.

Another important point of the optimization is represented by the number of HTS tapes operating in parallel. Because the FEM model that is used as a function in the procedure is a volume integral model with a dense mutual inductances' matrix, simulating many tapes in parallel implies having a large number of equations that need to be solved for Eq. (28) which in turns might entail a not manageable computational time. To address this issue, only one HTS tape can be simulated during the first optimization, and, if necessary, more tapes are added in parallel later if the generation current capacity requirement remains to be met. In fact, previous studies demonstrated that the current capability of HTS flux pumps increases linearly with the number of tapes in parallel [77]. The simulation of multiple tapes operating in

131

parallel, subjected to the same flux pumping conditions, can be achieved by employing the comprehensive equivalent circuit illustrated in Figure 46.b. This eliminates the necessity of utilizing the FEM model to simulate the system with the final quantity of HTS tapes. The following analysis is carried out in support of the previous claim. If the equivalent circuit of Figure 46.b is already known for one tape, adding N total identical tapes in parallel can be represented in the circuit of Figure 65, where only the component of the equivalent circuits of tape number 1 and N are shown for simplicity. Now the goal is deriving a simplified equivalent circuit of the one of Figure 65, but in the form of the one of Figure 66. Since the equivalent circuits of the parallel tapes are identical by definition, the total open circuit loss can be evaluated as follows:

$$P_0^{tot} = \sum_{i=1}^{N} \frac{V_{oc}^2}{R_0^i} = N \frac{V_{oc}^2}{R_0} = \frac{V_{oc}^2}{R_0^{eq}} \tag{54}$$

Consequently, the R_0^{eq} parameter of Figure 66 can be expressed as:

$$R_0^{eq} = \frac{R_0}{N} \tag{55}$$

The longitudinal resistance equivalent parameter can be easily found as the Thevenin equivalent resistance of the circuit of Figure 65:

$$R_{eff}^{eq} = \left(\sum_{i=1}^{N} \frac{1}{R_{eff}^i} \right)^{-1} \tag{56}$$

Which under the current hypothesis gives:

$$R_{eff}^{eq} = \frac{R_{eff}}{N} \tag{57}$$

And the Thevenin equivalent voltage of the circuit of Figure 65 is obviously V_{oc} itself.

$$V_{oc}^{eq} = V_{oc} \qquad\qquad (58)$$
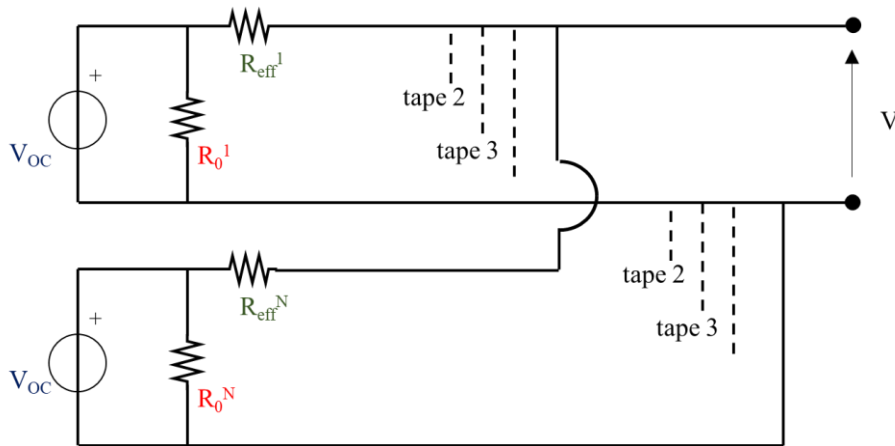
Figure 65 Equivalent circuit of N identical tapes operating in parallel according to the same operating conditions of flux pumping (only the component of the equivalent circuit of tape number 1 and N are shown for simplicity).
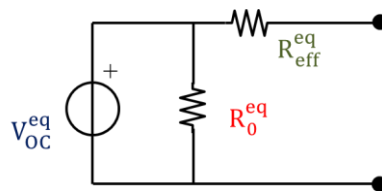
Figure 66 Simplified equivalent circuit Figure 65.

To validate Eq. (55) and (57), one HTS dynamo is simulated for N varying from 1 to 5 calculating the values of R_{eff} and R_0 each time according to the definitions given in section 2.1.5. R_{eff} and R_0 are then also obtained with the analytical formulas of Eq. (55) and (57) using the corresponding values for $N = 1$.

After normalizing R_{eff} and R_0 to 100 %, where 100 % corresponds to $N = 1$, the outcomes obtained through the FEM model and the analytical formulas are juxtaposed for comparison in Figure 67. It can be observed that R_{eff} and R_0 exhibit similar values, whether determined through simulating the flux pump with the actual number of HTS tapes or calculated using the parameters of the equivalent circuit with a single tape and employing Eq. (55) and (57).
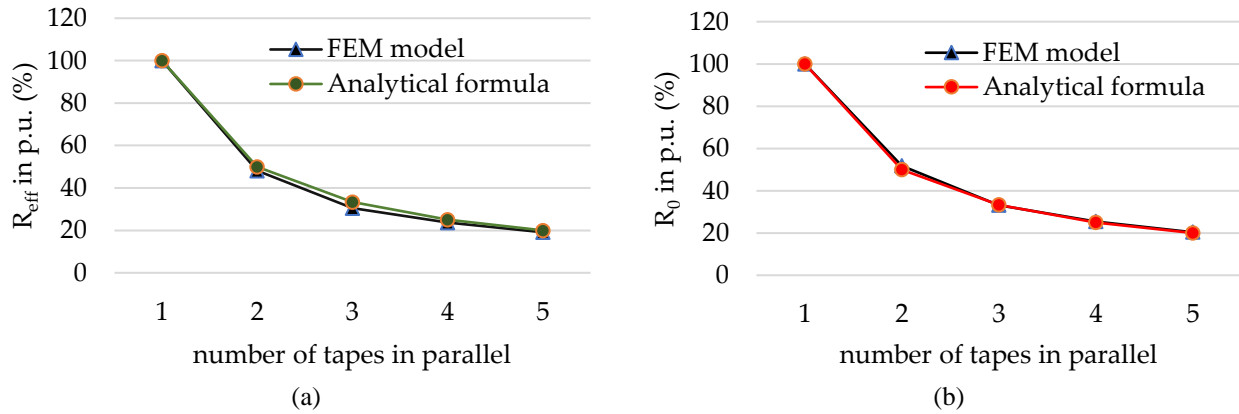
Figure 67 Validation of the analytical formulas of Eq. (55) and (57) by comparison with the FEM model results for equivalent parameters (a) Reff and (b) R0, with N ranging from 1 to 5 (values normalized to 100).

For completeness, the relative error between the R_{eff} and R_0 values obtained through the FEM model and analytical formulas are calculated and reported in Figure 68. It can be seen that the FEM model and Eq. (55) little diverge from each other when predicting R_0, yielding a relative mismatch ranging from a minimum of −0.76 % (for N = 3) to a maximum of 3.49 % (for N = 2). However, Eq. (57) is less effective in accurately reproducing the values of the FEM model for R_{eff}, as it gives relative errors up to −9.32 % (for N = 3). Nonetheless, since all relative errors are lower than 10 %, Eq. (55) and (57) are considered acceptable zero-order approximations for deriving the complete equivalent circuit of a flux pump with multiple HTS tapes. This enables simulating only one tape during the optimization process in step D of Figure 64, deferring the computationally intensive final simulation, which includes the total number of HTS tapes, to the last validation step.
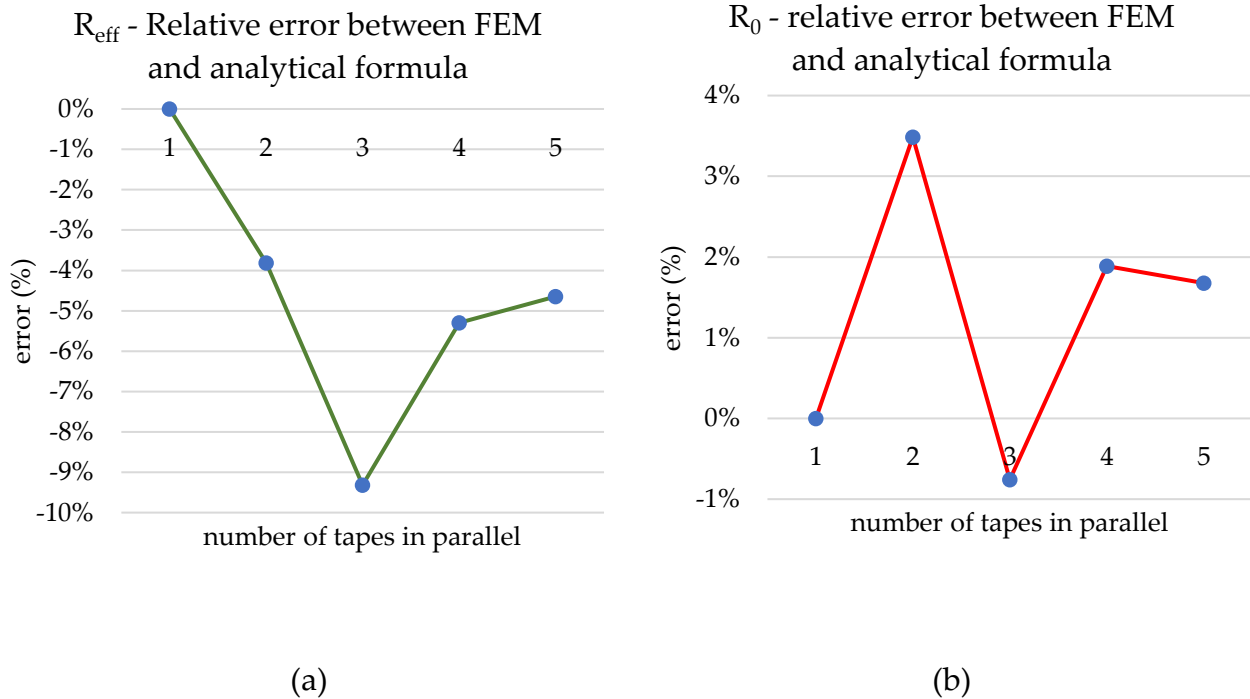
Figure 68 Relative error between the analytical formulas of Eq. (55) and (57) and the FEM model computing the equivalent parameters (a) Reff and (b) R0, with N ranging from 1 to 5.

In the next sections, the design of travelling field flux pump using the aforementioned procedure is carried out and their performance are analyzed and discussed.

3.2. A case study for the design of a HTS dynamo: The EcoSwing wind turbine

The first real application for which the designing procedure was applied to design a HTS dynamo was a superconducting machine and, more in particular, the field winding of the world first superconducting generator: the EcoSwing wind turbine.

The EcoSwing wind turbine is the milestone result of an EU H2020 project carried out by a consortium of nine partners from industry and academia and concluded in 2019 [166]. A full-scale 3.6 MW direct drive (DD) HTS generator was designed, developed, installed, and operated in an existing wind turbine [167]. The generator

consists of a 20 poles pairs rotor made of HTS field winding and a conventional stator. The detailed specifics can be found in [168]. A 24 % overall weight reduction and 26 % size reduction with respect to the conventional counterpart used for the same wind turbine were achieved.

The system performed stable operation at 2 MW and was boosted to 3 MW as well. Overall, the generator delivered 600 MWh to the grid over a continuous operation period of more than 650 hours, proving on field the technological feasibility of HTS wind turbines and improving its TRL from 4-5 to 6-7 [168].

The HTS field winding consists of 40 racetrack-shaped HTS coils [169] located inside a self-sustaining vacuum insulation that are cooled at an operating temperature lower than 30 K [170] by nine rotating compressor-driven cold heads (Sumitomo F70). The iron poles of the rotor are integrated into the cryostat and operates at cryogenic temperature as the windings. The cold heads are mounted onto the rotor, and are fed for their operation with high pressure helium gas by means of nine stationary compressors using a rotating joint THEVA provided the high performance 2G HTS conductor (ReBCO TPL 2100) used in the field magnets. Detailed specifications about the tape and the coils can be found in [171]. The schematic of the rotor's electrical circuit is shown in Figure 69. The power supply system of the HTS field winding involves a voltage source, a dump resistor, a freewheeling diode, and an insulated gate bipolar transistor (IGBT) [172]. More details on the rotary joint assembly, comprising the coupling joint of the stationary and rotating helium gas pipes system and the slip rings and brushes providing electrical connection between the power supply and field winding are given in [169].
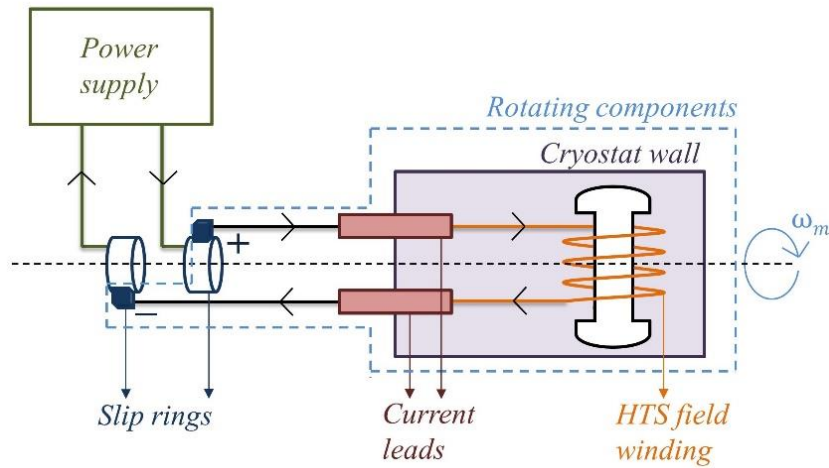
Figure 69 Schematic of the supply system of the rotor HTS field winding of the EcoSwing turbine.

The main characteristics of the HTS field winding system are reported in Table 9.

Table 9 HTS field winding specifications of the EcoSwing generator

I_n – Rated current	330 A
Number of poles	40
ω_m – Rated speed	15 rpm
R_{load} – Estimated total resistance of joints	4.128 μΩ
$L_{load}(I_n)$ – Inductance at rated current	10 H
Total cooling power requested	35 kW
P_{cl}^{amb} – Cooling power requested due to current leads heat load	726 W

Overall, the HTS field winding of the EcoSwing requires about 35 kW cooling power to maintain the operating temperature of the coils at 30 K. Different contributions are responsible for this amount of power: HTS magnets AC loss, thermal radiation, thermal income from the current leads, and additional loss. Among those, the coils AC loss and the thermal radiation do not change according to which power supply is employed, therefore they are not taken into account in this comparison. A pair of hybrid Cu/HTS current leads are used to connect the HTS field winding to the power supply. The leads consist of a copper feedthrough bar with one end connected to the power supply and the other end anchored at an operating temperature of 60 K

137

inside the cryostat by means of a dedicated cryocooler (which is also used for anchoring the temperature of the radiation shield) [167]. An assembly of HTS tapes in parallel (HTS stage of the lead) is used, inside the cryostat, for connecting the 60 K end of the Cu bar to the input terminal of the HTS field winding, that is maintained at 30 K by means of eight dedicated cryocoolers. Based on common engineering experience, a heat load of 50 W/kA at 60 K can be assumed per each of the current leads [173] [174] [175]. By considering the rated current of the EcoSwing rotor (I_n = 0.330 kA), the total (for both the leads) heat invasion P_{cl}^{cryo} cryogenic temperature due to current leads is found to be 33 W for the considered supply system. A coefficient of performance (the ratio between the power to be supplied at ambient temperature to the cooling system and the thermal power extracted for the cryogenic environment and transferred to the ambient) COP = 22 W/W is assumed based on the typical performance of conventional cryocooler performances operating between 300 K [176] and the operating temperature of 60 K of the current leads. Hence, the input power P_{cl}^{amb} of the cooling system at ambient temperature is calculated as:

$$P_{cl}^{amb} = P_{cl}^{cryo} \times \text{COP}$$

(59)

According to Eq. (59), an input power of 726 W is obtained for the cooling system for retaining the current leads at the required temperature. The circuit model of the winding is the fundamental input needed for carrying out the design of the flux pumps and therefore it is discussed here. Overall, the field winding corresponds to the non-linear two terminal RL component shown in Figure 70. The constant resistance R_{load} accounts for the losses in all the electrical connections (joints) between the different modules of the field winding as well as the electrical joint between different sections on one module, while the non-linear inductance L_{load} represents the overall terminal inductance of the winding. The inductance is non-linear due to the iron poles that reaches saturation at the nominal current of the winding. Neglecting the dependance

of the inductance on the current would not be acceptable for the proper design of the flux pumps supply.
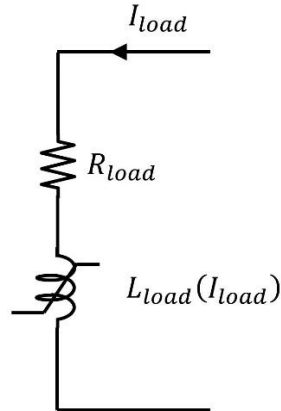
Figure 70 Equivalent circuit scheme of the HTS field winding.

An inductance L_{load} = 10 H at rated rotor current I_n is considered [177]. This corresponds to a total flux φ = 3330 Wb linked by the winding. For obtaining the L-I curve, the whole φ -curve was deduced as a first approximation from the B_0-i curve reported in [167], where B_0 is the measured field at the center of one coil. The L-I curve of the rotor winding, in the current range from 0 to 330 A, was finally obtained by taking the numerical derivative of the φ -I curve and it is show in Figure 71. As for the resistance R_{load}, we report that each of the HTS coil of the rotor winding has up to 10 lap joints, with an interface resistance of 36 ± 9 $n\Omega cm^{-2}$, and a 5 cm overlap. Furthermore, all adjacent coils are connected in anti-series with a hybrid copper-HTS design connection with an average resistance of 32 $n\Omega$ at 77 K. By considering all the intra and the inter coil joints, a total resistance R_{load} of 4.13 $\mu\Omega$ is found for the field winding. No further resistance exists in the model of the winding since the coil current is below the critical current of the superconductor at the chosen operating temperature and magnetic field. Possible additional resistance may arise during normal operation of the generator due to AC field ripple on the field windings [39] [178], but this is not considered in the present study. In the next sections, the L vs I curve and the total joints resistance R_{load} are used in the equivalent circuits of the systems for simulating the

energization of the field coils for all the cases of dynamo and rectifier flux pumps as power supplies.
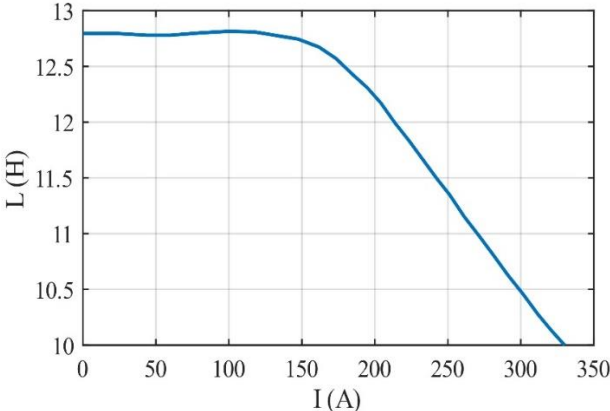
Figure 71 Coefficient of self-inductance over transport current curve for the EcoSwing rotor, derived based on the information in [167].

3.2.1. Design and characteristics of the HTS dynamo for the EcoSwing field windings

Since this study was carried out before the application of AI-based optimization algorithms (GA and PSO), step D indicated in the flowchart of Figure 64 was achieved empirically with the aim of maximizing the power output and the efficiency at the rated current. More in particular, the sensitivity analysis of the DoF of the dynamo were produced to find a HTS dynamo whose generator limit current was 660 A with the highest possible efficiency. The rationale behind selecting a generator current limit of 660 A stems from the findings elucidated in Chapter 2, where it was revealed that the optimal operating efficiency occurs at approximately half of the generator's current limit. In principle, the DoF of the design could be as many as the number of specifications in Table 1, or even more. It is evident that these many variables would arguably not be manageable, therefore some specifications were fixed a priori. The operating temperature of 77 K was chosen based on the results described in section 2.5. Moreover, since the performance of dynamo flux pumps increases with the

magnetic field acting on the HTS tape and a short distance from the permanent magnets is desirable [101]. An air gap of 5 mm between the permanent magnets (PMs) and the HTS tapes is chosen to incorporate the cryostat wall. This airgap is feasible by means of an optimized design of the section of the cryostat hosting the flux pump (and in particular of the vacuum system) which can be independent from, though it can be conveniently integrated with, the main cryostat of the HTS rotor winding. It is also reported that novel dynamo configurations have been recently investigated that allow to reach a substantial increase of the magnetic field on the tape even in the presence of larger air gaps by including back iron in the magnetic circuit [78] [85] [179]. Hence, the dynamo used in this work can be considered as a conservative design that can be further improved in the future by means of innovative solutions. It is also noted that the operating temperature of the dynamo's tapes differs from the EcoSwing field winding. Such an operating condition can be obtained by means of a specific cold head dedicated to the cooling of the flux pump. Since it is reminded that one cryocooler has been specifically dedicated to currents leads in the EcoSwing machine, no additional cooling devices are required. On the other hand, a cheaper cryocooler with lower cooling capacity can be used instead. Other fixed parameters were the remanence geometrical dimensions of each permanent magnet (taken from commercial catalogs) and the active length of the dynamo, which has the only impact of increasing the output voltage, and so was taken as long as it could reasonably be to fit inside the wind generator (350 mm). The width of the HTS tape was assumed to be 12 mm, as it is a typical commercial size. Given the aforementioned fixed parameters, the DoF of the HTS dynamo during the design process were: the number of PMs, the number of HTS tapes, the angular velocity of rotation of the PMs with respect to the HTS tapes, and the radius of the dynamo.

The main characteristics of the final design are reported in Table 10, and a 3D schematic of the designed dynamo flux pump is shown in Figure 72.

Table 10 Specifications of the HTS dynamo for the EcoSwing field windings

Number of permanent magnets (PMs)	20
Number of HTS tapes	3
Width of each PM	6 mm
Height of each PM	12 mm
Depth of each PM	350 mm
Remanence of each PM	1.25 T
Width of each HTS tape	12 mm
Thickness of each HTS layer	1 μm
Operating temperature of the HTS tapes	77 K
External radius of the rotor (radial position of tapes)	300 mm
Airgap between the PMs and the HTS tape	5 mm
ω_r - Relative angular velocity of PMs and tapes	1500 rpm (0.25 Hz)
ω_{PM} - Angular velocity of the PMs in the stationary frame of the rotor	1485 rpm (24.75 Hz)

The dynamo consists of 3 THEVA Pro-Line 2G HTS with 12 mm width exposed to the field produced by 20 permanent magnets. The HTS tapes are fixed with respect to the HTS field winding and move with the generator's rotor. The magnets are mounted on a separate, and free to rotate, assembly, and their rotational velocity ω_{PM} in the stationary frame can be controlled independently from the rotational velocity ω_m of the generator's rotor. The permanent magnets (PMs) rotate with respect to the tapes with a relative angular velocity ω_r given by:

$$\omega_r = \omega_{PM} - \omega_m$$

(60)

ω_r = 1500 rpm between PMs and tapes is needed for producing the required voltage (see Table 10). By considering the rated speed ω_m = 15 rpm of the generator's rotor [168] (See Table 9), an angular velocity ω_{PM} = 1485 rpm needs to be applied to the permanent magnets.

The 3 HTS tapes are connected in parallel and each carries one third of the overall current supplied to the load winding. Two collector rings (highlighted with – and +

signs in Figure 72) connected to the opposite ends of the tapes form the terminals of the flux pump to which the load is connected.
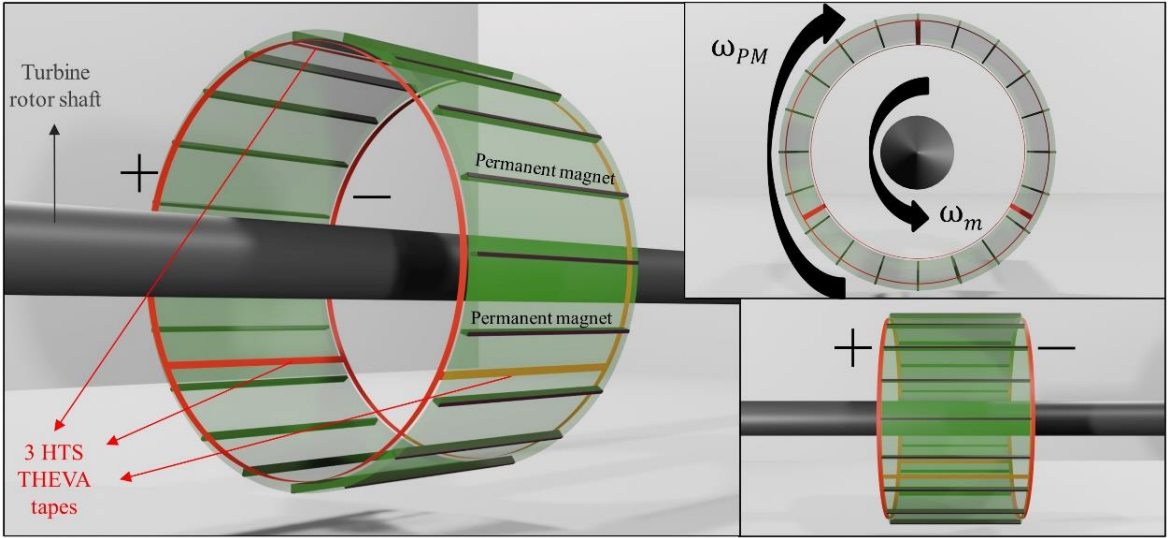
Figure 72 3D scheme of the dynamo flux pump. ωm is the rated rotating speed of the turbine and thus refers to both the rotor shaft and the 3 HTS tapes. + and − indicate the superconducting terminals to which the field winding is connected. The HTS tapes are fixed with respect to the HTS field winding and move with the generator's rotor.

The schematic of the overall contactless power supply system of the HTS field winding is shown in Figure 73.
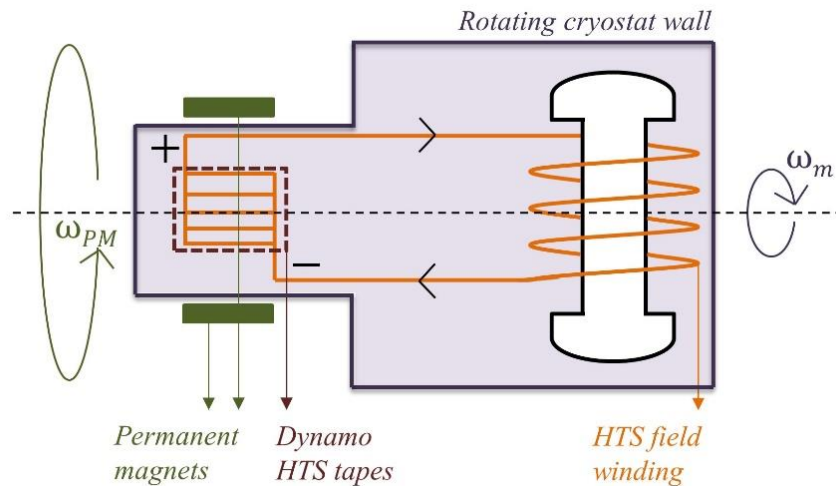
Figure 73 Contactless supply system of the rotor HTS field winding of the EcoSwing turbine based on the dynamo flux pump.

3.2.2. Electrical characteristics and performances of the HTS dynamo

The modelling approach described in sections 2.1.3-2.1.6 has been used for characterizing the dynamo in terms of electric output and performance, as well as for simulating its integration with the EcoSwing field windings. The V-I characteristic of the dynamo, as well as its performance in terms of losses and efficiency over a wide range of transport current are shown in Figure 74. The value I_0 = 658 A fixes the limit beyond which the flux pump is not able to operate as a generator and proves that the design objective has been fulfilled. The output power at the terminal also changes approximately quadratically with the output current. It is zero in no load conditions and at the boundary I_0 of the generator region, and reaches a maximum of the 19.8 W when the transport current approaches I_{load} = 400 A. The dynamo dissipates about 300 W in no load condition at zero transport current (that is, when the PMs are rotating while no load is connected to its terminals). The losses follow a quadratically like trend with the transport current as well. As a result, the efficiency of the device, defined as the ratio between the output power at the terminals and the mechanical power

supplied by the rotor, is maximum at I_{load} = 350 A where it reaches the value of 5.78%, and is equal to 5.74% at I_{load} = 330 A, namely the rated current of the field winding.
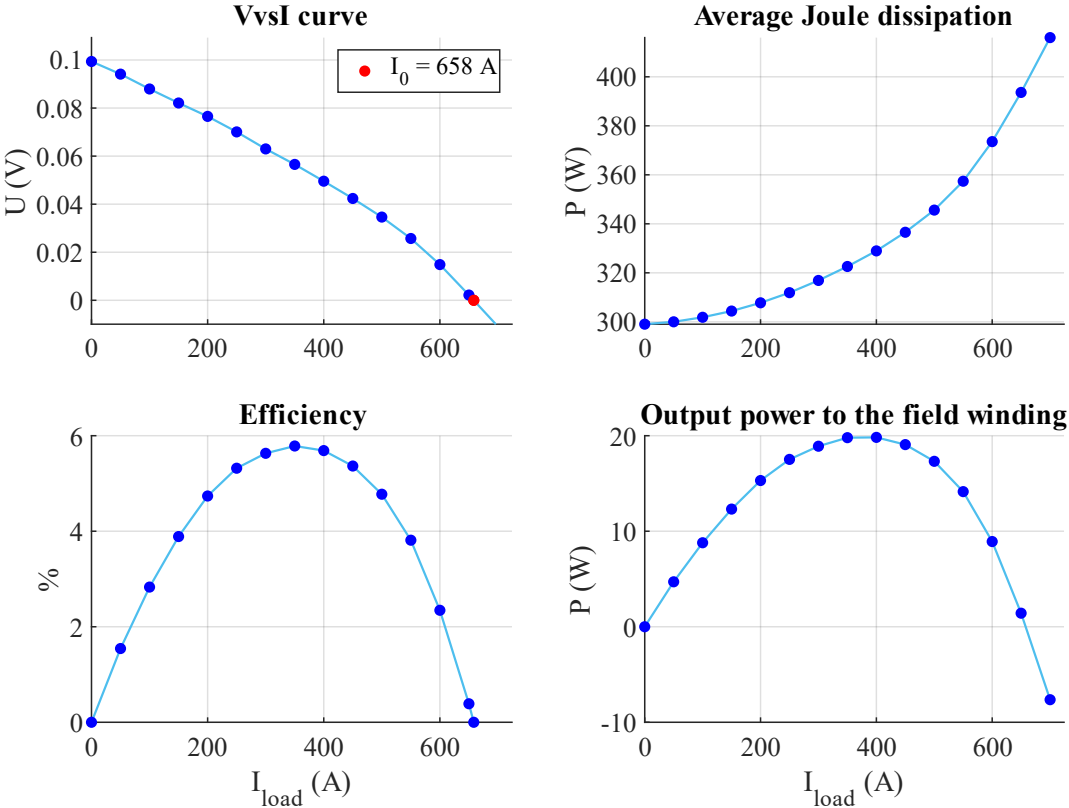
Figure 74 V vs I relation, Power dissipated vs Iload, efficiency vs Iload, and Power delivered to the field winding vs Iload of the dynamo flux pump.

It must be specified that setting the relative angular speed of the PMs and the tapes equal to zero cancels the voltage at the terminals. As a result, no power is supplied nor absorbed (as mechanical power at the rotor) by the flux pump in this condition and the HTS tape form a short circuit connection at the terminals of the HTS field winding. This operating conditions are hereinafter referred to as "off-state", whereas the operating conditions based on Table 10 which give the results of Figure 74 are referred to as "on-state".

The equivalent circuit of the dynamo flux pump coupled with the one of the EcoSwing field winding's is shown in Figure 75, and the values of the its parameters

are listed in Table 11. In this study, the equivalent circuit includes the cycle average of the open circuit output voltage, therefore $R_{instrinsic}$ is calculated according to Eq. (46).
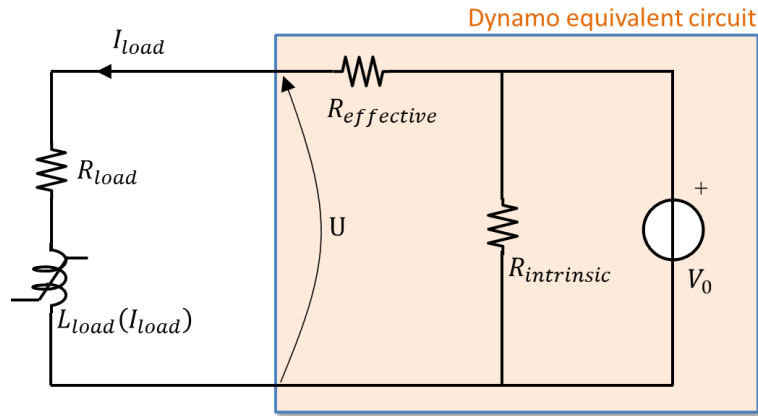
Figure 75 Equivalent circuit of the dynamo flux pump supplying the field winding of the HTS generator.

Table 11 Dynamo flux pump – equivalent circuit parameters

V_0	99.4 mV
$R_{instrinsic}$	33.0 µΩ
$R_{effective}$	150.9 µΩ

The solution of the circuit of Figure 75 at regime conditions would yield I_{load} = 658 A (corresponding to $V_0/(R_{effective}+R_{load})$). Thus, in order to achieve steady DC operation at the rated current of I_n = 330 A, a closed loop hysteresis control has been implemented by switching the flux pump from the on and the off-state with rated duty cycle, as it was previously suggested in [85]. In particular, during the first charge (ramp-up) of the field wilding the flux pump is continuously in the on-state, meaning that the PMs of the rotor rotate with the rated relative velocity of 1500 rpm with respect to the tapes and the current injection takes place according to the circuit of Figure 75. At the very first instant of the energization (I_{load} = 0 A) a voltage V_0 = 99.4 mV is produced by the flux pump causing the increase of the current of the coil following the profile shown in Figure 76. As I_{load} increases, the output voltage of the flux pump

146

decreases according to the load curve of Figure 74. When the transport current exceeds I_n by a threshold of + 0.2 %, the hysteresis control intervenes so that flux pumping is stopped by changing the angular velocity of the PMs so that they move synchronously to the tapes, the off-state is entered. In this condition no voltage is produced at the terminals and the tapes of the dynamo flux pump, which naturally offers a negligible resistance path for the circulation of the DC HTS field winding current, hence no dissipation occur in the flux pump in the off-state. It is specified that the + 0.2 % threshold of the hysteresis control is a completely arbitrary choice which can be adjusted according to different circumstances and end user requirements (for example, the magnet field acceptable ripple). During the off-state, due to R_{load}, I_{load} undergoes a slow decay with a time constant of $L_{coil}(I_{load})/R_{load}$. As soon as, due to this decay, a current 0.2% lower than I_n is reached, the on-state is restored, meaning that it is simulated that the PMs start rotating at angular velocity ω_{PM} back again. As a result, after the ramp-up, the current reaches a cyclic steady state in which it oscillates around the nominal value I_n = 330 A with a ± 0.2 % ripple. This is abundantly lower than 1 %, therefore it is assumed that the AC loss in the coils due to current ripple is neglectable compared to the other loss contributors, hence it is not taken into account in the total loss evaluation.
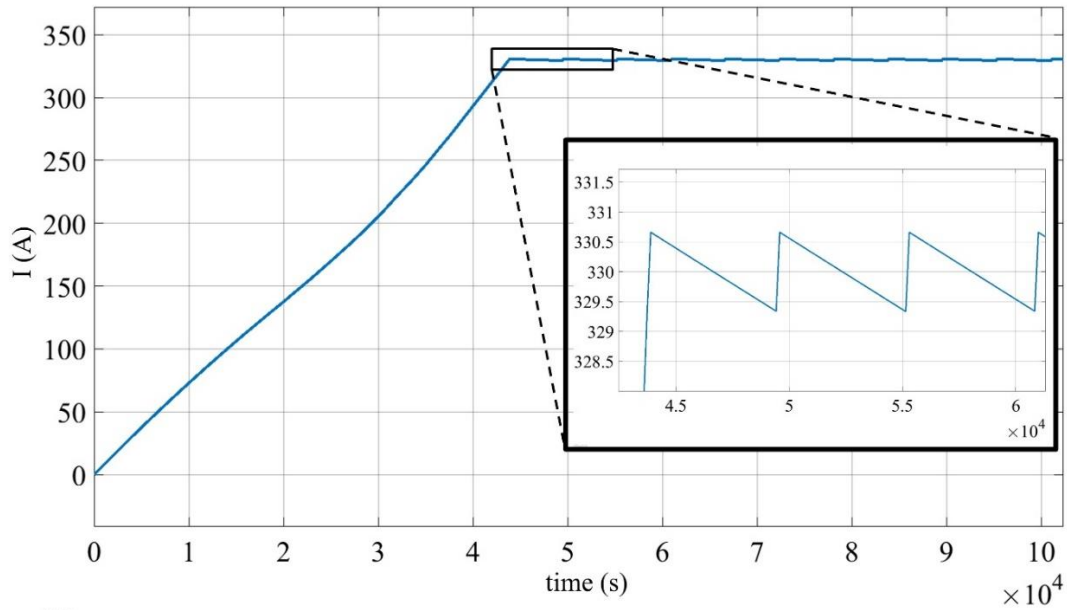
Figure 76 Ramp-up transient and maintenance of current of the EcoSwing field winding supplied by the dynamo flux pump.

The rated current I_n is reached by the dynamo during the ramp-up phase after about 12 h (43805 seconds). After this phase the current is kept between 330.66 and 329.34 A by the controller that switches the dynamo between the on and the off- state, as it is displayed in Figure 76. It is noted that such a long charging time may represent a drawback for the practical commissioning of the turbine. However, if needed this drawback can be overcome by de-signing a dynamo with a higher output voltage. As an example, a dynamo with an output voltage of 500 mV voltage (against 99.4 mV of the one considered in this study) would allow a charging time reduction down to 2 hours and could meet the requirement of a shorter energization time if required.

During current maintenance, on-states and off-states alternate over a cycle lasting 95 minutes (5695 seconds). The on-state only last 157 seconds, corresponding to a duty cycle of 2.76 %. The power dissipated by the flux pump during the process is shown in Figure 77. It can be noted that loss occurs in the flux pump as soon as the rotation and the charging of the HTS field coil begins. During the charging the loss slightly increases with the load current. A heat load $P_{dynamo\,(on)}^{cryo}$ = 315.5 W is produced when the flux pump is in the on-state and the nominal current is reached. However, once the

148

ramp-up is complete the current of the load remains practically constant and the flux pump alternate between the on and the off-state, with loss only occurring in the on-state occupying 2.76 % of the cycle.
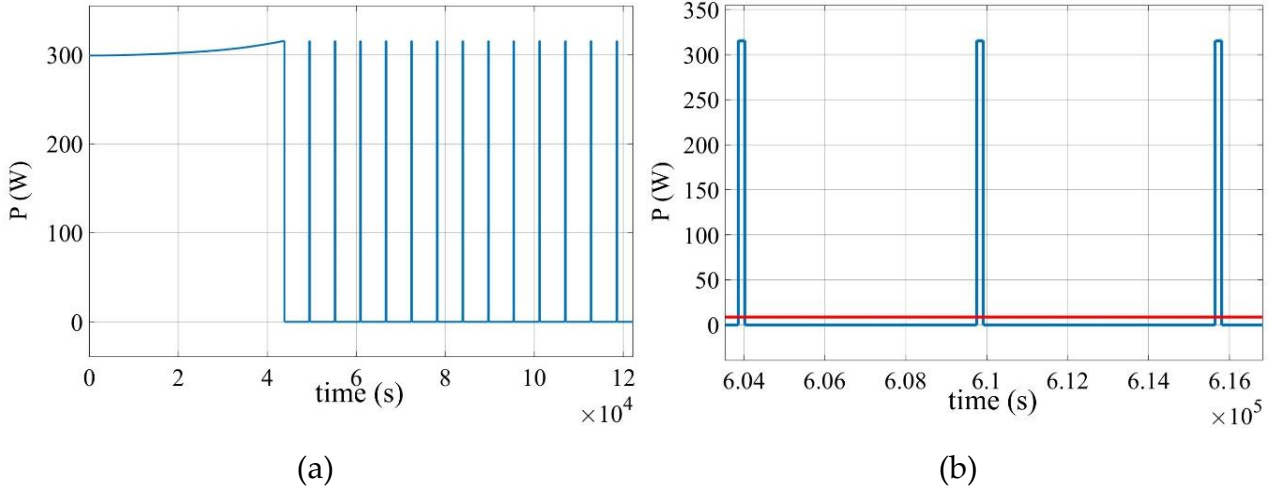
Figure 77 (a) Dynamo losses vs time, (b) Dynamo losses vs time enlargement, blue line is the instant dissipated power, red line is average dissipated power.

The average dissipation at cryogenic temperature of the dynamo flux pump during the cyclic operation at nominal current can be computed as follows:

$$P_{dynamo\ (average)}^{cryo} = P_{on}^{cryo} \times \delta \tag{61}$$

where δ is the duty cycle, resulting in 8.7 W. This value must be compared with a heat load of 33 W reached with the current leads. It is stressed that, despite the much lower average value, a substantial dissipation (315.5 W) is produced during the ramp-up. Thus, appropriate sizing of the dedicated cooling apparatus must be considered for preventing excessive temperature of the HTS field winding during the charging process. Finally, the input power needed at ambient temperature for cooling the flux pump is obtained by taking the COP into account as in Eq. (59) and gives $P_{dynamo\ (average)}^{amb}$ = 191 W. Since a cooling power P_{cl}^{amb} = 726 W was obtained in section 3.2 for the conventional, current leads based supply system, a drastic reduction (74%) of cooling cost for energizing the HTS field winding of a 3.6 MW wind turbine is

achieved with the flux pump. Moreover, it should be reminded that flux pumps are contactless power transfer devices requiring no slip rings, which means that reliability is improved, and complexity reduced by avoiding electrical rotary coupling and simplifying thermal coupling. Such an overall improvement results in decreasing both the investment and the operating and maintenance costs of the system, resulting in a reduced levelized cost of energy.

The purpose of this study was to compare different energization systems of the field winding of a full-scale wind turbine in terms of total equivalent heat load. However, compatibility of the considered solutions with fast de-energization of the coil in case of failure of the system must be considered. As for the dynamo flux pump, a resistor with a normally closed switch in parallel can be included in the superconducting loop of Figure 73. Both the switch ad the resistor operate at cryogenic temperature. When the discharge is needed the switch is open and the current flows in the resistor discharging the coil. Research is in progress for developing quench protection systems fully integrated inside the cryogenic environment, delivering promising results [180]. Both mechanical and solid-state solutions can be considered for the switch. Whereas using a mechanical switch would not impact very much the behavior of the system, additional losses would be added by the static solid state switch requiring a higher output voltage of the flux pump. However, several experimental studies have reported substantial improvement of performance of electronic switches at cryogenic temperature, including reduction of forward voltage drop and switching performance [181] [182] [183], thus making their adoption viable.

3.3. A case study for the design of a linear flux pump: The Divertor Tokamak Test

The development of contactless superconducting power supplies is driven by the urgent need for efficient means to energize the high-current DC magnets employed in future nuclear reactors. With transport currents reaching tens of kiloamperes,

traditional systems, comprising power electronic converters, lengthy and convoluted busbars, and current leads, pose significant challenges in terms of efficiency, footprint, and reliability. These obstacles pose a threat to the viability and reliability of fusion reactors.

The aforementioned circumstances are now described for the specific case of the Divertor Tokamak Test (DTT).The DTT facility is an european initiative to establish a specialized facility for testing and evaluating a range of potential solutions for the DEMOnstration Fusion Power Plant (DEMO) [184], including cutting-edge magnetic configurations and molten metal divertors. The DTT is designed to address the power handling discrepancies between existing devices and ITER (International Thermonuclear Experimental Reactor) [185] and DEMO experiments. The project is managed by a DTT legal entity comprising ENEA, ENI S.p.A., and CREATE, with the involvement of prominent italian research institutions and universities. The DTT is expected to start operating by the end of 2026 and continue for at least 25 years, up to the early stages of DEMO's realization [186].

As typical for tokamaks [187], the DDT magnet system comprises a set of Toroidal Field (TF) coils dedicated to the generation of the magnetic field for the plasma confinement. TF coils operate in direct current, so in principle they are suitable for being supplied by a flux pump. The final design of the DDT TF power supply circuit is described in detail in [188]. The DTT TF magnet system incorporates 18 identical superconducting coils made from Nb_3Sn and cooled with supercritical helium at a frigid 4.5 Kelvin. These 18 TF coils are linked in series and powered by a solitary power supply, which is connected to the 20-kV level distribution power grid through four converter transformers with resin insulation and extended-delta/delta connections. Each TF coil is rated for a current of 42.5 kiloamperes, and the power supply is a 24-pulse thyristor-based converter capable of delivering up to 44 kiloamperes of direct current. In the event of a quench, a rapid discharge is crucial to extract the magnetic energy stored within the superconducting coils. This is accomplished by three Fast Discharge Units (FDUs) linked in series with three sectors

comprising six TF coils. The power supply is connected to the 18 superconducting coils through DC copper busbars [188]. The electrical scheme of the system just described is shown in Figure 78, where TFC stands for TF coils and the four transformers are not shown.
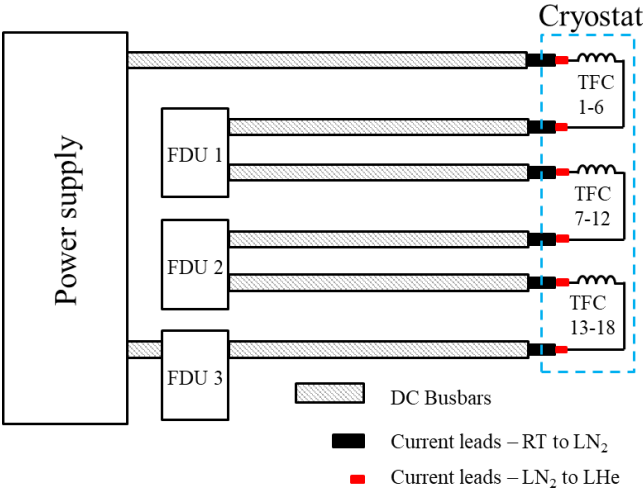
Figure 78 Electrical scheme of the DTT TF magnets, its power supply system, busbars, and the FDUs.

The power supplies occupy space for hundreds of cubic meters (almost filling a room of dimensions 26 m × 13 m × 8 m). The copper busbars bulkiness is also worth mentioning, as they follow intricated pathways to reach the magnets' current leads starting from the room of the power supplies, weighting and occupying about 150 Tons and 16.5 m3 respectively. In terms of dissipation, the permanent losses that will take place during normal operation when a 42.5 kA current flows through the TFC for the thyristor-based power supply, the busbars, and the RT to LN_2 (liquid nitrogen) current leads are about 245 kW, 320 kW, and 230 kW respectively [188] [189] [190]. Therefore, it is evident that from an economic standpoint these traditional systems significantly impact both capital and operating expenses. Moreover, the substantial heat generation associated with these losses raises additional concerns about reliability. The buildup of heat in confined spaces can lead to premature failures of electronic components, jeopardizing the overall integrity of the power supply systems. Unreliable power supply systems can hinder the economic feasibility of nuclear

reactors, discouraging investment in the entire sector. It is noted that no considerations have been made on the FDUs. In fact, the purpose of this section is setting the bases for a comparison between the traditional power supply solutions and flux pumps for the energization of DC fusion magnets. It must be considered that effective protection devices for the magnets will be implemented even in the case a flux pump power supply is employed. The assessment of both the comparison and the integration considerations of flux pumps with quench protection systems will be elaborated later in the thesis.

To conclude on this introductive section of the DTT TF magnets, the specifications their specifications are listed in Table 12 [191]. The operating current is updated according to [188].

Table 12 Specifications of the DTT TF coils [188] [191]

Number of coils	18
Number of turns per coil	80
Total Inductance of the 18 coils	≈ 2 H
Total stored energy	≈ 2 GJ
Operating current	42.5 kA
Design margin for current	10 %
Current including margin	≈ 48.5 kA
Time constant for TFC emergency discharge	5 s
Number of FDUs	3
Available area for the TFC PS and FDUs	13 m x 26 m
Dimensions of the busbar tunnel	2.84 m x 2.96 m

3.3.1. The design of a linear flux pump for the DTT Frascati Coil Cold Test Facility

The Frascati Coil Cold Test Facility (FCCTF), whose operations are scheduled to start in mid-2024, will be dedicated to the testing the 18 DTT TF coils at full current and operating temperature 42.5 kA and 4 K, respectively. This work presents the design study of a linear flux pump to be integrated into the Frascati Coil Cold Test

Facility. The choice of addressing a linear-type flux pump instead of other topologies is motivated by its controllability, scalability, and experimentally proven high current capability [115]. The proposed flux pump is designed for a target current of 2 kA for safety reasons with regard to the TF coils.

In linear flux pumps, the outputs and performance are determined by the features of the travelling magnetic field wave seen by the tape, that are: the wavelength (λ), the frequency (f), the amplitude of the AC field component (B_{ACmax}), and the value of the DC field component (B_{DC}) [112] [113] [115]. The strategy assumed in this study for designing the flux pump consisted of the two following steps:

- The search for the optimum travelling magnetic field wave to reach the required current capacity. For this purpose, step D of flowchart in Figure 64 was used.

- The synthesis of the optimal travelling magnetic field wave by designing the magnetic circuit (exciter composed by the core and field coils).

During the first design step the effect of the ferromagnetic core was not considered. It must also be mentioned that the considered tape width was 96 mm, which is equivalent to using 8×12mm tapes in parallel and the operating temperature is chosen to be 70 K, since this allows a good trade-off between performance and temperature margin (see Figure 63).

Continuing the description of the firs step, after discretization of the HTS tape in 222 elements similar to what had been done in section 2.1, calculation of coefficients $\overline{\overline{M}}$ and $\bar{u}$ appearing in Eq. (28), as well as its solution and calculation of the V-I curve at the terminals was performed directly following the approach developed in chapter 2. The objective of the optimization was the current capability of the linear flux pump, hereafter referred to as I_{max}, to be equal to 2 kA. The DoF of the optimization were parameters λ, f, B_{ACmax} and B_{DC} of the magnetic field waveform, as already mentioned. A genetic algorithm (GA) was used to find the combination of field features that gives a current capability that satisfies the objective, which is mathematically expressed through the least squares function to be minimized, according to Eq. (62).

$$\text{Objective funcion} = (2000 - I_{MAX}(\lambda, f, B_{ACmax}, B_{DC}))^2 \qquad (62)$$

Where $I_{MAX}(\lambda, f, B_{ACmax}, B_{DC})$ is found for each combination of DoF as explained in section 2.1.3. It is also reported that the SuperOx YBCO 2G HTS was considered since this tape gives the best flux-pump performance, as previous shown in section 2.4. The results of the GA optimization, which represent the target field waveform, are listed in Table 13

Table 13 Features of the target excitation field waveform

B_{ACmax}	0.68 T
B_{DC}	0.68 T
Frequency (f)	12 Hz
Wavelength (λ)	42 mm

Next, as the second design step, the target field waveform was synthesized by designing the magnetic circuit able to produce the identified travelling field wave. This magnetic circuit is hereinafter referred to as the exciter. The exciter comprises a system of three-phase AC copper windings and one DC copper winding enclosed into a ferromagnetic core. The AC windings are fed with sinusoidal AC currents shifted in time by one third of the period, and the DC winding is fed with a steady DC current. This design layout of the flux pump exciter is equivalent to the stator winding system of a conventional linear induction motor, with the difference of the presence of the DC winding needed to create the B_{ACmax} field component. A 3D layout of the designed magnetic circuit is shown in Figure 79. A 1 mm air-gap is placed between the upper (comb-shaped) part of the magnetic circuit and the lower yoke for allowing the insertion of the HTS tape. The details of the air-gap and the HTS tape are shown in Figure 80. The main specifications of the linear flux pump are listed in Table 14.
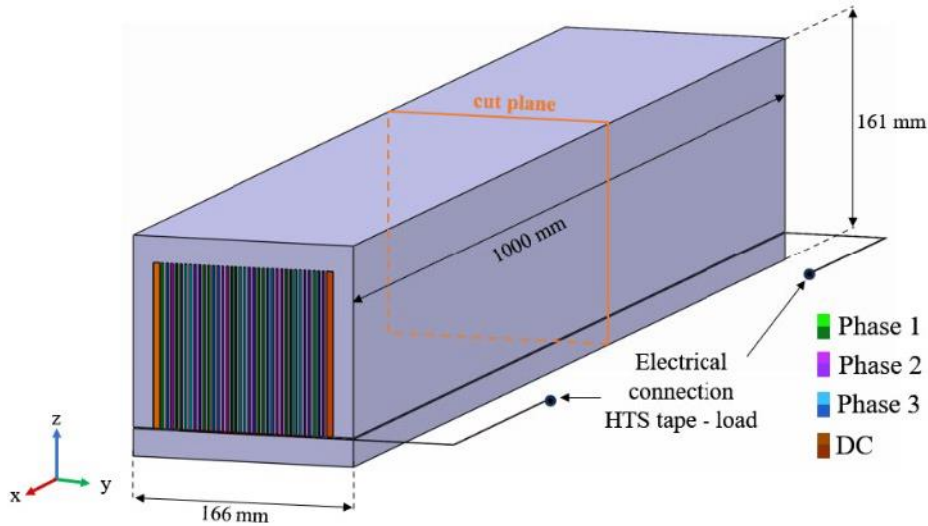
Figure 79 3D layout of the linear flux pump. The drawing is not to scale.

It is assumed that all the three AC windings and the DC winding are realized by means of a round wire with 1 mm2 cross section and consist of 300 turns each.
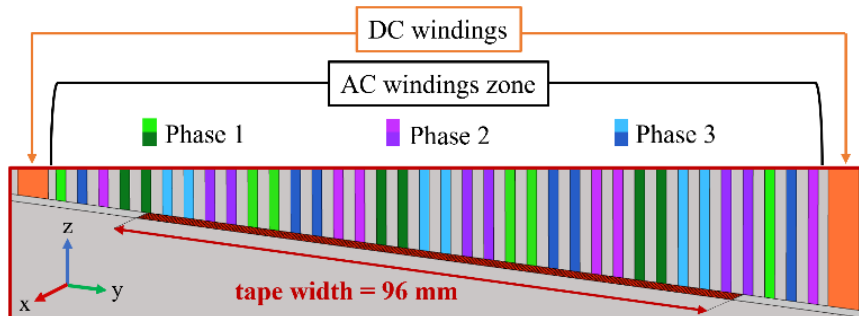
Figure 80 Particular of the yz cut plane of Figure 79, taken at the mid-section along the x direction of the flux pump. The plot shows HTS tape located in the air-gap and the details of the copper winding above it.

the evaluation of quantities $\bar{\bar{M}}$, $\vec{B}^{ext}$, and $\vec{A}^{ext}$ were obtained by 3D simulations of the magnetostatics of the linear flux pump in COMSOL Multiphysics®, under the assumption of linear behavior for the ferromagnetic core (μ_R = 4000). Separate simulations were carried out to find the coefficients of matrix $\bar{\bar{M}}$, and of vectors $\vec{B}^{ext}$ and $\vec{A}^{ext}$ respectively. In particular, the entries of the matrix $\bar{\bar{M}}$ were obtained by supplying individual filaments (i.e. the 222 elements of the discretization of the HTS

tape) with a unit current and by taking the line integral of the calculated magnetic potential $\vec{A}^J$ along the filaments' length. Similarly, entries of vectors $\vec{B}^{ext}$ and $\vec{A}^{ext}$ were obtained by individually exciting the AC and the DC coils with unit currents. Clearly, $\vec{B}^{ext}$ and $\vec{A}^{ext}$ are vectors of length 222, and $\overline{\overline{M}}$ is a 222 × 222 dense matrix.

Table 14 Linear flux pump specifications

Total active length	1000 mm
Total height	161 mm
Total width	166 mm
Air-gap	1 mm
AC pole pairs	3
Slots per pole per AC phase	2
AC windings current density peak	7 A/mm²
DC windings current density	7.5 A/mm²
Operating temperature	70 K
Estimated total copper weight	91.4 Kg
Estimated total iron weight	144.8 Kg

The waveform of the resulting magnetic field produced by the designed exciter, at a specific instant, at the mid-line of the HTS tape is shown in Figure 81.b. The target field that was from the GA optimizer during the first design step is also shown in the figure. Although it can be observed that the field inevitably comprises unwanted harmonics due to the presence of winding slots, the good match with B$_{ideal}$ validates the exciter design. $\vec{B}^{ext}$ at any time step is used to derive $J_c(\vec{B}^{ext}, T)$ that goes into Eq. (23), while $\partial \vec{A}^{ext} / \partial t$ determines the values of vector $\bar{u}$ for Eq. (28).
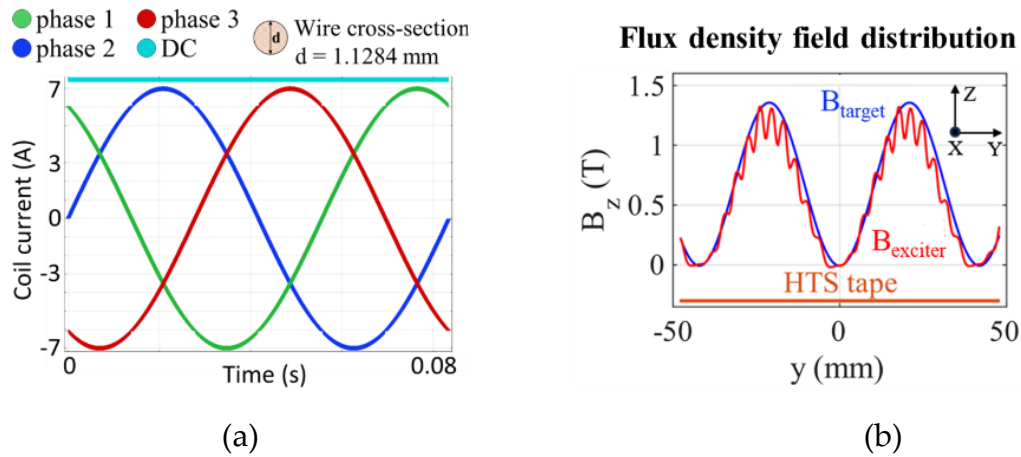
Figure 81 (a) current of the AC and DC windings and (b) the excitation field generated by the exciter (Breal) compared with the target magnetic field. The orange line represents the length of 96 mm the HTS tape on which the field translates.

After the solving system of equations (Eq. (28) combined with the condition $I= \sum \bar{I}_w$) is obtained, the performance of the designed flux pump can be evaluated. Figure 82.a shows the average DC voltage V produced at the terminals as a function of the DC current I delivered to a load. The typical quasi-linear V-I characteristic, with an open circuit voltage VOC of 154 mV and a maximum current capability Imax of 2296 A, compliant with designing requirements, can be observed. Figure 82.b and Figure 82.d show output power delivered at the load and efficiency. The latter is defined and calculated as the ratio between the output power and the sum of the output and the power loss occurring in the tape, that is the total power transferred into the tape by the traveling magnetic field. The peak of output power and efficiency occur around 1200 A. In this condition, the power delivered to the load is about 100 W with a maximum efficiency of about 7.35%. A significant open circuit loss (P_0) of 1200 W can be seen in Figure 82.c.
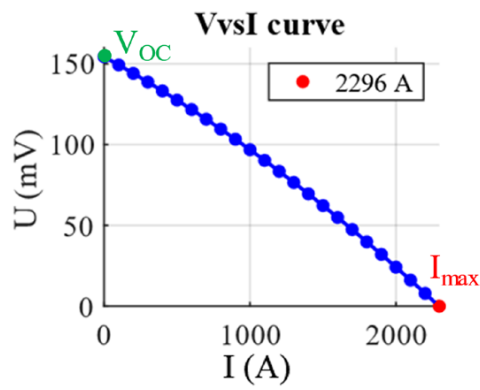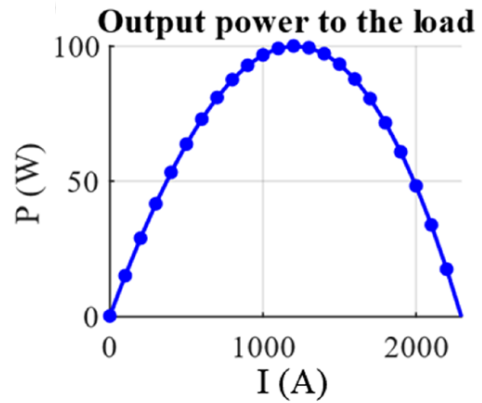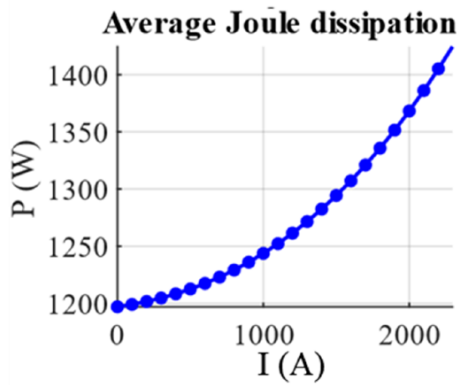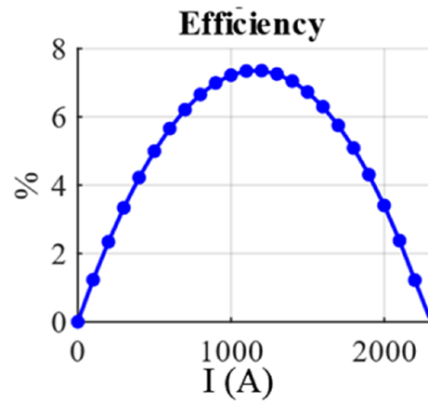
Figure 82 Linear flux pump electrical characterization: a) V-I curve, b) Output power vs transport current, c) Losses vs transport current, d) Efficiency vs transport current.

3.3.2. Linear flux pump modularity exploitation for the energization of the DTT TF coil

The performance of the designed flux pump in the previous section fits the current requirements of 2000 A that was addressed. However, since the best efficiency is observed around 1200 A, for supplying the target current of 2000 A it is chosen to employ two flux pump modules in parallel, each of them delivering 1000 A and operating close to optimal efficiency conditions. The equivalent circuit of two flux pumps modules in parallel supplying the DTT TF coil, is shown in Figure 83. The

lumped parameters $R_{TF\ module}$ = 100 nΩ and $L_{TF\ module}$ = 48 mH of the DTT TF coil module are estimated based on [192] and taken from [188] respectively, whereas R_{eff} (67.1 μΩ) and R_0 (19.8 μΩ) are evaluated as explained in section 2.1.5. It is emphasized that the $R_{TF\ module}$ incorporates the resistance of the joints linking the flux pump to the coil. This joint resistance is the sole obstacle to overcome when maintaining current, aligning with a similar assumption made in a prior case study [3]. Additional support for this estimation comes from a recent investigation involving a linear flux pump, consisting of only 4×12mm tapes in parallel, where the joints between the flux pump and the load displayed a resistance on the order of tens of nano Ohms [106]. As will become clearer later, the $R_{TF\ module}$ holds paramount importance and significantly influences the performance of the flux pump, especially during steady state. While its value has been estimated based on literature references for this study, it is underscored that a precise evaluation will be essential for future studies aiming at experimental implementations. The equivalent circuit of Figure 83 is valid during the on-state of the flux pump, whilst the equivalent circuit simply consists of a short circuit during the off-state. On-state and off-state are defined as in section 3.2.2. The circuit of Figure 83 is controlled by implementing a hysteresis control (like for the HTS dynamo of section 3.2.2) on the linear flux pump, switching it on and off to maintain the current I oscillate around the target value of 2000 A with a ±0.1% ripple. The use of the on-state and off-state equivalent circuits to dynamically control the flux pump is justified by its negligible inductive effect, which was previously discussed in chapter 2.
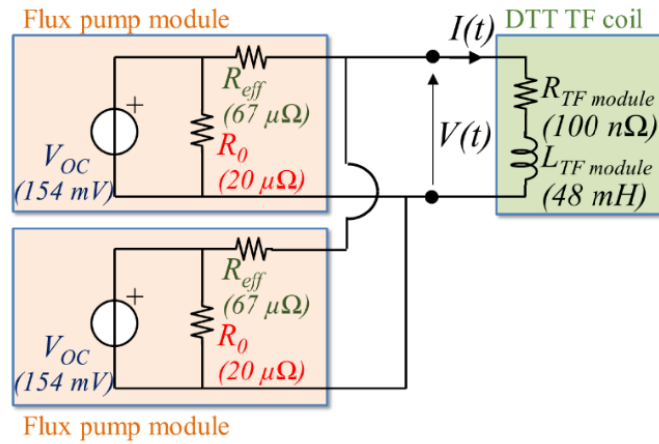
Figure 83 Equivalent circuit of the DTT TF coil supplied by two linear flux pumps modules in parallel.

The current of the TF coil module during energization and during sustainment at the target value of 2000 A ±0.1% is shown in Figure 84. It is obtained that, after a charging transient of 819.4 s during which the flux pump constantly operates in the on-state, the hysteresis control switches the flux pumps into the off-state, as the current *I* of the coil has reached 2000 A + 0.1%. During the off-state the flux pump behaves like a short circuit. Hence a slow decay of the coil current is due to the internal resistance of the coil, with a time constant $\tau_{\text{off-state}} = L_{TF\ module} / R_{TF\ module} = 4.8 \times 10^5$ s. Due to this decay the current reached the lower threshold of 2000 A − 0.1% after 960 s. Then, the flux pump is reactivated until the current is raised back to the upper threshold of after 2000 A + 0.1%, taking 2.2 s. This alternative on-off operation of the flux pump, with a resulting cycle time of 962.2 s (16 minutes) and a resulting duty cycle of 0.23 %, is permanently continued in order to maintain the coil's current within the target range of 2000 A ±0.1%.
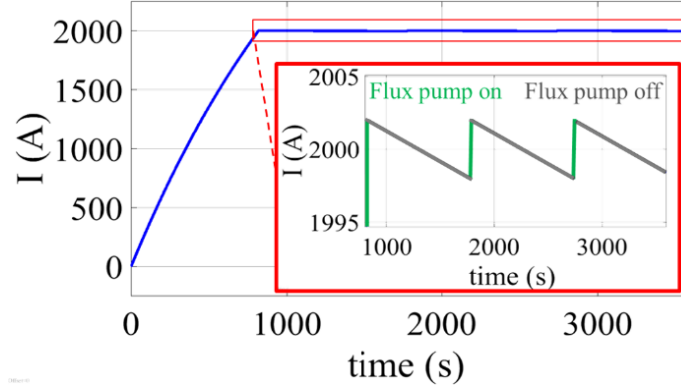
Figure 84 Simulation of the current transient and maintenance of a DTT TF coil using two designed linear flux pumps in parallel.

In order to be more general, this analysis is carried out for number N of flux pump modules in parallel ranging from 1 to 4, though it is already anticipated that for the considered case $N = 2$ (that is, two models in parallel as shown in Figure 83) gives the better energy performance during current sustainment. When N modules in parallel are considered the equivalent circuit of the flux pump system is the one of Figure 85, where V_{OC}, R_{eff}, and R_0 refer to the equivalent circuit of one single flux pump module.
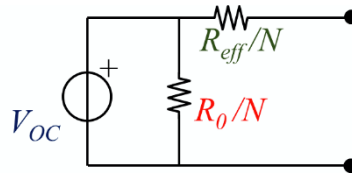
Figure 85 . Equivalent circuit of N identical flux pump modules in parallel.

The current $I(t)$ of the coil supplied by N flux pumps in parallel during the charging transient is given in Eq (63):

$$I(t,N) = \frac{V_{OC}}{R_{TF\,module} + \dfrac{R_{eff}}{N}}\left(1 - e^{-\frac{t}{\tau(N)}}\right) \tag{63}$$

with the time constant given in Eq. (64).

$$\tau(N) = \frac{L_{TF\ module}}{R_{TF\ module} + \dfrac{R_{eff}}{N}} \qquad (64)$$

It can be observed from the previous two equations that the higher the number of modules in parallel, the shorter the time constant of the circuit, due to the fact that the equivalent series effective resistance R_{eff} scales with $1/N$. Thus, for a given final current, a higher N leads to a faster charging transient. In Figure 86, the charging transients of the DTT TF coil for N values of 1, 2, 3, and 4 are shown. The corresponding energization times are 1471, 819, 737, and 704 seconds, respectively. The overall energy loss during the energization of the coil increases with higher N. This is due to the fact that the largest part of the loss of the flux pump is due to its intrinsic behavior and occurs also in open circuit condition. Hence adding modules in parallel means adding resistance. Regarding equivalent circuits, this concept can be grasped by recognizing that, for N modules in parallel, the resistance to be connected in parallel to the voltage source scales with $1/N$ (see Figure 85). This results in intrinsic power loss that linearly increases with N. The shorter charging time is not good enough to compensate the higher loss rate that is produced, resulting in increased energy loss at the end of the ramp up. The energy dissipated by every contributor (R_{eff}/N, R_0/N, and $R_{TF\ module}$) during the transient, for the cases of N equal to 1, 2, 3, and 4, is shown in Figure 86 as well. It is confirmed that the loss contribution due to R_0/N is largely dominant, as it is one order of magnitude larger than the one due to R_{eff}/N, and even four orders of magnitude higher than the one due to $R_{TF\ module}$. Because of the R_0/N dissipation dominancy, using more flux pumps in parallel is counterproductive in terms of charging dissipation, even if it is beneficial in terms of charging duration.

Beside the charging of the SC coil up to the nominal current, with a typical time in the order of tens of minutes or hours at the most, flux pumps must sustain the high current of the coil during their entire service life, which is in the order of tens of years. During the sustainment phase, the power delivered to the coil is needed to compensate the losses occurring in the internal resistance (due to joints) only and is much lower

than the one needed during the energy generation phase where the magnetic energy store must be set up. Therefore, careful analysis of the energy performance of the flux pump during the sustainment phase must be carried out in order to choose the optimal number N of modules in parallel.
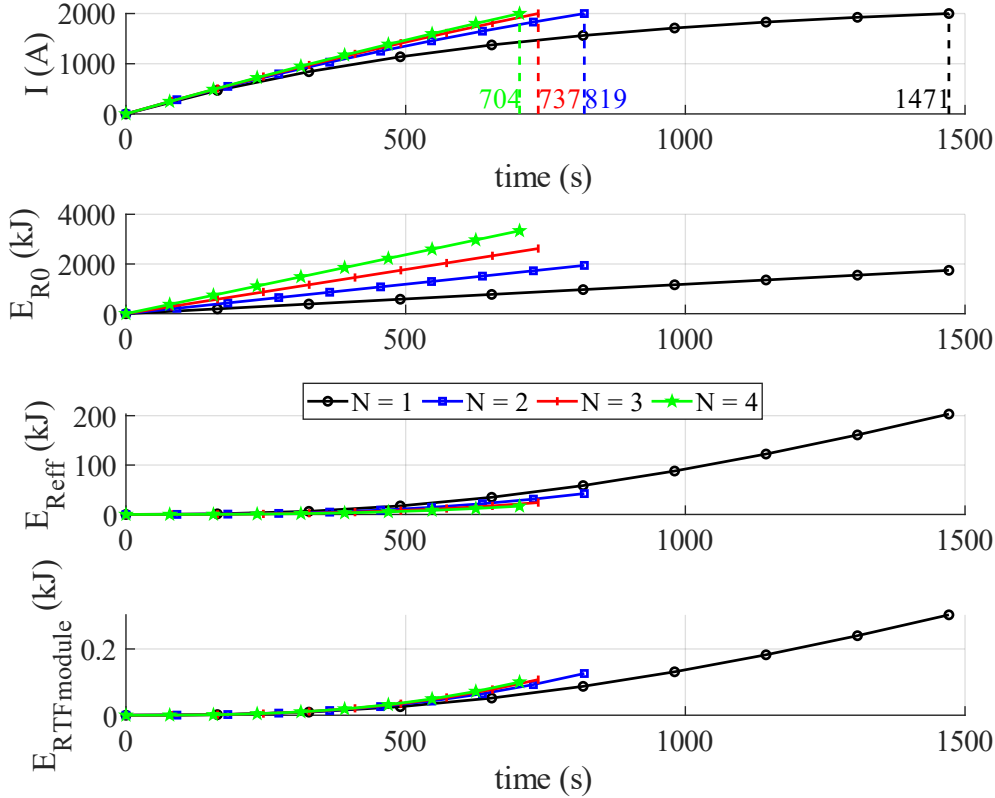
Figure 86 Impact of the number of flux pump modules in parallel (N) on the charging transient and on all loss contributions.

The flux pump is constantly operating in the on state during the ramp-up, however, during sustainment it alternatively operates in on and off state at practically constant current I with a given duty cycle δ. This duty cycle can be calculated by imposing that the increase of current during the on-state (green segments of Figure 84) of the cycle is equal to the decrease of current during the following off-state (grey segments of Figure 84).

$$\frac{V_{OC-}\left(\frac{R_{eff}}{N} + R_{TF\ module}\right) I}{L_{TF\ module}} T_{ON} = \frac{R_{TF\ module}\ I}{L_{TF\ module}}\left(T_{cycle} - T_{ON}\right) \qquad (65)$$

from which the following duty cycle δ is obtained.

$$\delta = \frac{\Delta t_{on-state}}{\Delta t_{off-state}} = \frac{R_{TF\ module}\ I}{V_{OC-}\dfrac{R_{eff}}{N}\ I} \qquad (66)$$

The duty cycle depends on the N number of modules. On one hand the higher N the shorter the on-state, which is the only dissipative phase of the cycle. On the other hand, however, as the value of N increases, so does the dissipation during the on phase (due to the lower value of the equivalent parallel resistance). The average power dissipated in the flux pump in one cycle is given by Eq. (67) and is shown in Figure 87 as a function of N. It can be seen that the minimum average loss is reached for $N =$ 2. This is consistent with the result of Figure 82.c, since when $N = 2$ is chosen each of the flux pump modules operate with a current of 1000 A that is close to one allowing the maximum efficiency. As a general rule, the number of modules in parallel must be chosen so that the individual flux pump modules operate as close as possible to the maximum efficiency current.

$$P_{loss}^{tot}(N) = \delta(N)\left[\left(\frac{R_{eff}}{N}\right) I^2 + \frac{V_{OC}^{\ 2}}{\left(\frac{R_0}{N}\right)}\right] \qquad (67)$$

The energy performances of the flux pump are summarized in Table 15. It is evident from the table that, when projected into the whole lifespan of the system, the contribution to energy loss of the energization phase is negligible and energy optimization of the flux pump should be made with reference to the sustainment phase.
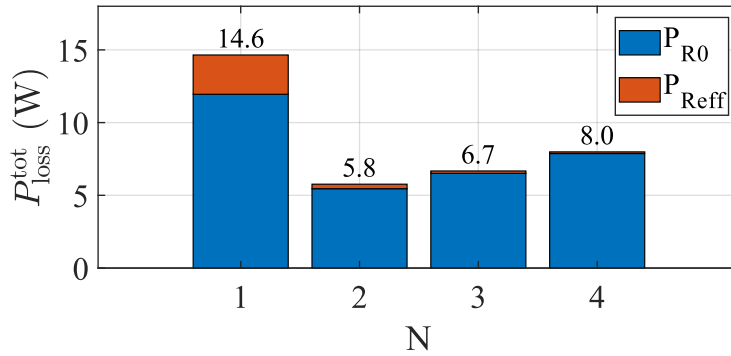
Figure 87 Impact of the number of flux pump modules in parallel (N) on the flux pump average total loss at steady state.

Table 15 Loss of the 2 flux pumps modules for the DTT TF coil ramp-up and flat top

	Energization to 2 kA	Sustainment at 2 kA
Duration, s	819.4	Life service
Energy loss, kJ	0.54 kWh	---
Average power, W	---	5.8 W
Energy loss for 30 years life service	---	1.52

The addition of flux pump modules in parallel entails an increase in volume and mass of the power supply system. As far as this study is concerned, this does not imply any critical issue. In fact, it is repeated that one flux pump module is estimated to weigh less than 250 kg, with a volume of approximately 0.03 m³. For reference, it is reminded that the conventional power supplies of the DTT TF coils occupy a 182 m² room and the copper busbars connecting them to the magnets weigh 150 tons, with a volume of 16.5 m³. To put this in perspective, it would take 600 modules to match the weight of the copper busbars alone. However, for future studies regarding different applications where weight and volume are critical factors, it is acknowledged that these specifications should be considered as design constraints.

From an energetic standpoint, it is also interesting to estimate the total dissipation if the rated current of the DTT TF coil was obtained with a supply system composed by flux pump modules like the one that has been design in this study. To

match the current capability of the conventional power supply, 44 linear flux pumps modules would be needed (considering that each one would transport 1 kA). Using Eq. (66) and (67) to calculate the average dissipation of 44 linear flux pump modules to maintain 42.5 kA in the DTT TF coil at current maintenance, and assuming a COP of 22 W/W (300K-70K) for the cryocooler [176], gives an estimation of 2.8 kilowatts of room temperature average electric power consumption. This would represent a massive energy saving for the Frascati Coil Cold Test facility (FCCTF) with respect to conventional systems, as it was explained in section 3.3 that they would entail hundreds of kilowatts of permanent losses. In fact, considering that the conventional power supply will dissipates around 245 kilowatts [188], and the two RT to LN_2 current leads will contribute for 75 kilowatts at room temperature (the copper busbars mentioned in section 3.3 are not present in the FCCTF), all operated continuously, this would translate into a consumption of 86 kWh of energy within 16 minutes. In that same timeframe and for the same purpose, 44 linear flux pump modules would only consume about 0.75 kWh of electric energy, which is less than 0.9 %.

However, if the same comparison analysis is carried out for the case related to the energization of the entire DTT TF system (18 coils), the result is rather surprising and disappointing. The energy consumption of the conventional system is first calculated during a linear ramp-up lasting 2000 seconds, following the methodology described in [188].

$$I(t) = \alpha \times t$$
$$\alpha = \frac{I_{rated}}{t_{ramp-up}} = \frac{42500\ A}{2000\ s} = 21.25\ A/s \tag{68}$$

Considering a heat load of 45 W/kA per current lead, a COP of 20 (300K-70K), and 6 current leads in total (see Figure 78), the current leads energy consumption at room temperature during the whole ramp-up is calculated using Eq. (69).

$$E_{CL}^{ramp-up} = \int_0^{2000} 6 \times 0.045 \times 20 \times I(t)dt = \frac{6 \times 20 \times 0.045 \times 42500^2}{2 \times \alpha} \quad (69)$$

Which gives 63.75 kWh. After having estimated the average resistance of the 6 copper busbars equal to 29.6 $\mu\Omega$, based on the information of the following report [190], the corresponding energy consumption during the ramp-up is calculated as follows:

$$E_{busbars}^{ramp-up} = \int_0^{2000} 6 \times R_{busbars} \times I(t)^2 dt = \frac{6 \times R_{busbars} \times 42500^3}{3 \times \alpha} \quad (70)$$

Which gives 53.34 kWh. To calculate the energy consumption during the ramp-up of the power supply, the energy balance is used considering $E_{CL}^{ramp-up}$, $E_{busbars}^{ramp-up}$, and the total stored energy in the TF coils E_{coils}^{stored}, at rated current (see Table 12). An efficiency (η_{PS}) of 95 % is considered based on thyristor AC/DC converters references [193].

$$E_{PS}^{ramp-up} = \frac{(1 - \eta_{PS})}{\eta_{PS}} \times \left(E_{CL}^{ramp-up} + E_{busbars}^{ramp-up} + E_{coils}^{stored} \right) \quad (71)$$

Which gives 35.72 kWh. Finally, it is found that 158.8 kWh of energy is consumed to perform the ramp-up in 2000 seconds for the case of the conventional power supply systems. Subsequently, based on the data already reported in section 3.3, a total of 795 kW is continuously consumed to maintain the rated current in the TF coils.

Now, the same quantities (energy consumption for ramp-up and power consumption at current maintenance) are calculated if 44 linear flux pumps modules are used in parallel. The energy spent to compensate the losses of the 44 flux pumps during ramp-up ($E_{FP}^{ramp-up}$) is calculated as described hereafter. First, Eq. (63) and (64) are used to find τ and the duration of the ramp-up (t_{end}) by imposing $N = 44$ and replacing $L_{TF\,module}$ with L_{TF} (2 H, as reported in Table 12) and $R_{TF\,module}$ with R_{TF} (1.8 $\mu\Omega$,

as assumed in previous studies [3] for analogue tokamaks). Next, the following integral is calculated:

$$E_{FP}^{ramp-up} = COP(70K) \times \int_0^{t_{end}} \frac{V_{OC}^2}{\frac{R_0}{N}} + \frac{R_{eff}}{N} I^2(t, N) \, dt \qquad (72)$$

Which gives 491.5 kWh. Where in this case the COP is 22 and $I(t, N)$ is found with Eq. (63). It is evident that a power supply based on 44 linear flux pumps is way more energy intensive than the traditional supply system for energizing the TF coils during charging. This is actually not a surprise, as it is acknowledged that open circuit losses of flux pumps are significant. To calculate the average dissipation during current maintenance with the flux pumps (operating them with an analogue hysteresis control as earlier), Eq. (66) is first used to find δ (0.857), and then Eq. (67) is multiplied by the COP at 70 K. Surprisingly, the calculations give that the average energy consumption of the flux pumps in this phase is over 1 MW, hence more than what is consumed with the traditional systems. A visual representation to depict the results of this analysis is provided in Figure 88, which shows the energy consumption (in MWh per day) of the two considered supply solutions.
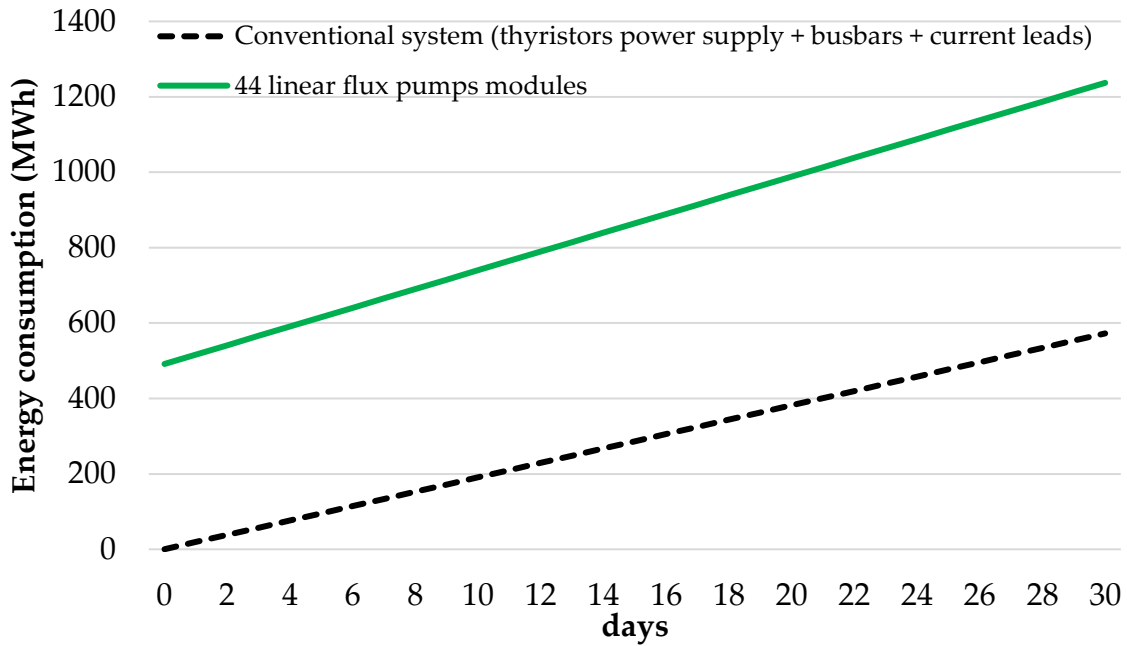
Figure 88 Energy consumption comparison for the supply of the DTT TF coils.

Not only the energy spent to reach 42.5 kA in the DTT TF coils is significant if 44 linear flux pumps are used in parallel, but the average consumption at current maintenance overcomes the one of the traditional solutions too (of about 30 %), which is apparently in contrast with the previous promising results referred to the supply of one single DTT TF coil in the FCCTF, for which the flux pumps solutions was the clear winner. However, a careful analysis of the previous results reveals a drastic increase in the duty cycle in the case of the energization of the entire DTT magnetic system (0.857 versus 0.0023 in the case of a single TF coil). This increase reflects the fact that the flux pumps must operate in the on-state for much longer, hence the high losses. The reason for the unfavorable results of the flux pumps, therefore, must be identified in the increase in the duty cycle. Based on Eq. (66), it can be deduced that the latter has increased due to the increase in the total resistance of the magnet and its operating current. Indeed, these two quantities have a crucial impact on the performance of a flux pump dedicated to the energization of a superconducting magnetic load, which can arrive at hindering this technology potential.

Despite the long-standing promise of flux pumps in revolutionizing the supply system of high current DC magnets, this critical issue has gone undetected because of the lack of the technology validation in relevant environments and the laboratory scale of the superconducting magnets on which they have been tested. This crucial aspect is investigated in a comprehensive analysis described in the next section of this thesis to unravel, once for all, the true potential of flux pumps.

3.3.3. On the role of the load resistance and rated current on the flux pump impact

The power flow scheme of a system comprising a superconducting coil (L_{coil}) energized by a flux pump coupled to its dedicated cryocooler is depicted in Figure 89. The general scheme in this figure assumes that the flux pump and the coil operate inside the same cryogenic environment and at the same temperature. If that was not the case, the temperature gradient should be addressed with current leads connecting the flux pump to the load, but this would not affect the scope of the following analysis. Moreover, the power contributions that are indicated in Figure 89 should be intended as the average powers relative to one cycle of the system operation after the rated current is reached (if the flux pump is managed through an hysteresis control like in section 3.2.2 and 3.3.2, the period over which the average powers are calculated is the one of the control).
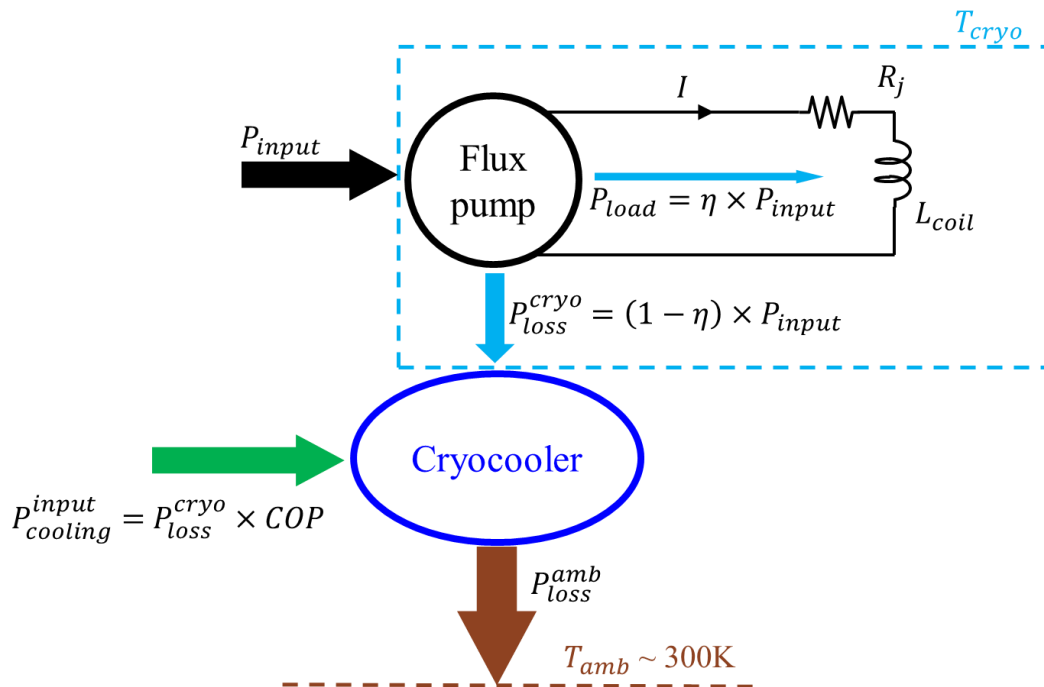

Figure 89 Power flow of a flux pump energizing a superconducting coil.

Over one period of operation, the sole energy contribution that the flux pump must deliver is related to the losses of the total resistance of the load (R_j) which can be

attributed to its joints (since the current in the coil is oscillating around the rated value, no net magnetic energy is passed to the coil by the flux pump or vice versa). This energy can only be a portion of the total input power to the flux pump because of its efficiency (η). The difference between the input power to the flux pump and the power delivered to the load coil is dissipated in losses that the dedicated cryocooler must work hard to remove. The electric power that the cryocooler needs for this purpose ($P_{cooling}^{input}$) is in turn dependent on the COP. Given the prerequisite that the flux pump can energize the load coil up to its rated current (I_{rated}), the remaining concern is that $P_{cooling}^{input}$ is minimized. $P_{cooling}^{input}$ determines the slope of the green line of Figure 88 and is the quantity that is compared to the total losses of the conventional power supply solutions when the energetic conveniency of the flux pump is explored. $P_{cooling}^{input}$ can be expresses as a function of the power that is delivered to the load as in Eq. (73).

$$P_{cooling}^{input}(R_j, I_{rated}) = COP \frac{(1-\eta)}{\eta} R_j (I_{rated})^2 \qquad (73)$$

The electric power required to remove the corresponding losses for a specific flux pump with a given efficiency and operating temperature (COP) is linearly dependent on the total resistance of the load coil and scales with the square of its rated current. Since the resistance and the rated current are, respectively, a specification and a requirement of the load, they should be addressed during the designing process of a flux pump so that its efficiency and operating temperature (hence the COP of the corresponding cryocooler) result in a value of $P_{cooling}^{input}$ lower that the total losses of the conventional power supply that would be used instead. The latter condition should be integrated as a constrained in the designing procedure previously described in the flowchart of section 3.1, step D.

Naming $P_{benchmark}$ the total losses of the conventional power supply, the efficiency of the flux pump should be compliant with Eq. (74) to be energetically convenient.

$$\eta > \frac{1}{\dfrac{P_{benchmark}}{COP\ R_j(I_{rated})^2} + 1} \qquad (\,74\,)$$

Eq. (74) explains why the 44 linear flux pumps in parallel designed in section 3.3.2 underperformed the conventional supply system of the DTT TF coils. In fact, it can be calculated that those flux pumps should have worked with an efficiency of at least 8.25 %, whereas they could achieve 7.35 % at most (see Figure 82). For real applications, Eq. (74) should incorporate a safety margin coefficient that accounts for several factors, such as the fact that the efficiency of a flux pump depends on its operating current, therefore it would be challenging to operate it at the very maximum efficiency point. Plotting $P_{cooling}^{input}$ from Eq. (73) as a function of the efficiency (imposing L_{coil} = 2 H and R_j = 1.8 μΩ as for the case of the DTT TF coils) and superimposing it with the line corresponding to the total dissipation of the DTT TF coils conventional power supply system (approximately 795 kW, as previously mentioned in section 3.3.2) gives the plot of Figure 90.
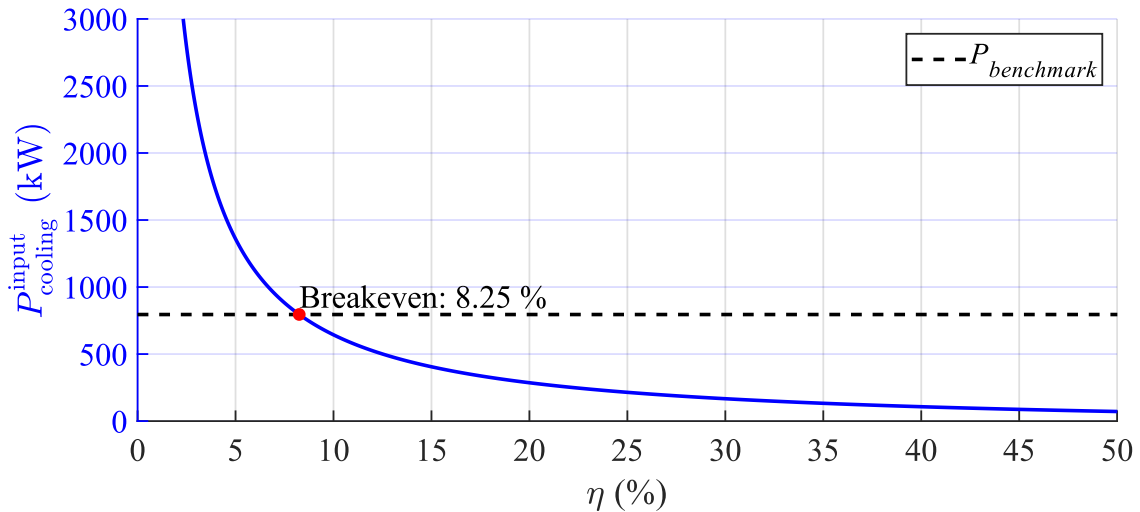
Figure 90 $P_{cooling}^{input}$ vs η for a flux pump energizing the 18 DTT TF coils. The red breakeven point marks the value of minimum efficiency of the flux pump to be energetically superior with respect of the conventional power supplies. COP = 22.

Obviously, the $P_{cooling}^{input}(\eta)$ is a vertically translated equilateral hyperbola whose slope increases as η decreases. Engineeringly speaking, this is advantageous because it entails that at low efficiencies, typical of travelling field flux pumps, minor improvements in efficiency result in significant reductions of loss during operation and increase of overall energy performance.

The impact of I_{rated} and R_j one the $P_{cooling}^{input}(\eta)$ is shown in Figure 91.a and Figure 91.b, respectively.
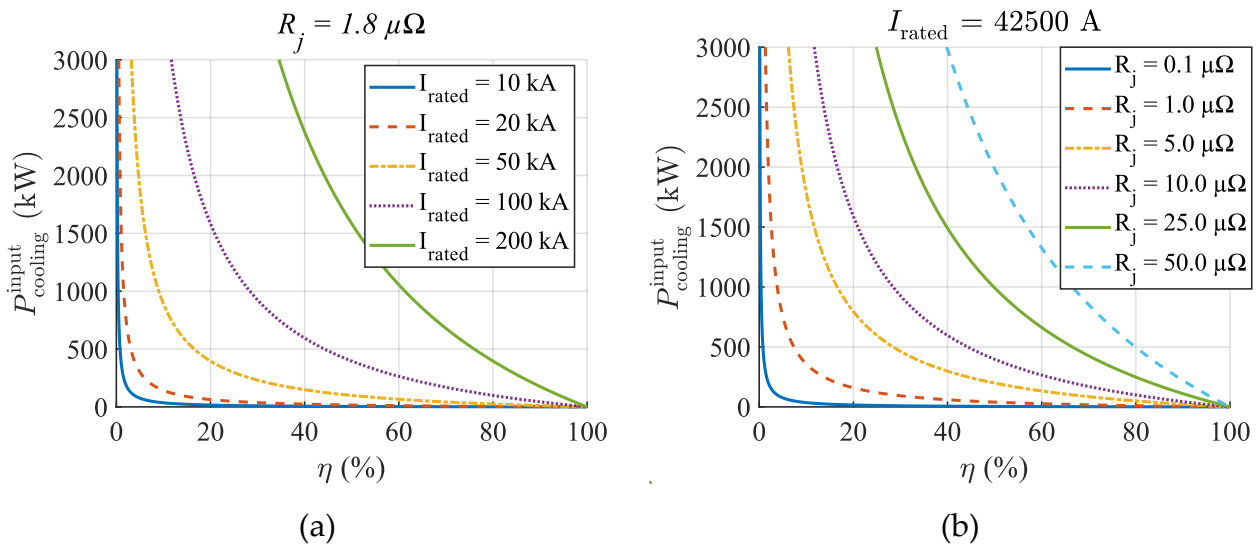
Figure 91 $P_{cooling}^{input}(\eta)$ curves for varying (a) I_{rated} and (b) Rj. COP = 22.

The impact of both the operating current of a superconducting magnet and its total resistance on the $P_{cooling}^{input}(\eta)$ is so significant that these quantities cannot be ignored when studying the feasibility of employing a flux pump as the power supply. While reducing the rated current of a magnet would seem counterproductive, as it would correspond to limiting the inherent advantages of HTS coils, it is reasonable to concentrate efforts in manufacturing low resistance joints for reducing R_j. It is noted that a reduction of R_j does not imply any advantage in terms of losses for the conventional power supply solutions, as their dissipation scales only with the current. Current progress in this sense seems to be favoring flux pumps [194].

If the negative outcome observed for the designed linear flux pump in comparison to the conventional system in section 3.3.2 may appear to question the feasibility of the technology, I personally believe that the findings presented in this section prove the contrary. If the design process of the linear flux pump of section 3.3.1 had incorporated the considerations that have been described above in the form of the constraint of Eq. (74), the result of the comparison could have been different. Besides, it is reminded that the minimum efficiency for the flux pump to be energetically convenient should have been 8.25 %, which can be reasonably considered achievable. Despite the fact that the efficiency is largely overlooked for linear type flux pumps, and it might turn out that this is an intrinsic weakness of the topology, it is demonstrated that HTS dynamos could overcome 15 % instead [87]. Parametrical studies have also investigated ways to increase the efficiency of travelling field flux pump. For example, Figure 28 from [87] shows that the slow velocities of the travelling field (frequency of rotation of the rotor for the case of [87]) boost the efficiency, even though this decreases the output voltage and, therefore, the output power. However, there are other factors that have positive impact on both the efficiency and the output voltage. That is the case of the airgap for HTS dynamos, as described in [165] and whose results are reported here in Figure 92.
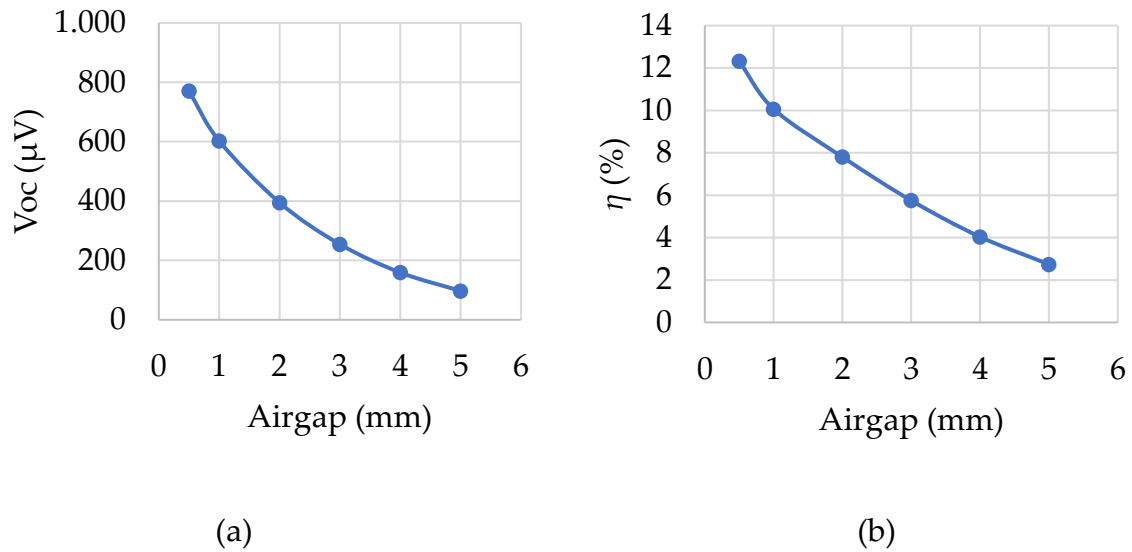
Figure 92 Impact of the airgap of a HTS dynamo on (a) the open circuit output voltage and (b) the efficiency. [165]

Actually, the impact of the airgap on the performance of a HTS dynamo should be no surprise because reducing the distance between the permanent magnets and the HTS tape has the sole effect of increasing the magnetic field acting on it, and the way this impacts the functioning of travelling field flux pumps was already widely described in section 1.4.1. This is a perfect opportunity to reiterate a fundamental aspect that was repeated frequently right in section 1.4.1: under the condition of a travelling field of such waveform that triggers a synchronous variations of local electromotive forces and resistivity as in Figure 21, the higher the applied field, the larger the critical current density suppression, the higher the local resistivity and the better flux pumping performance.

To my view, if there is one plot that demonstrates the potential of flux pumps for the energization of superconducting magnets, that plot is exactly the one of Figure 90, which shows that HTS flux pumps of efficiency above just 10-15 % would have a disruptive impact in the supply systems for fusion magnets. In this sense, it is worth remembering that it was just 1993 that a flux pump of the transformer rectifier type reached 98 % efficiency during current maintenance [30]. As described in section 1.3.2, the flux pump of [30] is made of LTS superconductors, which facilitates the switching

operation. Nonetheless, [30] is an irrefutable proof that the viability of 1 Ω open-state class, with a fast dynamic (< 1 s) to change state, superconducting switches is the ultimate enabler of high efficiency flux pumps. Paradoxically, being LTS is also a great disadvantage for the transformer rectifier of [30], because working at 4.2 K entails that the corresponding cryocooler will work with a COP as high as 7000 W/Wcold [176]. Under these circumstances, the $P_{cooling}^{input}(\eta)$ curve of Figure 90 is readapted in Figure 93, where the Y-axis is set to a logarithmic scale due to the extremely high values that emerged from the calculations. In this case, the breakeven efficiency has raised up to 96.62 %.

The bottom line is that if HTS switches of the same class and performance of the ones of [30] were viable, a transformer rectifier based on them could overcome the breakeven efficiency by a great margin, as well as exhibit output voltage in the range of 1 V [30]. Based on the latest progress in the field [51], this seems to be happening as I am writing these words.
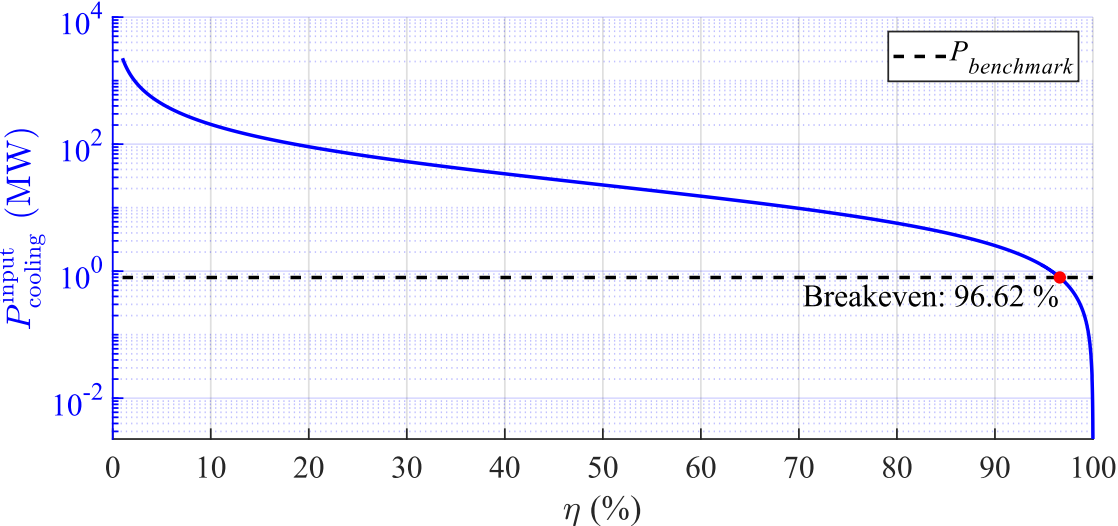

Figure 93 $P_{cooling}^{input}$ vs η for the case of a flux pump energizing the 18 DTT TF coils while working at 4.2 K (COP = 7000). The red breakeven point marks the value of minimum efficiency of the flux pump to be energetically superior with respect of the conventional power supplies.

The majority of the novel work conducted during this Ph.D. project has focused on traveling field flux pumps, namely the HTS dynamo and linear type, due to the significant scientific research gap that was present surrounding these devices. Their physical mechanism was a subject of ongoing debate until a few years ago, and previous studies, both experimental and numerical, to explore their operation were primarily empirical and lacked generalizability. On the other hand, the operating mechanism of the transformer rectifier is relatively straightforward, and it was widely acknowledged that its development was heavily dependent on the progress on superconducting switches. To my view, the findings of this project reveal that, in terms of efficiency, the transformer rectifiers that utilize high-resistance open-state superconducting switches hold an inherent advantage with respect to traveling field flux pumps. However, it is worth pointing out that HTS dynamos and linear flux pumps comprise a limited number of components with respect to transformer rectifiers (in particular, they lack the need of the transformer), therefore they could be preferable for applications that prioritize mass and volume over efficiency. Evidently, the definitive choice of which flux pump topology is most suitable for a given application is an engineering challenge that needs to be resolved case by case, because it is intrinsically tied to the unique demands and specifications of the considered application in terms of rated current, inductance, required ramp rate, total resistance, and possibly other specifications.

Progress in flux pump development is ongoing, and the prospect of efficient and high-current HTS transformer rectifier becoming a reality is promising. However, the feasibility of implementing these advancements in practical applications will ultimately depend on a critical engineering aspect that remains to be addressed, that is its integration with the fast discharge units of the quench protection system for the superconducting magnet. Excluding a few exceptional cases, a superconducting magnet is usually connected in series with a switch that is in turn connected in parallel to the dump resistor. This system is called fast discharge unit. During normal operation, the switch is closed and carries the same current of the magnet, but when

179

the protection system detects a quench, the switch opens and the magnet's current is redirected to the dump resistor on which its energy is dissipated following a discharge transient. Inevitably, the switch of the fast discharge unit has a non-negligible resistance that is in series with the one of the joints and therefore will contribute to increase R_j in Figure 89. If the quench protection system incorporates multiple fast discharge units and/or if their switches exhibit significant resistance, the analysis outlined in this section indicates that a power supply relying on a flux pump may not be feasible, as achieving the required efficiency would be impractical.

Future studies following this Ph.D. project will be focused on the investigation of the integration of flux pumps with the fast discharge units of superconducting magnets, as well as on the improvement of their efficiency and the identification of the most suitable topology based on the addressed application.

Other technological advancements regarding the quench protection that could avoid resistive fast discharge unit switches, hence facilitating the penetration of flux pumps as power supplies for superconducting magnets, will be explored. It should be mentioned, in fact, that innovative protection solutions are being developed in this sense, such as discharge units that employ superconducting switches with negligible resistance during normal operation [195] [196] [197] and varistor insulation for non insulated or partially insulated coils that act as a distributed quench heater [198].

4.Conclusions

This Ph.D. project has been dedicated to the numerical modelling, investigation, and engineering analysis of flux pumps. This research has been driven by the potentially disruptive impact that flux pumps can have in enabling contactless and efficient energization of superconducting magnets, as well as by the scientific research gaps that have been surrounding the technology for a long time. After the technology was reviewed and the main characteristics of each topology were summarized in chapter 1, a FEM model based on the volume integral equation (VIE) method has been developed and validated against experimental results to unravel the intricacies related to the voltage rectification that characterizes travelling field flux pumps. The results of this modeling action, presented in chapter 2, describe the behavior of the traveling field flux pumps. The findings illustrate that, under specific conditions, these devices operate in the generation mode, displaying both current and output voltage located in the first quadrant when staying within two operational limits: the open circuit output voltage and the generator current limit. Of utmost importance is the energetic balance calculation that yields the complete equivalent circuit of Figure 46.b. Previous studies relied of the equivalent circuit of Figure 46.a which does not account for the largest dissipation contribution, the open circuit losses. This complete equivalent circuit is a useful tool for fast system oriented analysis of the flux pump, as shown in chapter 3. Chapter 2 also presents a novel approach to address the relationship between the critical current and the n-value of HTS tapes concerning temperature and magnetic field, utilizing artificial intelligence methods. This methodology enabled an exploration of the influence of operating temperature and allowed an assessment of the performance of various commercial HTS tapes in the context of traveling field flux pumping.

Then, the numerical model is exploited to develop an application oriented optimal design procedure of travelling field flux pumps, presented in chapter 3. This

designing procedure is tested to design, and later characterize, a HTS dynamo for energizing the field windings of the EcoSwing wind turbine, and a linear flux pump for serving the toroidal field magnets of the Divertor Tokamak Test. The integration of the designed flux pumps with the load for which they are produced is analyzed as well, finding that, in terms of total losses, the performance of the flux pumps is highly dependent on the rated current and its total resistance. The influence of these two load parameters on the viability of flux pumps is discussed in section 3.3.3, where it is described that the expected difference in efficiency between the three topologies plays a crucial role for real applications.

By combining the development of new tools, such as the complete equivalent circuit and the application-oriented designing procedure, with novel findings, like the crucial impact of the load characteristics on the flux pump integration, this Ph.D. project has made an attempt at overcoming the empirical approach with which flux pumps have been addressed for decades and applied a structured engineering method to facilitate its implementation in real applications. Future works will be dedicated to the investigation of the integration of flux pumps with the fast discharge units of superconducting magnets.

Hopefully, this work can pave the way toward the validation of flux pumps in relevant environments.

Per aspera sic itur ad astra.

Grazie nonno

References

[1]   Sung, H. J. et al "Design and Heat Load Analysis of a 12 MW HTS Wind Power Generator Module Employing a Brushless HTS Exciter," in IEEE Trans. Appl. Supercond, 2016, 26, no. 4, pp. 1-4, 5205404.

[2]   Tuvdensuren, O., et al. Structural design and heat load analysis of a flux pump-based HTS module coil for a large-scale wind power generator. In: Journal of Physics: Conference Series. IOP Publishing, 2018. 1054, p. 012084.

[3]   Rice, J. H. P. et al., "Design of a 60 kA Flux Pump for Fusion Toroidal Field Coils," in IEEE Trans. Appl. Supercond, 2022, 32, no. 4. 1-5 5500205..

[4]   Wang, X. et al An HTS NI Magnet Charged by Multiple Flux Pumps: Construction and Test of the Prototype. IEEE Trans. Appl. Supercond., 2020, 30, no 4, pp. 1-5.

[5]   Wei, J. et al. Improving the central magnetic field of an HTS magnet using multiple flux pumps. IEEE Trans. Appl. Supercond., 2022, 32(6), pp. 1-5.

[6]   Öztürk, Y. et al. Current Status in Building a Compact and Mobile HTS MRI Instrument. IEEE Trans. Appl. Supercond., 2021, 31, no. 5, pp. 1-5.

[7]   Collier-Wright, Marcus, et al. "High-temperature superconductor-based power and propulsion system architectures as enablers for high power missions." Acta Astronautica 201 (2022): 198-208.

[8]   Mendelssohn, K. Production of High Magnetic Fields at Low Temperatures. Nature 132, 602 (1933). https://doi.org/10.1038/132602a0.

[9]   Felici, N. J. C. R. Acad. Sci., Paris 206, 242, 599 (1938).

[10]   Felici, N. J. Ann. Phys., Paris 13, 266 (1940).

[11]   Van Suchtelen, J., J. Volger, and D. Van Houwelingen. "The principle and performance of a superconducting dynamo." Cryogenics 5.5 (1965): 256-266.

[12]   L. J. M. v. d. Klundert e H. H. J. ten Kate, Fully superconducting rectifiers and flux pumps part 1: Realized methods for flux pumping, Cryogenics, vol. 21, n. 4, pp. 195-206, 1981..

[13]   L.J.M. van de Klundert and H.H.J. ten Kate, On fully superconducting rectifiers and fluxpumps. A review. Part 2: Commutation modes, characteristics and switches, Cryogenics, vol. 21, Issue 5, pp. 267-277, 1981.

[14]   Ten Kate, H. HJ. "Superconducting rectifiers." (1984).

[15]   J. Van Nugteren, "High temperature superconductor accelerator magnets", Ph.D. dissertation, Twente.

[16]   Geng, J.; Matsuda, K.; Fu, L.; Shen, B.; Zhang, X.; Coombs, T. Operational research on a high-Tc rectifier-type superconducting flux pump. Supercond. Sci. Technol. 2016, 29, 035015.

[17]   Geng, J.; Coombs, T. Mechanism of a high-Tc superconducting flux pump: Using alternating magnetic field to trigger flux flow. Appl. Phys. Lett. 2015, 107, 142601.

[18]   Geng, J.; Painter, T.; Long, P.; Gawith, J.; Yang, J.; Ma, J.; Dong, Q.; Shen, B.; Li, C.; Coombs, T. A kilo-ampere level HTS flux pump. Supercond. Sci. Technol. 2019, 32, 074004.

[19]   Zhang, H.; Geng, J.; Coombs, T. Magnetizing high-Tc superconducting coated conductor stacks using a transformer–rectifier flux pumping method. Supercond. Sci. Technol. 2018, 31, 105007.

[20]   Gawith, J. D. D., et al. "A half-bridge HTS transformer–rectifier flux pump with two AC field-controlled switches." Superconductor Science and Technology 31.8 (2018): 085002.

[21]   Rice, James HP, et al. "A full-wave HTS flux pump using a feedback control system." Superconductivity 8 (2023): 100064.

[22]   Leuw, Bradley, et al. "A half-wave superconducting transformer-rectifier flux pump using Jc(B) switches." Superconductor Science and Technology 35.3 (2022): 035009.

[23]   Clarke, Jordan, et al. "Temperature Dependent Performance of a Conduction-Cooled J c (B) Transformer-Rectifier Flux Pump." IEEE Transactions on Applied Superconductivity 33.5 (2023): 1-6.

[24] Geng, Jianzhao, Rodney A. Badcock, and Chris W. Bumby. "A wireless rectifier for inductively energizing high direct-current high-temperature superconducting magnets." IEEE Transactions on Industrial Electronics 68.4 (2020): 3273-3281.

[25] Homer, G., Houzego, P., Scott, C., & Wilson, M. (1975). A thermally switched flux pump. IEEE Transactions on Magnetics, 11(2), 576-579.

[26] Oomen, Marijn P., et al. "HTS flux pump for cryogen-free HTS magnets." IEEE transactions on applied superconductivity 15.2 (2005): 1465-1468.

[27] S. Jeong, H. Lee, and Y. Iwasa, "Superconducting flux pump for hightemperaturesuperconductor insert coils of NMR magnets," AIP Conf. Proc.613, 441 (2002).

[28] D. Park, et al "HTS shim coils energized by a flux pump for the MIT 1.3-GHz LTS/HTS NMR magnet: Design, construction, and results of a proof-of-concept prototype," IEEE Trans. Appl. Supercond. 28(3), 4301105 (2018).

[29] G. B. J. Mulder, H. H. J. ten Kate, H. J. G. Krooshoop, and L. J. M. van de Klundert, "Development of a thermally switched superconducting rectifier for 100 kA," IEEE Trans. Magn. 27(2), 2333–2336 (1991).

[30] O. A. Shevchenko, H. H. J. ten Kate, H. J. G. Krooshoop, N. V. Markovsky, and G. B. J. Mulder, "Development of a 50–60Hz thermally switched superconducting rectifier," IEEE Trans. Appl. Supercond. 3(1), 590 (1993).

[31] Laquer, H. L., K. J. Carroll, and E. F. Hammel. "An automatic superconducting flux pump." (1966): 539-544.

[32] Y. Deng et al., "Performance Optimization and Verification of the Transformer-Rectifier Flux Pump for HTS Magnet Charging," in IEEE Transactions on Applied Superconductivity, vol. 30, no. 4, pp. 1-5, June 2020, Art no. 4603105, doi: 10.1109/TASC.2020.2990.

[33] Zhou, P.; Ma, G.; Deng, Y.; Nie, X.; Zhai, Y.; Liu, K.; Zhang, H.; Li, Y. A contactless self-regulating HTS flux pump. IEEE Trans. Appl. Supercond. 2020, 30, 3603006.

[34] Geng, J.; Bumby, C.W.; Badcock, R.A. Maximising the current output from a self-switching kA-class rectifier flux pump. Supercond. Sci. Technol. 2020, 33, 045005.

[35] Zhai, Y.; Zhou, P.; Li, J.; Sun, C.; Li, Y.; Xiao, L.; Deng, Y.; Ma, G. Performance Investigation of Contactless Self-Regulating HTS Flux Pump. IEEE Trans. Appl. Supercond. 2021, 31, 4603105.

[36] Mallett, B. P. P., et al. "Effective circuit modelling and experimental realization of an ultra-compact self-rectifier flux pump." Superconductor Science and Technology 36.6 (2023): 065005.

[37] Zhai, Yao, et al. "Modeling and characteristics investigation of self-regulating HTS flux pump." Cryogenics 124 (2022): 103486.

[38] Morandi, Antonio. "HTS dc transmission and distribution: concepts, applications and benefits." Superconductor Science and Technology 28.12 (2015): 123001.

[39] Oomen, M.; Rieger, J.; Leghissa, M.; ten Haken, B.; ten Kate, H.H. Dynamic resistance in a slab-like superconductor with Jc (B) dependence. Supercond. Sci. Technol. 1999, 12, 382.

[40] Ogasawara, T., et al. "Effective resistance of current-carrying superconducting wire in oscillating magnetic fields 1: Single core composite conductor." Cryogenics 16.1 (1976): 33-38.

[41] Zhang, H.; Hao, C.; Xin, Y.; Mueller, M. Demarcation currents and corner field for dynamic resistance of HTS-coated conductors. IEEE Trans. Appl. Supercond. 2020, 30, 6601305.

[42] Li, Chao, et al. "Impacts of the saturated transformer on the HTS flux pump." IEEE Transactions on Applied Superconductivity 31.8 (2021): 1-4.

[43] Kim, Y. B., C. F. Hempstead, and A. R. Strnad. "Critical persistent currents in hard superconductors." Physical Review Letters 9.7 (1962): 306.

[44] Anderson, Philip W., and Y. B. Kim. "Hard superconductivity: theory of the motion of Abrikosov flux lines." Reviews of modern physics 36.1 (1964): 39.

[45] Shah, A., et al. "A Novel Switch Design for Compact HTS Flux Pump." IEEE Transactions on Applied Superconductivity 32.6 (2022): 1-5.

[46] Li, Chao, et al. "Persistent current switch for HTS superconducting magnets: Design, control strategy, and test results." IEEE Transactions on Applied Superconductivity 29.2 (2018): 1-4.

[47] Geng, J., et al. "HTS persistent current switch controlled by AC magnetic field." IEEE Transactions on Applied Superconductivity 26.3 (2016): 1-4.

[48] Gawith, J. D. D., et al. "An HTS power switch using YBCO thin film controlled by AC magnetic field." Superconductor Science and Technology 32.9 (2019): 095007.

[49] Li, Chao, et al. "Design for a persistent current switch controlled by alternating current magnetic field." IEEE Transactions on Applied Superconductivity 28.4 (2018): 1-5.

[50] Mulder, G. B. J., et al. "Thermally and magnetically controlled superconducting rectifiers." IEEE transactions on magnetics 25.2 (1989): 1819-1822.

[51] Bykovskiy, Nikolay, Alexey Dudarev, and Herman Ten Kate. "Thermally activated ReBCO switches for charging high-current magnets." IEEE transactions on applied superconductivity 29.5 (2019): 1-5.

[52] Weiss, Jeremy D., et al. "Introduction of CORC® wires: highly flexible, round high-temperature superconducting wires for magnet and power transmission applications." Superconductor science and technology 30.1 (2016): 014002.

[53] Jurčo, Róbert, et al. "MOSFET-based HTS flux pump." Superconductor Science and Technology 36.11 (2023): 115025.

[54] JG, BEDNORZ. "Possible highT_c super-conductivity in the Ba-La-Cu-O system." Z Physik B 64 (1986): 189-193.

[55] Marchand, J.F., Volger, J. Radiation induced transport of magnetic flux along a superconducting sheet, Phys Lett 2 (1962) 118.

[56] Volger, J., Admiraal, P.S. A dynamo for generating a persistent persistent current in a superconducting circuit Phys Lett 2 (1962) 257.

[57] van Beelen, H., Arnold, AJ.P.T., de Bruyn Ouboter, R., Beenakker, J.J.M., Taconis, K.W. A flux pump for the generation of high persistent currents in a superconducting foil magnet, Phys Lett 4 (1963) 310.

[58] Volger, J. A superconducting homopolar dynamo for the production of large persistent currents and the problem of energizing a coil, Philips Technicla Rev 24 (1963) 399.

[59] van Houwelingen, D., Admiraal, P.S., van Suchtelen, J. A superconducting de dynamo driven by a rotary magnetic field Phys Lett 8 (1964) 310.

[60] Blaisse, B.S., Kiekert, O., Bots, GJ.C., Sipman, L.A. A small size superconducting dynamo powered by ac current, Phys Lett 14 (1965) 5.

[61] van Beelen, H., van Braam Houchgeest, J.P., de Bruyn Outober, R., Taeonis, K.W. Remarks on a moving-flux experiment in superconducting sheets, Physica 36 (1967) 107.

[62] Atherton, D,L High efficiency superconducting homopolar dc generators, JApplPhys 39 (1968) 2639.

[63] Mawardi, O.K., Muelder, S.A., Micbelotli, R.A. Brushless superconducting alternators, IEEE MAG--13 (1977) 780.

[64] Arsala, N.K., Louzada, E.G., van Beelen, H. The penetration of a local magnetic field through large sheets of type-1 superconductors, Physica 9313 (1978) 75.

[65] Hoag, E.D. Superconductive device, US patent 3,292,021 (1966).

[66] Volger, J. Device for producing a current, US patent 3,336,489 (1967).

[67] Atherton, D.L. Method and means for obtaining high magnetic fields, US patent 3,336,509 (1967).

[68] Pearl, J. Motors and generators employing superconductors, US patent 3,402,307 (1968).

[69] Eder, F.X., Voigt, H. Superconductive generators, US 3,478,232 (1969).

[70] Voigt, IL Superconducting generator, US patent 3,519,892 (1970).

[71] McFarlane, I.D. Superconducting dynamoelectric machine, US patent 3,560,773 (1971).

[72] Kawabe, U. Flux pump, US patent 3,602,854 (1971).

[73] Bergmann, W.IL Method and means for charging or discharging superconducting windings, US patent 3,667,029 (1972).

[74] Rabinowitz, M., Rodenbaugh, IJ.~Superconducting hybrid magnetic flux pump, US patent 4,096,403 (1978).

[75] Wipf, S.L A 50 kA flux pump for the superconducting transmission line test bed, Los Alamos Sd Lab., Informal Report LA-6953-MS (1974, revised 1978).

[76] Hoffmann, C.; Pooke, D.; Caplin, A.D. Flux Pump for HTS Magnets. IEEE Trans. Appl. Supercond. 2011, 21, 1628–1631.

[77] Hoffmann, C., et al. "Design parameters for an HTS flux pump." Physics Procedia 36 (2012): 1324-1329.

[78] Bumby, C.W.; Pantoja, A.E.; Sung, H.J.; Jiang, Z.; Kulkarni, R.; Badcock, R.A. Through-Wall Excitation of a Magnet Coil by an External-Rotor HTS Flux Pump. IEEE Trans. Appl. Supercond. 2016, 26, 0500505. 10.1109/TASC.2016.2526605.

[79] Mataira, R.; Ainslie, M.; Pantoja, A.; Badcock, R.; Bumby, C. Mechanism of the high-Tc superconducting dynamo: Models and experiment. Phys. Rev. Appl. 2020, 14, 024012. https://doi.org/10.1103/PhysRevApplied.14.024012.

[80] Jiang, Zhenan, et al. "Dynamic resistance of a high-Tc superconducting flux pump." Applied Physics Letters 105.11 (2014).

[81] Ma, J., Geng, J., Gawith, J., Zhang, H., Li, C., Shen, B., ... and Coombs, T. A. Rotating permanent magnets based flux pump for HTS no-insulation coil. IEEE Trans. Appl. Supercond., 2019, 29(5), 1-6. 10.1109/TASC.2019.2901915.

[82] Pantoja, A.E.; Storey, J.G.; Badcock, R.A.; Jiang, Z.; Phang, S.; Bumby, C.W. Output during continuous frequency ramping of adynamo-type HTS flux pump. IEEE Trans. Appl. Supercond. 2018, 28, 5202205.

[83] Jiang, Zhenan, et al. "A novel rotating HTS flux pump incorporating a ferromagnetic circuit." IEEE Transactions on Applied Superconductivity 26.2 (2016): 84-89.

[84] Bumby, Chris W., et al. "Through-wall excitation of a magnet coil by an external-rotor HTS flux pump." IEEE Transactions on Applied Superconductivity 26.4 (2016): 1-5.

[85] Bumby, Chris W., et al. "Development of a brushless HTS exciter for a 10 kW HTS synchronous generator." Superconductor Science and Technology 29.2 (2016): 024008.

[86] Hamilton, K., Pantoja, A. E., Storey, J. G., Jiang, Z., Badcock, R. A., and Bumby, C. W. Design and performance of a "squirrel-cage" dynamo-type HTS flux pump. IEEE Trans. Appl. Supercond, 2018, 28(4), 1-5. 10.1109/TASC.2018.2805161.

[87] Hamilton, K., Mataira, R., Geng, J., Bumby, C., Carnegie, D., and Badcock, R. Practical estimation of HTS dynamo losses. IEEE Trans. Appl. Supercond, 2020, 30(4), 1-5. 10.1109/TASC.2020.2980830.

[88] K. Hamilton, A. E. Pantoja, J. G. Storey, Z. Jiang, R. A. Badcock and C. W. Bumby, "Asynchronous Magnet–Stator Topologies in a Squirrel-Cage Superconducting Dynamo," in IEEE Transactions on Applied Superconductivity, vol. 29, no. 5, pp. 1-5, Aug. 2019.

[89] Geng, J., et al. "Voltage-ampere characteristics of YBCO coated conductor under inhomogeneous oscillating magnetic field." Applied Physics Letters 108.26 (2016).

[90] Bumby, C. W., et al. "Anomalous open-circuit voltage from a high-Tc superconducting dynamo." Applied Physics Letters 108.12 (2016).

[91] G. P. Mikitk and E. H. Brandt, "Generation of a DC voltage by an AC magnetic field in type-II superconductors," Phys. Rev. B 64, 092502 (2001).

[92] Wang, Wei, and Tim Coombs. "Macroscopic magnetic coupling effect: The physical origination of a high-temperature superconducting flux pump." Physical Review Applied 9.4 (2018): 044022.

[93] Geng, Jianzhao, et al. "Origin of dc voltage in type II superconducting flux pumps: field, field rate of change, and current density dependence of resistivity." Journal of Physics D: Applied Physics 49.11 (2016): 11LT01.

[94] Mataira, R. C., et al. "Origin of the DC output voltage from a high-Tc superconducting dynamo." Applied Physics Letters 114.16 (2019).

[95] Brandt E H 1996 Superconductors of finite thickness in a perpendicular magnetic field: strips and slabs Phys. Rev. B 54 4246.

[96] Brandt E H 1998 Superconductor disks and cylinders in axial magnetic field: I. Flux penetration and magnetization curves Phys. Rev. B 58 6506.

[97] N Bykovskiy et al 2023 Supercond. Sci. Technol. 36 034002.

[98] Millman, Jacob (1940). "A Useful Network Theorem". Proceedings of the IRE. 28 (9): 413–417.

[99] C. W. Bumby et al., "Frequency Dependent Behavior of a Dynamo-Type HTS Flux Pump," in IEEE Transactions on Applied Superconductivity, vol. 27, no. 4, pp. 1-5, June 2017, Art no. 5200705, doi: 10.1109/TASC.2016.2643498.

[100] A. E. Pantoja, Z. Jiang, R. A. Badcock and C. W. Bumby, "Impact of Stator Wire Width on Output of a Dynamo-Type HTS Flux Pump," in IEEE Transactions on Applied Superconductivity, vol. 26, no. 8, pp. 1-8, Dec. 2016, Art no. 4805208, doi: 10.1109/TASC.2016.

[101] Jiang, Z.; Bumby, C.W.; Badcock, R.A.; Sung, H.J.; Long, N.J.; Amemiya, N. Impact of flux gap upon dynamic resistance of a rotating HTS flux pump. Supercond. Sci. Technol. 2015, 28, 115008.

[102] P. Zhou et al., "Impact of Magnet Number on the DC Output of a Dynamo-Type HTS Flux Pump," in IEEE Transactions on Applied Superconductivity, vol. 33, no. 8, pp. 1-9, Nov. 2023, Art no. 4603509, doi: 10.1109/TASC.2023.3299601.

[103] R. A. Badcock et al., "Impact of magnet geometry on output of a dynamo-type HTS flux pump", IEEE Trans. Appl. Supercond., vol. 27, no. 4, Jun. 2017.

[104] Chung, Yoondo, et al. "Performances of a linear type magnetic flux pump for compensating a little decremented persistent current of HTS magnets." IEEE transactions on applied superconductivity 14.2 (2004): 1723-1726.

[105] Bai, Zhiming, et al. "Effect of various pulse wave forms for pulse-type magnetic flux pump." Cryogenics 51.9 (2011): 530-533.

[106] Fu, Lin, et al. "A flux pumping method applied to the magnetization of YBCO superconducting coils: frequency, amplitude and waveform characteristics." Superconductor Science and Technology 29.4 (2016): 04LT01.

[107] Fu, Lin, et al. "Linear flux pump device applied to high temperature superconducting (HTS) magnets." IEEE Transactions on Applied Superconductivity 25.3 (2015): 1-4.

[108] W. Wang, et al "Charging 2G HTS Double Pancake Coils With a Wireless Superconducting DC P ower Supply for Persistent Current Operation," in IEEE Transactions on Applied Superconductivity, vol. 28, no. 3, pp. 1-4, Apr. 2018, Art no. 0600804.

[109] Zhang, Yuntian, et al. "Compact linear-motor type flux pumps with different wavelengths for high-temperature superconducting magnets." IEEE Transactions on Applied Superconductivity 30.4 (2020): 1-5.

[110] Ye, Hanxin, et al. "A linear-motor type HTS flux pump with pumped current exceeding 640 A." IEEE Transactions on Applied Superconductivity 31.8 (2021): 1-5.

[111] Fu, Lin, et al. "HTS flux pump charging an HTS coil: Experiment and modeling." IEEE Transactions on Applied Superconductivity 31.8 (2021): 1-5.

[112] Ye, Hanxin, et al. "Measuring the output voltage of a linear-motor type flux pump with an insulated HTS coil." IEEE Transactions on Applied Superconductivity 30.4 (2020): 1-5.

[113] J. Wei et al., "Build Charging Database of Linear-Motor Type Flux Pump and Analyze the Influence of DC-Bias Field Using Fixed Step Size Search Algorithm," IEEE Trans. Appl. Supercond., vol. 31, no. 8, pp. 1-5, Nov. 2021, Art no. 0500305.

[114] Xu, Hang, et al. "Control the output of an HTS dynamo with a DC background field." IEEE Transactions on Applied Superconductivity 32.6 (2022): 1-5.

[115] Wang, Wei, et al. "A kilo-amp linear-motor type flux pump." IEEE Transactions on Applied Superconductivity 32.6 (2022): 1-5.

[116] Kulkarni, Ravichandra, Krishnamachar Prasad, and Tek Tjing Lie. "Flux pump for HTS rotating machinery applications." 2015 IEEE Eindhoven PowerTech (2015): 1-5.

[117] Coombs, Timothy Arthur, et al. "An overview of flux pumps for HTS coils." IEEE Transactions on Applied Superconductivity 27.4 (2016): 1-6.

[118] Coombs, T. A. "Superconducting flux pumps." Journal of Applied Physics 125.23 (2019).

[119] Zhai, Yujia, et al. "Research progress of contactless magnetization technology: HTS flux pumps." IEEE Transactions on Applied Superconductivity 30.4 (2020): 1-5.

[120] Wen, Zezhao, Hongye Zhang, and Markus Mueller. "High temperature superconducting flux pumps for contactless energization." Crystals 12.6 (2022): 766.

[121] Wang, Wei, et al. "Review of high temperature superconducting flux pumps." Superconductivity (2022): 100022.

[122] Ainslie, M., Queval, L., Mataira, R., Badcock, R., and Bumby, C. Modelling an HTS dynamo using a segregated finite-element model. 2019 https://core.ac.uk/download/pdf/237398489.pdf.

[123] Prigozhin, L.; Sokolovsky, V. Two-dimensional model of a high-Tc superconducting dynamo. IEEE Trans. Appl. Supercond. 2021, 31, 5201107.

[124] Prigozhin, L.; Sokolovsky, V. Fast solution of the superconducting dynamo benchmark problem. Supercond. Sci. Technol. 2021, 34, 065006.

[125] Campbell, A. M. A finite element calculation of flux pumping. Supercond. Sci. Technol., 2017, 30(12), 125015.

[126] Ainslie, M. D. "Numerical modelling of high-temperature superconducting dynamos: a review." Superconductivity, 2022, 100033. https://doi.org/10.1016/j.supcon.2022.100033.

[127] Ainslie, M. D., Quéval, L., Mataira, R. C., and Bumby, C. W. Modelling the frequency dependence of the open-circuit voltage of a high-T c superconducting dynamo. IEEE Trans. Appl. Supercond, 2021, 31(5), 1-7.

[128] Mataira, R., Ainslie, M. D., Badcock, R., and Bumby, C. W. Modeling of Stator Versus Magnet Width Effects in High-Tc Su-perconducting Dynamos. IEEE Trans. Appl. Supercond, 2020 30(4), 1-6.

[129] Geng, Jianzhao, and Timothy Arthur Coombs. "Modeling methodology for a HTS flux pump using a 2D H-formulation." Superconductor Science and Technology 31.12 (2018): 125015.

[130] Wen, Z., Zhang, H., and Mueller, M. Sensitivity analysis and machine learning modelling for the output characteristics of rotary HTS flux pumps. Supercond. Sci. Technol, 2021, 34(12), 125019.

[131] Zhou, Pengbo, et al. "Characterization of flux pump-charging of high-temperature superconducting coils using coupled numerical models." Superconductor Science and Technology 36.11 (2023): 115002.

[132] Ainslie, Mark, et al. "A new benchmark problem for electromagnetic modelling of superconductors: The high-T c superconducting dynamo." Superconductor Science and Technology 33.10 (2020): 105009.

[133] Ghabeli, Asef, et al. "Modeling the charging process of a coil by an HTS dynamo-type flux pump." Superconductor Science and Technology 34.8 (2021): 084002.

[134] A. Morandi e M. Fabbri, «A unified approach to the power law and the critical state modeling of superconductors in 2D», 2015, Superconductor Science and Technology, Volume 28, Number 2, 024004.

[135] John David Jackson, Classical Electrodynamics, 3rd Edition, Jhon Wiley & sons, August 1998, pp 208-212.

[136] Jiang, Z., Bumby, C.W., Badcock, R.A., ...Sung, H.J., Park, M., A rotating flux pump employing a magnetic circuit and a stabilized coated conductor HTS stator Journal of Magnetics, 2016, 21(2), pp. 239–243.

[137] Gömöry, F., et al. "Phenomenological description of flux pinning in non-uniform high-temperature superconductors in magnetic fields lower than the self-field." Superconductor Science and Technology 20.9 (2007): S271.

[138] Majoros, M., B. A. Glowacki, and A. M. Campbell. "Critical current anisotropy in Ag/(Pb, Bi) 2Sr2Ca2Cu3O10+ x multifilamentary tapes: influence of self-magnetic field." Superconductor Science and Technology 14.6 (2001): 353.

[139] Pardo, E., et al. "Low-magnetic-field dependence and anisotropy of the critical current density in coated conductors." Superconductor Science and Technology 24.6 (2011): 065007.

[140] Zermeño, Víctor MR, et al. "A parameter-free method to extract the superconductor's Jc (B, θ) field-dependence from in-field current–voltage characteristics of high temperature superconductor tapes" Superconductor Science and Technology 30.3 (2017):034001.

[141] Viljamaa J. et al 2011 Comparison of Different Critical Current Density Models for Undoped Monofilamentary Ti-Sheathed MgB2 Tapes. Journal of Superconductivity and Novel Magnetism. 24. 287-297. 10.1007/s10948-010-1021-4.

[142] «CA19108 - High-Temperature SuperConductivity for AcceLerating the Energy Transition,» COST, European cooperation in science & technology, [Online]. Available: https://www.cost.eu/actions/CA19108/.

[143] Robinson Research Institute," [Online]. Available: http://htsdb.wimbush.eu/.

[144] Wimbush S. C. and Strickland N. M. 2017 "A Public Database of High-Temperature Superconductor Critical Current Data," IEEE Transactions on Applied Superconductivity, vol. 27, no. 4.

[145] Yazdani-Asrami, Mohammad, et al. "Advanced experimental-based data-driven model for the electromechanical behavior of twisted YBCO tapes considering thermomagnetic constraints." Superconductor Science and Technology 35.5 (2022): 054004.

[146] "sklearn.model_selection.GridSearchCV," [Online]. Available: https://scikit-learn.org/stable/modules/generated/sklearn.model_selection.GridSearchCV.html.

[147] McCulloch W. S. and Pitts W. 1943 "A logical calculus of the ideas immanent in nervous activity," Bull. Math. Biol., vol. 5, pp. 115–133.

[148] Abiodun O. I. et al 2018 "State-of-the-art in artificial neural network applications: A survey" Heliyon, vol. 4, no. 11, p. e00938.

[149] Graupe D. 2013 Principles of artificial neural networks. World Scientific Publishing.

[150] Krogh A. 2008 "What are artificial neural networks?," Nat. Biotechnol., vol. 26, no. 2, pp. 195–197.

[151] "github," [Online]. Available: https://github.com/dmlc/xgboost.

[152] Chen T. and Guestrin C. 2016. XGBoost: A Scalable Tree Boosting System. Association for Computing Machinery, New York, NY, USA, 785–794. DOI:https://doi.org/10.1145/2939672.2939785.

[153] Murphy, K. P. 2012 "Machine Learning: A Probabilistic Perspective" - chapter 14.4.3, pp. 492-493, The MIT Press.

[154] Hofmann M. 2006 "Support vector machines-kernels and the kernel trick." Notes 26.3: 1-16.

[155] Pedregosa et al. 2011 JMLR 12, pp. 2825-2830.

[156] Cortes C. et al 2012 "L2 regularization for learning kernels." arXiv preprint arXiv:1205.2653.

[157] "sklearn.gaussian_process.kernels.RationalQuadratic," [Online]. Available: https://scikit-learn.org/stable/modules/generated/sklearn.gaussian_process.kernels.RationalQuadratic.html.

[158] Duvenaud D. 2014. "The Kernel Cookbook: Advice on Covariance functions" URL https://www. cs. toronto. edu/duvenaud/cookbook.

[159] Vovk V. 2013 "Kernel ridge regression." Empirical inference: 105-116.

[160] Zhao Z.-W. et al 2020 "Effect of Increasing the Descriptor Set on Machine Learning Prediction of Small Molecule-Based Organic Solar Cells," Chemistry of Materials, vol. 32, no. 18, pp. 7777-7787.

[161] Ghabeli, A.; Pardo, E.; Kapolka, M. 3D modeling of a superconducting dynamo-type flux pump. Sci. Rep. 2021, 11, 10296.

[162] Ghabeli, A., Pardo, E. Modeling of airgap influence on DC voltage generation in a dynamo-type flux pump. Supercond. Sci. Technol, 2020, 33(3), 035008.

[163] Forrest, Stephanie. "Genetic algorithms." ACM computing surveys (CSUR) 28.1 (1996): 77-80.

[164] Reyes-Sierra, Margarita, and CA Coello Coello. "Multi-objective particle swarm optimizers: A survey of the state-of-the-art." International journal of computational intelligence research 2.3 (2006): 287-308.

[165] Emiliano Guerra, "Dimensionamento di un impiando di alimentazione contactless di tipo dynamo flux pump per magneti superconduttivi di centrali a fusione", Master thesis, University of Bologna, 2022.

[166] E. Commisison, "EcoSwing - Energy Cost Optimization using Superconducting Wind Generators - World's First Demon-stration of a 3.6 MW Low-Cost Lightweight DD Superconducting Generator on a Wind Turbine," https://cordis.europa.eu/project/id/656024.

[167] Bergen, A., Andersen, R., Bauer, M., Boy, H., Ter Brake, M., Brutsaert, P., ... & Yagotyntsev, K., Design and in-field testing of the world's first ReBCO rotor for a 3.6 MW wind generator. Supercond. Sci. Technol. 2019, 32, 12.

[168] Song, X., Bührer, C., Mølgaard, A., Andersen, R. S., Brutsaert, P., Bauer, M., ... Seitz, E. Commissioning of the World's First Full-Scale MW-Class Superconducting Generator on a Direct Drive Wind Turbine. IEEE Trans. on Ener. Conv. 2020, 35, 1697-1704.

[169] Song, X. et al "Designing and Basic Experimental Validation of the World's First MW-Class Direct-Drive Superconducting Wind Turbine Generator." IEEE Trans. on Ener. Conv. 2019, 34, 2218-2225.

[170] Wiezoreck, J. Cryogenic design of the EcoSwing 3.6 MW superconducting wind generator. In proceeding of the 2nd International Workshop HTS Applications, Karlsruhe, Germany, Sep. 13–15, 2017.

[171] THEVA. Available online: https://www.theva.com. (accessed on 31/05/2022).

[172] Song, X., Bührer, C., Brutsaert, P., Ammar, A., Krause, J., Bergen, A., ... Seitz, E. Ground Testing of the World's First MW-Class Direct-Drive Superconducting Wind Turbine Generator. IEEE Trans. on Ener. Conv. 2020, 35, 757-764.

[173] Allweins, K., Marzahn, E. Feasibility of HTS dc cables on board a ship. 10th EPRI Superconductivity Conf. Nexans Deutschl. GmbH, 2011.

[174] Morandi, A. HTS dc transmission and distribution: concepts, applications and benefits. Supercond. Sci. Technol. 2015, 28, 12.

[175] Morandi, A., Gholizad, B., Stieneker, M., Stagge, H., De Doncker, R. W. Technical and Economical Evaluation of DC High-Temperature Superconductor Solutions for the Grid Connection of Offshore Wind Parks. IEEE Trans. Appl. Supercond. 2016, 26, 1-10.

[176] Masson, P. Power devices design and optimization. In proceeding of the ASC Short Course, Portland, Oregon, USA 7/10/2012.

[177] Bauer, B. (ThyssenKrupp Transrapid GmbH, München, Bayern, Germany) Personal communication 2021.

[178] Kails, K., Zhang, H., Machura, P., Mueller, M., Li, Q. Dynamic loss of HTS field windings in rotating electric machines. Su-percond. Sci. Technol. 2020, 33, 4.

[179] Sung, H. J., Badcock, R. A., Go, B. S., Park, M., Yu, I. K., Jiang, Z. Design of a 12-MW HTS wind power generator including a flux pump exciter. IEEE Trans. Appl. Supercond. 2016, 26, 1-5.

[180] Kirby, G., Galvin, T., Coll, D., Stevenson, R., Livesey, P. Varistor Insulation for HTS Magnets. IEEE Trans. Appl. Supercond. 2022, 32, 1-4.

[181] Yang, S. Cryogenic characteristics of IGBTs. Doctoral dissertation, University of Birmingham, Birmingham July 2005.

[182] Rajashekara, K., Akin, B. A review of cryogenic power electronics-status and applications. In proceeding of the International Electric Machines & Drives Conference. IEEE, May 2013, 899-904.

[183] Gui, Handong, et al. "Review of power electronics components at cryogenic temperatures." IEEE transactions on power electronics 35.5 (2019): 5144-5156.

[184] Federici, G., et al. "The EU DEMO staged design approach in the Pre-Concept Design Phase." Fusion Engineering and Design 173 (2021): 112959.

[185] Claessens, Michel. ITER: The giant fusion reactor. Cham, Switzerland: Springer International Publishing, 2020.

[186] Ambrosino, R. "DTT-Divertor Tokamak Test facility: A testbed for DEMO." Fusion Engineering and Design 167 (2021): 112330.

[187] Mitchell, N., et al. "The ITER magnet system." IEEE Transactions on applied superconductivity 18.2 (2008): 435-440.

[188] Zito, P., et al. "Final design of the DTT Toroidal power supply circuit." Fusion Engineering and Design 192 (2023): 113595.

[189] A. Cocchi, G. De Marzi, A. Lampasi, and R. Romano, "Electrothermal design of DC busbars for fusion facilities", Fusion Engineering and Design, vol.170, Sept. 2021, Art. no. 112662.

[190] DTT S. c. a r. l. "Design of DC busbars", Internal report (2022) pg 1-19.

[191] «ENEA & DTT, "Divertor Tokamak Test facility Interim Design Report", April 2019».

[192] Y. Kim et al., "YBCO Bi2223 coils high field LTS/HTS NMR magnets: HTS-HTS joint resistivity," IEEE Trans. Appl. Supercond., vol. 23, no. 3, Jun. 2013, Art. no. 6800704.

[193] S. K. Jhajharia, "Thyristor converters are more energy efficient than diode converters for the electrolysis of the non-ferrous metals-A case study in aluminium smelters at Hindalco, India," 2016 doi: 10.1109/POWERI.2016.8077151.

[194] Weiss, Jeremy D., et al. "Performance of low-loss demountable joints between CORC® cable-in-conduit-conductors at magnetic fields up to 8 T developed for fusion magnets." Superconductor Science and Technology (2023).

[195] Ballarino, Amalia, and Thomas Taylor. "Scaling of superconducting switches for extraction of magnetic energy." IEEE Transactions on Applied Superconductivity 20.3 (2010): 2031-2034.

[196] Bykovskiy, Nikolay, Alexey Dudarev, and Matthias Mentink. "10. Superconducting switches for energy extraction in fusion magnets." Superconductors for Fusion: a Roadmap 6 56.

[197] Mitchell, Neil, et al. "Superconductors for fusion: a roadmap." Superconductor science and technology 34.10 (2021): 103001.

[198] Kirby, G., et al. "Varistor Insulation for HTS Magnets." IEEE Transactions on Applied Superconductivity 32.6 (2022): 1-4.